Dynamics in colloid and protein systems: Hydrodynamically structured particles, and dispersions with competing attractive and repulsive interactions

Inaugural-Dissertation

zur Erlangung des Doktorgrades
der Mathematisch-Naturwissenschaftlichen Fakultät
der Heinrich-Heine-Universität Düsseldorf

vorgelegt von

Jonas Riest
aus Freudenberg

Düsseldorf, Februar 2016

aus dem Institute of Complex Systems (ICS-3),
Forschungszentrum Jülich GmbH

Gedruckt mit der Genehmigung der
Mathematisch-Naturwissenschaftlichen Fakultät der
Heinrich-Heine-Universität Düsseldorf

Referent: Prof. Dr. Gerhard Nägele

Koreferent: Prof. Dr. Hartmut Löwen

Tag der mündlichen Prüfung: 27.04.2016

Preface

Part of the work presented in this thesis is already published in peer-reviewed international journals, or is in preparation. In the following, I list all these publications, specify my personal contributions therein, and denote where a specific publication is used in the thesis.

1. **Short-time dynamics in dispersions with competing short-range attraction and long-range repulsion**
   J. Riest and G. Nägele, *Soft Matter* **11**, 9273-9280 (2015).
   I performed all the theoretical calculations shown in the paper based on discussions with G. Nägele. The mansuscript was jointly written by G. Nägele and me.
   The content of this article is used in Sec. 2.3 and Chapter 8.

2. **Dynamics of suspensions of hydrodynamically structured particles: analytic theory and applications to experiments**
   J. Riest, T. Eckert, W. Richtering and G. Nägele, *Soft Matter*,**11**, 2821-2843 (2015).
   This comprehensive publication was written in collaboration with T. Eckert and W. Richtering from the RWTH Aachen University who provided already published data of SLS and DLS measurements on non-ionic microgel suspensions. I performed all the theoretical calculations, and I did all the data analysis including the fitting of the experimental data presented in the paper, supported by helpful discussions with G. Nägele. The manuscript was jointly written by G. Nägele and me.
   Subsecs. 4.1.4, 4.4.1-4.4.3, Sec. 2.1, and Chapter 5 are based on this reference.

3. **Comparison of the microstructure of stimuli responsive zwitterionic PNIPAM-co-sulfobetaine microgels with PNIPAM microgels and classical hard-sphere Systems**
   A. J. Schmid, J. Riest, T. Eckert, P. Lindner, G. Nägele, and W. Richtering, *Zeitschrift für Physikalische Chemie* **228**, 1033-1052 (2014).
   This paper is based on a collaboration with A. J. Schmid, T. Eckert and W. Richtering from the RWTH Aachen University, and P. Lindner from the ILL Grenoble. These experimental collaborators performed the SANS measurements on zwitterionic microgels. I did all the polydisperse hard-sphere calculations, and part of the experimental data analysis. Moreover, I wrote the theory part of the paper, the results part about the experiment-theory comparison, and contributed to the writing

of the introduction and conclusion. G. Nägele provided valuable input especially regarding the theoretical methods.
This publication is used in Secs. 2.4, 3.5 and Chapter 7.

4. **Ultrafilltration of charge-stabilized colloidal dispersions at low salinity**
R. Roa, D. Menne, P. Buzatu, J. Riest, J. K. G. Dhont, E. Zholkovskiy, M. Wessling and G. Nägele, to be submitted (2016)
In this joint theoretical-experimental collaboration in the framework of the SFB 985 (project B6), the cross-flow ultrafiltration (UF) of charge-stabilized silica suspensions is studied mostly theoretically, but also including a comparison with UF experiments. The cross-flow UF experiments have been performed by P. Buzatu and D. Menne in the group of M. Wessling (RWTH Aachen University and DWI Aachen). My contribution to this paper is the calculation of all discussed thermodynamic and transport properties of the charged-particles dispersion, which constitutes the main contribution to the publication. Using my theoretical and numerical input, R. Roa performed the UF model calculations with my support, and additionally the PB calculations. G. Nägele and J. K. G. Dhont initiated the collaboration and provided guidance through many discussions.
The content of this article is used in Subsec. 2.2.2 and Sec. 6.2.

5. **Short-time dynamics of Lysozyme solutions with competing short-range attraction and long-range repulsion: Experiment and theory**
J. Riest, Y. Liu, G. Nägele, N. J. Wagner, and P. D. Godfrin, in preparation (2016).
This manuscript in preparation is based on a collaboration with Y. Liu (NIST, Gaithersburg), N. J. Wagner (UDEL, Delaware), and P.D. Godfrin (UDEL/MIT, Delaware/Boston) who performed the SANS and NSE measurements, and provided the pair potential parameters deduced from the experimental data. I did all the static and dynamic theoretical calculations, and performed the comparison with the experimental data.
This article is used in Sec. 8.2.

6. **Simulation and theory of generalized Lennard-Jones Yukawa systems with competing interactions**
J. Riest, S. Das, G. Gompper, G. Nägele, and R. G. Winkler, in preparation (2016).
In this joint theoretical-simulation study, the MPC simulation part has been performed in the IAS-2 / ICS-2 of the Forschungszentrum Jülich by S. Das, G. Gompper, and R. G. Winkler. I performed the ZH-IET theory part, and the BM-PA calcula-

tions of static and dynamic transport properties, with some guidance by G. Nägele. The paper is used in Subsec. 8.3.3.

7. **Systematic study of diffusion and rheology in systems with competing short-range attraction and long-range repulsion**
   J. Riest, and G. Nägele, in preparation (2016).
   I did all the theoretical calculations and computer simulations which have been analyzed theoretically by G. Nägele and me.
   Results in this manuscript in preparation are used in 8.1.

Additional publications by the author of this thesis:

8. **Elasticity of polymeric nanocolloidal particles**
   J. Riest, L. Athanasopoulou, S. A. Egorov, C. N. Likos, and P. Ziherl, *Scientific Reports* **5**, 15854 (2015).

9. **Coarse-graining of ionic microgels: Theory and experiment**
   J. Riest, P. Mohanty, P. Schurtenberger, and C. N. Likos, *Zeitschrift für Physikalische Chemie* **226**, 711-735 (2012).

10. **Ultrafiltration modeling of charge-stabilized colloidal dispersions**
    R. Roa, J. Riest, M. Brito, and G. Nägele, in preparation (2016).

Previous theses:

- Master thesis: **Molekulardynamiksimulationen zur Bestimmung der elastischen Eigenschaften sphärischer Polymerbürsten**
  J. Riest, Supervisor: Prof. C. N. Likos, University of Vienna, 2012.

- Bachelor thesis: **Dichtefunktionaltheorie deformierbarer Kugeln**
  J. Riest, Supervisor: Prof. C. N. Likos, Heinrich-Heine-Universität Düsseldorf, 2010.

Abstract

In this thesis, we develop and apply a toolbox of versatile theoretical methods of calculating structural, and short-time and long-time dynamic properties of three classes of industrially important dispersions. The first one are suspensions of hydrodynamically structured colloidal particles, and here most notably non-ionic microgels. The second class are dispersions of submicron sized charge-stabilized colloidal globules, and the third one are globular protein solutions with competing short-range attraction (SA) and long-range repulsion (LR). The results for the transport, structure, and thermodynamic properties of charge-stabilized colloids are used as input in our realistic macroscopic diffusion-advection modeling of the membrane cross-flow ultrafiltration of silica particles dispersions. The thesis bridges thus the gap from the theoretical exploration of intra-particle properties such as solvent permeability, particle softness, and surface charge, to the calculation of transport, structural, and thermodynamic properties of concentrated dispersions, and to the modeling of a technologically important filtration process. The accuracy of our toolbox methods is assessed by the comprehensive comparison with experimental measurements of, and simulation results for static and dynamic properties. The considered dynamic properties include short- and long-time self-diffusion and sedimentation coefficients, the wavenumber-dependent diffusion function determined routinely in dynamic scattering experiments, and the zero- and high-frequency shear viscosities.

In particular, we provide various analytic transport coefficient expressions for rigid permeable particles that can be readily used for the analysis of dynamic scattering and rheology data. The toolbox methods for the calculation of transport properties of concentrated dispersions of globular colloidal particles with internal hydrodynamic structure are based on the hydrodynamic radius model (HRM) wherein the internal particle structure is mapped on an effective hydrodynamic radius for unchanged direct interactions. The good performance of the HRM is demonstrated by comparison with dynamic light scattering experiments on concentrated suspensions of solvent permeable non-ionic microgels. Furthermore, we quantify the effect of particle softness and permeability on the dynamics of ionic microgel suspensions, and we characterize the particle interactions and microstructure in polydisperse amphoteric microgel systems in the zwitterionic regime.

In addition, we thoroughly investigate the influence of transient clustering on the statics and dynamics of globular particles dispersions with competing short-range attractive (SA) and long-range repulsive (LR) interactions. SALR systems such as low-salinity protein solutions have attracted considerable interest over the past years, due to the observation of

a low-wavenumber peak of the static structure factor indicative of particle clustering. In this thesis, we present the first systematic theoretical study of the effect of clustering on short-time transport properties. Using our analytic toolbox methods, we systematically explore two classes of SALR models, in conjunction with computer simulations and experiments on Lysozyme protein solutions. Our results show that the low-wavenumber peak is present also in the hydrodynamic function characterizing the short-time dynamics, in good qualitative agreement with neutron spin echo measurements. The subtle interplay of SA and LR is highlighted by an unusual non-monotonic interaction strength dependence of the mean sedimentation velocity.

Finally, we describe theoretically the membrane ultrafiltration (UF) process of low-salinity charge-stabilized particles dispersions. The importance of accurate thermodynamic and transport properties as salient inputs to the macroscopic modeling is demonstrated by the excellent agreement of our theoretical model predictions with UF measurements of the permeate flow for low-salinity silica suspensions.

Zusammenfassung

In der vorliegenden Dissertation befassen wir uns mit der Entwicklung und Anwendung einer vielseitig anwendbaren Sammlung von theoretischen Methoden ("Toolbox") zur Berechnung von Kurzzeit- und Langzeittransportkoeffizienten sowie struktureller Größen von drei Klassen industriell relevanter Dispersionen. Die erste Klasse sind Suspensionen kolloidaler Teilchen mit innerer hydrodynamischer Struktur und hier insbesondere nicht-ionische Mikrogele. Die zweite Klasse umfasst ladungsstabilisierte Dispersionen sphärischer kolloidaler Teilchen und die dritte Lösungen sphärischer Proteine mit vergleichbar starker kurzreichweitiger Attraktion und langreichweitiger Repulsion. Die mit unserer analytischen Toolbox gewonnenen Ergebnisse über das Transportverhalten, Mikrostruktur und thermodynamischen Eigenschaften dieser Systeme sind wichtiger Input für unsere realistische Modellierung der Querfluss-Ultrafiltration von wässrigen Suspensionen geladener Silicateilchen. Diese Modellierung basiert auf einer makroskopischen Diffusions-Advektions-Beschreibung von Teilchen und dispergierender Flüssigkeit. Die Dissertation schlägt somit eine Brücke von der grundlegenden theoretischen Beschreibung intrinsischer Teilcheneigenschaften, wie z.B. der Lösungsmittelpermeabilität, Oberflächenladung und Elastizität, zu der Berechnung von Transport-, Struktur- und thermodynamischen Größen konzentrierter Dispersionen von Teilchen und darüber hinaus zu der Modellierung eines technologisch wichtigen Filtrationsprozesses. Die Genauigkeit der verwendeten Toolbox-Methoden wird geklärt durch umfassende Vergleiche mit Simulationen und experimentellen Ergebnissen statischer und dynamischer Messgrößen. Die dynamischen Größen umfassen dabei Kurzzeit- und Langzeit-Selbstdiffusionskoeffizienten, Sedimentationsgeschwindigkeiten, routinemäßig in dynamischen Lichtstreuexperimenten bestimmten wellenzahlabhängigen Diffusionsfunktionen sowie Viskositäten unter Hochfrequenz- und Nullfrequenzbedingungen.

Für Suspensionen harter permeabler Teilchen leiten wir analytische Ausdrücke für diverse Transportkoeffizienten her, welche für die Analyse dynamischer Lichtstreu- sowie rheologischer Messungen vorteilhaft genutzt werden können. Unsere Toolbox-Methoden zur Berechnung der Transporteigenschaften konzentrierter Dispersionen hydrodynamisch strukturierter Teilchen basieren auf dem hydrodynamischen Radius Modell (HRM). In diesem Modell wird die innere hydrodynamische Struktur eines Teilchens durch einen effektiven hydrodynamischen Radius beschrieben, wobei die direkten Wechselwirkungen unverändert bleiben. Wir demonstrieren die Leistungsfähigkeit des HRM durch den Vergleich unserer theoretischen Ergebnisse mit dynamischen Lichtstreumessungen an konzentrierten,

nicht-ionischen und permeablen Mikrogel Suspensionen. Des Weiteren quantifizieren wir den Einfluss der Elastizität und Permeabilität ionischer Mikrogelteilchen auf die Systemdynamik. Für Suspensionen polydisperser amphoterischer Mikrogele im zwitterionischen Bereich berechnen wir aus den Teilchenwechselwirkungen die resultierende Mikrostruktur. Weiterhin analysieren wir für Dispersionen sphärischer Teilchen mit vergleichbarer kurzreichweitiger attraktiver (SA) und langreichweitiger repulsiver (LR) Wechselwirkung den Einfluss transienter Teilchencluster auf die statischen und dynamischen Eigenschaften des Systems. Vor allem die Struktur und das Phasenverhalten von SALR Systemen wurden in den vergangenen Jahren eingehend untersucht. Insbesondere findet man für diese Systeme einen Strukturfaktorpeak bei niedrigen Wellenzahlen, welcher als eine Signatur für die Existenz (transienter) Cluster interpretiert wird. Wir beschreiben in der vorliegenden Dissertation die erste systematische theoretische Analyse des Einflusses transienter Clusterbildung auf Kurzzeittransporteigenschaften. Unter Verwendung unserer analytischen Toolbox-Methoden und mittels des Vergleiches mit Computersimulationen und Experimenten untersuchen wir eingehend zwei Klassen von SALR Systemen. Wir zeigen in guter Übereinstimmung mit Neutronenspinecho Messungen, dass ein Peak bei niedrigen Wellenzahlen auch in der die Kurzzeitdiffusion charakterisierenden hydrodynamischen Funktion auftritt. Das subtile Wechselspiel von SA und LR manifestiert sich weiterhin in einer überraschend nicht-monotonen Abhängigkeit der mittleren Sedimentationsgeschwindigkeit von dem globalen Wechselwirkungsstärkeparameter.
Abschließend diskutieren wir unsere theoretische Beschreibung des Membran-Ultrafiltrationsprozesses (UF) angewandt auf Suspensionen ladungsstabilisierter Teilchen mit niedrigem Salzgehalt. Durch den Vergleich unserer theoretischen Ergebnisse für den Permeatfluss mit entsprechenden UF Messungen an Silicateilchen Suspensionen zeigen wir, dass für eine quantitative makroskopische Modellierung präzise analytische Ausdrücke für thermodynamische- und Transportgrößen von großer Bedeutung sind.

Contents

1. Introduction

Soft matter systems are ubiquitously found in nature and daily-life products. Examples are blood, ink, adhesives, cosmetics, dairy products, paints, polymer melts, foams, micelles, emulsions, microemulsions, soft glasses, proteins, cells and aerosols. An important subclass of soft matter systems are colloidal dispersions, consisting of mesoscopically sized particles of linear extension $1\,\mathrm{nm} - 1\,\mu\mathrm{m}$ dispersed in a low-molecular solvent such as water or an organic fluid. This definition of colloids includes in particular protein solutions. On the spatial resolution $\gtrsim 1\,\mathrm{nm}$, the solvent can be described as a continuum. For particle radii $\lesssim 1\,\mu\mathrm{m}$ and a lower-viscosity solvent such as water, Brownian particle motion is strong and sedimentation is accordingly weak. While the term colloid was originally used for suspensions of mesoscopic rigid particles, nowadays a broad class of particles of different shapes, stiffness and intra-particle structures such as rods and micelles, are referred to as colloids, and studied using a variety of experimental techniques and theoretical and computer simulation methods [1].

An important feature of colloidal systems is that particles of special size, shape, and electric charge can be readily synthesized. Furthermore, the interaction potentials can be largely varied in range and strength, e.g. by changing the solvent, or by using additives such as small depletants or salt ions. In certain charge-stabilized dispersions, particle charge inversion can be induced by the addition of multivalent ions, or by a temperature change in case of amphiphilic particles. This makes colloids well suited for the design of macroscopic materials of desired properties, and for medical applications such as targeted drug delivery in the case of microgels. The structure and dynamics of bigger colloidal particles can be studied using microscopy, and that of smaller ones by light scattering techniques, allowing for gaining detailed insight into the system behavior.

In the past few years, the study of sophisticated bio-particle systems has shifted into the focus of Soft Matter science [2]. Interestingly, theoretical methods designed for traditional colloidal systems are meanwhile successfully applied to more complicated nanometer-sized particles such as globular proteins and monoclonal antibodies that can have anisotropic interactions [3, 4]. Regarding the dynamics of colloids, not only their direct and hydrodynamic interactions (HIs), but also the internal hydrodynamic particle structure are of importance. The development and validation of calculation methods for static and dynamic properties of biological soft matter systems are important tasks. These methods can contribute to a better understanding of biological processes such as the formation of protein aggregates, and its effect on the Alzheimer and Parkinson diseases [5]. Moreover,

the theoretical modeling of industrial soft matter processes necessitates accurate transport properties expressions. An example in case where biological systems are involved is the filtration of protein suspension in medical industry [6, 7].
In this thesis, we provide and evaluate a toolbox of easy-to-apply analytic methods for the calculation of static and dynamic properties of colloidal systems of globular particles, including globular protein solutions and microgel suspensions. The high accuracy of the employed theoretical methods is validated by a comprehensive comparison with computer simulation results, and with measurements of static and dynamic properties. In contrast to expensive computer simulations, our methods allow for extensive parameter variation studies, providing thus a convenient tool for the analysis of experimental data. The presented methods are applied to a variety of experimental systems spanning a broad size and complexity range. First, neutral microgel particles suspensions are studied where both hard and soft steric interactions are present. Second, we study the structure and dynamics of dispersions of particles with surface or internal charges, namely charged silica particles, and ionic and amphoteric microgel systems, respectively. In addition, we successfully demonstrate the applicability of our calculation methods to low-salinity Lysozyme protein solutions, by focusing here on the structural and dynamic effects arising from the competition of short-range attractive and long-range repulsive (SALR) interaction forces. In the thesis, we bridge the gap from individual intra-particle properties such as softness, fluid permeability, and charge to collective behavior, namely the pair-structure and various transport properties, and furthermore to an important technological process, namely the cross-flow ultrafiltration of charged-particles dispersions. In this context, we demonstrate the importance of the hydrodynamic particle structure, and the usage of accurate transport property expressions as salient input to our filtration model. In fact, analytic transport coefficients are highly useful also for the optimization of industrial processes, i.e, for improving the performance of the filtration process regarding product and energy cost, and product output.
For the calculation of the short-time dynamic properties, notably the hydrodynamic function, $H(q)$, diffusion function, $D(q)$, short-time self-diffusion coefficient, d_{S}, sedimentation velocity, K, collective diffusion coefficient, d_{C}, and high-frequency viscosity, η_{∞}, we employ two convenient analytic calculation schemes. These are the Pairwise-additivity (PA) approximation and the Beenakker-Mazur (BM) methods, respectively. In particular, we present and discuss a PA-BM hybrid scheme combining the advantages of the two methods, and we give generalized transport properties expressions based on the hydrodynamic radius model (HRM). In this model, the internal particle structure is mapped on an effective hydrodynamic radius for unchanged direct interactions. Long-time dynamic properties,

and here most notably the long-time self-diffusion coefficient, d_{L}, and the zero-frequency viscosity, η, are calculated using general scaling relations, and a (simplified) mode-coupling theory method for the memory contribution part.
Considered static properties include the static structure factor, $S(q)$, radial distribution function, $g(r)$, isothermal compressibility, χ_{T}, and the particle osmotic pressure Π. Here, $g(r)$ and $S(q)$ serve as salient input to the PA and BM methods. Depending on the investigated system, we use for their calculation appropriate Ornstein-Zernike integral equation schemes, namely the Percus-Yevick with Verlet-Weis correction, and the hypernetted chain and Zerah-Hansen schemes.
The focus of our theoretical analysis is set on two classes of dispersions of technological and biological importance, respectively. The first class are microgels consisting of cross-linked polymer chains that can be synthesized using a variety of polymeric materials, allowing for the control of their intra-particle properties. The latter are in particular influenced by the interplay with the penetrating solvent molecules. Microgels are highly sensitive to external stimuli such as pH, temperature, salinity, and concentration that influence the particle swelling. This renders microgels as promising candidates for many applications such as carriers in drug delivery [8–11], the engineering of tissues [12–15], the design of switchable membranes for separation processes in water purification and medical technology [16] [17], the modification of rheological properties [18], e.g., in cosmetics and hand soaps [19], and the design of photonic crystals with tunable band gaps and defects [20–23].
Microgels have typically a radially decaying cross-linker density giving rise to soft interactions during inter-penetration. However, we show by comparison with experimental static structure factor measurements that for larger non-ionic microgels, this softness is a very minor effect, with the consequence that the hard-sphere description of microgels becomes quite accurate. Based on this finding, we present a comprehensive toolbox of analytic methods for the calculation of short-time transport properties of particles with internal hydrodynamic structure and hard-sphere-type direct interactions. We exemplify the high accuracy of our toolbox methods by the comparison with dynamic light scattering (DLS) experiments on non-ionic microgels and with simulations, where in the latter case the effect of HIs is included. In addition, we discuss the impact of softness and solvent permeability on the dynamics of ionic microgel systems where the effect of intra-particle hydrodynamics is attenuated by the long-ranged electrostatic repulsion.
Moreover, we extend our toolbox to long-time dynamic properties of concentrated systems of hydrodynamically structured particles. Different from their short-time siblings, long-time transport properties are affected additionally by the non-instantaneous microstructural relaxation of the clouds of neighboring Brownian particles. This relaxation is con-

trolled both by direct and hydrodynamic interactions. Our toolbox extension to long-time properties combines the HRM with a factorization approximation method introduced originally by Medina-Noyola [24], and elaborated subsequently by Brady [25, 26] and Banchio *et al.* [27].

Different from the aforementioned microgel systems, amphoteric microgels contain both acidic and basic co-monomers. As a consequence, they do not just show a single volume phase transition but swell in acidic and basic environments, and collapse in the intermediate pH-regime. In this so-called zwitterionic regime, the particle collapse is caused by the domination of ion pairing between oppositely charged groups over the repulsion between groups of the same charge [28]. Thus, internal salts are forming accompanied by the release of counterions [29]. To investigate the influence of the oppositely charged groups on the interaction potential of zwitterionic microgels, we compare concentration series measurements of the measurable static structure factor on samples with various amounts of the zwitterionic co-monomer with polydisperse hard-sphere calculations. We observe that the zwitterionic microgels are well described by the hard-sphere model for total volume fractions $\phi_{\mathrm{T}} \lesssim 0.4$, irrespective of the amount of zwitterionic co-monomer.

In addition to microgel systems, we further study Brownian particle systems with short-range attraction (SA) and long-range repulsion (LR) such as low-salinity lysozyme protein solutions, and suspensions of micron-sized charged colloidal particles with added depletant. SALR systems have been intensely studied over the past years [2, 30–36]. In particular, the interesting phase behavior of SALR systems including equilibrium-cluster and percolated-cluster states has been investigated. These investigations have been triggered by the finding of a low-wavenumber (low-q) peak in the static structure factor $S(q)$, indicative of intermediate-range microstructural ordering arising from the competing SA and LR [2, 32]. SALR protein systems are particularly interesting since the clustering of proteins can result in severe diseases such as Alzheimer and Parkinson [5, 37], or cateract formation [38].

In comparison with the large body of work on the structure and phase behavior of SALR systems, little is known to date about their dynamic properties. This concerns in particular theoretical and simulation works on these systems that are challenging owing to the important influence of the HIs. A complication in the theoretical description of cluster states arises from the presence of additional time and length scales associated with the distributions of cluster lifetimes, sizes and charges. This hampers a clear distinction between colloidal short-time and long-time regimes, as it can be made for a homogeneous suspension of individually diffusing monodisperse particles. An interesting experimental observation pointing to these complications is the surprising observation that the short-

and long-time self-diffusion coefficients for salt-free lysozyme solutions deduced from neutron spin echo (NSE) data share roughly the same concentration dependence [32].
As an important part of this thesis, we present a generic theoretical study of short-time diffusion and rheological transport properties of two SALR model systems by employing our toolbox of well tested analytic methods that account for the salient HIs. We use isotropic pair potentials to describe phenomenologically the orientationally averaged SA of globular proteins, plus the for low salinity systems long-ranged electric double layer repulsion originating from the protein charges and surface-released counterions. The static input to our toolbox of dynamic methods can be calculated to excellent accuracy for the dispersed-fluid phase region, as we are going to show in comparison with Monte-Carlo simulation data of the radial distribution function, $g(r)$, using the thermodynamically self-consistent Zerah–Hansen (ZH) integral equation scheme. We show that the dynamics has unusual features compared to reference systems with pure repulsion or attraction, and we reveal the presence of a low-q peak in the hydrodynamic function $H(q)$, resulting from the competition of SA and LR.
Static and dynamic dispersion properties including the osmotic suspension pressure, Π, and compressibility, $\chi_{\rm OSM}$, and the dispersion viscosity, η, and (long-time) collective diffusion coefficient, $d_{\rm C}^{\rm L}$, are salient inputs to the modeling of ultrafiltration (UF) processes. UF is an extensively used low-energy cost method for the separation and concentration of smaller colloidal or bio-particles [39] such as proteins, macromolecular drugs, and nano-sized microgel particles. In UF, Brownian motion is strong but hydrodynamic diffusion and migration mechanisms are weak in comparison. In this thesis, we address in addition to transport bulk properties calculations the cross-flow UF of electrostatically strongly repelling colloidal silica particles under low-salinity conditions. We use a theoretical description based on the one-component macroion fluid model which ignores the electrokinetic microionic effects but accounts for the strong influence of surface-released counterions on the renormalized colloidal charge and screening parameter. The static suspension properties are calculated by using integral equation theory in combination with a Poisson-Boltzmann (PB) cell model, and are employed as input to our analytic calculations of accurate transport coefficients. These coefficients are used as input to the cross-flow UF model previously employed by Roa *et al.* [39] for permeable hard-sphere suspensions. Our theoretical results for the cross-flow permeate flux are shown to be in very good agreement with filtration experiments on aqueous suspensions of charge-stabilized silica particles.

The thesis is organized as follows:

In Chapter 2, we describe the explored systems and pose our main research questions.

Moreover, we put our work in the context of recent research, and point to possible applications.

The essentials of the equilibrium microstructure methods of calculation, and the employed Ornstein-Zernike closure relations used for the calculation of static dispersion properties are presented in Chapter 3.

In Chapter 4, we discuss the time- and length scales, and the governing equations associated with the Brownian motion of colloidal particles in a low-molecular solvent. We focus especially on hydrodynamic particle models and boundary conditions used to account for the internal hydrodynamic particle structure. Furthermore, we discuss the notion of hydrodynamic interactions (HIs), and transport properties characterizing the system dynamics. Chapter 4 is complemented by the explanation of the methods of calculation employed in this thesis for various short- and long-time dynamic properties.

The results of our analytic toolbox of methods for calculating short- and long-time transport properties of permeable hard-sphere dispersions are presented in Chapter 5. In addition, we exemplify the high accuracy of our toolbox methods by comparison with benchmark simulations, and experimental data for the wavenumber-dependent diffusion function, $D(q)$, of non-ionic microgel particles. Moreover, we test the accuracy of generalized Stokes-Einstein relations relating rheological and diffusion properties.

In Chapter 6, we discuss first the impact of softness and permeability on the short-time dynamics of ionic microgel suspensions. Secondly, we model and study the cross-flow UF process of charged silica particle systems. For this purpose, we employ a charge renormalization procedure to account for the effects of surface released counterions on static and transport properties. The Chapter is concluded by a comparison of the predictions by our UF model with UF experiment results on charged silica particles, showing the good accuracy of our model calculations.

The measured static structure factors, $S_{\mathrm{M}}(q)$ of zwitterionic microgels are compared to polydisperse hard-sphere calculations in Chapter 7, in order to investigate the influence of the zwitterionic co-monomer on the particle interactions.

In Chapter 8, we thoroughly discuss static and transport properties of SALR systems. To this end, we systematically study parameter variations of the SALR potential to reveal the individual effect of SA and LR. We show that a balance between SA and LR is necessary for a low-q peak not only of the static structure factor, $S(q)$, but also of the hydrodynamic function $H(q)$. In particular, we highlight that intermediate-range microstructural ordering is a general feature of SALR systems and is not explainable using a purely monotonic continuous pair potential part, as we show by the comparison with the theoretical predictions for the hard-core two-Yukawa and Lennard-Jones Yukawa SALR potential

systems. In the first considered SALR model, hard-core excluded volume interactions are combined with short- and long-range Yukawa potential parts. In the second considered model referred to as the LJY model, a $100-50$ Lennard-Jones (LJ) potential is used to describe the soft steric plus SA interactions, while the LR part is modeled by a repulsive Yukawa potential. Note that in low-salinity protein solutions, LR is caused by electrostatic particle interactions while the origin of the SA is still under debate (c.f. Sec. 2.3). Furthermore, we discuss the applicability of generalized Stokes-Einstein (GSE) relations to SALR systems. A comparison of our theoretical $H(q)$ predictions with neutron spin echo (NSE) measurements of $H(q)$ for Lysozyme solutions shows qualitative agreement. As an outlook, we present first results of an ongoing theory-simulation collaboration where the accuracy of our analytic toolbox calculations of transport properties for a LJY-SALR system is assessed through the comparison with multi-particle collision dynamics (MPC) computer simulations that fully account for the HIs.
The thesis is concluded in Chapter 9, where also possible future applications and extensions of the presented work are discussed.
In the Appendix, we give the details of the employed integral equation schemes, and explain the dynamic calculation methods.

2. Explored systems and interaction models

In this chapter, we introduce the central research questions addressed in the thesis. For this purpose, we provide an overview over the explored systems, discuss their importance, and describe exemplary applications. In particular, we show that colloidal methods help to understand and predict the equilibrium structure and dynamics of a broad variety of particulate systems ranging from classical colloidal systems of submicron sized particles to biological macromolecules of a few nanometers in diameter. We are especially interested in how single particle properties such as permeability, softness and electric charge are affecting the transport properties. The results for the systems introduced in this Chapter are presented in Chapters 5 ff.

2.1. Hydrodynamically structured particles

2.1.1. Necessity of hydrodynamic particle modeling

Suspensions of globular colloidal particles with internal hydrodynamic structure and different surface boundary conditions are abundant in Soft Matter science. Examples of technological and biomedical relevance are non-ionic and ionic microgel suspensions, and spherical core-shell particles consisting of a dry core and a shell of a soft material such as a polymer brush. The particles in these systems are to a certain degree permeable to the solvent. Microgel particles in particular consist of a network formed by cross-linked polymer chains. They have useful features such as a temperature-, pH-, salinity- and concentration-dependent [40] swelling behavior, as well as elasticity and flexibility. This renders microgels as good candidates for various applications such as drug delivery [8–10], the engineering of tissues [12–15], and the modification of rheological properties e.g. in cosmetics [18, 19]. Additionally, microgels have been employed in the design of photonic crystals with tunable band gaps and defects [20–23] and the fabrication of switchable membranes for separation processes in water purification and medical technology [16, 17]. The elasticity of microgels can be controlled, e.g., by the amount of cross-linker and the length of polymer chains used in their synthesis. Microgels can be therefore considered as bridging the gap between genuine colloidal hard spheres and ultra-soft colloids [41].
Although microgel and core-shell particle systems have been intensely studied experimentally over the past years, a quantitative theoretical description of the diffusion and rheological properties of concentrated suspensions is still in demand. This is owed to the

complicated many-particle hydrodynamic interactions (HIs) which are significantly influenced by the internal hydrodynamic structure of the particles. Surprisingly, despite the commonly complex internal structure of colloidal systems, it is usually sufficient to use only a single parameter for the description of solvent particle interactions such as the effective solvent penetration depth. The simplicity of hydrodynamic particle models allows for the calculation of analytic expressions for transport properties. In Fig. 2.1, the hydrodynamic particle modeling procedure and a selection of models is sketched. We will discuss the different models in detail in Subsec. 4.1.4

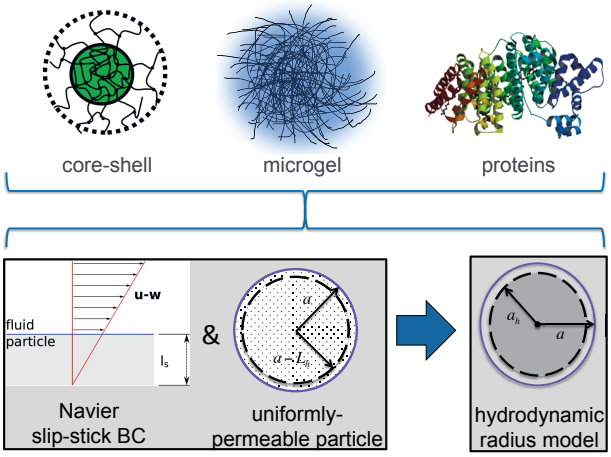

Fig. 2.1.: Sketch of the simplifying hydrodynamic particle modeling procedure. For details about the different particle models, see Subsec. 4.1.4.

The theoretical understanding of the influence of HIs on colloidal transport properties such as translational and rotational diffusion coefficients, the hydrodynamic function, and high-frequency and zero-frequency viscosities is of key importance also in process engineering, e.g. in filtration and fractionation processes [39, 42], and for the energy cost reduction in the transportation of colloidal suspensions by means of viscosity minimization. Technological applications require analytic expressions of transport properties, serving as input and allowing for easy parameter variation.

On a coarse-grained level, the porosity-averaged fluid flow inside a solvent-permeable particle is commonly described by the Brinkman-Debye-Bueche (BDB) equation invoking the Darcy permeability, κ^2, where $1/\kappa$ is the hydrodynamic penetration length [43, 44]. Globular particles with an on average spherically symmetric hydrodynamic structure can be characterized by a permeability coefficient, $\kappa(d)$, depending on the radial distance, d, from the particle center [45]. Versatile hydrodynamic simulation tools such as the HY-

DROMULTIPOLE hydrodynamic force multipole method [46] have been developed which allow for calculating transport properties of concentrated dispersions of hydrodynamically structured particles with the full inclusion of HIs. However, these simulations are numerically expensive, and in principle they must be performed separately for each particle model. In a recent series of papers, various short-time dynamic properties of dispersions of uniformly permeable spheres [47–50], and of core-shell particles with uniformly permeable shell [51–53], have been calculated using the HYDROMULTIPOLE method, as functions of particle concentration, reduced Darcy permeability, and shell-thickness to particle size ratio. The non-hydrodynamic direct particle interactions in these simulations have been taken for simplicity as pure hard-core interactions characterized by the excluded volume particle radius $a = \sigma/2$. Any softness in the effective pair potential, $V(r)$, between two globular particles at the center-to-center distance r is hereby disregarded.

As discussed in Refs. [52–54], a simplifying concept allowing for abstracting from specific intra-particle structures is the so-called hydrodynamic radius model (HRM) which invokes the notion of an apparent no-slip hydrodynamic particle radius $a_{\rm h}$ (see also Refs. [55, 56]). The HRM amounts to approximating a globular particle of spherically symmetric hydrodynamic structure by a no-slip sphere of hydrodynamic radius a_h, while leaving the effective pair potential unchanged. Under from an experimental viewpoint surprisingly general conditions, a_h is unequivocally determined from the measurement of a single-particle transport property such as the translational diffusion coefficient, d_0, or the intrinsic viscosity $[\eta]$. The definition of the HRM includes also spherical particles with fuzzy hydrodynamic structure and no sharp outer boundary, and with a soft pair potential such as for weakly cross-linked ionic microgels [40, 57, 58]. For spherical particles with excluded volume interactions only where $a_h < a$, the HRM reduces to the so-called spherical annulus model. For the annulus model, numerically precise simulation results for various short-time dynamic properties have been given in Ref. [51]. The good accuracy of the simplifying HRM was demonstrated in Refs. [49, 51, 59] for uniformly permeable and core-shell spheres with pure excluded volume interactions, by a thorough comparison with simulation results. While a single hydrodynamic radius suffices to characterize the hydrodynamic intra-particle structure of many experimentally realized suspensions regarding its influence on configuration-averaged transport properties, the replacement of the soft pair potential by an effective hard-core potential is in general a less successful strategy regarding the statics. Methods of calculating static suspension properties based on an effective hard-sphere potential such as the Barker-Henderson perturbation scheme, a second virial coefficient mapping method, and variational methods commonly fail if the longer-ranged soft part of the pair potential stretches out significantly beyond the physical

excluded volume radius. For charge-stabilized colloids, e.g., this has been shown in Refs. [60, 61].
We will exemplify the applicability of the HRM in this thesis by the comparison with short-time measurements on non-ionic microgels discussed in Chapter 5. For this purpose, we will use both the hard-sphere and soft Hertz potentials. Both potentials have been successfully employed in studies of microgels, which show a mesh-like structure accompanied by (size-dependent) stiff particle interactions. In addition, we present an extensive toolbox of methods for the calculation of short- and long-time dynamic properties of concentrated dispersions of stiff, permeable particles, based on the HRM and the hard-sphere interaction potential.

2.1.2. Pair potential models

Owing to many possible applications, various theoretical schemes have been developed for the analytic calculation of static properties of microgel suspensions. Progress in this direction was made in particular for ionic microgels through the development of effective pair potentials characterized by the suspension temperature and salinity, and the bare charge of the microgel particles [62–64]. The validity of these effective pair potentials has been scrutinized in various joint theoretical-experimental studies (see e.g. Refs. [57, 65]). In contrast to ionic microgels, the effective pair potentials used for non-ionic soft microgels where short-range interactions are not masked by the longer-ranged electrostatic repulsion, are to date still on a more heuristic level. The pronounced dependence of the pair potential in non-ionic microgel systems on ambient and intra-particle conditions such as the solvent quality and temperature, number and distribution of cross-linker, and the length and functionality of polymer chains requires a larger number of parameters characterizing the effective pair potential on a microscopic scale. On a more coarse-grained level, simplifying pair potentials have been used such as the hard-sphere [66] and elastic Hertz [57, 67] potentials, and certain ultra-soft pair potentials [41]. The intricate dependence on environmental parameters is hidden in these coarse-grained potentials in a reduced number of interaction parameters such as the effective interaction strength and the effective particle radius.

Hertz potential

A useful coarse-grained effective pair potential for non-ionic globular microgel particles of low cross-link density, and for the excluded volume interaction part of ionic microgels (c.f.

Sec. 2.2.1), is given by the Hertz potential,

$$\beta V(r) = \begin{cases} \epsilon \left(1 - \frac{r}{\sigma_\mathrm{s}}\right)^{\frac{5}{2}} & r \leq \sigma_\mathrm{s} \\ 0 & r > \sigma_\mathrm{s} \,. \end{cases} \tag{2.1}$$

This potential describes the energy penalty caused by the elastic deformation of two colliding spheres [57, 68]. Here, $\beta = 1/(k_\mathrm{B}T)$ is the reduced inverse temperature with Boltzmann constant k_B and absolute temperature T, and σ_s plays the role of an effective soft particle diameter. For distances $r \geq \sigma_\mathrm{s}$, two Hertz-model particles do not interact with each other. The strength of the continuous potential is quantified by the non-dimensional elasticity parameter (effective potential strength),

$$\epsilon = \frac{2Y\sigma_\mathrm{s}^3}{15k_\mathrm{B}T\left(1-\nu^2\right)} \,, \tag{2.2}$$

depending on the bulk modulus, Y, and the Poisson ratio, ν, of a particle [57, 68]. On approximating the mesoscopic particle elastic moduli Y and ν by macroscopic values, the estimate $\epsilon \approx 10^4 \sim 10^5$ is obtained for more strongly cross-linked micron-sized microgels [57]. Note here the strong size dependence $\epsilon \propto \sigma_\mathrm{s}^3$, implying a significantly decreased potential strength for smaller microgel particles. As an aside, we note that this is of course only a rough estimate since the elastic moduli of a macroscopic material are in general different from the ones associated with the deformation of a microscopic particle. This has been recently discussed in [69, 70].

In addition, while our work is concerned with the fluid-like concentration regime only, we remark that quite different solid phases are observed in concentrated Hertz potential systems for different values of ϵ [71]. To use the Hertz potential for the steric interaction potential part has been shown to provide a nearly fit-parameter-free description of the structure and phase behavior of ionic and non-ionic microgel systems, in good agreement with experimental results for various particle sizes [57, 67], and values of ϵ in the range from $10^2 - 10^4$. This is found even though the particles are of a distinctly inhomogeneous structure. The strong effect of changing ϵ in the Hertz potential is visualized in Fig. 2.2. Note that the Hertz potential is continuous and non-diverging in the overlap region. However, large ϵ values give rise to practically impenetrable particles.

While for large ϵ the Hertz and hard-sphere potentials give very similar results for the equilibrium microstructure, the effective diameter σ_s in the Hertz potential is in general somewhat larger than the corresponding hard-sphere diameter σ, i.e. $\sigma_\mathrm{s} \gtrsim \sigma$. This reflects the fact that the Hertz potential incorporates overall the softness of a microgel

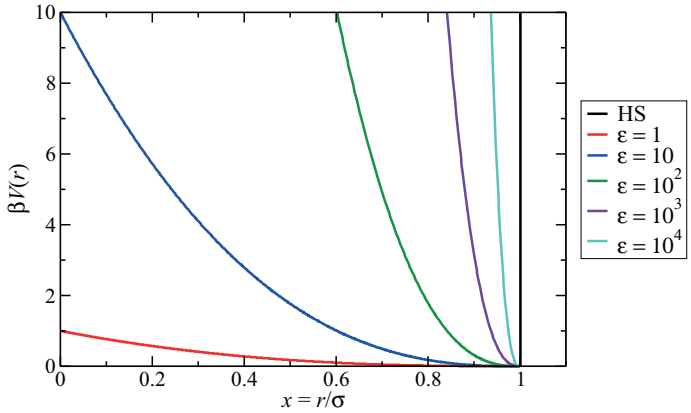

Fig. 2.2.: Comparison of the hard-sphere interaction potential (HS) with the Hertz potential for interaction strengths values $\epsilon \in [1 - 10^4]$

particle which in turn originates from the radially inhomogeneous cross-linker density. (See Chapter 5 for details.)

Hard-sphere potential

For very large values of ϵ, the Hertz potential becomes practically indistinguishable from the hard-sphere potential (c.f. Fig. 2.2),

$$V_{\mathrm{HS}}(r) = \begin{cases} \infty & r \leq \sigma = 2a \\ 0 & r > \sigma\,, \end{cases} \tag{2.3}$$

with hard-sphere diameter σ. Employing the Hertz potential in the fitting of the static structure factor, $S(q)$, data of non-ionic submicron-sized poly(N-isopropylacrylamide) (PNIPAM) microgel samples, we determined an ϵ value of 10^4. Considering such a large deformation energy penalty, the usage of the hard-sphere potential in place of the Hertz potential is well justified in the complete fluid-phase concentration regime. This is advantageous from a theoretical viewpoint since colloidal hard spheres are among the best studied soft matter systems.

In addition of being the key quantities in static scattering experiments on concentrated suspensions, $S(q)$, and its associated radial distribution function (RDF), $g(r)$, are required as inputs in theoretical methods for calculating colloidal transport properties. For the Hertz potential model, we have determined the two functions numerically from solving the approximate Percus-Yevick (PY) integral equation [72, 73]. The corresponding pair correlation functions for the hard-sphere model are determined from the analytic

PY solution combined with the Verlet-Weis (VW) correction [74], by which the accurate Carnahan-Starling equation of state is incorporated via $S(0)$ (see also Ref. [75]). The VW correction compensates, in particular, the overestimation by the PY solution of the principal peak height, $S(q_m)$, of the hard-sphere structure factor, for volume fractions $\phi = (\pi/6)\rho\sigma^3 \gtrsim 0.4$. Here, ρ is the number density of particles.
Since for the hard-sphere interaction potential analytic expressions for $g(r)$ and $S(q)$ are known, we are in the position to derive analytic expression for a broad variety of short-and long-time transport properties of hard-sphere systems.

2.1.3. Analytic toolbox for the hydrodynamic radius model (HRM)

Our toolbox of analytic methods for calculating colloidal transport properties is based on the HRM, and it takes advantage of the tabulated simulation data for spherical annulus particles listed in Ref. [51]. The toolbox incorporates in particular useful approximate scaling relations for the wavenumber-dependent sedimentation coefficient, $H(q)$, the short-time translational self-diffusion coefficient, d_{S}, and the high-frequency viscosity η_∞. These quantities are routinely determined in dynamic scattering experiments and oscillatory rheometry measurements. The scaling relations for permeable particles with hard-core interactions are known to be in remarkably good agreement with simulation data [47, 48, 76]. We show that they apply likewise to particles with a soft pair potential, and we augment them by scaling expressions for the collective diffusion coefficient, d_{C}, and the associated sedimentation coefficient K.
Moreover, we extend the toolbox to long-time dynamic properties of concentrated systems of hydrodynamically structured particles, including the low-shear zero-frequency suspension viscosity, η, and the long-time translational self-diffusion coefficient d_{L}. Different from their short-time siblings, long-time transport properties are affected additionally by the non-instantaneous microstructural relaxation of the cloud of neighboring Brownian particles. This relaxation is controlled both by direct and hydrodynamic interactions (c.f Sec. 5.4). The toolbox extension to long-time properties combines the HRM with a factorization approximation method introduced originally by Medina-Noyola [24], and elaborated subsequently by Brady [25, 26] and Banchio *et al.* [27]. The HRM is also useful for long-time properties, since the hydrodynamic mobilities in the generalized many-particle Smoluchowski diffusion equation describing the configurational distribution function are time-independent [61].
We demonstrate the accuracy of our user-friendly toolbox through the analysis of a static and dynamic light scattering study on a concentration series of non-ionic, submicron-sized

PNIPAM microgel particles dispersed in dimethylformamide (DMF) (see Chapter 5). We show that the static and dynamic scattering data for $S(q)$ and $H(q)$, respectively, can be quantitatively described, in the complete experimental wavenumber range, by using a reduced solvent penetration length equal to three percent of the particle diameter.

2.2. Charge-stabilized particles

A vast number of biological and synthesized soft matter systems includes charged particles or macromolecules, e.g. due to the chemical reactions invoked in the particle production process or due to surface-ion dissociation triggered by a polar solvent. Accordingly, the study of charged-particles systems is of high interest. However, the consideration of particle-charge related effects such as counterion condensation makes the theoretical description quite complex.
We study two different charged-particles systems, which we describe in detail in this section. Firstly, we apply the concept of the hydrodynamic radius model to charged (ionic) microgel particles, and investigate how softness and permeability affect their transport properties. This is of special interest for the analysis of dynamic light scattering measurements, and to obtain information about the particle sizes and structures based on these measurements.
Secondly, we highlight the importance of an appropriate calculation of diffusion and rheological properties for charged-particle systems in the framework of a technological application, namely the ultrafiltration (UF) of charged silica particles suspensions.

2.2.1. Ionic microgels

As discussed earlier, microgel particles consist of an intramolecular cross-linked polymer network [41]. The microgel intra-particle properties can be directly modified, e.g. by a specific choice of polymer and the amount of cross-linker during the synthesis. The intra-particle properties are intimately linked to the particles collective behavior influencing thermodynamic properties, phase states and transport coefficients. Since microgels can be synthesized from a broad variety of polymeric materials, particles with specific intra-particle properties can be designed. To manufacture systems with specific features, it is thus essential to understand how intra-particle properties affect the collective behavior of the dispersion. This knowledge is important also for the deduction of particle properties from measurements of the collective behavior, such as encoded in the diffusion function, $D(q)$, measured in dynamic light scattering (DLS) experiments. For the definition and

meaning of $D(q)$ we refer to Subsec. 4.2.1.

In general, the effect of fluid permeability of particles can be expected to be smaller for charge-stabilized particles at moderate volume fractions than for uncharged ones since near-contact configurations are more unlikely. A quantitative investigation of the effect of permeability on the transport properties of ionic microgels is still in demand. The benefit of treating the soft short-range interactions of microgels by using the Hertzian interaction potential has been shown in several studies [57, 67, 77]. We re-emphasize the strong size dependence of the Hertz potential strength ϵ (c.f. Eq. (2.2)), which scales with the cube of the particle diameter. The broad size distribution of synthesized microgel particles in the range from a few tenths of nm to several μm, is reflected in the broad parameter range $\epsilon \sim 1 - 10^6$, (c.f. Fig. 2.2), as estimated on the basis of Young's modulus and Poisson's ratio for macroscopic PNIPAM gels. In addition, microgel particles show typically a radially decaying cross-linking density which leads to the formation of dangling polymer chains on the particles surfaces [41] so that the two-particle interaction right at the onset of overlap is softened.

Hence, the softness and permeability are two important properties of microgels with high impact on the system's collective behavior. The understanding of their effects on the equilibrium structure and transport properties is thus an important topic in soft matter science. It is further essential for the usage of microgels in many applications such as for drug delivery.

This amply motivates our investigation of the influence of microgel permeability and softness on statics and dynamics of ionic microgel systems. The direct interaction between ionic microgels is very well described by an effective interaction potential by Denton which he derived from a coarse-graining procedure [57, 63, 78]. For the steric interaction of microgels, we use the Hertz potential introduced in Eq. (2.1). The main difference between ionic microgels and charge-stabilized rigid silica spheres, the latter discussed in the upcoming subsection, is that the counterions and the solvent can penetrate into the polymer-mesh of the microgel particles. This lowers the effective microgel charge and affects the screening of the particle interactions.

In the Denton potential [63, 78], the overlap ($r \leq \sigma_s$) and non-overlap regions ($r > \sigma_s$) are distinguished. For $r \leq \sigma_s$, in addition to the elastic Hertz potential, there is an electrostatic potential contribution given by [57, 63, 78]

$$\beta V_{\text{eff}}(r) = \frac{2Z^2 l_{\text{B}}}{\sigma_s}\left[\frac{6}{5} - 2\left(\frac{r}{\sigma_s}\right)^2 + \frac{3}{2}\left(\frac{r}{\sigma_s}\right)^3 - \frac{1}{5}\left(\frac{r}{\sigma_s}\right)^5\right] - \frac{72Z^2 l_{\text{B}}}{\kappa^4 \sigma_s^4 r}\,\Phi_{\text{ind}}(r), \qquad (2.4)$$

with

$$\begin{aligned}\Phi_{\mathrm{ind}}(r) = &\left(1 - e^{-\kappa r} + \frac{1}{2}\kappa^2 r^2 + \frac{1}{24}\kappa^4 r^4\right)\left(1 - \frac{4}{\kappa^2\sigma_s^2}\right)\\ &+\frac{4}{\kappa\sigma_s}e^{-\kappa\sigma_s}\sinh(\kappa r)\\ &+\left[e^{-\kappa\sigma_s}\sinh(\kappa r) + \kappa^2\sigma_s r + \frac{1}{6}\kappa^4\left(\sigma_s^3 r + r^3\sigma_s\right)\right]\left(1 + \frac{4}{\kappa^2\sigma_s^2}\right)\\ &-\frac{4r}{\sigma_s}\left(1 + \frac{1}{2}\kappa^2\sigma_s^2 + \frac{1}{30}\kappa^4\sigma_s^4\right) - \frac{8r^3}{3\sigma_s^3}\left(\frac{\kappa^2\sigma_s^2}{4} + \frac{\kappa^4\sigma_s^4}{12}\right)\\ &-\frac{1}{180}\frac{\kappa^4}{\sigma_s^2}r^6\,.\end{aligned} \tag{2.5}$$

Here $l_{\mathrm{B}} = e^2/(\epsilon k_{\mathrm{B}}T)$ is the Bjerum length of the solvent, ϵ the solvent macroscopic dielectric constant, and e the proton charge. For water at room temperature, $l_{\mathrm{B}} = 0.7\,\mathrm{nm}$.
When the microgel particles are non-overlapping, the pair potential continuously crosses over into a Yukawa-type screened Coulomb potential, differing from that of non-permeable charge-stabilized colloids in Eq. (2.8) by a different effective charge, i.e. [57]

$$\beta V_{\mathrm{eff}}(r) = \frac{144 Z^2 l_{\mathrm{B}}}{\kappa^4\sigma_s^4}\left[\cosh(\kappa\sigma_s/2) - \frac{2\sinh(\kappa\sigma_s/2)}{\kappa\sigma_s}\right]^2\frac{e^{-\kappa r}}{r}. \qquad (r > \sigma_s)\,. \tag{2.6}$$

The bare charge number of the microgels is Z, and κ is the inverse Debye screening length which for a $1-1$ electrolyte is given by

$$\kappa = \sqrt{4\pi(n_c + 2n_s)\lambda_{\mathrm{B}}}\,. \tag{2.7}$$

Here, n_c is the counterions number density, and n_s the number density of $1-1$ electrolyte salt ion pairs in cgs units [57].
For our discussion of the effect of permeability and softness on the short-time dynamics of ionic microgels presented in Sec. 6.1, we use realistic system parameters from a previous theoretical-experimental study by Riest *et al.* [57]. In this earlier publication, we have shown that the Denton plus Hertz pair potential allows for an accurate and fit-parameter-free description of static properties of ionic microgels.

2.2.2. Ultrafiltration (UF) of charge-stabilized suspensions

In a broad variety of applications, membrane ultrafiltration (UF) plays an important role. The notion ultrafiltration refers to the filtration of smaller and typically nanosized particles

using higher trans-membrane pressure values (TMP). It needs to be distinghuised from the so-called microfiltration (MF) of larger particles, where a lower TMP is applied and higher permeation flux occurs [39]. While in UF, the effect of Brownian motion is strong, with the system remaining basically in local thermal equilibrium, the dominant effect in MF is shear-induced hydrodynamic migration and non-isotropic hydrodynamic diffusion. The important role of the thermodynamic osmotic pressure in UF is taken over by an effective osmotic pressure in MF which can be characterized by an effective temperature [79, 80].

An important example of UF is the purification of proteins. Due to the wide-spread usage of proteins also in industrial applications, there is a large interest in optimizing protein UF procedures.

In earlier work, Roa *et al.* [39] analyzed the performance of a new cross-flow UF model for permeable hard-sphere suspensions highlighting in particular the importance of using accurate transport coefficient expressions as model inputs. We study here the cross-flow UF of charged silica suspensions which necessitates the consideration of counterion and electrolyte screening effects. For this purpose, we use a Poisson-Boltzmann (PB) cell model based charge-renormalization procedure for the calculation of the state-dependent interaction potential parameters.

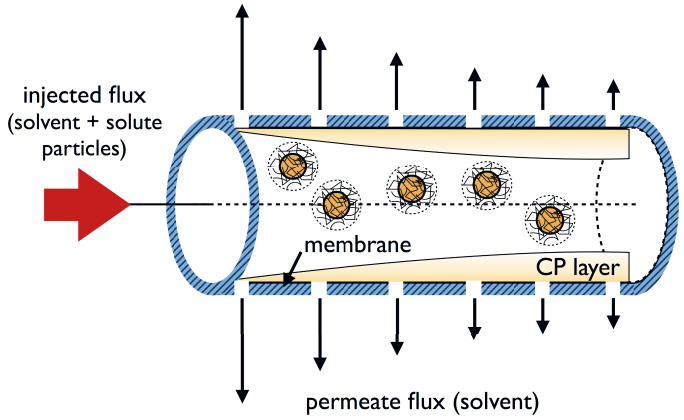

Fig. 2.3.: Sketch of the hollow-fiber membrane used in the inside-out cross-flow ultrafiltration process. Sketch kindly provided by R. Roa [39].

A typical cross-flow, inside-out UF setup is presented in Fig. 2.3. A suspension of particles is pumped through a hollow-fiber membrane of inner radius R. The applied pressure difference between the pressure at the inlet, p_{in}, and the outlet, p_{out}, is denoted as $\Delta p_L = p_{\text{in}} - p_{\text{out}}$. It is important, and realized in most instances, that the length L of the fiber is large compared to its radius, i.e. $R \ll L$. Ideally, the membrane is only permeable

to the solvent molecules which are permeating through the membrane due to an applied transmembrane pressure difference Δp_{TMP}. The pure-fluid hydraulic permeability of the clean membrane, L_p^0, characterizes its solvent permeability in the absence of colloidal particles.

In our model calculations, we assume the membrane to be fully retentive to the colloidal particles. A small fraction of the axially in-flowing solvent permeates the membrane to the outside of the fiber into the permeate bath. This process can be continuated to achieve a higher degree of purification. In this so-called inside-out cross-flow setup, the particle advection towards the membrane by the permeating solvent, driven by the difference between the trans-membrane pressure, Δp_{TMP}, and transmembrane osmotic particle pressure, Π, is balanced by the diffusive back transport of particles away from the inner membrane surface. This leads to the formation of a concentration-polarization (CP) layer, i.e. a particle-enriched region of mobile particles near to the inner membrane surface (see Fig. 2.3).

For the theoretical determination of the CP profile and permeate flux, the knowledge of accurate transport properties, namely the collective diffusion coefficient, $d_{\mathrm{C}}(\phi)$, and the steady low-shear viscosity, $\eta(\phi)$, of the suspension are required as functions of the colloidal volume fraction ϕ. In addition, the suspension osmotic pressure $\Pi(\phi)$ and the related isothermal osmotic compressibility $\chi_{\mathrm{OSM}}(\phi)$ needs to be known for the filtration modeling.

For the charged-silica system studied in this thesis, these properties can be obtained in principle on basis of the so-called Primitive Model (PM) [61, 73, 81], where the large colloidal macroions and small surface-released counterions, and the electrolyte ions (termed microions for short), are treated on equal footing as different species of uniformly charged hard spheres immersed in a structureless dielectric (Newtonian) fluid of dielectric constant ϵ and shear viscosity η_0. PM-based theoretical calculations and computer simulations are in general quite elaborate, owing to the disparate length and time scales characteristic of the spatio-temporal coupling of the various ion species.

In taking advantage of the strong size asymmetry of microions and monodisperse colloidal macroions, the one-component macroion fluid model (OCM) is frequently used. In the OCM, the effective pair interaction potential, $V_{\mathrm{eff}}(r)$, between two microion-dressed charged colloid spheres of diameter $\sigma = 2a$ at center-to-center distance r is modeled, to decent accuracy in general, by the sum of a hard-sphere and screened Coulomb potential

of the form [61, 81–83]

$$\beta V_{\mathrm{eff}}(r) = \begin{cases} \infty & r < \sigma \\ l_B Z_{\mathrm{eff}}^2 \left(\frac{\exp\{\kappa_{\mathrm{eff}} a\}}{1+\kappa_{\mathrm{eff}} a} \right)^2 \frac{\exp\{-\kappa_{\mathrm{eff}} r\}}{r} , & r \geq \sigma \, . \end{cases} \tag{2.8}$$

Here, Z_{eff} and κ_{eff} are the in general concentration and temperature dependent effective colloid charge number and electrostatic screening parameter, respectively. The OCM potential is state-dependent as a consequence of having traced out the microion degrees of freedom by starting, e.g., from the multi-component PM description. In using the OCM, it is assumed that van der Waals attraction and other non-electric short-range colloid-colloid interactions are negligible. This assumption is justified for sufficiently strongly charged colloids, if the salt concentration is small enough so that near-contact configurations are unlikely, or if the solvent dielectric constant nearly matches that of the particles, or if the charged particles are (additionally) sterically stabilized by surface-grafted short polymers [84]. Systems describable by the OCM model range from charge-stabilized suspensions of rigid colloidal spheres [85] to ionic microgels [40] and globular protein solutions [86, 87]. In this thesis the hypernetted-chain approximation (HNC) in conjunction with the OCM is employed for calculating the colloid $g(r)$ and the associated $S(q)$. These entities are used as input in the dynamic calculation schemes applied for the calculation of the zero-frequency viscosity, η, the sedimentation velocity, K, and the (short-time) collective diffusion coefficient d_{C}. Subsequently, the precise transport properties are used as input to the calculation of the permeate flux in the framework of the UF model, which results in good agreement of the model results with UF experiments on charged silica spheres dispersed in water. The static and dynamic suspension properties, and the filtration modeling results in comparison to the experiment are discussed in Sec. 6.2.

2.3. SALR systems

2.3.1. Importance and examples of these systems

Brownian particles dispersions with short-range attraction (SA) and long-range repulsion (LR) such as low-salinity lysozyme protein solutions, and suspensions of micron-sized charged colloidal particles with added depletant, have been intensely studied over the past years [2, 30–36]. SALR protein systems are particularly interesting since the clustering of proteins can result in severe diseases such as Alzheimer and Parkinson [5, 37]. Stradner *et al.* [2] observed experimentally a small-wavenumber peak in the static structure fac-

tor, $S(q)$, at a wavenumber, q_c, distinctly smaller than the wavenumber, q_m, where the next-neighbor peak of individual particles of height $S(q_m)$ is located. They attributed the structure factor peak at q_c to the formation of particle clusters. A cluster peak of $S(q)$ is indeed observed for the mesoscopically inhomogeneous equilibrium-cluster phase of reversibly formed fluid-like clusters in equilibrium with individually dispersed particles (monomers) [30, 33, 35]. This phase is stabilized against macroscopic phase separation by the long-range repulsive interaction part which limits the mean cluster size and suppresses cluster-cluster aggregation.

Liu *et al.* [32, 33] showed subsequently that a small-wavenumber peak at a wavenumber $q_c < q_m$ is indicative not only of the equilibrium-cluster phase. It is present, in particular, also in the so-called dispersed-fluid phase of SALR systems occurring for smaller concentrations and interaction strengths (i.e., larger reduced temperatures) where non-associated monomers are dominant, and where the $S(q_c)$-peak is indicative of intermediate-range microstructural ordering (IRO) arising from the competing SA and LR.

In the past few years, the microstructure and cluster states of the two-Yukawa [33, 88] SALR potential model, and the generalized ($2\alpha^*$-α^*) Lennard-Jones (LJ) - Yukawa SALR potential for typical LJ power law exponents $\alpha^* \sim 45 - 50$ [34], have been intensely studied. Associated reduced temperature-concentration state diagrams [30, 33, 34] have been mapped out, and compared with experimental results in particular for zero-salt lysozyme solutions [30, 33, 35]. Depending on particle concentration, relative strength and range of the competing SA and LR potential parts determining the size and shape, and the lifetime of clusters, various dynamically arrested modulated phases have been found in addition to the dispersed-fluid and equilibrium-cluster phases, including cluster-percolated gels and glasses composed of clusters [30, 31, 33–35, 88, 89]. See here Subsec. 2.3.3 for details.

In comparison with the large body of work on the structure and phase behavior of SALR systems, little is known to date about their dynamic properties. This concerns in particular theoretical and simulation works on these systems that are challenging owing to the important influence of the HIs. The HIs need to be accounted for in a realistic modeling. Rigid clusters behave hydrodynamically different from fluid-like ones since there is no hydrodynamic screening in the latter case. In earlier Brownian dynamics simulation calculations [30] of the dynamic structure factor, $S(q,t)$, and the wavenumber dependent short-time diffusion function, $D(q)$, based on the generalized Lennard-Jones-Yukawa SALR model, HIs were completely disregarded. As discussed in the introduction, the surprising experimental observation that the short- and long-time self-diffusion coefficients for salt-free lysozyme solutions deduced from neutron spin echo (NSE) data share roughly the same

concentration dependence [32], indicates the complications in the theoretical description of cluster states, arising from the presence of additional time and length scales associated with the distributions of cluster lifetimes, sizes and charges. Therefore, a clear distinction between colloidal short-time and long-time regimes, as it can be made for a homogeneous suspension of individually diffusing monodisperse particles, is hampered.

In this thesis, we present a generic theoretical study of short-time diffusion and rheological transport properties of two SALR model systems where the salient HIs are accounted for. Firs,t we consider an isotropic hard-core plus two-Yukawa pair potential, and second a Lennard-Jones plus Yukawa potential presented further down in Subsec. 2.3.2. Both potentials include, complementary to an (effective) hard core, an SA part originating either from the short-ranged Yukawa or the LJ-type interaction contribution. The long-ranged electrostatic repulsion is modeled in both cases by a Yukawa potential. These two SALR potentials are frequently used in studies of microstructural properties and phase behavior [31, 34, 36, 90, 91]. They describe phenomenologically the orientationally averaged short-range attraction of globular proteins, and the for low-salinity systems long-ranged electric double layer repulsion originating from the protein charges and surface-released counterions. The detailed origin of the SA for protein suspensions is not understood to this day [92]. Yet, Tardieu *et al.* [93] found that in addition to LR, SA is needed for a theoretical description of small-angle X-ray (SAXS) measurements on the static structure factor of Lysozyme.

Proteins show a chemically complex structure including positive and negative charges, and hydrophilic and hydrophobic regions with the latter potentially inducing short-range interparticle attractions. In addition, van der Waals forces can contribute to the SA. For protein systems such as Lysozyme the Hamaker constants, characterizing the strength of dispersion forces, are in the range of $1-2\,k_{\mathrm{B}}T$ as measured in [94–96]. When the Hamaker constant is used instead as free paramter in the fit of the measured second virial coefficients B_2 (see Subsec. 8.1.1 for its definition) of Lysozyme using the Derjaguin-Landau-Verwey-Overbeek (DLVO) potential, values of this constant from $4-9$ up to $55\,k_{\mathrm{B}}T$ [94] have been obtained. The difference in the Hamaker constant values obtained by direct measurement and $B_2(T)$ fitting suggests that not only dispersion forces are at the origin of the SA but further short-range interactions must be present. These additional interactions artificially raise the Hamaker constant values in the $B_2(T)$ fitting procedure [97]. In addition to the aforementioned hydrophobic and electrostatic particle interactions, hydrogen bonding is considered as a potential cause of the SA in protein suspensions [92, 98]. We note that these interactions may be strongly anisotropic. Yet, in the fluid phase, and at least for volume fractions $\phi \lesssim 0.25$, integral equation theory (IET) calculations using isotropic pair

potentials have been shown to agree with the measured $S(q)$'s of Lysozyme solutions and other proteins such as BSA [86, 98, 99].
In our analytic-dynamic calculations, we focus on SALR systems in the homogeneous dispersed-fluid phase state where most of the particles diffuse individually. However, the tendency of clustering is noticeable also in this phase as hallmarked, e.g., by the occurrence of an IRO peak in $S(q)$ as the transition line to the equilibrium-cluster phase is approached. For the calculation of equilibrium (short-time) diffusion and rheological properties in the dispersed-fluid phase, we employ our analytic toolbox developed for colloidal systems. Its applicability to bio-particle systems such as proteins is by no means evident.

2.3.2. Two models

Hard-sphere plus two-Yukawa potential

The hard-sphere plus two-Yukawa SALR pair potential, $V(r)$, used in our theoretical study of short-time diffusion and rheological properties presented in Sec. 2.3 reads explicitly [100, 101],

$$\beta V(x) = \begin{cases} \infty\,, & x < 1 \\ \alpha\left[-K_1 \frac{e^{-z_1(x-1)}}{x} + K_2 \frac{e^{-z_2(x-1)}}{x}\right], & x \geq 1\,. \end{cases} \tag{2.9}$$

Here, $x = r/\sigma$ is the inter-particle center-to-center distance, r, in units of the particle diameter σ. Moreover, z_1 and z_2 determine the range of the attractive and repulsive Yukawa potential parts in units of σ, respectively, and $\overline{K}_1 = \alpha K_1$ and $\overline{K}_2 = \alpha K_2$ are the respective SA and LR potential strengths in units of $k_\mathrm{B}T$. To achieve a systematic variation of the potential shape, and to reduce the number of adjustable potential parameters, we follow Costa *et al.* [91] in demanding that

$$\alpha = -\beta V\left(x = 1^+\right)\,, \tag{2.10}$$

which implies that $K_2 = K_1 - 1$. Accordingly, α is identified as the depth of the potential well at two-particle contact in units of $k_\mathrm{B}T$. It plays thus the role of an interaction strength parameter equal to the inverse of the reduced effective temperature T^*. In the high-T^* limit for which $\alpha = 0$, the two-Yukawa soft potential contribution in Eq. (2.9) is vanishing, and the particles behave practically as hard spheres.
In the present thesis, $\alpha = 1/T^*$ is varied in the interval $[0 - 3]$ so that for the maximal potential depth, $-3\,k_BT$, particles in contact can still disintegrate by thermal motion. As shown in Fig. 2.4, with increasing α, the potential well deepens, and a shallow potential barrier of height $\beta V(x_\mathrm{max})$ develops at x_max, followed for distances $x > x_\mathrm{max}$ by a

monotonic decay within the range set by $1/z_2$.

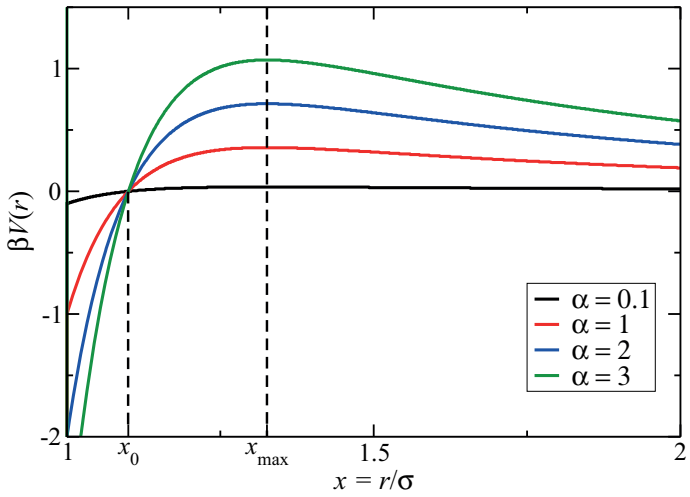

Fig. 2.4.: Plot of the hard-sphere plus two-Yukawa SALR pair potential for various values of α, and fixed parameters $K_1 = 1.6306$, $K_2 = 0.6306$, $z_1 = 10$, and $z_2 = 0.5$. The dashed vertical lines mark the effective attraction range $x_0 = 1.1$, and the location of the potential maximum $x_{\max} \approx 1.326$.

A systematic study of the effect of varying attraction/repulsion strength/range on structural and dynamic system properties necessitates restrictions on the 4-dimensional parameter space spanned by $\{K_1, K_2, z_1, z_2\}$. To this end, Costa *et al.*[91] have fixed, in addition to $\alpha = 1$, the effective attraction range x_0. The latter is defined as the first zero-crossing of the pair potential for $x > 1$. This leads to the following constraints for the attraction and repulsion strengths [91]:

$$K_1 = \frac{1}{1 - \exp\left[(z_2 - z_1)\,(x_0 - 1)\right]} \tag{2.11}$$

$$K_2 - K_1 = -1. \tag{2.12}$$

We consider three different values of the effective atrracion range, namely $x_0 = \{1.05, 1.1, 1.2\}$ realistic, e.g., for globular proteins such as Lyszoyme [31, 32, 90]. The studied z_1 and z_2 values and a scheme allowing for the systematic variation of potential features are presented in Subsec. 8.1.1.

LJ-Yukawa potential

The modified Lennard-Jones-Yukawa potential (LJY) is another SALR system showing IRO peak formation. The advantage of considering this system is the straightforward ap-

plicability of simulation techniques owing to the lack of a sharp hard-core excluded volume potential part. Hence, Molecular Dynamics (MD) simulations can be used for the investigation of static properties, and the multi-particle collision dynamics (MPC) simulation method, accounting for the full HIs, for the investigation of the particle dynamics.
The LJY potential consists of a 100-50 Lennard-Jones potential with a Born-type short-range $\mathcal{O}(x^{-100})$ repulsion part, a short-range $\mathcal{O}(x^{-50})$ attraction part, and a long-range screened Coulomb part. In total,

$$\beta V(x) = 4\epsilon \left[\left(\frac{1}{x}\right)^{100} - \left(\frac{1}{x}\right)^{50} \right] + \frac{A\xi}{x} e^{-\frac{x}{\xi}}, \tag{2.13}$$

where ϵ is the strength of short-range attraction/repulsion, and A the prefactor of the Yukawa term. The potential parameter A is related to the surface potential of the colloids [34, 102], and ξ :r σ.

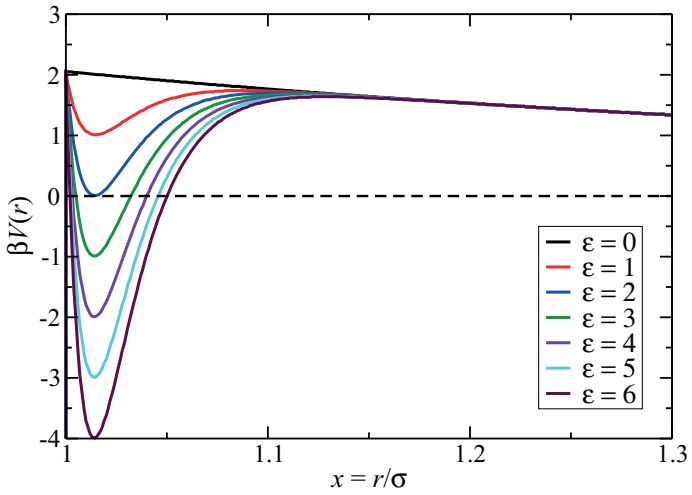

Fig. 2.5.: Lennard-Jones-Yukawa potential in Eq. (2.13), for various values of ϵ used in the present thesis, and fixed LR parameter $A = 2$ and $\xi = 1.794$ independent of ϵ. The potential minimum is to a good approximation located at $x_{\min} = 1.014$, with depth $\beta V(x_{\min}) \approx 2 - \epsilon$.

As we will discuss in Subsec. 2.3.3, the phase behavior of this pair potential model has been intensively studied by Mani *et al.* [34] using MD simulations and the thermodynamic Gibbs-Duhem integration method. These authors used the fixed parameter values $A = 2$ and $\xi = 1.794$, varying only the attraction strength ϵ and the reduced number density, $\rho^* = 6\phi/\pi$, in units of σ^3. Their choice of the reduced screening length ξ corresponds, for a typical colloidal size of $\sigma \approx 100\,\text{nm}$, to a 1:1 salt concentration in water of about

3μM [34]. The corresponding minimum of $V(r)$ for nonzero ϵ is $x_{\min} = 1.014$, with the approximate potential depth $\beta V(x_{\min}) = 2 - \epsilon$ as shown in Fig. 2.5. For the here used parameter range, $\epsilon = 0 - 6$, the effective attraction range x_0 of the LJY system varies between $x_0 \approx 1.032$ for $\epsilon = 3$ and $x_0 = 1.05$ for $\epsilon = 6$ (c.f. Subsec 2.3.2).

2.3.3. Phase behavior

The phase behavior of SALR potential systems has been intensively studied over the past years. To this end, and in addition to computer simulation methdods various theoretical schemes have been used, including Gibbs-Duhem integration [34], discrete perturbation theory [33, 103, 104], and self-consistent Ornstein Zernike schemes [105, 106]. Except for [34], all studies focused for simplicity on the calculation of the liquid-liquid (liquid-vapor) coexistence curves of so-called attractive reference potentials. These purely attractive potentials usually consist of the SALR potential set to zero for distances greater than the effective attraction range x_0.

Noro and Frenkel have proposed an extended law of corresponding states (ELCS) for systems of different ranges of attractive interactions. Their extension states that for SA systems the second virial coefficient, B_2, the effective hard-core diameter, σ_{eff}, and the depth of the potential well, $V(r_{\min})$, allow for the estimation of the liquid-gas critical point temperature [107]. For more details see Subsecs: 8.1.1 and 8.1.2. Recently, Platten *et al.* [108] successfully applied the ELCS to map the experimentally determined gas-liquid binodals of protein solutions to the binodals of short-range square-well fluids, with the latter determined by Monte Carlo (MC) simulations.

Godfrin *et al.* [33] have presented a detailed computer simulation study of the phase behavior of the hard-sphere two-Yukawa and the LJY potential models for a variety of parameter sets. They have generated a temperature - volume fraction generalized phase diagram of clustered states. For this purpose, they scale the temperature and volume fraction by the respective liquid-vapor critical point values associated with the two interaction potential models and the investigated parameter sets.

The phase diagram of Godfrin *et al.* [33] is sketched in Fig. 2.6. The authors distinguish four different states, the dispersed-fluid, equilibrium-cluster, random-percolated and cluster-percolated states, on basis of the cluster-size distribution function (CSD) calculated from MC simulation data. The CSD gives the average fraction of particles, $N(s)$, in the system which are members of a cluster of size s. For more details of the CSD, its definition, and its characteristic behavior for the four distinct states see Subsec. 8.1.3.

In the dispersed-fluid state, no equilibrium-cluster formation is observed. For low temper-

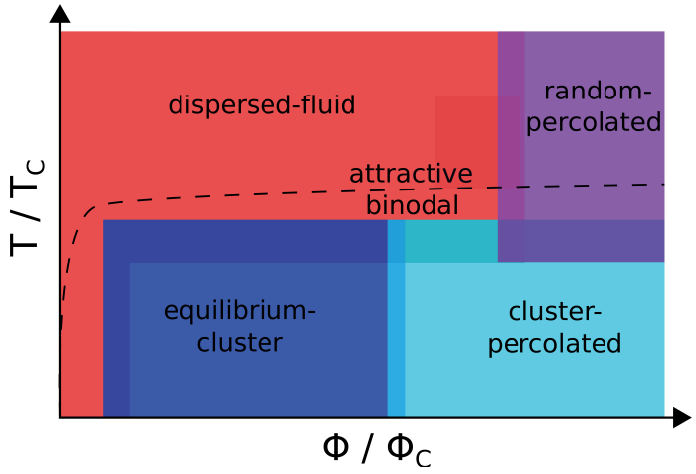

Fig. 2.6.: Rough sketch of the generalized temperature, T, volume fraction, ϕ, phase diagram of clustered states for SALR systems (hard-sphere plus two-Yukawa potential and LJY potential) generated by Godfrin *et al.* [33]. The temperature and volume fraction are normalized by the respective liquid-vapor critical point values, T_c and ϕ_c, of the reference attractive potential. The dashed line denotes the liquid-liquid binodal of the purely attractive reference potential system. The sketch is based on Fig. 4 of [33].

atures in the dispersed-fluid state however, an IRO peak is found at q_c. The IRO peak is not a direct sign for equilibrium-cluster formation or a preferred cluster size. It just indicates the emergence of highly transient clusters typically with mean cluster size smaller than $\sim 2-3$. Monomers are the most important species in the fluid state [98].
If for small ϕ-values the temperature is lowered to states well below the binodal of the attractive reference system, a first-order phase transition to the equilibrium-cluster phase is found. In contrast to the dispersed-fluid phase, in the eqilibrium-cluster phase clusters of preferred size are in equilibrium with monomers [33, 109]. Thus, the thermodynamic properties of the system can be expected to be dominated by clusters and not by monomers [98]. That the equilibrium-cluster phase of SALR potential systems is located underneath the liquid-liquid binodal of the purely attractive reference system (c.f. Fig. 2.6) suggests that long-range repulsion suppresses the phase separation observed in a SA system, causing instead the formation of equilibrium clusters [33]. For larger ϕ values, two distinct percolated states are found. Below the liquid-liquid binodal of the attractive reference system, finite clusters serve as building blocks of the percolated system (cluster-percolated state) whereas for higher temperatures the system randomly percolates (random-percolated state).
In this thesis, we focus on SALR systems in the dispersed-fluid phase where only transient clustering occurs. Here, the applicability of the employed Zerah-Hansen (ZH) IET-scheme

is guaranteed, and our analytic toolbox for the dynamics of colloidal suspensions mentioned already in Subsec. 2.1.3 can be used. To ensure that the studied systems are in the fluid state, we have calculated the liquid-gas critical temperature T_c^* of the reference attractive fluid using the ELCS. Following the generalized phase diagram of Godfrin *et al.* (see Fig. 2.6), we consider only SALR systems at reduced temperatures $T^* > T_c^*$ and limit our considerations to small volume fractions well below the ϕ values associated with the dynamic percolation line of the attractive reference fluid (c.f. [98]). In addition, we use MC and MD simulations of selected systems to calculate the CSD, and to verify our ZH results for $g(r)$. The agreement of simulation and self-consistent ZH approximation results is an indicator of the fluid structure of the system, since the ZH closure can be expected to fail in reproducing the sharp peaks of the simulated $g(r)$ associated with equilibrium-cluster formation (c.f. Subsec. 8.3.3). In addition, Godfrin *et al.* [33] have presented a heuristic criterion allowing to distinct between dispersed-fluid and random-percolated vs. equilibrium-cluster and cluster-percolated states. At low ϕ, the critical value $S_{\mathrm{crit}}(q_c) \sim 2.7$ of the IRO peak marks the first-order transition from the dispersed-fluid ($S(q_c) < S_{\mathrm{crit}}(q_c)$) to the equilibrium-cluster phase ($S(q_c) > S_{\mathrm{crit}}(q_c)$). All SALR systems discussed in this thesis have IRO peak values well below this threshold. Furthermore, the IRO peak position, q_c, of the explored systems is shifting to larger values as ϕ is increased. As discussed by Cardinaux *et al.* [30] based on Lyszoyme experiments and computer simulations of SALR systems, a ϕ-independence of the cluster peak position can be considered as an indicator of the equilibrium-cluster phase.

Mani *et al.* [34] theoretically studied LJY systems using MD and MC simulations and the analytic Gibbs-Duhem integration method. They showed that the equilibrium-cluster and part of the non-equilibrium-cluster and gel (percolated) phases, are outside of the solid-liquid coexistence region. Here, crystallization is suppressed in favor of cluster or gel formation.

A detailed analysis of the cluster shapes found in the equilibrium and non-equilibrium cluster phases highlights the subtle interplay of SA and LR for the resulting phase behavior. If the attraction strength is above a certain threshold, elongated clusters, such as Bernal spirals [110] are formed instead of spherical ones even though the latter have a smaller potential energy [34]. The creation of elongated clusters is triggered by the LR interactions. Considering two particles in contact, a third one experiences the lowest energy barrier when it approaches the two along the connection line of their centers. If the depth of the attractive well is too large, and can hardly be overcome by thermal energy, the particle rearrangement becomes very slow which results in a kinetic trapping of the configuration [34]. Hence, equilibrium cluster formation necessitates the detailed balance between SA,

favoring aggregation, and LR, suppressing macroscopic phase separation.

2.4. Polydisperse zwitterionic microgels

We have identified microgels already as model systems of permeable particles with tunable softness. In addtion, they have features of practical importance such as temperatue and pH-dependent volume phase transitions. This renders them as promising candidates for a variety of applications in a diversity of fields such as in medicine, membrane science and cosmetics [10, 15, 16, 19].
As discussed earlier, microgels consist of cross-linked polymer chains. Through the selection of the cross-linker and employed polymer, and their mass composition, properties of the synthesized microgel particles such as size, softness, charge and permeability can be affected. We have been involved in a joined experimental-theoretical study of amphoteric microgels containing both positive and negative charges of equal amount. We explored if and when the intra-particle charges start to affect the inter-particle interactions.
Introducing weak acidic [111–114] or basic [115–117] comonomers into PNIPAM microgels leads to multisensitive microgels to, e.g., temperature, pH, and ionic strength. The pH-dependent swelling of ionic microgels is caused by the osmotic pressure of the counterions [118]. Recently, Holmqvist *et al.* [40] published a combined theoretical-experimental study of the structure and dynamics of negatively charged PNIPAM microgels. They show that the swelling of the particles depends on the number density of particles, in addition to their dependence on pH and salinity.
The amphoteric microgels studied in this thesis contain both acidic and basic comonomers. Consequently, the microgels show not only a a single volume phase transition as observed, e.g., for PNIPAM suspensions but a more complicated three-state transition. They swell in acidic or basic environments, and collapse for intermediate pH values. The intermediate pH-regime, where the amphoteric microgels are collapsed, is referred to as the zwitterionic regime. The simplest way to synthesize amphoteric microgels is to use a zwitterionic comonomer, e.g. sulfobetaine [119]. The betaines carry an identical number of opposite charges in a well-defined distance, which renders zwitterionic microgels into ideal model systems of amphoteric microgels. On first sight, one might expect that the presence of opposite charges in the microgel network influences the interactions between the particles. To investigate the inter-particle interactions of amphoteric microgels, we have systematically varied the amount of zwitterions, and compared the resulting concentration series of measured structure factors to polydisperse hard-sphere calculations. In this way, we revealed when the charges inside a microgel start to affect the inter-particle interactions.

It can be expected that the positive and negative charges inside a particle cause deviations from the hard-sphere interactions, at least for large volume fractions when particles are close to each other. The usage of the hard-sphere interaction potential for the theoretical description of zwitterionic microgels is justified since the interaction strength parameter of the Hertz potential is large, i.e. $\epsilon \approx 10^3$.

2.4.1. Schulz particle size distribution

Basically all one-component colloidal systems, regardless synthetic or biological ones are not perfectly monodisperse in size. A monodisperse theoretical description is thus usually only an approximation. Yet, if the polydispersity is low, the particles can be considered as practically monodisperse.
However, the chemically produced zwitterionic microgels explored in detail in Chapter 7 necessitate a polydisperse description. The size polydispersity is characterized by the particle size distribution function (PSD), $p_{\mathrm{s}}\left(R;\overline{R},s_{\mathrm{R}}\right)$, which is the probability density of finding a particle with radius R in a suspension of polydisperse particles of mean particle radius $\overline{R}$ and relative standard deviation s_{R}. The latter reads explicitly,

$$s_{\mathrm{R}} = \frac{\left[\overline{R^2} - \overline{R}^2\right]^{\frac{1}{2}}}{\overline{R}} = [t+1]^{-\frac{1}{2}} \ , \tag{2.14}$$

where t is the non-dimensional width parameter.
For the PSD, we use the unimodal and skew-symmetric Schulz distribution function given by (see, e.g. [61])

$$p_{\mathrm{s}}\left(R;\overline{R},s_{\mathrm{R}}\right) = \left[\frac{t+1}{\overline{R}}\right]^{t+1} \frac{R^t}{\Gamma\left(t+1\right)} \exp\left[-\frac{t+1}{\overline{R}}R\right], (t>0) \ , \tag{2.15}$$

with moments

$$\overline{R^n} = \int_0^\infty \mathrm{d}R \ R^n p_{\mathrm{S}}\left(R;\overline{R},s_{\mathrm{R}}\right) = \frac{(n+t)!}{t!\left(t+1\right)^n}\overline{R}^n \ , \tag{2.16}$$

for $n = \{0,1,\ldots\}$. For small s_{R}, the Schulz distribution is well approximated by a Gaussian distribution function centered at $\overline{R}$.
In Fig. 2.7, we show the unimodal Schulz distribution for mean diameter $\overline{\sigma} = 2\overline{R} = 1$, and standard deviation $s_{\mathrm{R}} = 0.18$. For a practical measurable structure factor calculation presented in detail in Subsec. 3.5, we approximate the continuous distribution by a

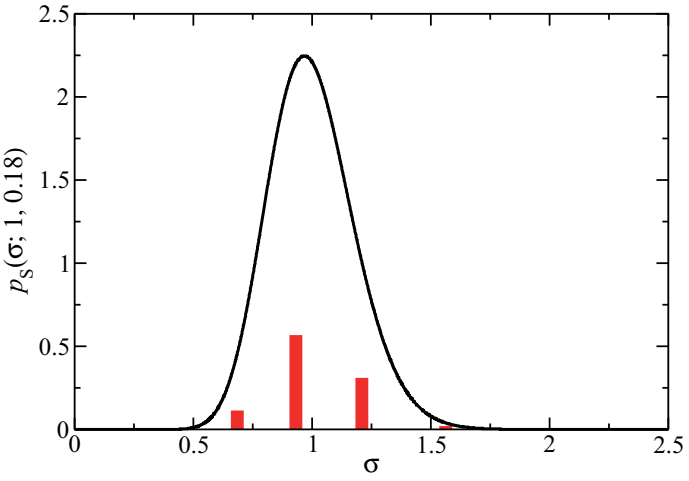

Fig. 2.7.: Solid line: continuous Schulz distribution $p_{\mathrm{s}}(\sigma; 1, 0.18)$ with mean diameter $\overline{\sigma} = 1$ and $s_{\mathrm{R}} = 0.18$, in comparison with its histogramatic representation $\{x_i, \sigma_i\}_{i=1}^{m}$ for $m = 4$ components (red vertical bars). The latter is determined by equating the first $2m = 8$ moments of the Schulz distribution with its histogramatic representation.

histogramatic one using m representative components

$$p_{\mathrm{s}}\left(R; \overline{R}, s_{\mathrm{R}}\right)\big|_{\mathrm{discrete}} = \sum_{i=1}^{m} x_i \delta\left(R - R_i\right) , \tag{2.17}$$

with $0 \leq x_i \leq 1$, and $\sum_{i=1}^{m} x_i = 1$.
The m particle sizes, R_i, and respective weights, x_i, are calculated by equating the first $2m$-moments of the histogramatic representation,

$$\overline{R^n}\big|_{\mathrm{discrete}} = \sum_{i=1}^{m} x_i R_i^n \quad ; \; i = 0 \ldots 2m-1 \, , \tag{2.18}$$

with the respective ones of the Schulz distribution in Eq. (2.16). The result is exemplified for $p_{\mathrm{s}}(\sigma; 1, 0.18)$ in Fig. 2.7.

2.4.2. Form factor model

The zwitterionic microgel systems investigated in Chapter 7 have a non-homogeneous spherical structure. Accordingly, the neutron scattering signal differs from that of a homogeneous sphere of same radius. This is accounted for by the scattering amplitude, $f(q)$, which quantifies the effect of the non-homogeneous distribution of intra-particle scatter-

ing sites. The different reaction kinetics of the cross-linkers BIS and NIPAM leads to an inhomogeneous cross-linker density inside the microgel, resulting in a fuzzy spherical surface. For the comparison of the measured static structure factor, $S_{\mathrm{M}}(q)$, with polydisperse IET calculations of this quantity, one needs thus to account for the specific intra-particle structure.

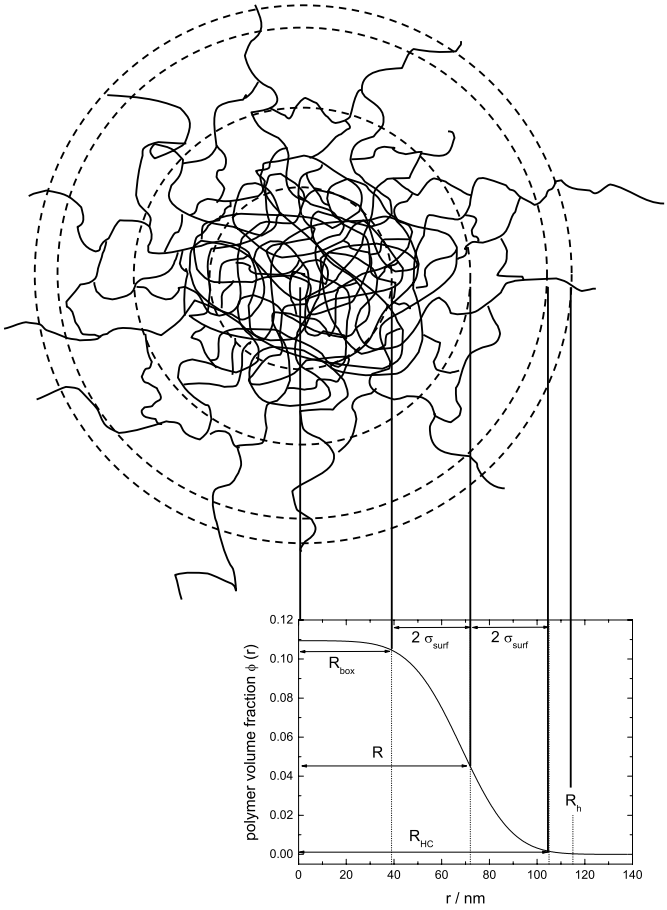

Fig. 2.8.: Schematics of the scattering amplitude model by Stieger *et al.* [120]. For details see [120].

For the zwitterionic microgels, we use the scattering amplitude model by Stieger *et al.* [120] depicted in Fig. 2.8. In this model, the scattering amplitude of a crosslinked microgel is related to that of a core-shell-like particle with core radius R, and a shell of width $2\sigma_{\mathrm{surf}}$. The scattering amplitude is obtained from the convolution of the radial scattering length distribution of a homogeneous sphere of radius R_{box} with a Gaussian function of constant

width $1/\sigma_{\text{surf}}$. The latter accounts for the inhomogeneous cross-linker density. Explicitly,

$$f\left(qR\right) = R^3 \left(\frac{j_1\left(qR\right)}{qR}\right) \exp\left[-\frac{\left(q\sigma_{\text{surf}}\right)^2}{2}\right], \tag{2.19}$$

where $R = R_{\text{box}} + 2\sigma_{\text{surf}}$, and $j_1\left(x\right)$ is the first-order spherical Bessel function. The total radius in the scattering amplitude model is here

$$R_{\text{HC}} = R + 2\sigma_{\text{surf}}. \tag{2.20}$$

The subscript HC (hard core) denotes that this radius is used as the particle excluded volume radius in our polydisperse static correlation function calculations. For the details of the IET calculations for polydisperse zwitterionic microgel systems, see Section 3.5. In Chapter 7, the results are compared with small angle neutron scattering (SANS) data.

3. Theory of equilibrium microstructure

A variety of methods has been developed for the calculation of static suspension properties. We discuss here the underlying concepts, followed by the presentation of the methods of calculation of $g(r)$ and $S(q)$ used in this thesis. The Chapter ends with the generalization of the presented methods to polydisperse systems, and the discussion of the cluster-size distribution function. The latter is useful for analyzing computer simulation results for clustering systems.

3.1. Static distribution functions

To calculate thermodynamic properties of an one-component many-body system using statistical mechanics the three macroscopic state variables volume of the system, V, number of particles, N, and total energy, E, need to be known. Dependent on the considered thermodynamic ensemble, these variables can vary. If not mentioned explicitly, we will focus in the following on the canonical ensemble where the temperature, T, particle number, N and system volume, V, are fixed. In the thermodynamic limit $N \to \infty$, $V \to \infty$ with $\rho = N/V$ constant the different ensembles are equivalent away from phase boundaries.
The key function relating the positions of N spherical colloidal particles to macroscopic state variables is the equilibrium probability density function (PDF) P_{N}. It is the probability density for N particles to attain center-of-mass positions $(\mathbf{r}_1, \mathbf{r}_2, \ldots, \mathbf{r}_N) = \mathbf{r}^N$ in a system of volume V and temperature T. Explicitly, P_{N} is given by [73]

$$P_{\mathrm{N}}\left(\mathbf{r}^N\right) = \frac{e^{-\beta U\left(\mathbf{r}^N\right)}}{Z_N}\,, \tag{3.1}$$

where $U\left(\mathbf{r}^N\right)$ is the N-particle potential energy which is often taken as pairwise additive, i.e.

$$U(\mathbf{r}^N) \approx \sum_{\substack{i,j=1 \\ i<j}}^{N} V\left(\mathbf{r}_i, \mathbf{r}_j\right)\,. \tag{3.2}$$

Here $V\left(\mathbf{r}_i, \mathbf{r}_j\right)$ is the effective pair potential of two particles i and j located respectively at $\mathbf{r}_i$ and $\mathbf{r}_j$. It is assumed here that three-body and higher-order effects are negligible.
In Eq. 3.1,

$$Z_{\mathrm{N}} = \int_{V^n} \mathrm{d}\mathbf{r}^N \, \exp\left[-\beta U\left(r^N\right)\right] \tag{3.3}$$

is the configurational integral.
For the calculation of thermodynamic functions and in scattering experiments accessible properties such as $S(q)$ and $g(r)$, only reduced distribution functions involving $n \ll N$ representative particles are required. The canonical n-particle density function is defined by [73]

$$\rho_{\mathrm{N}}^{(n)}\left(\mathbf{r_1},\ldots,\mathbf{r_n}\right) = \frac{N!}{(N-n)!}\int \mathrm{d}\mathbf{r}^{(N-n)}\, P_N\left(\mathbf{r}^N\right)\,, \tag{3.4}$$

and it is the probability density of finding n particles at positions $\mathbf{r}_1$ to $\mathbf{r}_n$. The factor $N!/(N-n)!$ accounts for classical indistinguishability of the N particles. In the fluid phase state without a symmetry breaking external field, the system is spatially uniform and isotropic [73]. Uniformity means here that [75]:

$$\rho_{\mathrm{N}}^{(n)}\left(\mathbf{r}_1,\mathbf{r}_2,\ldots,\mathbf{r}_n\right) = \rho_{\mathrm{N}}^{(n)}\left(\mathbf{r}_1+\boldsymbol{\Delta}\mathbf{r},\mathbf{r}_2+\boldsymbol{\Delta}\mathbf{r},\ldots,\mathbf{r}_n+\boldsymbol{\Delta}\mathbf{r}\right) \tag{3.5}$$

where $\boldsymbol{\Delta}\mathbf{r}$ is an arbitrary displacement vector. In particular, this implies that

$$\rho_N^{(1)}\left(\mathbf{r}\right) = \rho\,. \tag{3.6}$$

Moreover, the two-particle density, $\rho_{\mathrm{N}}^{(2)}\left(\mathbf{r},\mathbf{r}'\right)$, is then solely a function of the distance $|\mathbf{r}-\mathbf{r}'|$ between two considered particles at position $\mathbf{r}$ and $\mathbf{r}'$, viz.

$$\rho_N^{(2)}\left(\mathbf{r},\mathbf{r}'\right) = \rho_{\mathrm{N}}^{(2)}\left(\left|\mathbf{r}-\mathbf{r}'\right|\right)\,, \tag{3.7}$$

when in addition d has been assumed.
In fluid colloidal systems away from a critical point, the correlation length ξ defined as the distance over which two particles are correlated is typically of the order of the range of the interaction pair-potential $V(\mathbf{r}_i,\mathbf{r}_j)$ [75]. Thus,

$$\rho_N^{(n)}\left(\mathbf{r}_1,\ldots,\mathbf{r}_n\right) \approx \prod_{i=1}^{n}\rho_N^{(1)}\left(\mathbf{r}_i\right) = \rho^n \tag{3.8}$$

for $|\mathbf{r}_i-\mathbf{r}_j| \gg \xi$, where the second equality holds only in a uniform system [75]. The deviation of a fluid system from the classical ideal gas behavior is quantified by the canonical n-particle distribution function

$$g_N^{(n)}\left(\mathbf{r}^n\right) = \frac{\rho_N^{(n)}\left(\mathbf{r}^n\right)}{\prod_{i=1}^{n}\rho_N^{(1)}\left(\mathbf{r}_i\right)} = \frac{\rho_N^{(n)}\left(\mathbf{r}^n\right)}{\rho^n}\,, \tag{3.9}$$

where the second equality holds for a homogeneous system [73]. Hence, $g_N^{(n)}(\mathbf{r}^n)$ is a measure of the n-particle local structure in a colloidal system.
Note that when the potential energy U_N is pairwise additive, $g^{(2)}(\mathbf{r}_i, \mathbf{r}_j)$ suffices to calculate thermodynamic properties as described in Sec. 3.3. The two-particle distribution function of an isotropic system depends on $r = |\mathbf{r}_i - \mathbf{r}_j|$ only, and it is referred to as the radial distribution function (RDF)

$$g(r) = \lim_{\infty} g_\mathrm{N}^{(2)}(r) = \lim_{\infty} \frac{N(N-1)}{\rho^2} \int \mathrm{d}\mathbf{r}_3 \ldots \mathrm{d}\mathbf{r}_N \, P_N(\mathbf{r}^N) \,, \tag{3.10}$$

where $\lim_\infty$ denotes the thermodynamic limit. Note that $g(r \gg \xi) = 1$ (c.f. Eq. (3.8)). Moreover [73]

$$g(r, \phi \to 0) = e^{-\beta V(r)} \,. \tag{3.11}$$

The RDF in a system of large colloidal particles can be directly determined by confocal microscopy. In a simulation study, it is obtained by counting the number of particles in a thin spherical shell, at distance r from a selected particle, of thickness Δr and volume $4\pi r^2 \Delta r$. This follows from [75]

$$\begin{aligned} \rho \int \mathrm{d}\mathbf{r}_{12} \, g_N^{(2)}(r_{12}) &\underset{(3.10)}{=} \frac{N(N-1)}{\rho} \int \mathrm{d}\mathbf{r}_{12} \int \mathrm{d}\mathbf{r}_3 \ldots \mathrm{d}r_N \, P_N(\mathbf{r}^N) \\ &= N - 1 \,, \end{aligned} \tag{3.12}$$

where $\mathbf{r}_{12} = \mathbf{r}_1 - \mathbf{r}_2$. Using $N \gg 1$ this implies

$$g(r) = \frac{N(r)}{4\pi\rho \, r^2 \Delta r} \,, \tag{3.13}$$

where $N(r)$ is the number of particles with centers inside the shell $[r, r + \Delta r]$.
The discussion of the reduced distribution functions was given here using the canonical ensemble. It can be repeated for the grand-canonical ensemble when the chemical potential μ is used in place of N which is now varied. In the thermodynamic limit of a very large system, the reduced distribution functions and thermodynamic properties are independent of the employed statistical ensemble. We finally note that $\rho^{(2)}(r)$ and $g(r)$ can be expressed

as [73]

$$\rho^{(2)}(\mathbf{r},\mathbf{r}') = \lim_{\infty} \left\langle \sum_{\substack{i,j=1 \\ i\neq j}}^{N} \delta\left(\mathbf{r}-\mathbf{r}_i\right)\delta\left(\mathbf{r}-\mathbf{r}_j\right) \right\rangle , \tag{3.14}$$

$$g(r) = \lim_{\infty} \frac{1}{\rho} \left\langle \frac{1}{N} \sum_{\substack{i,j=1 \\ i\neq j}}^{N} \delta\left(\mathbf{r}-\left(\mathbf{r}_j-\mathbf{r}_i\right)\right) \right\rangle , \tag{3.15}$$

where the first equation is valid also for an inhomogeneuos system. Here, $\langle \ldots \rangle$ denotes likewise the canonical or grand-canonical ensemble average.

3.2. Static structure factor

The Fourier transform of $g(r)$, or more precisely that of the total correlation function, $h(r) = g(r) - 1$, with $h(r \to \infty) = 0$, is the static structure factor $S(q)$. The latter is measured in a static scattering measurement. If monochromatic radiation of wavelength λ impinges on a sample cell of volume V, it gets scattered by the included Brownian particles. To infer information about the system microstructure, the scattering experiment needs to probe distances in the order of the particle sizes and typical next-neighbor distances [121]. For colloidal systems where these distances are typically of the order of a few nm to μm, scattering techniques such as DLS and SANS are widely used.
In a static scattering measurement, the mean intensity of scattered light, $I(q)$, is measured as a function of the wavenumber q. The latter is related to the scattering angle α by $q = \frac{4\pi}{\lambda}\sin\left(\frac{\alpha}{2}\right)$, where λ is the scattering wavelength inside the medium. For an ergodic system of monodisperse particles, one has

$$I(q) \propto \langle N \rangle \, P(q) S(q) , \tag{3.16}$$

where $\langle N \rangle$ is the mean number of particles in the scattering volume, $P(q)$ is the particle form factor describing the distribution of intra-particle scattering sites, and $S(q)$ is the correlation function of the q-th component of microscopic density fluctuations characterizing

the inter-particle correlations. The function $S(q)$ is defined by [121]

$$S(q) = \lim_{\infty} \left\langle \frac{1}{N} \sum_{j,l=1}^{N} e^{i\mathbf{q}(\mathbf{r}_j - \mathbf{r}_l)} \right\rangle \tag{3.17}$$

$$= \lim_{\infty} \left\langle \frac{1}{N} \rho_{\mathbf{q}} \rho_{-\mathbf{q}} \right\rangle \geq 0\,, \tag{3.18}$$

with the q-th Fourier component of density fluctuations [121]

$$\rho_{\mathbf{q}} = \sum_{l=1}^{N} e^{i\mathbf{q}\mathbf{r}_l} - N\delta_{\mathbf{q},\mathbf{0}}\,. \tag{3.19}$$

Using the definition of the two-particle distribution function in Eq. (3.10) and Eq. (3.17), $S(q) - 1$ is basically identified as the Fourier Transform of $h(r)$, i.e.

$$S(q) - 1 = \rho \int \mathrm{d}\mathbf{r}\, e^{i\mathbf{q}\mathbf{r}}\; h(r) \tag{3.20}$$

$$= 4\pi\rho \int_0^{\infty} \mathrm{d}r\, r^2 h(r)\, j_0(qr)\,. \tag{3.21}$$

Here, an isotropic system is assumed, and $j_0(x)$ denotes the zeroth-order spherical Bessel function. Note that Eq. (3.20) allows in principle for inferring $g(r)$, and from this indirectly $V(r)$, from an experimental $S(q)$. In practice, however, experimental noise and the limited q-range ($q_{\max} = 4\pi/\lambda$) severely hamper this procedure (see, e.g., [99, 122–124]).
In a system of hard spheres or purely repulsively charged particles, the distance, r_m, where the principal peak of $g(r)$ occurs is related to the principal peak position, q_m, of $S(q)$ approximately by $r_m \approx 2\pi/q_m$. In Chapter 8, we will discuss this inverse relationship in more detail, by investigating if the IRO peak position q_c of $S(q)$ can be used to infer the mean distance, r_c, between transient clusters.

3.3. Thermodynamic properties

We discuss here expressions for the internal energy, E, pressure, P, and osmotic compressibility, χ_T, of a suspension in relation to $g(r)$ and $U(r)$.
We mentioned in Section 3.1 that distribution functions contain all the information about the system thermodynamics. Following [75, 121], we discuss how three different thermodynamic properties are linked to the $g(r)$ and $U(r)$, on assuming pairwise additivity of $U(\mathbf{r}^N)$. First, we discuss the energy, pressure, and thermodynamic compressibility for

state-independent interaction potentials, meaning that the latter are independent of temperature and density. Generalized expressions for state dependent potentials are discussed in Subsec. 3.3.2.

3.3.1. State-independent pair potentials

For pairwisse additive U, thermodynamic properties can be obtained via the equation

$$\lim_{\infty}\left(\frac{E}{N}\right) = \frac{1}{2}\rho\int_0^\infty \mathrm{d}r\, 4\pi r^2 g(r)V(r)\,. \tag{3.22}$$

for the internal energy E. Likewise, the pressure (virial) equation

$$P = P_{\mathrm{id}} + P_{\mathrm{int}} = \rho k_{\mathrm{B}}T - \frac{2\pi}{3}\rho^2\int_0^\infty \mathrm{d}r\; r^3 g(r)\frac{dV(r)}{\mathrm{d}r}\,. \tag{3.23}$$

can be used for the calculation of the system pressure P, which is composed of two contributions. The first is the kinetic ideal gas pressure P_{id}. The second part P_{int}, is due to the interaction of particles, causing $P > P_{\mathrm{id}}$ for a purely repulsive systems where $V'(r) < 0$. For a discontinuous interaction potential the derivative in Eq. (3.23) causes problems. By introducing the cavity function, $\Xi(r) = \exp(\beta V(r))g(r)$, in place of $g(r)$, the pressure equation for a system with hard-core diameter σ is derived which reads [73]

$$\frac{P}{P_{\mathrm{id}}} = 1 - \frac{2\pi}{3}\rho\int_\sigma^\infty \mathrm{d}r\; r^3 g(r)\frac{\mathrm{d}V(r)}{\mathrm{d}r} + 4\phi\; g\left(\sigma^+\right)\,, \tag{3.24}$$

where $g(r<\sigma) = 0$ has been used. Here, $g(\sigma^+)$ is the contact value of the RDF.
A third route for the calculation of thermodynamic properties is provided by the compressibility equation,

$$\frac{\chi_{\mathrm{T}}}{\chi_{\mathrm{T}}^{\mathrm{id}}} = \lim_{q\to 0} S(q) = 1 + \rho\int \mathrm{d}\mathbf{r}\,[g(r)-1]\,, \tag{3.25}$$

with isothermal compressibility χ_{T} defined by

$$\chi_{\mathrm{T}} \equiv -\frac{1}{V}\left.\frac{\partial V}{\partial P}\right|_{\mathrm{T}} = \frac{1}{\rho}\left.\frac{\partial \rho}{\partial P}\right|_{\mathrm{T}}\,. \tag{3.26}$$

In the framework of the grand canonical ensemble, χ_{T} can be related to the fluctuation in the particle number N. Different from the energy and pressure equation, the pairwise additivity of the potential energy U is not required for the applicability of the compressibility

equation.

3.3.2. State-dependent pair potentials

State-dependent potentials arise when a coarse-graining procedure has been used where in a mixture of large and small particles the small particles degrees of freedom have been integrated out. This results in the description of the large particles as pseudo-particles interacting by a state-dependent effective potential that implicitly accounts for the integral effect of the small particles. Examples in case are the effective depletion potential of polymer-dressed colloidal particles in a colloid-polymer mixture, and the Yukawa-type effective potential of microion-dressed charged spheres.
In the calculation of thermodynamic properties, the state-dependence of the effective interaction potential needs to be accounted for. The energy Eq. (3.22), and the pressure Eq. (3.23), are generalized for state-dependent potentials to [75]

$$\lim_{\infty}\left(\frac{E}{N}\right) = \frac{3}{2}k_{\mathrm{B}}T + f_0\left(\rho\right) + \frac{1}{2}\rho\int_0^\infty \mathrm{d}r\; 4\pi r^2\, g(r)\frac{\partial\left[\beta V(r;T,\rho)\right]}{\partial\beta}\,, \tag{3.27}$$

$$P = P_{\mathrm{id}} + \rho^2\frac{\partial f_0(\rho)}{\partial\rho} - \frac{2\pi}{3}\rho^2\int_0^\infty \mathrm{d}r\; r^2\, g(r)\left[r\frac{\partial}{\partial r} - 3\rho\frac{\partial}{\partial\rho}\right]V(r;T,\rho)\,, \tag{3.28}$$

where $V(r;T,\rho)$ is the state-dependent effective pair potential of the large particle species. Here, f_0 denotes an additional structure-independent contribution to the total free energy per (larger) particle which is called volume energy. For fixed T, it depends on the density ρ of pseudo particles [57, 75]. The related osmotic pressure in the context of charge-stabilized dispersions is discussed in detail in Sec. 6.2.4.

3.4. Ornstein-Zernike based integral equations

For given effective pair potential, $S(q)$ and $g(r)$ can be calculated using either elaborate MC or MD simulations, or an appropriately selected Ornstein-Zernike (OZ) integral equation scheme. The integral equation schemes are based on the OZ equation describing the correlation of two particles at distance r. For a one-component homogeneous and isotropic colloidal system, the OZ equation reads

$$h(r) = c(r) + \rho\int \mathrm{d}\mathbf{r}' c(\left|r - r'\right|)h(r') \tag{3.29}$$

$$= c(r) + \rho\left(c * h\right)(r)\,, \tag{3.30}$$

where $(c * h)(r)$ denotes the convolution of the direct, and total correlation functions, $c(r)$ and $h(r)$, respectively.
In terms of $S(q)$, the OZ equation is

$$S(q) = \frac{1}{1 - \rho\tilde{c}(q)}\,, \tag{3.31}$$

where $\tilde{c}(q)$ is the three-dimensional Fourier transform of $c(r)$. For the calculation of $g(r)$ or $h(r)$, a second so-called closure equation is needed which relates $h(r)$, $c(r)$, and $V(r)$. There are various ways to derive approximate closures for specific purposes. One way is to use density functional theory (DFT), where different approximations for the excess Helmholtz free energy functional give rise to different closure relations. An example in case is the hypernetted-chain approximation (HNC) discussed in Section 3.4.2. For details about its derivation starting from DFT see [1, 125].
Another way is to use diagramatic expansions of $h(r)$ in terms of $c(r)$ and $V(r)$. An exact but formal closure relation is given by [1, 73]

$$g(r) = \exp\left[-\beta V(r) + g(r) - 1 - c(r) + B(r)\right]\,, \tag{3.32}$$

where $B(r)$ is the so-called bridge function which is rather short-ranged and not very sensitive to the specific form of $V(r)$ [1, 126]. Different approximations for $B(r)$ result in different closure relations of accuarcy depending on the specific $V(r)$. In the following, we discuss the closure relations used in this thesis. The numerical solution of the integral equation system consisting of Eq. (3.30) and an appropriately selected closure was gained iteratively, starting with the Mayer function approximation for $c(r)$ or, in extended parameter studies, starting from a previous solution for $c(r)$. In our implementation of the iteration procedure, the Fourier-transformed OZ-equation has been used, combined with the FFTW software package (3.3.3) [127].

3.4.1. Verlet-Weis corrected Percus-Yevick solution for hard spheres

The Percus-Yevick (PY) closure reads [72]

$$c(r) \approx g(r)\left[1 - e^{\beta V(r)}\right]\,. \tag{3.33}$$

It is quite accurate for systems with short-ranged repulsion [73] and for hard spheres, it has an analytic solution presented in Appendix A.1. This solution is known to be accurate for $\phi \lesssim 0.4$. For larger ϕ, it overestimates the next-neighbor peak height $S(q_m)$. To remedy

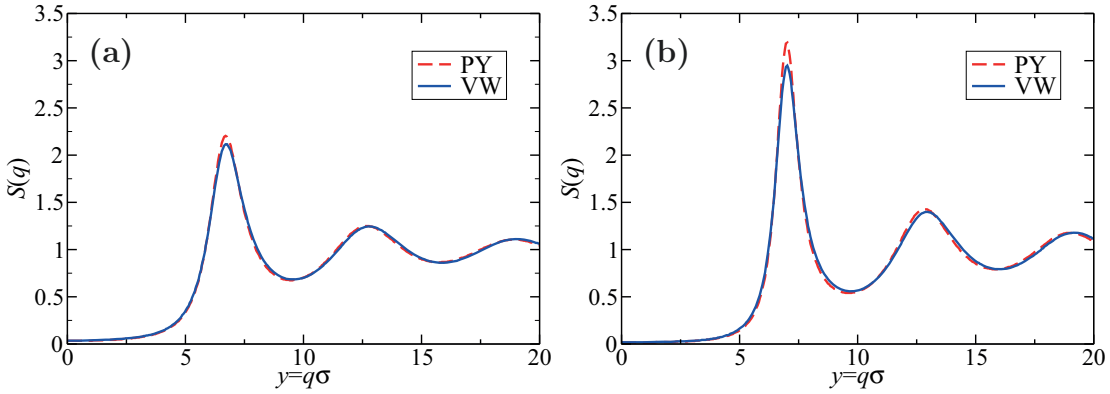

Fig. 3.1.: Comparison of the PY and VW solutions for the $S(q)$ of a hard-sphere suspension with (a) $\phi = 0.419$, and (b) $\phi = 0.497$.

this, Verlet and Weis (VW) [74] introduced a refinement by incorporating the accurate Carnahan-Starling (CS) expressions for $g_{\mathrm{CS}}(\sigma^+)$ and the osmotic compressibility $\chi_{\mathrm{T}}|_{\mathrm{CS}}$ [75], viz.

$$g_{\mathrm{CS}}\left(\sigma^+;\phi\right) = \frac{1-0.5\phi}{(1-\phi)^3}\,, \tag{3.34}$$

$$\left.\frac{\chi_{\mathrm{T}}}{\chi_{\mathrm{T}}^{\mathrm{id}}}\right|_{\mathrm{CS}} = \frac{(1-\phi)^4}{(1+2\phi)^2+\phi^3\,(\phi-4)}\,. \tag{3.35}$$

The explicit VW expression for $g(r)$ is given in Appendix A.2.
In Fig. 3.1, the PY and VW results for the $S(q)$ of hard spheres are compared for (a) $\phi = 0.419$, and (b) $\phi = 0.497$. For $\phi > 0.4$, the PY solution overestimates somewhat the oscillations in $S(q)$. This overestimation is largest around the principal peak region.

3.4.2. HNC scheme

The non-linear hypernetted-chain closure is

$$g(r) \approx e^{-\beta V(r)}\, e^{h(r)-c(r)}\,. \tag{3.36}$$

Different from the PY closure it guarantees that $g(r) \geq 0$, but there exists no analytic solution. While the HNC scheme is ill-suited for hard-sphere systems, it applies well for systems with soft interactions such as the Hertz potential for smaller ϵ (see e.g. [57, 125]), and systems with long-ranged soft-repulsive interactions such as the Coulomb or Yukawa interactions [121].

3.4.3. Zerah-Hansen scheme

The closure relations presented thus far lack thermodynamic self-consistency, in the sense that the isothermal compressibilities calculated using the energy, pressure, and compressibility equations are in general different (c.f. Sec. 3.3). The accuracy of a closure is significantly increased when hybrid schemes are used which (partially) restore thermodynamic self-consistency by interpolating between two appropriately selected pure closures. The interpolation parameter is fixed by enforcing (partial) thermodynamic consistency. An important example of a self-consistent closure scheme is the Rogers-Young (RY) scheme [128] interpolating between the HNC and PY closures. It works well for systems with purely repulsive $V(r)$.

A hybrid scheme for pair potentials including attractive potential parts was proposed by Zerah and Hansen [129]. It interpolates between the HNC closure (3.36) for long, and the soft-core mean spherical approximation (SMSA) for short-distances. The Zerah-Hansen (ZH) scheme is in particular suited for systems with a soft-core repulsion plus an additional attraction as discussed in Chapter 8 [129–131].

In the ZH scheme, $V(r)$ is split into a reference part, $V_1(r)$, and a perturbation part $V_2(r)$. In this splitting, Zerah and Hansen [129] used the procedure proposed by Weeks *et al.* [132].

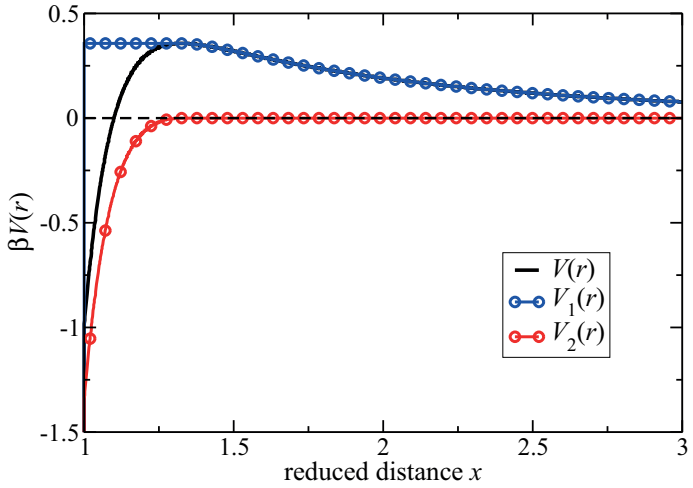

Fig. 3.2.: Decomposition of the hard-core double Yukawa SALR potential $V(r)$ in an attractive reference potential part, $V_1(r)$, and repulsive perturbation potential part $V_2(r)$. The parameters of the hard-core plus two-Yukawa SALR potential in Eq. (2.9) are $\alpha = 1$, $K_1 = 1.6306$, $K_2 = 0.6306$, $z_1 = 10$, and $z_2 = 0.5$.

For the two-Yukawa (Eq. (2.9)) and LJY SALR potentials (Eq. (2.13)) discussed in this

thesis, we use the potential splitting $V = V_1 + V_2$, with

$$V_1(r) = \begin{cases} \infty\,, & r < \sigma \\ V(r_{\text{shift}})\,, & r \leq r_{\text{shift}} \\ V(r)\,, & r > r_{\text{shift}}\,. \end{cases} \tag{3.37}$$

$$V_2(r) = \begin{cases} V(r) - V(r_{\text{shift}})\,, & \sigma \leq r \leq r_{\text{shift}} \\ 0\,, & r > r_{\text{shift}}\,, \end{cases} \tag{3.38}$$

and $r_{\text{shift}} = r_{\max} > \sigma$. Here, $r_{\max}$ is the distance where $V(r)$ has its maximum. Accordingly, $V_2(r)$ is purely attractive , as seen in Fig. 3.2, and $V_1(r)$ is purely repulsive. The ZH closure reads

$$g(r) \approx e^{-\beta V_1(r)} \left[1 + \frac{e^{f(r)[h(r)-c(r)-\beta V_2(r)]} - 1}{f(r)} \right], \tag{3.39}$$

with the mixing function

$$f(r) = 1 - e^{-\vartheta r}\,, \tag{3.40}$$

where ϑ is determined from enforcing equality of the compressibility derived from the virial and compressibility route. In taking the concentration derivative of the virial pressure, we assume for simplicity that the mixing parameter is density independent. This additional approximation is justified, since ϑ is only a slowly varying function of ρ [129]. In the limit of $\vartheta\, r \to \infty$, the ZH closure reduces to the HNC closure (Eq. (3.36)) while for $\vartheta\, r \to 0$ the SMSA closure

$$g(r) \approx e^{-\beta V_1(r)} \left[1 + h(r) - c(r) - \beta V_2(r) \right] \tag{3.41}$$

is recovered.
Since different choices for $V_1(r)$ and $V_2(r)$ are possible, the comparison with simulation data for $g(r)$ is a necessary prerequisite to assess the accuracy of the ZH scheme [129]. Our choice of the potential splitting leads to ZH results for $g(r)$ in excellent agreement with computer simulations (MC, MD and MPC), as shown in Subsecs. 8.1.3 and 8.3.

3.4.4. Random phase approximation

In random phase approximation (RPA), $c(r)$ of an isotropic and homogeneous colloidal system with interaction potential $V(r)$ is approximated by

$$c(r) \approx c_0(r) - \beta w(r)\,. \tag{3.42}$$

Here, c_0 is the direct correlation function of an appropriately chosen reference system with interaction potential V_0, and $w(r)$ the so called perturbation potential part,

$$V(r) = V_0(r) + w(r)\,. \tag{3.43}$$

The RPA for $c(r)$ is justified if the contribution by the perturbation potential is small, or if the particles are very soft. Insertion of Eq. (3.42) in Eq. (3.31) results in the RPA expression for $S(q)$,

$$\frac{1}{S_{\mathrm{RP}}(q)} = \frac{1}{S_0(q)} + \beta\rho\,\tilde{w}(q)\,. \tag{3.44}$$

Here, $S_0(q)$ is the static structure factor of the reference system, and $\tilde{w}(q)$ the Fourier transform of the perturbation potential, the latter appropriately continuated in the overlap region for a system with excluded volume interactions. Typically, $w(r < \sigma) = 0$ is used here. It should be noted that $g(r < \sigma) = 0$ is not enforced by this simple scheme.
The accuracy of RPA results depends strongly on the suitable choice of the reference potential. The perturbation potential, and the concentration should be small. Mathematically this is expressed by the condition $S_0(q)\beta\rho\tilde{w}(q) > -1$ resulting from demanding that $S(q) > 0$. The RPA is a useful tool for systems such as polymer blends [75, 133], allowing for an analytic solution for $S(q)$ in systems which otherwise are not analytically treatable.

3.5. Polydispersity and decoupling approximation

So far only monodisperse systems have been discussed. The generalization of the OZ integral equation methods to polydisperse systems is computationally more demanding. In the following, we discuss how the so-called measurable static structure factor, $S_{\mathrm{M}}(q)$, of a polydisperse system is related to the mean intensity, $I(q)$, measured in a SANS experiment which is the method used in the study of the zwitterionic microgels discussed in Chapter 7
The scattering intensity, $I(q)$, is proportional to the differential cross section, $\mathrm{d}\sigma\,(q)\,/\mathrm{d}\Omega$, defined as the number of neutrons scattered into an element of solid angle $\mathrm{d}\Omega$ in the direction of the scattering vector $\mathbf{q}$. The differential scattering cross section corrected for incoherent flat background at large momentum transfer, is for a polydisperse dispersion of spherical colloidal particles of same material given by

$$\frac{\mathrm{d}\sigma\,(q)}{\mathrm{d}\Omega} \propto I\,(q) \propto \rho_{\mathrm{T}}\,\overline{f^2}\,(q)\,S_{\mathrm{M}}\,(q) \tag{3.45}$$

where ρ_{T} is the total number density of particles in the scattering volume [61], and single

scattering has been assumed. Here, $\overline{f^2}(q)$ is the second moment of the particle scattering amplitude with respect to the particle size distribution function given in Eq. (2.15). The overline characterizes the average with respect to this distribution. Moreover, $S_{\mathrm{M}}(q)$ describes the scattering-amplitude-averaged inter-particle correlations encoded in the neutron beam interference pattern. For a polydisperse system, $S_{\mathrm{M}}(q)$ is not a purely statistical mechanical quantity, since it depends also on the intra-particle scattering properties. Thus, $S_{\mathrm{M}}(q \to 0)$ is in general different from the total isothermal osmotic compressibility. For non-dilute suspensions, $S_{\mathrm{M}}(q)$ is obtained experimentally by dividing the measured intensity, $I(q)$, of the non-dilute sample of number density ρ_{T} by the scaled intensity, $I_0(q)$, of a dilute reference sample at density $\rho_{\mathrm{T}}^0 \ll \rho_{\mathrm{T}}$ where $S_{\mathrm{M}}^0(q) \cong 1$, i.e.

$$S_{\mathrm{M}}(q) = \frac{I(q)}{I_0(q)} \frac{\rho_{\mathrm{T}}^0}{\rho_{\mathrm{T}}} . \tag{3.46}$$

It is assumed here that the particle scattering amplitudes and the size distribution do not change with concentration. For a polydisperse (multicomponent) system, the measurable form factor, $P_{\mathrm{M}}(q)$, is given by

$$P_{\mathrm{M}}(q) = \frac{\overline{f^2(q)}}{\overline{f^2(q=0)}} , \tag{3.47}$$

and normalized such that $P_{\mathrm{M}}(q=0) = 1$.
For the size distribution $p_{\mathrm{s}}\left(R; \overline{R}, s_{\mathrm{R}}\right)$, we use the unimodal and skew-symmetric Schulz distribution function in Eq. (2.15) to describe the polydisperse zwitterionic microgels. In accordance with experimental observations, only the particle core of radius R and thus R_{HC} (c.f. Eq. (2.20)) is treated as polydisperse, whereas the shell width $2\sigma_{\mathrm{surf}}$ is kept constant.
For calculating $S_{\mathrm{M}}(q)$, we use the m-component histogrammatic approximation of the continuous Schulz distribution introduced in Subsec 2.4. The $m(m+1)/2$ partial static structure factors, $S_{\alpha\beta}(q)$, are related to the partial total correlation functions, $h_{\alpha\beta}(r)$, of α and β type particles by

$$S_{\alpha\beta}(q) = \delta_{\alpha\beta} + 4\pi\rho_{\mathrm{T}} \left(x_\alpha x_\beta\right)^{\frac{1}{2}} \int_0^\infty \mathrm{d}r \; r^2 h_{\alpha\beta}(r) \frac{\sin(qr)}{qr} . \tag{3.48}$$

For size polydispersity $s_{\mathrm{R}} < 0.3$, it is sufficient to use a $m = 4$ component histogrammatic representation. For the $S_{\alpha\beta}(q)$ of a mixture of hard spheres of radius distribution $\{R_\alpha\}$,

we use the analytic PY solution for the Laplace transform,

$$\tilde{H}_{\alpha\beta}(s) = \int_0^\infty \mathrm{d}r\; r\, h_{\alpha\beta}(r)\, e^{-sr} \tag{3.49}$$

of $rh_{\alpha\beta}(r)$ provided by Blum and Hoye [134]. Using this solution, $S_{\alpha\beta}(q)$ is obtained straightforwardly from

$$S_{\alpha\beta}(q) = \delta_{\alpha\beta} + \frac{4\pi\left(\rho_\alpha\rho_\beta\right)^{\frac{1}{2}}}{q}\,\mathrm{Im}\left[\tilde{H}_{\alpha\beta}\left(s=iq\right)\right]\,, \tag{3.50}$$

with $\rho_{\{\alpha,\beta\}} = \rho_{\mathrm{T}} x_{\{\alpha,\beta\}}$.
The total volume fraction, ϕ_{T}, of the polydisperse hard-sphere system is related to the third moment of the hard-core radii distribution by

$$\phi_{\mathrm{T}} = \frac{4\pi}{3}\rho_{\mathrm{T}}\overline{R^3_{\mathrm{HC}}}\,. \tag{3.51}$$

The polydisperse PY hard-sphere solution for fluid mixtures is known to be decently good for $\phi_{\mathrm{T}} \lesssim 0.3$ and $s_{\mathrm{R}} \lesssim 0.15$. In place of the multi-component PY solution, we employ here for analytic simplicity the so-called decoupling approximation expression, $S_{\mathrm{D}}(q)$, of $S_{\mathrm{M}}(q)$ [61, 135]. This approximation uses the VW closure for monodisperse hard spheres, with size polydispersity accounted for in the scattering amplitudes only. Thus, $h_{\alpha\beta}(r)$ is approximated by the total correlation function, $h_{\mathrm{id}}(r)$, of an ideally monodisperse system of volume fraction ϕ_{T}, and total number density ρ_{T} equal to that of the actual polydisperse system. Explicitly,

$$h_{\alpha\beta}(r) \approx h_{\mathrm{id}}\left(r;\phi_{\mathrm{T}},R^*_{\mathrm{HC}}\right) \tag{3.52}$$

where

$$R^*_{\mathrm{HC}} = \left(\overline{R^3_{\mathrm{HC}}}\right)^{\frac{1}{3}} = \overline{R_{\mathrm{HC}}}\left[1+\mathcal{O}\left(s^2_{\mathrm{R}}\right)\right]\,. \tag{3.53}$$

In the decoupling approximation, $S_{\mathrm{D}}(q)$, is given by

$$S_{\mathrm{M}}(q) \approx S_{\mathrm{D}}(q) = \left[1-X(q)\right] + X(q) S_{\mathrm{id}}\left(q;\phi_{\mathrm{T}},R^*_{\mathrm{HC}}\right) \tag{3.54}$$

where $S_{\mathrm{id}}\left(q;\phi_{\mathrm{T}},R^*_{\mathrm{HC}}\right)$ is the static structure factor of the ideally monodisperse system [61]. The function $X(q)$ incorporates the scattering amplitude polydispersity and reads [61]

$$X(q) = \frac{\left[\,\overline{f}(q)\,\right]^2}{\overline{f^2}(q)}\,. \tag{3.55}$$

Note that $0 \leq X(q) \leq 1$.

As shown in [136], the principal peak height of the Verlet-Weis (VW) corrected hard-sphere structure factor at wave-number q_{m} is, up to $\phi_{\mathrm{T}} \lesssim 0.54$, to a good approximation given by

$$S_{\mathrm{id}}(q_{\mathrm{m}}) \approx 1 + 0.644\,\phi_{\mathrm{T}}\, g_{\mathrm{id}}^{\mathrm{CS}}\left(2R_{\mathrm{HC}}^{*}; \phi_{\mathrm{T}}\right) , \tag{3.56}$$

where $g_{\mathrm{id}}^{\mathrm{CS}}\left(2R_{\mathrm{HC}}^{*}; \phi_{\mathrm{T}}\right)$ is the CS contact value of the hard-sphere RDF. According to MD simulation results by Rintoul and Torquato [137, 138], the CS contact value expression applies also to the metastable fluid branch of the hard-sphere phase diagram, up to the melting point volume fraction $\phi_{\mathrm{m}} = 0.54$.

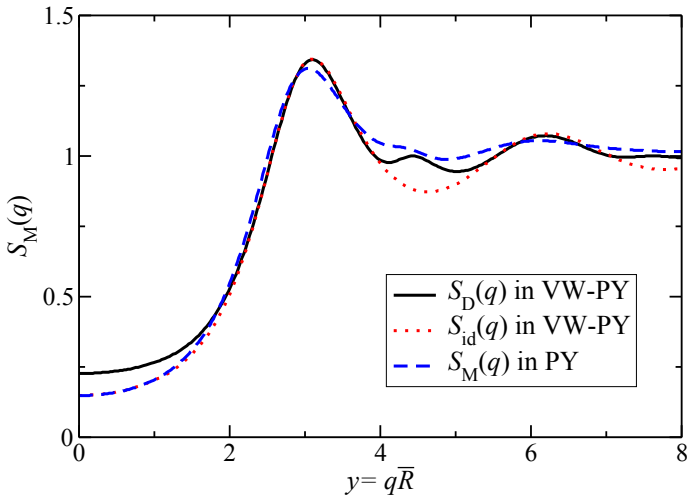

Fig. 3.3.: Comparison of the decoupling approximation form $S_{\mathrm{D}}(q)$ (solid line) of $S_{\mathrm{M}}(q)$ with the polydisperse PY solution for homogeneously scattering spheres of mean radius $\overline{R}$, polydispersity $s_{\mathrm{R}} = 0.105$, and $\phi_{\mathrm{T}} = 0.25$ (dashed line). Further shown is the VW-PY structure factor $S_{\mathrm{id}}(q)$ of an ideally monodisperse system (dotted line, see Eq. 3.54).

A comparison of the decoupling approximation result with the polydisperse PY solution for $S_{\mathrm{M}}(q)$ is presented in Fig. 3.3. For illustrative purposes, the calculations have been performed for a system of homogeneously scattering spheres of mean radius $\overline{R}$, $s_{\mathrm{R}} = 0.105$ and $\phi_{\mathrm{T}} = 0.25$. Polydispersity leads to a damping of the maxima and minima of $S_{\mathrm{M}}(q)$, and to a reduction of the principal peak height compared to that of the monodisperse system characterized by $S_{\mathrm{id}}(q)$ [61]. The decoupling approximation overestimates $S_{\mathrm{M}}(q)$ at low q, and it predicts a deeper first minimum than the polydisperse structure factor. Nonetheless, the principal peak shape of $S_{\mathrm{M}}(q)$ is nicely reproduced in decoupling approximation, for the considered s_{R} values.

We mention that an analytic extension of the polydisperse PY solution for $\tilde{H}_{\alpha\beta}(s)$, valid for higher volume fractions, has been provided by Santos *et al.* [139]. For simplicity, and since the considered s_{R} values are rather small, we can restrict ourselves here to the decoupling approximation with VW-PY input for $S_{\mathrm{id}}(q)$.

4. Dynamic properties

The particles in soft matter systems have sizes in the range from a few nanometers to μm and are embedded in a solvent whose molecules being orders of magnitude smaller. As a consequence, the solvent can be treated as a continuum, affecting the motion of embedded particles by HIs. In addition, the solute particles are affected by the thermal kicks of the solvent molecules adding up to a non-directional stochastic force termed Brownian force. The resulting Brownian motion is fundamental for the understanding of soft matter systems since it is the driving force for the homogenization, and the achievement of thermodynamic equilibrium.

4.1. Fundamentals

4.1.1. Hydrodynamic time- and length-scales

For colloidal particles, one has the time scale separation

$$\tau_{\mathrm{D}} = \frac{a^2}{d_0} \gg \tau_{\mathrm{B}} = \frac{m}{\zeta_0} \,. \tag{4.1}$$

Here, the structural relaxation time, τ_{D}, is a typical colloidal single-particle diffusion time across the characteristic length, usually set equal to the particle radius a, and d_0 is the Stokes-Einstein single-particle self-diffusion coefficient; τ_{B} quantifies the momentum relaxation of a colloidal Brownian particle of mass m in the suspending fluid. For correlation times large compared to the typical solvent molecules collision time, $\tau_{\mathrm{S}} = 10^{-14}\,\mathrm{s}$, the mean motion of a colloidal particle can be described by the averaged Langevin equation,

$$m\frac{\mathrm{d}}{\mathrm{d}t}\left\langle \mathbf{v}(t)\right\rangle = -\zeta_0 \left\langle \mathbf{v}(t)\right\rangle \,, \tag{4.2}$$

with solution

$$\left\langle \mathbf{v}(t)\right\rangle \ = \mathbf{v}_0 e^{-\frac{t}{\tau_{\mathrm{B}}}} \,, \tag{4.3}$$

where $\mathbf{v}_0$ is the initial velocity, and $\zeta_0 = 6\pi\eta_0 a$ the friction coefficient. For a time resolution $t \sim \tau_{\mathrm{D}} \gg \tau_{\mathrm{B}}$ where a detectable change in the particle position is observed, the Brownian particles move essentially inertia-free.
This is consistent with the dynamics of the embedding fluid which, as we show now, is

likewise inertia-free for $t \gg \tau_{\mathrm{B}}$. In this thesis, we are considering colloids in low molecular weight solvents, such as H_2O, D_2O and DMF and hence a Newtonian fluid characterized by a constant shear viscosity η_0. Thus, for $t \gg \tau_{\mathrm{s}}$ the fluid can be described as a homogeneous, incompressible medium governed by the Navier-Stokes equation of incompressible flow,

$$\rho_{\mathrm{s}} \frac{\mathrm{d}\mathbf{u}\,(\mathbf{r},t)}{\mathrm{d}t} = -\nabla p(\mathbf{r},t) + \eta_0 \Delta \mathbf{u}(\mathbf{r},t) + \mathbf{f}^e(\mathbf{r},t)\,, \tag{4.4}$$

with

$$\nabla \cdot \mathbf{u}(\mathbf{r}) = 0\,, \tag{4.5}$$

where ρ_{s} is the constant fluid mass density, and $\mathbf{u}$ and p are the fluid velocity and pressure fields, respectively. Moreover, $\mathbf{f}^e(\mathbf{r},t)$ is an external volumetric body force density acting on the fluid at position vector $\mathbf{r}$. It can be due to an externally applied force field, such as an electric, magnetic, or gravitational field, or to system and particle surface boundaries. The motion of a Brownian particle is coupled to the fluid via particle surface boundary conditions (BCs) such as the no-slip BC

$$\mathbf{u}(\mathbf{r})|_{\mathbf{r}\in S_i^+} = \mathbf{v}_i + \mathbf{\Omega}_i \times (\mathbf{r} - \mathbf{r}_i) \tag{4.6}$$

where $\mathbf{v}_i$ and $\mathbf{\Omega}_i$ are the translational and angular velocities, respectively, of a rigid particle i with surface S_i and center position $\mathbf{r}_i$. Note that S_i^+ is the fluid layer adjacent to the particle surface S_i.
Since the Reynolds number associated with the characteristic length a, fulfills

$$\mathrm{Re}_{\mathrm{a}} = \frac{\rho_{\mathrm{s}} v_{\mathrm{p}} a}{\eta_0} \sim \frac{|\rho_{\mathrm{s}} \mathbf{u} \cdot \nabla \mathbf{u}|}{|\eta_0 \Delta \mathbf{u}|} \ll 1\,, \tag{4.7}$$

for colloidal particles, where $|\mathbf{u}| \sim v_{\mathrm{p}}$ is the characteristic particle velocity and $\nabla \sim 1/a$, the Navier-Stokes equation reduces to the time-dependent linear Stokes equation

$$\rho_{\mathrm{s}} \frac{\partial}{\partial t}\mathbf{u} = -\nabla p(\mathbf{r},t) + \eta_0 \Delta \mathbf{u}(\mathbf{r},t) + \mathbf{f}^e(\mathbf{r},t)\,. \tag{4.8}$$

Moreover, since $t \gg \tau_{\mathrm{B}} = (2/9)\tau_\eta$ for neutrally buoyant particles, where

$$\tau_\eta = \frac{\rho_{\mathrm{s}} a^2}{\eta_0} \tag{4.9}$$

is the characteristic time for the transversal diffusive momentum transport in a viscous

fluid, one finds

$$\left|\frac{\rho_{\mathrm{s}}\frac{\partial}{\partial t}\mathbf{u}}{\eta_0\Delta\mathbf{u}}\right| \sim \frac{\tau_\eta}{t} \ll 1\,, \tag{4.10}$$

so that the $\partial_t\mathbf{u}$ part in the Stokes equation (4.8) can be likewise neglected.
As a consequence, the quasi-stationary fluid flow associated with the non-inertial particle motion is described by the linear Stokes equation,

$$-\eta_0\Delta\mathbf{u}(\mathbf{r}) + \nabla p(\mathbf{r}) - \mathbf{f}^e(\mathbf{r}) = 0\,, \qquad \nabla\cdot\mathbf{u}(\mathbf{r}) = 0\,, \tag{4.11}$$

expressing a local force balance between viscous, pressure, and external body forces.
Accordingly, the hydrodynamic force balance for each colloidal particle i is given by

$$\mathbf{F}_i^{\mathrm{h}} + \mathbf{F}_i = 0\,, \tag{4.12}$$

where

$$\mathbf{F}_i^{\mathrm{h}} = \oint_{S_i^+} \mathrm{d}S\; \boldsymbol{\sigma}(\mathbf{r})\cdot\hat{\mathbf{n}}(\mathbf{r}) \tag{4.13}$$

is the hydrodynamic force on particle i exerted by the surrounding fluid through its surface S_i. Here, $\hat{\mathbf{n}}$ is the unit vector normal to the particle surface at surface point $\mathbf{r}$ pointing out of the particle into the fluid [140], and

$$\boldsymbol{\sigma} = -p\mathbb{1} + \eta_0\left[(\nabla\mathbf{u}) + (\nabla\mathbf{u})^{\mathrm{T}}\right] \tag{4.14}$$

is the Newtonian hydrodynamic stress tensor. The superscript T denotes matrix transposition, and $\mathbb{1}$ is the unit matrix. Moreover, $\mathbf{F}_i$ is the sum of all non-hydrodynamic forces acting on particle i. Note that $\nabla\cdot\boldsymbol{\sigma} = \eta_0\Delta\mathbf{u} - \nabla p = 0$ in the absence of a volumetric body force.

4.1.2. Generalized Smoluchowski equation

The time evolution of the probability distribution function (PDF), $P(X,t)$, with $X = \{\mathbf{r}_1,\ldots,\mathbf{r}_N\}$, of finding the centers of N particles at the configuration X at time t is described by an N-particle diffusion equation termed the generalized Smoluchowski equation (GSE). This quantity is obtained heuristically from combining the exact continuity

equation,

$$\frac{\partial}{\partial t}P(X,t) + \sum_{i=1}^{N} \nabla_i \left[\mathbf{v}_i\, P(X,t)\right] = 0\,, \tag{4.15}$$

expressing particle conservation with the force balance (c.f. Eq. (4.12))

$$\mathbf{F}_i^{\mathrm{h}} + \mathbf{F}_i^{\mathrm{int}} + \mathbf{F}_i^{\mathrm{B}} = 0 \tag{4.16}$$

for each Brownian particle i. Here, $\mathbf{F}_i^{\mathrm{int}} = -\nabla_i U(X)$ is the direct force on particle i due to the interaction with the other particles, and

$$\mathbf{F}_i^{\mathrm{B}} = -k_{\mathrm{B}}T\nabla_i \ln\left[P(X,t)\right] \tag{4.17}$$

is a generalized chemical potential gradient force on particle i, termed Brownian force, which has been introduced to enforce equilibration

$$P(X,t) \to P_{\mathrm{eq}}(X) \tag{4.18}$$

for $t \to \infty$, in the absence of external forces acting on the particles and no macroscopic flow.
Using the linearity and instantaneity of Stokes flow (c.f. Eq. (4.11)), it follows

$$\mathbf{F}_i^{\mathrm{h}} = -\sum_{j=1}^{N} \boldsymbol{\zeta}_{ij}(X) \cdot \mathbf{v}_j\,, \tag{4.19}$$

where $\boldsymbol{\zeta}_{ij}(X)$ are the N particle friction tensors forming the elements of a symmetric and positive definite position-dependent $3N \times 3N$ hydrodynamic friction matrix. Eq. (4.19) substituted into Eq. (4.16) can be used to express the particle configurational velocities $\mathbf{v}_i$ in terms of the hydrodynamic forces. This leads to the GSE,

$$\frac{\partial}{\partial t}P(X,t) = \hat{O}(X)P(X,t) \tag{4.20}$$

where

$$\hat{O}(X) = \sum_{i,j=1}^{N} \nabla_i \cdot \boldsymbol{\mu}_{ij}(X) \cdot \left[k_{\mathrm{B}}T\nabla_j - \mathbf{F}_j^{\mathrm{int}}(X)\right] \tag{4.21}$$

is the second-order Smoluchowski differential operator. Inversion of (4.19) gives

$$\mathbf{v}_i = -\sum_{i,j=1}^{N} \boldsymbol{\mu}_{ij}(X) \cdot \mathbf{F}_j^{\mathrm{h}} \,, \tag{4.22}$$

where the $\boldsymbol{\mu}_{ij}$ are the hydrodynamic mobility tensors forming the elements of a $3N \times 3N$ symmetric and positive definite mobility matrix.

4.1.3. Hydrodynamic interactions

The generalized Stokes law presented in Eqs. (4.19) and (4.22) states that the velocity of a colloidal particle is influenced by the instantaneous hydrodynamic forces exerted on all particles in the system. To visualize this, consider a particle i moving in the presence of $N-1$ other particles in a viscous fluid. Due to its motion, particle i exerts a force $\mathbf{F}_i = -\mathbf{F}_i^{\mathrm{h}}$ on the surrounding fluid resulting in a perturbation of the fluid velocity field. This perturbation is for $t \gg \{\tau_\eta, \tau_{\mathrm{B}}\}$ quasi-instantaneously transmitted through the fluid as described by Eq. (4.11) inducing forces not only on neighboring particles but due to hydrodynamic back-reflections also on the particle i itself.
The matrices $\boldsymbol{\mu}$ and $\boldsymbol{\xi}$ are solely dependent on the particle configuration X, and the hydrodynamic particle surface boundary conditions. The latter are discussed in detail in Subsec. 4.1.4. The difficult theoretical treatment of HIs originates firstly from their long-range nature. The disturbance of the fluid velocity field induced by the forced motion of a particle decays with distance r as $1/r$ [141]. Moreover, two particles are strongly affected hydrodynamically by a neighboring one. In contrast to effective direct interactions, which often can be treated as pairwise additive, HIs can be described as pairwise additive for semidilute systems of particles repelling each other over larger distances.
In the absence of HIs (free-draining limit), the mobility tensors reduce to

$$\boldsymbol{\mu}_{ij} = \delta_{ij}\mu_0 \mathbb{1} \,, \tag{4.23}$$

where $\mu_0 = 1/\zeta_0$. Provided the particles are mutually distinct so that they can be described hydrodynamically as point-like, one has

$$\boldsymbol{\mu}_{ii} = \mu_0 \mathbb{1} \,, \tag{4.24}$$

$$\boldsymbol{\mu}_{ij} \approx \mathbf{T}\left(\mathbf{r}_i - \mathbf{r}_j\right) \,, \tag{4.25}$$

where

$$\mathbf{T}(\mathbf{r}) = \frac{1}{8\pi\eta_0 r}\left[\mathbb{1} + \hat{\boldsymbol{r}}\hat{\boldsymbol{r}}\right] \tag{4.26}$$

is the so-called Oseen tensor for an unbounded quiescent fluid and $\hat{\mathbf{r}} = \mathbf{r}/r$. The Oseen tensor linearly relates a point force $\mathbf{F}_0$ acting on the fluid at $\mathbf{r}_0$ to the resulting flow-field according to

$$\mathbf{u}(\mathbf{r}) = \mathbf{T}(\mathbf{r} - \mathbf{r}_0) \cdot \mathbf{F}_0 \,. \tag{4.27}$$

The next step beyond the far-distance point-particle approximation is to account for the non-zero particle volume while maintaining the pairwise additivity of the point-particle approximation. This leads to the Rotne-Prager (RP) approximation for no-slip spheres (c.f Eq. (4.6))

$$\boldsymbol{\mu}_{ii}^{\mathrm{RP}} = \mu_0\mathbb{1} + \mathcal{O}\left[\left(\frac{a}{r_{ij}}\right)^4\right], \tag{4.28}$$

$$\boldsymbol{\mu}_{ij}^{\mathrm{RP}} = \mu_0\left[\frac{3}{4}\frac{a}{r_{ij}}\left(\mathbb{1} + \hat{\mathbf{r}}_{ij}\hat{\mathbf{r}}_{ij}\right) + \frac{1}{2}\left(\frac{a}{r_{ij}}\right)^3\left(1 - 3\hat{\mathbf{r}}_{ij}\hat{\mathbf{r}}_{ij}\right)\right] + \mathcal{O}\left[\left(\frac{a}{r_{ij}}\right)^4\right], \tag{4.29}$$

where $\hat{\mathbf{r}}_{ij} = (\mathbf{r}_i - \mathbf{r}_j)/\left|\mathbf{r}_i - \mathbf{r}_j\right|$ and $r_{ij} = |\mathbf{r}_{ij}|$.
The RP approximation can be applied to charged-particles dispersions where the mutual distance is large compared to the particle radius a, and the importance of the near-field HIs is minor. Only under these conditions is the approximation of the self-mobility $\boldsymbol{\mu}_{ii}$ by $\mu_0\mathbb{1}$ justified.
The RP approximation cannot be used for hard spheres where near-contact particle configurations are likely, requiring instead the inclusion of lubrication-forces. However, its analytic form allows for the calculation of analytic expressions for certain transport properties. This is exemplified by Eq. (5.3), giving the sedimentation coefficient, K, of permeable hard spheres in RP approximation. In spite of the limited accuracy, such expressions provide valid estimates for trends. Very importantly, the RP approximation preserves the positive definiteness of the exact mobility matrix, guaranteeing that $P(X, t \to \infty) = P_{\mathrm{eq}}(X)$.
The mobility matrix elements for higher orders in $1/r$ beyond the monopole and dipole order can be calculated using various methods such as, e.g., the method of reflections [142] and scattering series expansion methods [143].
Here, we discussed torque-free colloidal particles in a quiescent fluid, only. Though, the presented concepts can be extended to particles with torque and to conditions where an external force, e.g. an external shear flow, is present.

4.1.4. Hydrodynamic particle modeling and boundary conditions

In Section 2.1, we have discussed the importance of appropriate hydrodynamic particle modeling of the internal particle structure. The modeling includes the selection of appropriate inner BCs for describing the solvent particle interactions. In this thesis, we take advantage of the fact that complex particle intrinsic structures can be mapped on the HRM, by considering the effect of solvent permeability through an effective reduced hydrodynamic radius $a_{\mathrm{h}} \leq a$, for which stick BCs apply. As an illustration, consider two simple hydrodynamic particle models, namely uniformly fluid-permeable rigid spheres [144, 145], and non-permeable rigid spheres with Navier partial-slip hydrodynamic surface boundary conditions [146].
In the uniformly-permeable sphere model, the pore-size averaged fluid flow inside a particle is described by the Brinkman-Debye-Bueche (BDB) equation, and outside by the Stokes equation [147] (c.f Eq. (4.11)). The BDB equation describes the pore-size averaged fluid flow inside a particle i of volume V_i by the inclusion of an additional friction [51, 59]

$$\eta_0 \Delta \mathbf{u}(\mathbf{r}) - \nabla P(\mathbf{r}) - \eta_0 \kappa^2 \left[\mathbf{u}(\mathbf{r}) - \mathbf{w}_i(\mathbf{r})\right] = 0 \,, \quad \text{for } \mathbf{r} \in V_i \,. \tag{4.30}$$

Here, $\mathbf{w}_i$ is the velocity of the rigid skeleton of particle i with translational velocity $\mathbf{v}_i$ and angular velocity $\mathbf{\Omega}_i$. Accordingly, $\mathbf{u}(r) - \mathbf{w}_i$ denotes the fluid velocity within the reference frame of the particle skeleton. This relative velocity causes an additional friction force characterized by the so-called inverse hydrodynamic penetration length, κ^{-1}, and the solvent viscosity η_0. The imposed particle boundary conditions are that the fluid velocity and tangential stress vary continuously across the particle surface. The suspension transport properties in this model depend on the material-specific quantity κ, or equivalently on the reduced parameter

$$\lambda_x = \frac{1}{\kappa a} \,, \tag{4.31}$$

equal to the ratio of the hydrodynamic penetration length, $1/\kappa$, [1] and particle radius a. The penetration length is roughly equal to the mean pore size of the rigid particle skeleton. In the limit $\lambda_x \to 0$ of vanishing mean pore size, a non-permeable sphere with no-slip hydrodynamic BCs on its surface is obtained. For the BDB equation to apply, the mean pore size should be smaller than one tenth of the particle radius, i.e. $\lambda_x \leq 0.1$. The present permeable particle model has been generalized to spherical particles with a non-constant permeability profile $\kappa(r)$, varying with the radial distance r (see, e.g. Ref.

[1] The hydrodynamic penetration length κ discussed in this section should not be confused with the Debye screening length denoted by the same letter.

[144]), such as core-shell particles [51, 148–150] consisting of a dry core and a permeable outer shell. The core-shell model describes, in a coarse-grained manner, the hydrodynamic effect of a polymer brush.

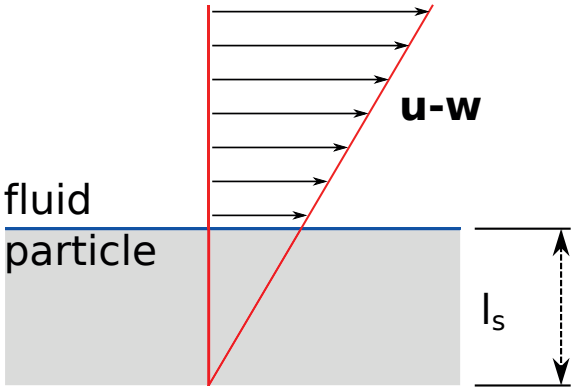

Fig. 4.1.: Sketch of Navier slip-stick boundary conditions, and the corresponding slip length l_s. Here, $\mathbf{u} - \mathbf{w}$ denotes the velocity of the solvent relative to the particle surface $\mathbf{w}$.

The Navier partial-slip model describes fluid-impermeable colloidal spheres where the fluid is allowed to partially slip along their surfaces. The associated Navier partial-slip BC demands, for a stationary sphere, at each surface point the proportionality of surface-tangential fluid velocity, $\mathbf{u}_\parallel$, and shear-stress, $\mathbf{t}_\parallel$, according to

$$\mathbf{u}_\parallel = \frac{l_s}{\eta_0}\,\mathbf{t}_\parallel\,. \tag{4.32}$$

The proportionality constant is given by the ratio of the so-called Navier length, l_s, and the fluid shear viscosity η_0. Here, l_s approximately characterizes the extrapolated distance over which the relative velocity of the solvent decays to zero as illustrated in Fig. 4.1. In the limit $l_s^* \to 0$, the no-slip BC describing zero surface slip is recovered. Here, $l_s^* = l_s/a$ is the reduced Navier length. In the opposite limit $l_s^* \to \infty$, the free-surface BC of zero tangential stress is obtained, corresponding to fluid perfectly slipping along the sphere surface in form of local plug flow. The Navier partial-slip BC can serve as an effective description of a hydrophobic particle surface, and of a rigid particle with surface roughness and corrugations [151]. It is also applicable when non-adsorbing (short) polymers are dispersed in the fluid, owing to the formation of a thin clear-fluid depletion layer at the particle surfaces [152].

The hydrodynamic radius is a single-particle property which depends on the intra-particle hydrodynamic structure of the spherical particle, and in principle also on the considered

single-particle transport property. It can be defined operationally through the Stokes-Einstein(-Debye) expressions

$$d_0^t(\alpha) = \frac{k_B T}{6\pi\eta_0\, a_h^t(\alpha)} \tag{4.33}$$

$$d_0^r(\alpha) = \frac{k_B T}{8\pi\eta_0\, a_h^r(\alpha)^3}\,, \tag{4.34}$$

for the translational and rotational diffusion coefficients d_0^t and d_0^r, respectively, of an isolated spherical particle in an infinite fluid. The single-particle diffusion coefficients are related to the respective mobilities by $d_0^{\{t,r\}} = k_{\mathrm{B}} T \mu_0^{\{t,r\}}$. An additional definition not considered here is based on the intrinsic viscosity, $[\eta]$, of dispersed spheres [49]. Here, α denotes a set of parameters characterizing the hydrodynamic particle structure. For the two considered models is $\alpha = \{\lambda_x, l_s^*\}$. The respective translational and rotational hydrodynamic radii are [144, 145]

$$\frac{a_h^t(\lambda_x)}{a} = \frac{2x^2\,(x - \tanh(x))}{2x^3 + 3(x - \tanh(x))} \tag{4.35}$$

$$\frac{a_h^r(\lambda_x)}{a} = \left[1 + \frac{3}{x^2} - \frac{3\coth(x)}{x}\right]^{\frac{1}{3}}\,, \tag{4.36}$$

for a homogeneously permeable sphere with $x = 1/\lambda_x$, and [146]

$$\frac{a_h^t(l_s^*)}{a} = \frac{1 + 2\,l_s^*}{1 + 3\,l_s^*} \tag{4.37}$$

$$\frac{a_h^r(l_s^*)}{a} = \left(\frac{1}{1 + 3\,l_s^*}\right)^{1/3}\,, \tag{4.38}$$

for a Navier partial-slip sphere.

One can associate each hydrodynamic radius, a_h, with a reduced hydrodynamic slip length, L_h^*, through

$$L_h^*(\alpha) = \frac{L_h(\alpha)}{a} = 1 - \frac{a_h(\alpha)}{a}\,. \tag{4.39}$$

The quantity L_h^* is the relative radial distance, $L_h = a - a_h$, of the apparent no-slip spherical surface inside the particle to its outside surface, in units of the outside surface, direct interaction radius a. Except for λ_x, the asterisk is used in the context of the HRM to label lengths given in units of a.

In the experimentally common situation where L_h^* is small, curvature effects are negligible and the particle-fluid interface can be described as flat. As it is explained in Ref. [53], the

key point to notice is that the reduced slip length, $L^*_{h,f} = 1 - a_{h,f}/a$, in the flat-interface approximation and its associated flat-interface hydrodynamic radius, $a_{h,f}$, are independent of the single-particle transport properties d^t_0, d^r_0 and $[\eta]$ used in their definition. Since each of these transport properties is associated with a particular ambient velocity field, e.g. with a constant flow field in case of d^t_0, an equivalent statement is that $L_{h,f}$ is independent of the ambient flow.
It was shown in Ref. [53] that the relations

$$L^*_h(\alpha) = L^*_{h,f}(\alpha)\left[1 + \mathcal{O}\left(L^*_{h,f}(\alpha)\right)\right] \tag{4.40}$$

$$a^*_h(\alpha) = a^*_{h,f}(\alpha)\left[1 + \mathcal{O}\left(L^*_{h,f}(\alpha)^2\right)\right] , \tag{4.41}$$

apply universally to rigid spheres with arbitrary, non-singular spherically symmetric hydrodynamic structures and boundary conditions, independent of the invoked single-particle transport property.
These relations are readily verified, using Eqs. (4.35) - (4.38), for the special case of a Navier partial-slip sphere where the flat-interface slip length is equal to

$$L^*_{h,f}(l^*_s) = l^*_s \, , \tag{4.42}$$

and for a uniformly permeable sphere where

$$L^*_{h,f}(\lambda_x) = \lambda_x \, . \tag{4.43}$$

Note that the slip length, L_h, is equal to the Navier length, l_s, in the flat-interface limit only.
Eqs. (4.40-4.41) do not apply to non-rigid particles such as spherical liquid droplets, and rigid particles of singular hydrodynamic structure. The latter case is exemplified in Ref. [145] by a hollow sphere with a uniformly permeable rigid shell of infinitesimal thickness. The hydrodynamic radii a^t_h and a^r_h of the ultra-thin hollow sphere differ already to linear order in the smallness parameter λ_x. As for a droplet, an inscribed apparent no-slip spherical surface which is necessarily rigid can not be introduced for the singular hollow-sphere example.
Eqs. (4.35-4.38) can be inverted to obtain the material-specific parameters λ_x and l^*_s in terms of the ratio

$$\gamma = \frac{a_h}{a} \, , \tag{4.44}$$

or likewise in terms of the reduced width (slip length), $\overline{\gamma} = 1 - \gamma$, of the apparent fluid annulus region surrounding the apparent no-slip sphere. The parameter γ completely characterizes the intra-particle hydrodynamic structure in the hydrodynamic radius model (HRM) where spherical particles of arbitrary hydrodynamic structure are described hydrodynamically as no-slip spheres of reduced radius a_h, for unchanged pair potential. This implies in particular an unchanged excluded volume radius $a > a_h$, c.f. Fig. 2.1.

Numerical results illustrating the inversion of Eqs. (4.35-4.38) are depicted in Fig. 4.2 where the reduced penetration length of a permeable sphere, $\lambda_x^{t,r}$, and the reduced slip length of a Navier partial-slip sphere, $(l_s^*)^{t,r}$, are plotted as functions of $\overline{\gamma}$. The reduced lengths derived from the translational (rotational) Stokes-Einstein-(Debye) relation are labeled by the superscript t (superscript r). For a thin annulus shell with $\gamma > 0.9$, the

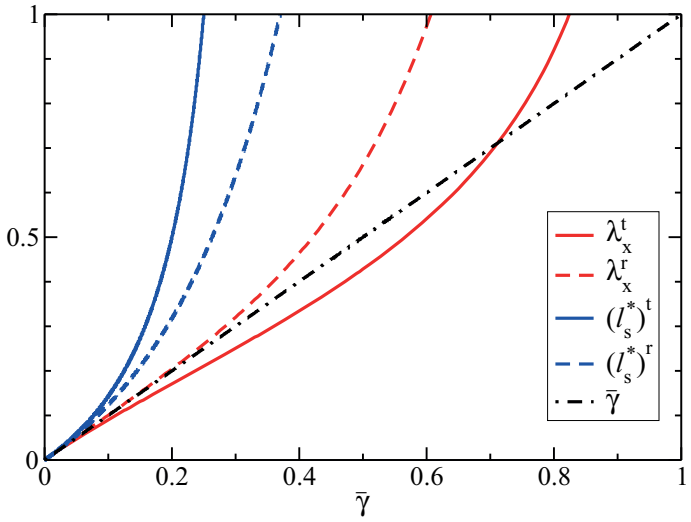

Fig. 4.2.: Reduced fluid penetration length $\lambda_x^{t,r}$ (red lines) and reduced Navier length $(l_s^*)^{t,r}$ (blue lines), as functions of the reduced fluid annulus width $\overline{\gamma} = 1 - \gamma$. Solid lines (dashed lines) describe quantities derived from the translational (rotational) single-sphere Stokes-Einstein-(Debye) relation.

four reduced lengths are small and commonly described by the dashed-dotted line $\overline{\gamma}$, corresponding to $\lambda_x \approx L_h$ and $l_s^* \approx L_h$. This situation is common to colloidal systems for which values $\lambda_x < 0.05$ are typically found, and for which the Navier length is commonly equal to a few nanometers.

Differences between the considered lengths are significant for larger values of $\overline{\gamma}$. For a given reduced hydrodynamic radius $\gamma = a_h/a$, two different values $\lambda_x^t \neq \lambda_x^r$ are then obtained. The perfect-slip limit $l_s^* \to \infty$ corresponds to $\overline{\gamma} = 1/3$ for translational, and to $\overline{\gamma} = 1$ for rotational diffusion. While a rotating perfect-slip sphere experiences no friction, akin to

a point particle for which $\gamma = 0$, the values of $\overline{\gamma}$ for a translating Navier sphere do not exceed 1/3. Regarding the translational diffusion coefficient, a perfect-slip sphere with $\gamma = 2/3$ has the same value, $d_0^t = k_B T/(4\pi\eta_0 a)$, as a uniformly permeable sphere with $\lambda_x \approx 0.278$. However, such a large value of λ_x is unrealistic. As mentioned before, in order for the BDB equation to describe flow inside a permeable particle, λ_x should be no larger than 0.1, corresponding to a maximally allowed penetration length equal to one-tenth of the particle radius.
Since in this thesis only translational diffusion properties are studied, the superscript t is omitted in the following.

4.1.5. Dynamic structure factor

The dynamic structure factor is given in Smoluchowski dynamics by [153]

$$S(q,t) = \left\langle \frac{1}{N} \sum_{i,j=1}^{N} e^{i\mathbf{q}\cdot\mathbf{r}_i} \left(e^{\hat{O}_{\mathrm{B}} t}\, e^{-i\mathbf{q}\cdot\mathbf{r}_j} \right) \right\rangle_{\mathrm{eq}} . \tag{4.45}$$

It is the time-dependent generalization of the static structure factor, $S(q) = S(q, t = 0)$, presented in Eq. (3.17), and is the time auto-correlation function of microscopic particle concentration fluctuations in Fourier space. In Eq. 4.45, $\langle \ldots \rangle_{\mathrm{eq}}$ denotes the equilibrium average and

$$\hat{O}_{\mathrm{B}}(X) = \sum_{i,j=1}^{N} \left[k_{\mathrm{B}} T\, \nabla_i + F_i^{\mathrm{int}}(X) \right] \cdot \boldsymbol{\mu}_{ij}(X) \cdot \nabla_j \,, \tag{4.46}$$

is the so-called backward Smoluchowski operator equal to the adjoint of $\hat{O}(X)$ in Eq. (4.21) with respect to the unweighted inner product $(f|g) = \int \mathrm{d}X\, f(X)\, g^*(X)$ for two arbitrary configuration-space functions f and g. Note that $S(q,t)$ is experimentally accessible using DLS or NSE. It can be shown, that $\hat{O}_B$ is a negative-semi definite operator so that $S(q,t)$ is a positive valued and strictly monotonic decaying function of time [153]. Eq. 4.45 will be used for the derivation of an expression for the hydrodynamic function which characterizes the influence of HIs on the short-time dynamics of colloidal suspensions (c.f. Subsec. 4.2.1).

4.1.6. Basics of DLS and NSE

Which experimental technique is useful for the measurement of $S(q,t)$ of a suspension of monodisperse colloidal particles depends on the particle sizes. For particles suspensions in the micrometer size range, dynamic light scattering is useful. For quasi-elastic scattering,

one infers in homodyne DLS the intensity auto-correlation function

$$g_{\mathrm{I}}(q,t) \propto \left\langle |E_S(\mathbf{q},0)|^2 \, |E_S(\mathbf{q},t)|^2 \right\rangle , \tag{4.47}$$

with the scattered light electric field strength amplitude

$$E_S(\mathbf{q},t) \propto \sum_{j=1}^{N} f(q) e^{i\mathbf{q}\cdot\mathbf{r}_j} E_0 \, . \tag{4.48}$$

Here, E_0 is the incident light electric field strength [75], $f(q)$ denotes the form factor of a spherical particle, and $\langle \ldots \rangle$ is likewise a time or ensemble average for ergodic systems. Using the Siegert relation valid for an ergodic medium and with $E_S(\mathbf{q},t)$ treatable as a Gaussian random variable, $S(q,t)$ can be inferred from a DLS measurement of $g_{\mathrm{I}}(\mathbf{q},t)$ according to

$$\frac{g_I(q,t)}{g_I(q,0)} \propto \beta^* \left(\frac{S(q,t)}{S(q,0)} \right)^2 , \tag{4.49}$$

where β^* with $0 < \beta^* \leq 1$ is a geometric correction factor depending on the number of collected speckles. For homogeneously scattering spherical particles is $f(q) \propto \sigma^3$. Thus DLS measurements on systems containing cluster of particles are subtle. The scattering signal from a large cluster can be dominant.

In a neutron spin echo experiment quasi-elastic scattering of an initially polarized neutron beam from a sample is used to determine directly $S(q,t)$ from the phase shift of the scattered neutron beam [98]. Because of the small De Broglie wavelength of thermal neutrons, distances on the inter-atomic length scale can be resolved. Different from DLS multiple scattering is very small even in a concentrated dispersion in NSE. Moreover, $S(q,t)$ is derived from atomic and molecular positions [154] so that in NSE there is not the strong particle size dependence of the scattering signal proportional to σ^6 as in DLS. This is a great advantage when the dynamics of (transient) clusters of particles is studied. Our American collaborators use NSE at the NIST Center for Neutron Research in Gaithersburg, MD, and the Institut Laue-Langevin in Grenoble to measure the short-time dynamics of Lysozyme protein solutions [98]. This is presented in Sec. 8.2. In the NSE measurements they consider short correlation times, typically less than 25 ns [32]. In the scanned q-range and time window the internal motion of Lysozyme domains, which in principle could be probed by NSE, can be ignored due to the strong rigidity of the Lysozyme protein [32, 155]. Note further that the rotation of the proteins is much slower than their translational motion [32].

4.2. Short-time dynamics

The short-time regime, $\tau_B \ll t \ll \tau_\mathrm{D}$, is distinct from the long-time regime, $t \gg \tau_\mathrm{D}$, as discussed in Sec. 4.1.1. For short times, the particle configuration change is so minuscule that the slowing influence of direct interactions is not yet operative, different from the solvent-mediated HIs which act quasi-instantaneously on the colloidal short-time scale. Short-time transport properties are thus expressible as simple equilibrium averages, with direct interactions entering only indirectly via their influence on the equilibrium microstructure, e.g on $g(r)$. Long-time transport properties are additionally influenced by the Brownian motion of the particles so that they depend in a direct way both on direct and hydrodynamic interactions.
In this section, we describe our analytic toolbox of calculating short-time diffusion and rheological properties of hydrodynamically structured particles, in the framework of the HRM.

4.2.1. Hydrodynamic function

The short-time dynamics is characterized by the initial decay of $S(q,t)$. For an analytic expression of $S(q,t)$ for $t \ll \tau_\mathrm{D}$, a cumulant expansion can be used,

$$S(q,t) = S(q,t=0)\, \exp\left[\sum_{l=1}^{\infty} \frac{(-t)^l}{l!}\Gamma^{(l)}(q)\right], \tag{4.50}$$

where $\Gamma^{(n)}$ is the n-th cumulant of $S(q,t)$. For uncorrelated particles in a dilute suspension for which the GSE is explicitly solvable, one shows that $\Gamma^{(1)}(q) = q^2 d_0$ with the Stokes-Einstein single-particle diffusion coefficient d_0. For correlated particles suspensions, the first cumulant is given by

$$\Gamma^{(1)}(q) = q^2\, D(q) \tag{4.51}$$

with the short-time diffusion function $D(q)$. The higher order cumulants characterize the deviation of $S(q,t)$ from a purely exponential decay for time $t \sim \tau_\mathrm{D}$ [153].
An analytic expression for $D(q)$ is derived from the first-order in time Taylor expansion of the rhs of Eq. (4.45). Comparison with Eq. (4.50) gives

$$\Gamma^{(1)}(q) = q^2 D(q) = q^2 d_0 \frac{H(q)}{S(q)} \tag{4.52}$$

with the positive-valued hydrodynamic function $H(q)$ given by

$$H(q) = \lim_{\infty} \frac{1}{N\mu_0} \sum_{i,j=1}^{N} \left\langle \hat{\boldsymbol{q}} \cdot \boldsymbol{\mu}_{ij}(X) \cdot \hat{\boldsymbol{q}}\, e^{i\mathbf{q}\cdot(\mathbf{r}_i - \mathbf{r}_j)} \right\rangle_{\text{eq}} , \tag{4.53}$$

where $\hat{q} = \mathbf{q}/q$.
This is the key-quantity classifying short-time diffusion on length scales $\sim 1/q$. It quantifies the effect of HIs on the short-time decay of $S(q,t)$. The thermodynamic limit used in Eq. (4.53) to describe a macroscopically large scattering volume. For hydrodynamically non-interacting colloidal particles is $\boldsymbol{\mu}_{ij} = \mu_0 \mathbb{1}\delta_{ij}$, so that $H(q) \equiv 1$ independent of q. In this case, the decay of concentration fluctuation correlations is governed solely by $S(q)$ according to

$$D(q)|_{\text{no-HI}} = q^2 \frac{1}{S(q)} . \tag{4.54}$$

Any oscillations in $H(q)$ are thus a hallmark for the influence of HIs. Note that $D(q)$ is directly accessible in DLS and NSE by the measurement of the short-time decay of $S(q,t)$. The employed hydrodynamic particle model in a theoretical calculation enters $H(q)$ via the hydrodynamic mobility tensor $\boldsymbol{\mu}$ for which analytic or numerical results are required.

Self-diffusion coefficient

Eq. (4.53) can be split into a self- and a distinct-part:

$$H(q) = \frac{1}{d_0} \langle \hat{\mathbf{q}} \cdot \boldsymbol{D}_{11}(X) \cdot \hat{\mathbf{q}} \rangle_{\text{eq}} + \lim_{\infty} \frac{N-1}{d_0} \langle \hat{\mathbf{q}} \cdot \boldsymbol{D}_{12}(X) \cdot \hat{\mathbf{q}}\, e^{i\mathbf{q}\mathbf{R}_{12}} \rangle_{\text{eq}} \tag{4.55}$$

$$= \frac{d_{\text{s}}}{d_0} + H^{\text{d}}(q) \tag{4.56}$$

where in place of the mobility tensor $\boldsymbol{\mu}$ the related diffusivity tensor $\boldsymbol{D} = k_{\text{B}}T\boldsymbol{\mu}$ with $d_0 = k_{\text{B}}T\mu_0$ has been used. The wavenumber-independent first part contains all self terms $i = j$. It is equal to the translational short-time self-diffusion coefficient, d_{S}, which quantifies the slope of the initial mean square displacement (MSD). Owing to the slowing influence of the near-field part of the HIs at non-zero particle concentrations, d_{S} is smaller than d_0 to which it reduces at infinite dilution only. The second, wavenumber-dependent distinct part, $H^{\text{d}}(q)$, is due to hydrodynamic cross correlations. It vanishes for $q \to \infty$.

sedimentation velocity

The hydrodynamic function has the physical interpretation of a short-time generalized sedimentation coefficient for a homogeneous suspension of monodisperse colloidal spheres subjected to a weak force field colinear with $\mathbf{q}$ and oscillating spatially as $\cos(\mathbf{q}\cdot\mathbf{r})$ with spatial position $\mathbf{r}$ [156]. For $q \to 0$, a uniform force field is recovered such as the buoyancy corrected local gravitational field on earth. As a consequence,

$$K = \frac{V_{\mathrm{sed}}}{V_0} = \lim_{q\to 0} H(q) \tag{4.57}$$

is the short-time average sedimentation velocity, V_{sed}, of hydrodynamically interacting colloidal particles, normalized by the particle model dependent mean sedimentation velocity, V_0, of an isolated particle sedimenting in the same force field. The sedimentation coefficient, K, is related to the short-time collective diffusion coefficient, d_{C}, by

$$d_{\mathrm{C}} = d_0 \frac{K}{S(0)}\,, \tag{4.58}$$

where for monodisperse particles $S(0) = S(q \to 0)$ is the relative osmotic compressibility of the suspension. At larger concentrations where $S(0)$ is small, d_{C} can be significantly larger than d_0 even though $K < 1$. In principle, the short-time coefficient d_{C} should be distinguished from the associated long-time collective diffusion coefficient, $d_{\mathrm{C}}^{\mathrm{L}}$ appearing in Fick's law, $\mathbf{j} = -d_{\mathrm{C}}^{\mathrm{L}}\nabla n$, of macroscopic gradient diffusion. The latter, however, is only slightly smaller than the short-time coefficient, by less than 7 % even for a concentrated suspension of no-slip colloidal hard spheres at volume fraction $\phi = 0.45$ [157]. The difference between the two collective diffusion coefficients can be expected to be even smaller for particles with weaker HIs such as permeable and partial-slip spheres, and charge-stabilized particles with long-range electrostatic repulsion. Different from collective diffusion and sedimentation, the long-time translational self-diffusion coefficient, d_{L}, can be substantially smaller than its short-time sibling d_{S}, owing to the retarding relaxation of next-neighbor particle cages which are slightly distorted from their equilibrium spherical symmetry at long times. For colloidal hard spheres at the freezing transition concentration, e.g., is $d_{\mathrm{L}}/d_{\mathrm{S}} \approx 0.1$ according to the empirical freezing rule by Löwen *et al.* [158, 159].

A key observation regarding the translational mobility tensors, $\boldsymbol{\mu}_{ij}$, of hydrodynamically structured spherical particles is the relation

$$\boldsymbol{\mu}_{ij}(\mathbf{X}) = \boldsymbol{\mu}_{ij;\mathrm{HRM}}(\mathbf{X}; a_{h,f}) \left[1 + \mathcal{O}\left(\left(L^*_{h,f}\right)^2\right)\right]\,, \tag{4.59}$$

where the $\boldsymbol{\mu}_{ij;\mathrm{HRM}}(\mathbf{X}; a_{h,f})$ are the mobility tensors of the associated HRM. The relation follows from Eqs. (4.40) and (4.41) in conjunction with a general scattering series expansion of the exact N-sphere translational mobility tensors [52, 53]. Since the short-time transport properties are equilibrium averages of specific mobility tensor elements, it follows that

$$H(q) = H_{\mathrm{HRM}}(q)\left[1 + \mathcal{O}\Big(\big(L^*_{h,f}\big)^2\Big)\right] \tag{4.60}$$

with an analogous expression valid for η_∞. Thus, the error introduced in calculating short-time transport properties of hydrodynamically structured particles using the simplifying HRM is of $\mathcal{O}((L^*_{h,f})^2)$ small.

For the calculation of the short-time self-diffusion coefficient and sedimentation velocity analytic expressions have been derived. We will present in Chapter 5 useful analytic scaling relations for the calculation of short-time diffusion dynamic properties of suspensions of internally structured particles. These relations are complemented by two semi-analytic and easy-to-implement approximation schemes which have been successfully applied in the past to suspensions of no-slip neutral and charge-stabilized spherical particles [65, 86, 136, 160]. The so called pairwise additivity (PA) and Beenakker-Mazur (BM) methods are presented in Secs. 4.4.1 and 4.4.2, and complemented by a discussion of a hybrid scheme in Sec. 4.4.3.

4.2.2. High-frequency viscosity

So far diffusion-related properties have been addressed. We discuss next a short-time rheological property, namely the high-frequency-limiting suspension viscosity η_∞. It linearly relates the average suspension shear stress to the applied rate of strain in a low-amplitude, high-frequency shear experiment. For frequencies $\omega \gg 1/\tau_{\mathrm{D}}$, the suspension microstructure remains practically unchanged so that like the short-time diffusion properties discussed before, η_∞ is a quantity of purely hydrodymanic origin, influenced by direct particle interactions through the equilibrium averaging only. For particles acting hydrodynamically like points ($\gamma = 0$), it reduces to the shear viscosity, η_0, of the suspending Newtonian fluid. In the limit of infinite dilution, the viscosity expression $\eta_0\,(1 + 2.5\phi)$ is obtained, which included the Einstein intrinsic viscosity contribution $5/2\phi$.

The high-frequency viscosity should be distinguished from the zero-frequency viscosity [161],

$$\eta\,(\phi) = \eta_\infty\,(\phi) + \Delta\eta\,(\phi)\ , \tag{4.61}$$

with the latter determined in a steady low-shear experiment. See Subsec. 4.3.2 for a

discussion of η.

4.3. Long-time dynamics

Long-time colloidal transport properties such as d_{L} and η characterize the particle dynamics on time scales $t \gg \tau_{\mathrm{D}}$ during which the particle configuration has changed significantly. Different from short-time properties, they are influenced by thermally driven microstructural relaxations depending on direct and hydrodynamic interactions alike. This renders a first-principles calculation of long-time properties demanding, both in theory and simulations, in particular when the salient HIs are accounted for. Consequently, in most simulation studies of the concentration dependence of d_{L} and η, the influence of the HIs has been ignored [162–164]. The few existing three-dimensional simulation studies where HIs are included focus on Brownian hard spheres with no-slip BCs [165–167]. Therefore, a theoretical scheme is in demand allowing for the approximate calculation of d_{L} and η for suspensions of hydrodynamically structured particles. Such a scheme is presented in detail in Sec. 5.4. In addition, simplified mode-coupling theory expressions for d_{L} and η are presented in Subsec. 4.4.4.
Here, we shortly introduce the long-time dynamic properties discussed in this work and highlight their physical origin.

4.3.1. Self-diffusion coefficient

The long-time self-diffusion coefficient, d_{L}, is equal to the slope of the MSD for times $t \gg \tau_{\mathrm{D}}$. It can be related to d_{S} with the help of the following configurational average expression [61],

$$d_{\mathrm{L}} = d_{\mathrm{S}} + \Delta D\,, \tag{4.62}$$

with

$$\Delta D = -\left\langle (\hat{\mathbf{q}}\cdot\mathbf{v}_1)\hat{O}_B^{-1}(\hat{\mathbf{q}}\cdot\mathbf{v}_1)\right\rangle\,. \tag{4.63}$$

The slowing effect on d_{L} by the dynamically restructuring cage of next neighbors formed around each particle is embodied in the negative valued relaxation contribution, ΔD, to D_L implying

$$0 \leq d_{\mathrm{L}} < d_{\mathrm{S}} < d_0\,, \quad \text{for}\, \phi > 0\,. \tag{4.64}$$

In Eq. (4.63), $\mathbf{v}_1 = \hat{O}_{\mathrm{B}}\mathbf{r}_1$ is the coarse-grained velocity of a representative particle 1 at po-

sition $\mathbf{r}_1$ whose Brownian motion is considered, and $\hat{O}_B(X)$ is the backward Smoluchowksi differential operator defined in Eq. (4.46), with its inverse denoted by $\hat{O}_B^{-1}(X)$.
The calculation of the long-time diffusion coefficient is an ambitious task since the distortion of the next-neighbor cage and its reformation need to be considered. For this reason, d_{L} can not be expressed as average over equilibrium distribution functions. Even using computer simulations, only few data, mainly for hard-sphere systems, exist since the computational cost of addressing the long-time regime is very high. This is going to improve in the near future due to the strong increase of computational resources.
However, there exist theoretical schemes for the calculation of long-time dynamic properties based on approximations required for the solution of the generalized Smoluchowski equation (4.20) in the long-time regime. For instance, d_{L} can be calculated using a linear response formalism [142, 153]. In addition, mode-coupling theory (MCT) can be used to calculate the time evolution of the dynamic structure factor based on a memory function formalism. The latter characterizes the fact that a particle configuration at time t depends on its previous history in a non-Markovian way. The MCT scheme is not central to the work presented here.

4.3.2. Zero-frequency viscosity

The zero frequency viscosity introduced in Eq. (4.61) linearly relates the shear stress τ exerted on a dispersion and the resulting shear rate $\partial u/\partial y$ for steady shear, i.e.

$$\tau = \eta \frac{\partial u}{\partial y} \,. \tag{4.65}$$

According to Fig. 4.3, we consider here simple shear flow where $\mathbf{u} = u\hat{\mathbf{e}}_x$ with $u = \dot{\gamma} y$ and constant shear rate $\dot{\gamma}$.
In comparison to the high-frequency viscosity η_∞ (c.f. Eq. 4.61), η has an additional contribution, $\Delta\eta > 0$, originating from the relaxation of the shear-distorted dynamic particle cage formed around each particle. Thus, $\Delta\eta$ is influenced both by direct and hydrodynamic interactions, with the consequence that for strongly correlated colloidal particles, it is substantially larger than η_∞. The long-time dynamic property η can be calculated for example using the simplified MCT expression presented in Sec. 4.4.4. In addition, in Subsec. 5.4.2, we discuss an analytic scaling relation which allows for the calculation of η for permeable particles within the HRM.

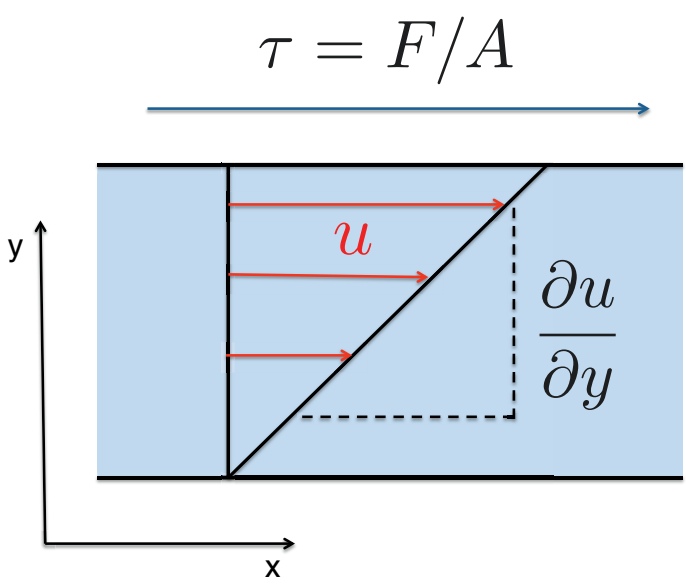

Fig. 4.3.: Sketch of a steady-shear experiment with applied stress $\tau = F/A$ and resulting velocity gradient $\partial u/\partial y$. F denotes the tangential force on the upper plate of the shear cell, and A its area.

4.4. Methods of calculations

In this section, we discuss three different analytic methods for the calculation of dynamic short-time properties, namely the pairwise-additivity approximation (PA), the Beenakker-Mazur method (BM), and a hybrid scheme (PA-BM) combining the advantages of the latter two methods. We present a generalization of these methods to the HRM that allows for an appropriate modeling in particular of particle permeability, and more generally an efficient treatment of different hydrodynamic particle models.

4.4.1. PA approximation for the HRM

The PA approximation of short-time diffusion properties is based on the cluster expansion of the N-particle translational mobility matrix of colloidal spheres,

$$\begin{aligned}\boldsymbol{\mu}_{ij}(\mathbf{X}) = \mu_0 \mathbb{1}\delta_{ij} + \left[\boldsymbol{\mu}_{ij}^{(2)}(\mathbf{X}) - \mu_0 \mathbb{1}\delta_{ij}\right] \\ + \text{three-body terms} + \dots ,\end{aligned} \tag{4.66}$$

with three-body and higher-order cluster contributions being disregarded. The single-particle translational mobility coefficient, $\mu_0 = d_0/(k_B T)$, is dependent on the hydrodynamic intra-particle structure. In the PA approximation, the hydrodynamic mobility

tensors on the pairwise additive level,

$$\boldsymbol{\mu}_{ij}^{(2)}\left(\mathbf{X}\right)=\mu_0\left[\delta_{ij}\left(\mathbb{1}+\sum_{l=1;l\neq i}^{N}\boldsymbol{\omega}_{11}\left(\mathbf{r}_{il}\right)\right)+\left(1-\delta_{ij}\right)\,\boldsymbol{\omega}_{12}\left(\mathbf{r}_{ij}\right)\right], \tag{4.67}$$

where $\mathbf{r}_{ij}=\mathbf{r}_i-\mathbf{r}_j$, are fully accounted for including near-contact lubrication terms. The two-particle tensors $\boldsymbol{\omega}_{11}$ and $\boldsymbol{\omega}_{12}$ describe the hydrodynamic self-interaction of a sphere through flow reflections at another one ($\boldsymbol{\omega}_{11}$), and interactions induced by the motion of a second particle ($\boldsymbol{\omega}_{12}$), respectively. The axial symmetry of the two-sphere hydrodynamic problem in an unbound fluid allows for splitting these tensors into longitudinal and transversal components (c.f. Fig. 4.4), i.e.

$$\boldsymbol{\omega}_{ij}(r)=x_{ij}(\mathbf{r})\hat{\mathbf{r}}\hat{\mathbf{r}}+y_{ij}\left(r\right)\left[\mathbb{1}-\hat{\mathbf{r}}\hat{\mathbf{r}}\right], \tag{4.68}$$

where $\hat{\mathbf{r}}=\mathbf{r}/r$.

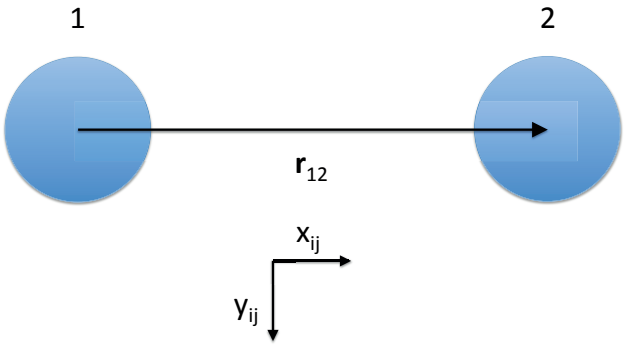

Fig. 4.4.: Symmetry of hydrodynamic interactions in the PA approximation, with corresponding longitudinal, $x_{ij}(r)$, and transversal, $y_{ij}(r)$, 2-sphere mobility coefficients.

The two-sphere mobilities $x_{ij}(r)$ and $y_{ij}(r)$, where $i,j\in\{1,2\}$, can be calculated recursively in the form of a power series in the reduced inverse pair distance, a_h/r, combined with known near-contact lubrication expressions [147, 168, 169] (c.f. Fig. 4.5). The respective truncated expressions up to second order (c.f. Eqs. 4.28 and 4.29) in RP approximation have been presented already in Subsec. 4.1.3, in the context of the mobility matrix.

Insertion of Eq. (4.67) into Eq. (4.53) leads to the PA approximation expressions for d_{S}

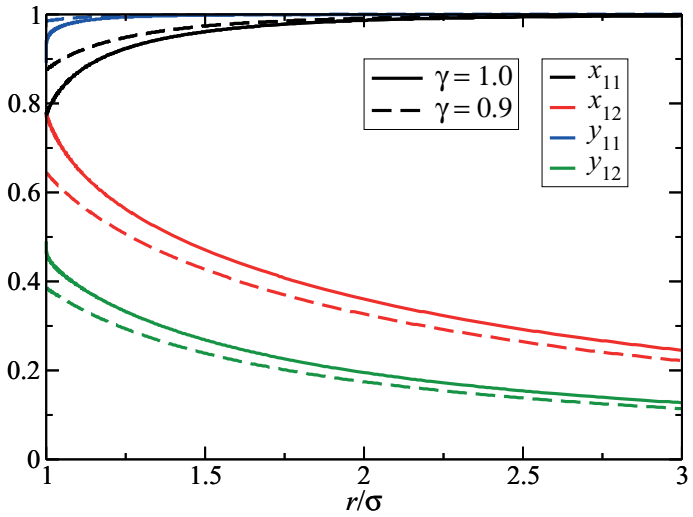

Fig. 4.5.: Longitudinal and transversal mobility coefficients, $x_{ij}(r)$ and $y_{ij}(r)$, tabulated by Jeffrey and Onishi [168] as functions of the interparticle distance r in units of the particle diameter σ. The scaled effective mobilities in the HRM for $\gamma = 0.9$ are represented by the dashed lines, illustrating the reduced strength of HIs with decreasing σ_h/σ.

and $H^d(q)$ [65]. We present these expressions in a form suitable for HRM particles where one distinguishes between the hydrodynamic particle diameter, $\sigma_h = 2a_h$, and the direct interaction diameter σ. For rigid spherical particles is $\sigma = 2a$ the hard-core diameter, while for mechanically soft particles, σ is identified with the characteristic soft diameter σ_s such as the one appearing in the Hertz potential in Eq. (2.1).
Introducing the reduced pair distance, $x = r/\sigma_\mathrm{h}$, and wavenumber, $y = q\sigma_\mathrm{h}$, the self-part contribution to $H(q)$ is given by

$$\left.\frac{d_\mathrm{S}(\phi,\gamma)}{d_0(\gamma)}\right|_\mathrm{PA} = 1 + 8\gamma^3\phi\int_0^\infty \mathrm{d}x\, x^2\, g(\gamma x)\left[x_{11}(x) + 2y_{11}(x) - 3\right]. \tag{4.69}$$

The distinct contribution to $H(y,\gamma)$ reads

$$\begin{aligned} H^d(y,\gamma)\Big|_{\mathrm{PA}} &= \gamma^3\phi \\ &+ 18\gamma\phi\int_0^\infty \mathrm{d}x\; xh(\gamma x)\left[j_0(xy) - \frac{j_1(xy)}{xy} + \gamma^2\frac{j_2(xy)}{6x^2}\right] \\ &+ 24\gamma^3\phi\int_0^\infty \mathrm{d}x\; x^2 g(\gamma x)\,\overline{y}_{12}(x)\,j_0(xy) \\ &+ 24\gamma^3\phi\int_0^\infty \mathrm{d}x\; x^2 g(\gamma x)\left[\overline{x}_{12}(x) - \overline{y}_{12}(x)\right]\left[\frac{j_1(xy)}{xy} - j_2(xy)\right], \end{aligned} \tag{4.70}$$

where j_n is the spherical Bessel function of order n, and $h = g - 1$ is the total correlation function. The overlines in $\overline{x}_{12}(x)$ and $\overline{y}_{12}(x)$ indicate that the respective far-field parts up to third order in $1/x$ have been subtracted off. The argument γx in g and h, with $\gamma = \sigma_h/\sigma$, is a reminder that the RDF is commonly calculated as a function of r/σ, such as in the VW-PY solution for hard spheres. In Fig. 4.5, we show the longitudinal, $x_{11}(r)$ and $x_{12}(r)$, and transversal, $y_{11}(r)$ and $y_{12}(r)$, mobility coefficients tabulated by Jeffrey and Onishi [168] as functions of the interparticle distance r in units of the particle diameter σ for $\gamma = 1$ and $\gamma = 0.9$. Values of $\gamma < 1$ lead to a shift of the $\gamma = 1$ mobility functions reflecting the reduced strengths of the HIs.

In our computations, we use accurate tables for the mobility coefficients provided by Jeffrey and Onishi [170–173] for $x = r\sigma_{\mathrm{h}} < 15$ which continuously cross-over into the corresponding far-distance expansion expressions provided in Appendix B.1.

According to Eq. (4.69), the first-order virial coefficient of the short-time self-diffusion coefficient, d_S, is given by

$$\lambda_{\mathrm{t}}(\gamma) = 8\gamma^3\int_0^\infty \mathrm{d}x\; x^2\exp\left[-\beta V(x)\right]\left[x_{11}(x) + 2y_{11}(x) - 3\right]. \tag{4.71}$$

With the invocation of the precisely tabulated mobilities, the PA-scheme accurately reproduces the first-order virial coefficients for d_{S}, K, and η_∞ [173].

The PA expression for the high-frequency limiting viscosity, generalized to the HRM, reads

$$\begin{aligned} \frac{\eta_\infty(\phi,\gamma)}{\eta_0}\Big|_{\mathrm{PA}} &= 1 + \frac{5}{2}\gamma^3\phi\left[1 + \gamma^3\phi\right] \\ &\quad + 60\left(\gamma^3\phi\right)^2\int_0^\infty \mathrm{d}x\, x^2 g(\gamma x)\, J(x), \end{aligned} \tag{4.72}$$

with the rapidly decaying two-sphere shear mobility function, $J(x)$, accounting for the two-body HIs. It decays asymptotically for distances x as $J(x) \sim (15/128)x^{-6}$. We employ

an accurate numerical table for $J(x)$, based on recursion expressions and the lubrication analysis given in Ref. [170], accompanied by the far-field expansion for distances $x > 15$. Finally, we note that in the spherical annulus model of hydrodynamically structured hard spheres, the lower integration boundary of all integrals in this subsection is given by $1/\gamma$.

4.4.2. Beenakker-Mazur method for the HRM

Except for η_∞, the applicability range of the PA method for short-time hydrodynamic properties is restricted to lower ϕ values. To first order in ϕ, the PA solution is exact. In contrast, the BM method for $H(q)$ and η_∞ by Beenakker and Mazur [174, 175] is applicable also to concentrated systems. We discuss here the standard version of this scheme, but generalized to the HRM where $S(q)$ is the only required input. The BM method is based on a renormalized concentration fluctuation expansion where many-particle HIs contributions are approximately accounted for in terms of so-called ring diagrams, but with lubrication corrections disregarded. Once the self-part d_S of $H(q)$ is suitably corrected [65, 85], as discussed in Sec. 4.4.3, the BM method provides a decent description of short-time transport properties, and this for neutral and charge-stabilized particle systems alike (see Ref. [65]). The BM method results for η_∞ and $H(q)$ reveal inaccuracies at all concentrations which can be partially attributed to its approximate treatment of the HIs. This is underlined in recent work by Makuch and Cichocki [176] where the approximation steps in the derivation of the BM method have been reduced. The fact that their revised version of the BM method with improved hydrodynamic mobility tensors does not significantly improve the agreement with simulation data for no-slip hard spheres points to a fortuitous cancellation of errors introduced in the approximate derivational steps of the original Beenakker-Mazur method.

The BM method expressions for d_s/d_0 and $H^d(q)$ [174, 175], generalized to the HRM, reads

$$\left.\frac{d_\mathrm{s}}{d_0}\right|_{\delta\gamma} = \frac{2}{\pi}\int_0^\infty \mathrm{d}k\, \left(\frac{\sin(x)}{x}\right)^2 \frac{1}{1+\lambda^3\phi S_{\gamma_0}(x)} \tag{4.73}$$

$$\begin{aligned} \left.H^d(y,\gamma)\right|_{\delta\gamma} = {} & \frac{3}{4\pi}\int_0^\infty \mathrm{d}y'\, \left(\frac{\sin\left(\frac{1}{2}y'\right)}{\frac{1}{2}y'}\right)^2 \frac{1}{1+\gamma^3\phi S_{\gamma_0}\left(\frac{1}{2}y'\right)} \\ & \cdot \int_{-1}^1 \mathrm{d}\mu\, \left(1-\mu^2\right)\left[S\left(\frac{1}{\gamma}\sqrt{y^2+y'^2-2yy'\mu}\right)-1\right], \end{aligned} \tag{4.74}$$

where $y = q\sigma_h$. The function $S_{\gamma_0}(x)$ consists of an infinite sum of wavenumber-dependent

contributions depending on the effective hydrodynamic volume fraction $\phi_h = \gamma^3\phi$, as well as on the inter-related scalar coefficients $\gamma_0^{(n)}$, with $n \in \{0, 1, 2, \cdots\}$. The explicit expressions for $S_{\gamma_0}(x)$ and $\gamma_0^{(n)}$, and details about our implementation of the BM method, are provided in the Appendix B.2. Higher-order versions of the BM method require higher than second-order static correlation functions [173] and hence are laborious to implement. The BM method expression for η_∞ by Beenakker [177], as adapted to the HRM, is given by

$$\left.\frac{\eta_\infty(\phi,\gamma)}{\eta_0}\right|_{\delta\gamma} = \frac{1}{\lambda^{(0)}(\phi,\gamma) + \lambda^{(2)}(\phi,\gamma)}, \tag{4.75}$$

where

$$\lambda^{(0)}(\phi,\gamma) = \left[1 + \frac{5}{2}\gamma^3\phi\tilde{\gamma}_0^{(2)}\right]^{-1} \tag{4.76}$$

$$\lambda^{(2)}(\phi,\gamma) = \frac{15}{2\pi}\gamma^3\phi\left[\tilde{\gamma}_0^{(2)}\lambda^{(0)}(\phi,\gamma)\right]^2 \int_0^\infty \mathrm{d}y \frac{j_1^2\left(\frac{1}{2}y\right)}{1+\gamma^3\phi S_{\gamma_0}\left(\frac{1}{2}y,\gamma^3\phi\right)}\left[S\left(\frac{y}{\gamma}\right) - 1\right], \tag{4.77}$$

and $\tilde{\gamma}_0^{(2)} = \gamma_0^{(2)}/\rho$. The argument y/γ in the static structure factor is used as a reminder that $S(q)$ is usually calculated as a function of $q\sigma$.

The approximate character of the BM method is highlighted by an analysis of the first-order virial results of the self-diffusion coefficient, the sedimentation velocity and the high-frequency viscosity. This analysis shows that for low ϕ the first-order virial coefficient is severely overestimated by up to $\sim 49\%$ [173]. In addition, the HRM self-diffusion coefficient in BM approximation depends solely on the hydrodynamic volume fraction, $\lambda^3\phi$, independent of the system configuration, e.g. $g(r)$ or $S(q)$. It has been shown to be a decently good approximation for hard-sphere systems only [173].

4.4.3. Hybrid BM-PA scheme

A simple yet significant improvement over the original BM method, preserving its analytic simplicity, is obtained from using it for the distinct part, $H^d(q)$, only, where it gives overall good results. This was shown in Refs. [65, 85, 136], both for neutral and charge-stabilized particles systems in comparison with elaborate hydrodynamic force multipole simulations and experimental data. Regarding the self-part, d_S, of $H(q)$, accurate expressions can be used instead, such as the scaling relations presented in Eq. (5.1) for particles with hard-

core interactions, or the PA approximation expression in Eq. (4.69) for lower-concentrated, charge-stabilized systems. This hybrid procedure is referred to as the self-part corrected BM or hybrid BM-PA scheme, respectively. It has been successfully applied to hard-sphere and charged-stabilized suspensions, as well as to BSA protein solutions [86, 178].
The success of the BM-PA hybrid scheme can be understood by the analysis of the advantages and disadvantages of the two involved methods. First, the PA-approximation is exact to first-order in ϕ. In contrast, the BM method is an approximation for the full liquid-state ϕ-range. The latter considers many-body hydrodynamic interactions but disregards lubrication effects. In this sense, it is complimentary to the PA-scheme. The PA-method accurately describes the HIs in systems at low concentrations and with a strong likelihood of near-contact configurations. This explains the good accuracy of the PA calculated self-diffusion coefficient that originates from the fast decay of the corresponding mobility coefficients, according to $\boldsymbol{\mu}_{ii} \sim 1/r^4$, and thus d_S is strongly influenced by the local surrounding of a particle. By its design, the BM method is here less accurate. The disregard of many-body HIs in the PA-scheme implies the neglect of any hydrodynamic shielding effects. The latter refers to the attenuation of the strength but not the range of the HIs [173]. Shielding needs to be discriminated from the screening of HIs by fixed objects, such as walls, pillars, or rigid clusters, which take momentum out of the system. Since the distinct parts of the hydrodynamic mobilities describe cross-particle HIs where shielding effects are important and which are of longer range than the self-parts, the BM method should be advantageous at least for more concentrated systems. This is supported by the observation that the PA-scheme provides an accurate description of the sedimentation velocity of hard-spheres only up to $\phi \approx 0.08$ while the self-diffusion coefficient is well described up to $\phi \approx 0.15$ [173].

4.4.4. Simplified MCT for the long-time dynamics

Here, we shortly explain the employed simplified mode-coupling theory (MCT) expressions for the zero-frequency viscosity η. Since the focus of this thesis is not on MCT calculations of long-time dynamic properties, the following discussion will be brief, in presenting only the simplified MCT expressions.

Zero-frequency viscosity

Different from the high-frequency viscosity, η_∞, where accurate analytic calculation tools such as the PA method (see Eq. (4.72)) exist, the calculation of the zero-frequency viscosity, $\eta = \eta_\infty + \Delta\eta$, is far more complicated. The reason for this lies in the relaxation part,

$\Delta\eta$, which accounts for the shear-induced dynamic deformation of next-neighbor cages discussed already in Subsec. 4.3.2. For simplicity, we start from the following simplified MCT expression for $\Delta\eta$ which disregards HIs (see, e.g., [179]),

$$\Delta\eta^{\mathrm{MCT}} = \frac{k_{\mathrm{B}}T}{60\pi^2}\int_0^\infty \mathrm{d}q\; q^4 \left(\frac{S'(q)}{S(q)}\right)^2 \int_0^\infty \mathrm{d}t\; \left(\frac{S(q,t)}{S(q)}\right)^2 > 0\,. \tag{4.78}$$

Here, $S'(q)$ is the derivative of $S(q)$ with respect to q. Instead of calculating $\Delta\eta^{\mathrm{MCT}}$ self-consistently together with the dynamic structure factor $S(q,t)$ by using the corresponding MCT memory equation for $S(q)$ [173, 180], we approximate $S(q,t)$ by its short-time form with HIs included. This results in the first-iteration MCT expression

$$\left.\frac{\Delta\eta}{\eta_0}\right|^{(1)}_{\mathrm{MCT}} \approx \frac{1}{40\pi}\int_0^\infty \mathrm{d}y\; y^2 \frac{(S'(y))^2}{S(y)}\frac{1}{H(y)}\,, \tag{4.79}$$

where $H(y)$ is the hydrodynamic function. The employed approximation of $S(q,t)$ by its short-time form

$$S(y,t) \approx S(y)\exp\left[-y^2\frac{H(y)}{S(y)}\frac{t}{\tau_\sigma}\right] \tag{4.80}$$

with $\tau_\sigma = \sigma^2/d_0$, gives rise to an underestimation of the relaxation part, i.e.

$$\Delta\eta|^{(1)}_{\mathrm{MCT}} < \Delta\eta|_{\mathrm{MCT}}\;. \tag{4.81}$$

This underestimation is more pronounced for higher volume fractions, with the consequence that in the first-iteration MCT no dynamic glass transition at a $\phi = \phi_{\mathrm{g}}$ is predicted.

5. Dispersions of hydrodynamically structured particles: Results

In this chapter, we discuss the dynamics of hydrodynamically structured colloidal particles systems. For this purpose, we employ the HRM introduced in Subsec. 4.1.4 to account, e.g., for (partial) particle solvent permeability. As model system, non-ionic PNIPAM microgel suspensions are investigated. We show by comparison of the experimental $S(q)$ with Hertz- and hard-core interaction potential based IET calculations, that the microgel particles are consistently and accurately described using the hard-sphere potential. The accurate structure functions $S(q)$ and $g(r)$ are used as input in the calculations of short-time dynamics properties, with results in excellent agreement with DLS measurements on PNIPAM microgels. Motivated by the good agreement of our dynamic transport properties calculations with the dynamic measurements on non-ionic microgels, we present an extensive analytic toolbox for the calculation of short- and long-time dynamic suspension properties of hydrodynamically structured particles with hard-core excluded volume interactions. Our easy-to-apply toolbox provides a ready tool for the analysis of dynamic experimental data, e.g., on permeable particles suspensions.

5.1. Equilibrium structure functions

In Fig. 5.1, we compare the PY-VW structre factors, $S(q)$, for the hard-sphere model (c.f. Subsec. 3.4.1) with static light scattering results by Eckert and Richtering [66] for a concentration series of non-ionic PNIPAM microgels in DMF. The details of the particle synthesis are given in Refs. [66, 181, 182]. In our PY-VW calculations, we have used the experimentally obtained (mean) particle diameter $\sigma = 240$ nm, and the (volume-swelling corrected) volume fractions ϕ as given in Ref. [66]. We refer to this reference for the details on how the volume fractions have been determined. The agreement between the experimental and PY-VW structure factors is good even for small wavenumbers q. There is in particular a significantly improved agreement for the largest considered volume fraction, as compared to the bare PY $S(q)$ used in the earlier work in [66] (dashed curve in Fig. 5.1). The remaining small deviations for the most concentrated system at $\phi = 0.5$ can be at least partially attributed to experimental uncertainties, and possibly also to the breakdown of the exact factorization of the mean scattered intensity into static structure and form factors as discussed by Likos *et al.* [183, 184]. In Fig. 5.2, the experimental

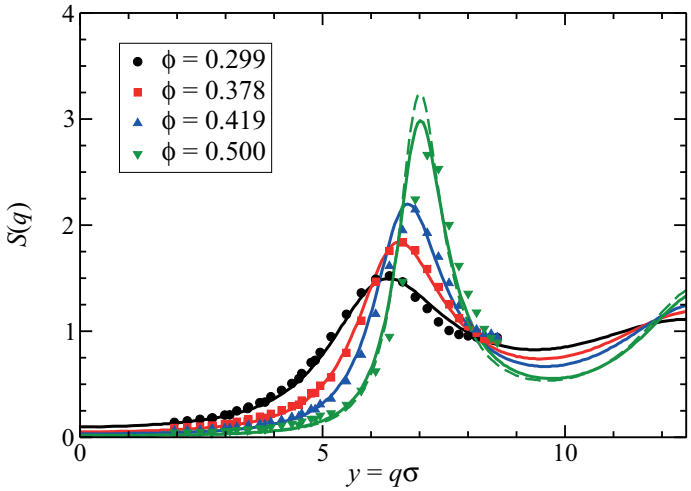

Fig. 5.1.: Comparison of the experimental static structure factor, $S(q)$, of PNIPAM microgels (filled symbols, taken from Ref. [66]) with the Verlet-Weis corrected Percus-Yevick prediction (solid lines), for various particle volume fractions ϕ as indicated. The bare PY structure factor for the largest considered volume fraction $\phi = 0.5$ is represented by the dashed curve.

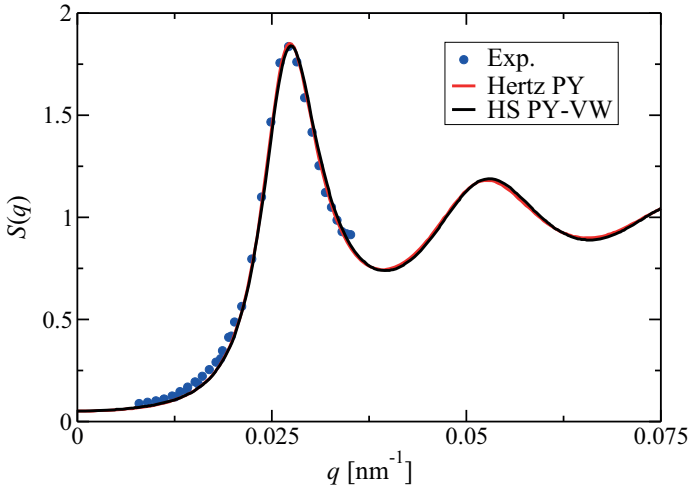

Fig. 5.2.: Experimental structure factor at $\phi = 0.378$ (filled circles) in comparison with the best-fit hard-sphere model PY-VW $S(q)$ (black solid line), and the best-fit Hertz model $S(q)$ calculated in PY approximation (red solid line). For the Hertz model, the parameters $\epsilon = 10^4$, $\sigma_s = 245$ nm, and $\phi_s = 0.398$ have been used.

structure factor of PNIPAM microgels is compared, for $\phi = 0.378$, with the best-fit hard-sphere and the best-fit Hertz potential structure factors. For the Hertz model system, the parameter values $\sigma_s = 245$ nm, $\epsilon = 10^4$, and $\phi_s = (\pi/6)\rho\sigma_s^3 = 0.398$ have been used. The theoretical curves coincide practically, as expected for the invoked large value of ϵ which restricts the softness range of the Hertz potential to a narrow interval around the effective diameter σ_s. This can be noticed from the inset of Fig. 5.3. The remnant potential softness still necessitates a slightly larger effective diameter σ_s than the hard-sphere model value $\sigma = 240$ nm, for the Hertz potential incorporates the interactions by dangling polymer chains at the periphery of microgel particles. The larger particle size in the Hertz potential model goes along with a larger volume fraction ϕ_s than that used in the best-fit hard-sphere model result. With increasing volume fraction in the range $\phi_s \in [0.299 - 0.5]$, a slight decrease of the best-fit effective diameter σ_s is observed. However, owing to the smallness of the particle size shrinkage, for the considered PNIPAM in DMF system this effect can be disregarded in its influence on static and dynamic properties.

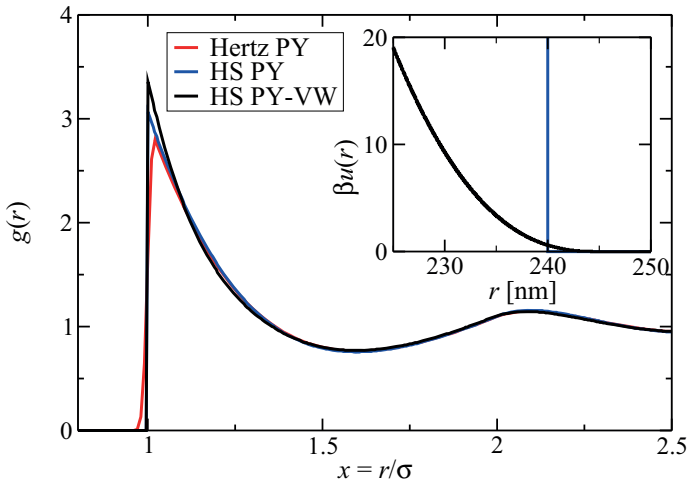

Fig. 5.3.: Radial distribution functions, $g(r)$, corresponding to the hard-sphere and Hertz potential structure factors in Fig. 5.2. The inset compares the hard-sphere and Hertz pair potential, for the parameters in Fig. 5.2.

The $g(r)$'s corresponding to the best-fit Hertz and hard-sphere model structure factors in Fig. 5.2 are depicted in Fig. 5.3. The slight softness of the Hertz potential is reflected in the somewhat reduced peak height of $g(r)$ (red solid curve), and in the slight extension of the RDF into the overlap region $r < \sigma_s$. From Figs. 5.2 and 5.3, we conclude that the pair correlations of the considered PNIPAM suspensions in the experimental concentration range are fully compatible with the simple hard-sphere potential. For microgels of lower

cross-linker density and smaller size where the softness of the particles is important, the Hertz potential model should be used.

5.2. Short-time dynamics

5.2.1. Self-diffusion coefficient

In Refs. [65, 76], it was shown by comparison with computer simulation results for uniformly permeable hard spheres with hydrodynamic screening length $\lambda_x < 0.2$ that the short-time translational self-diffusion coefficient d_S normalized by its infinite dilution value d_0 is well represented by the simple scaling relation,

$$\frac{d_{\mathrm{S}}\left(\phi, \lambda_{\mathrm{t}}\right)}{d_0\left(\lambda_{\mathrm{t}}\right)} = 1 + \lambda_{\mathrm{t}}\,\phi\left(1 + 0.12\phi - 0.70\phi^2\right) , \tag{5.1}$$

for all $\phi \leq 0.5$, and with an accuracy of 3.5 % or better. A similar scaling relation has been obtained for the short-time rotational self-diffusion coefficient of permeable-sphere suspensions with hard-core interactions [76]. The only dependence in Eq. (5.1) on the permeability parameter λ_x characterizing the intra-particle hydrodynamic structure is contained in the first virial coefficient, $\lambda_{\mathrm{t}} = \lambda_t(\lambda_x)$, which is the linear coefficient in the expansion of d_S in powers of ϕ. Eq. (5.1) states that the d_S for hydrodynamically structured particles can be scaled to the corresponding coefficient of no-slip hard spheres where $\lambda_x = 0$ and $\lambda_t(\lambda_x = 0) = -1.8315$.

In fact, on the level of the HRM model, Eq. (5.1) is applicable to suspensions of hard spheres of arbitrary hydrodynamic structure, with deviations from the d_{S} of the actual particle system being of quadratic order small in the reduced slip length L_h^* according to Eq. (4.60). On recalling that for spherical particles with hard-core direct interactions only, the HRM reduces to the spherical annulus model, the only input required in Eq. (5.1) is the second virial coefficient, $\lambda_t(\gamma)$, of spherical annulus particles depending on the ratio, $\gamma = a_h/a$, of hydrodynamic and hard-core radius. Using for $\lambda_t(\gamma)$ the Eq. (4.71) in Subsec. 4.4.1 in conjunction with tabulated numerical values for the longitudinal and transversal mobility coefficients, $x_{11}(r)$ and $y_{11}(r)$, of two no-slip spheres of radius a_h calculated using the method of Jeffrey and Onishi [168], we have obtained numerically precise values for the first-order virial coefficient of spherical annulus particles. These values are described

to high accuracy by the polynomial fit

$$\begin{aligned}\lambda_{\mathrm{t}}(\gamma) = &-1.8315 + 7.820\overline{\gamma} - 14.231\overline{\gamma}^2 \\ &+ 14.908\overline{\gamma}^3 - 9.383\overline{\gamma}^4 + 2.717\overline{\gamma}^5\,,\end{aligned} \tag{5.2}$$

(with $\overline{\gamma} = 1-\gamma$) accounting for the numerically correct limiting value $\lambda_{\mathrm{t}}(\gamma = 1) = -1.8315$ of no-slip hard spheres.

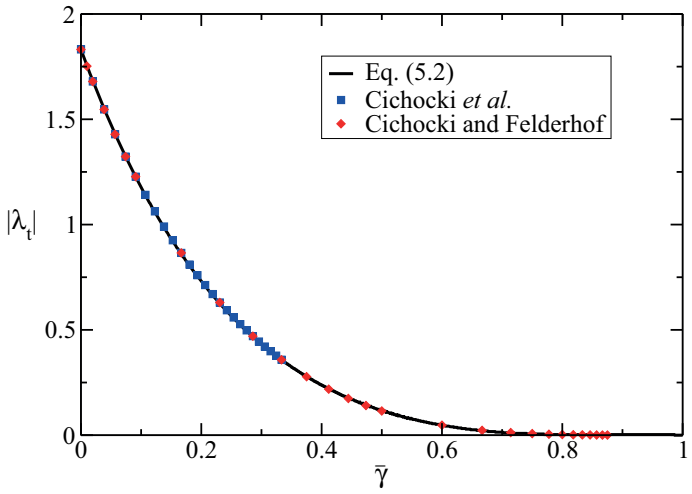

Fig. 5.4.: Modulus $|\lambda_{\mathrm{t}}|$ of the first-order virial coefficient of d_S in the spherical annulus model, as a function of the reduced fluid annulus shell width $\overline{\gamma} = 1 - \gamma$. Solid line: Polynomial fit according to Eq. (5.2). Filled squares: Tabulated values by Cichocki *et al.* [52] for spherical annulus particles with $\overline{\gamma} \leq 1/3$. Filled diamonds: Tabulated values by Cichocki and Felderhof [185].

In Fig. 5.4, the high accuracy of the polynomial fit in Eq. (5.2) is shown in comparison with earlier numerical results [52, 185] for the first-order virial coefficient of spherical annulus particles. Note that $\lambda_{\mathrm{t}}(\gamma = 0) = 0$ relates to the limiting case of spherical annulus particles interacting hydrodynamically as point particles for which there are no hydrodynamic self-reflections so that d_S reduces to the Stokes-Einstein value d_0 independent of ϕ. The associated long-time coefficient d_L for $\gamma = 0$ is still ϕ-dependent and smaller than d_0.
The accuracy of the analytic scaling formula in Eq. (5.1) in combination with Eq. (5.2) for the short-time self-diffusion coefficient of spherical annulus particle systems is established in Fig. 5.5 by the comparison with high-precision benchmark simulation data for the spherical annulus [51] and uniformly permeable particle models [47]. Regarding the latter model, the conversion of λ_x to the related reduced hydrodynamic radius parameter γ in the spherical annulus model was done using Eq. (4.35) for $d_0(\lambda_x)$. This corresponds to

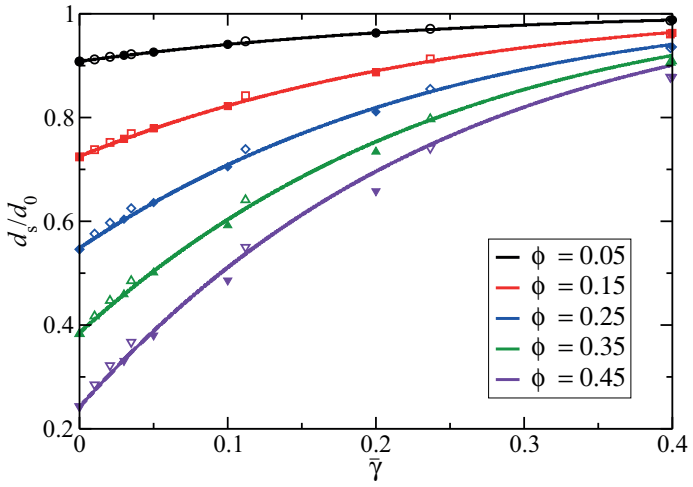

Fig. 5.5.: Results for the reduced self-diffusion coefficient, d_S/d_0, of the spherical annulus model as function of $\overline{\gamma} = 1 - \gamma$, for several volume fractions ϕ as indicated. Solid lines: Prediction by the scaling formula in Eq. (5.1) in combination with the first order virial coefficient fitting polynomial in Eq. (5.2). Closed symbols: HYDROMULTIPOLE simulation data for the spherical annulus model tabulated in Ref. [51]. Open symbols: Simulation data for uniformly permeable spheres tabulated in Ref. [47], with Eq. (4.35) used in mapping the permeability parameter λ_x onto the annulus model parameter $\gamma = a_h/a$ (recall Fig. 4.2).

the inversion of the curve for λ_x^t in Fig. (4.2) in terms of γ. For example, the smallest reasonably selected value $\lambda_x = 0.1$ corresponds to $\gamma = 0.89$. Results for d_S are depicted in Fig. 5.5 in dependence on the reduced slip length $\overline{\gamma}$, for volume fractions extending over a broad concentration range.

The excellent agreement between the scaling formula for d_S (solid lines), and the simulation data (symbols) does not only validate this formula. For the special case of permeable hard spheres, it additionally highlights the good performance of the HRM, for a broad concentration range and permeability values largely exceeding the ones discussed earlier in the thin shell-limit discussion of the core-shell model in Ref. [52].

In summary, the analytic formulas in Eqs. (5.1) and (5.2) allow for a quick and accurate calculation of the translational short-time self-diffusion coefficient of hydrodynamically structured spherical particles with hard-core interactions. The only input is the single-particle property a_h/a which can be determined experimentally, e.g., by a DLS measurement of d_0 in conjunction with a static scattering experiment determining the excluded volume radius. The formula for d_S is applicable also to particles with a short-range, weakly soft pair potential such as the Hertz potential for non-small potential strengths ϵ, provided

the effective diameter σ_s and the related volume fraction ϕ_s are used instead of σ and ϕ. The formula for d_S in Eqs. (5.1) and (5.2) based on its virial expansion is not valid for particles with a long-range, soft pair potential where an (effective) excluded volume diameter is not the characteristic parameter. An example in case are low-salinity suspensions of charge-stabilized colloidal spheres, where according to theory, simulation and experiment d_S has to good accuracy the fractional concentration dependence $1 - d_S/d_0 \approx A_S\,\phi^{4/3}$, with a coefficient $A_S \approx 2.5 - 2.9$ which varies to a small extent with the particle size and charge [136, 186]. The initial slope of d_S at $\phi = 0$ is thus zero in these charge-stabilized systems. Different from the formula in Eqs. (5.1) and (5.2), the HRM is applicable also to spherical particles with arbitrary soft direct interactions, and to particles of fuzzy hydrodynamic structure without a sharp outer boundary. In the framework of the HRM, the coefficient d_S and other short-time transport properties of particles with soft interactions can be approximately and semi-analytically calculated using the PA method at smaller, and the self-part corrected $\delta\gamma$ method at larger concentrations. The inputs $g(r)$ and $S(q)$ to these methods can be obtained from OZ integral equation schemes such as the ones presented in Sec. 3.4.

5.2.2. Sedimentation velocity

Different from self-diffusion, the neglect of hydrodynamic near-distance and particularly lubrication effects in approximate analytic calculations is less consequential regarding sedimentation. Therefore, K can be described semi-qualitatively on the RP type level where only the long-distance dipolar contribution to the mobility tensors is accounted for. This amounts hydrodynamically to the neglect of all hydrodynamic flow reflection by the particles.

Using the RP approximation in conjunction with the analytic PY solution for the Laplace transform of $r\,g(r)$, Contreras-Aburto *et al.* [187] have derived analytic expressions for the short-time sedimentation coefficient of Navier partial-slip and uniformly permeable spheres with hard-core interaction. Here, we present the according expression for spherical annulus particles,

$$K_{\mathrm{RP}}\,(\phi,\gamma) = 1 + \gamma\,\phi\left(\gamma^2 + 12\left[\frac{\phi\,(2-\phi) - 10}{20\,(1+2\phi)}\right]\right)\,, \tag{5.3}$$

which includes hydrodynamic point particles as a limiting case for which $K(\phi, \gamma = 0) = 1$. In the opposite limit, $\gamma = 1$, of no-slip hard spheres, Eq. (5.3) reproduces an expression by Banchio and Nägele [136] which was rederived subsequently by Gilleland *et al.* [188] using a variational method.

The comparison in Fig. 5.6 of the RP based analytic formula in Eq. (5.3) with benchmark

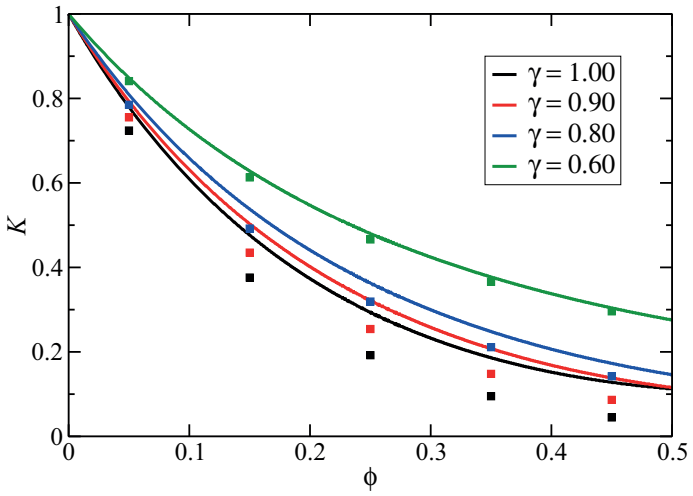

Fig. 5.6.: Concentration dependence of the sedimentation coefficient, K, of the spherical annulus model for reduced hydrodynamic radius values γ as indicated. Solid lines: RP approximation K_{RP} in Eq. (5.3). Filled symbols: Simulation data taken from Ref. [51].

simulation data for spherical annulus hard spheres [51] shows that the sedimentation velocity is overestimated by the formula at larger concentrations. This is a consequence of the neglect of flow reflections in the RP approximation which becomes less severe with decreasing annulus parameter γ, owing to the, for a fixed ϕ, increasing distances between the hydrodynamic particle surfaces. For the lowest considered value $\gamma = 0.6$, excellent agreement between the simulation data and K_{RP} is observed. The largest deviations occur for no-slip hard spheres where K_{RP} provides an upper bound to the exact sedimentation coefficient [156, 188]. As an aside, we note that even at $\phi = 0.5$, K_{RP} changes only slightly if the VW-corrected $g(r)$ is used instead of the bare PY $g(r)$.
While K_{RP} nicely describes the trends of the exact spherical annulus sedimentation coefficient K in its ϕ and γ dependence, in search of an improved analytic expression we make the ansatz

$$\begin{aligned} K(\phi,\gamma) &= 1 + \lambda_{\mathrm{k}}(\gamma)\; u_{\mathrm{k}}(\phi,\gamma) \\ &= 1 + \lambda_{\mathrm{k}}(\gamma)\,\phi\,[1 + \mathcal{O}(\phi)]\;, \end{aligned} \tag{5.4}$$

where $\lambda_{\mathrm{K}}(\gamma)$ is the first-order virial coefficient of the sedimentation coefficient for which high-precision values have been provided by Cichocki *et al.* [52, 185]. According to Fig.

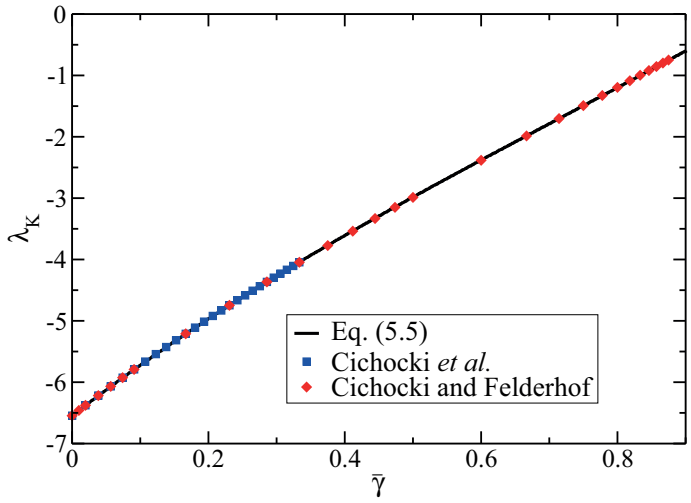

Fig. 5.7.: First-order virial coefficient, λ_K, of the sedimentation coefficient of spherical annulus particles. Filled symbols: Tabulated values by Cichocki *et al.* for thick (diamonds) [185] and thin annulus shell (squares) systems [52], in comparison with the polynomial in Eq. (5.5) (black solid line).

5.7, these tabulated values are well represented by the polynomial,

$$\lambda_{\mathrm{K}}(\gamma) = -6.5464 + 8.592\bar{\gamma} - 3.901\bar{\gamma}^2 + 2.011\bar{\gamma}^3 - 0.142\bar{\gamma}^4 \tag{5.5}$$

in the full parameter range $0 < \gamma \leq 1$. At $\gamma = 1$ in particular, the known value $\lambda_{\mathrm{K}} = -6.5464$ of no-slip hard spheres is recovered from the polynomial.

In the first equality in Eq. (5.4), we have introduced the sedimentation scaling function $u_{\mathrm{K}} = (K-1)/\lambda_{\mathrm{K}}$. In Ref. [76], a scaling ansatz analogous to Eq. (5.4) was used for the short-time translational and rotational self-diffusion coefficients of uniformly permeable hard spheres. By the comparison with simulation data, it was shown therein that the scaling functions $u_{\mathrm{S}}(\phi, \lambda_x)$ and $u_{\mathrm{R}}(\phi, \lambda_x)$ associated with translational and rotational self-diffusion, respectively, are practically independent of the permeability coefficient for all values $\lambda_x \leq 0.1$. They are therefore well approximated by (i.e. scaled to) the respective functions $u_{\mathrm{S,R}}(\phi, \lambda_x = 0)$ of non-permeable solid spheres. On using a third-order polynomial fit of $u_{\mathrm{S}}(\phi, \lambda_x = 0)$ obtained from simulation data of no-slip hard spheres, and the first two known virial coefficients of $d_{\mathrm{S}}(\phi, \lambda_x = 0)$, Eq. (5.1) for $d_{\mathrm{S}}(\phi, \lambda_x)$ has been obtained [65, 76].

As noticed already in the context of permeable spheres [76], u_{K} depends significantly on the intra-particle hydrodynamic structure, different from its self-diffusion siblings. In

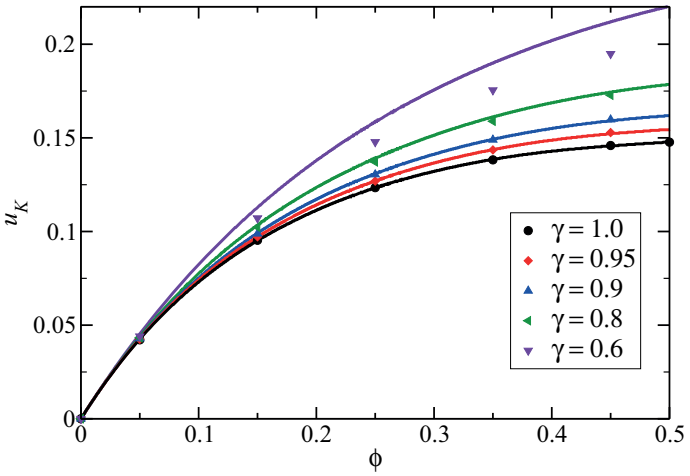

Fig. 5.8.: Concentration dependence of the scaling function $u_{\mathrm{K}}(\phi,\gamma)$ associated with the sedimentation coefficient of spherical annulus particles, for values of γ as indicated. Colored filled symbols: Values obtained from simulation data of $K(\phi,\gamma)$ [51]. Colored solid lines: Semi-empirical formula in Eq. (5.6).

Fig. 5.8, this is demonstrated for the spherical annulus system using tabulated simulation data for $K(\phi,\gamma)$ in Ref. [51]. The simulation data of $u_{\mathrm{K}}(\phi,\gamma)$ for a fixed $\phi > 0$ clearly differ from each other for different γ values. Thus, the γ-dependence of $K(\phi,\gamma)$ cannot be embodied solely in terms of the first-order virial coefficient, in contrast to Eq. (5.1) describing d_{S}. However, as it is shown in Fig. 5.8, the simulation data for $u_{\mathrm{K}}(\phi)$ are well described for $\gamma \geq 0.8$ by a forth-order polynomial in $\gamma\phi$, namely

$$u_{\mathrm{K}}(\phi,\gamma) = \phi\left[1 - 3.348\gamma\phi + 7.426\,(\gamma\phi)^2 - 10.034\,(\gamma\phi)^3 + 5.882\,(\gamma\phi)^4\right]. \tag{5.6}$$

The resulting analytic expression,

$$K(\phi,\gamma) = 1 + \lambda_{\mathrm{K}}(\gamma)\,\phi\left[1 - 3.348\gamma\phi + 7.426\,(\gamma\phi)^2 - 10.034\,(\gamma\phi)^3 + 5.882\,(\gamma\phi)^4\right], \tag{5.7}$$

for the sedimentation coefficient provides, in conjunction with Eq. (5.5) for $\lambda_K(\gamma)$, an accurate description in the from the experimental viewpoint sufficiently broad parameter range $\gamma \in [0.8 - 1]$. The numerical coefficient 3.348 in the bracket of Eq. (5.7) is selected such that at $\gamma = 1$ the correct numerical value 21.918 of the second virial coefficient of no-slip rigid spheres [185] is recovered.

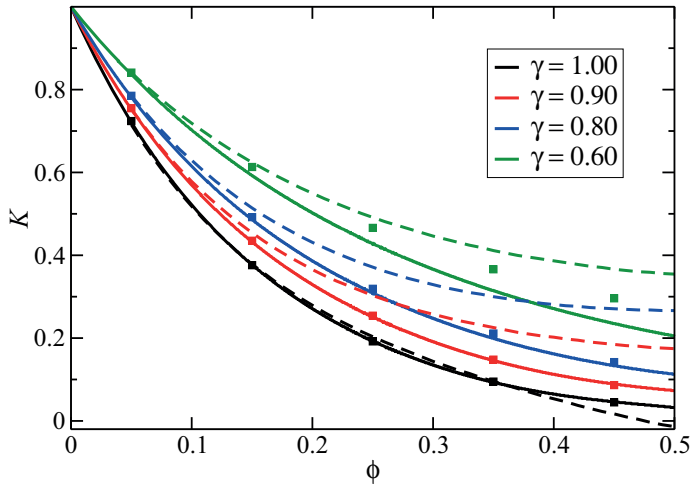

Fig. 5.9.: Sedimentation coefficient of the spherical annulus model as a function of ϕ, for values of γ as indicated. Filled squares: Simulation data for spherical annulus particles [51]. Solid lines: Analytic formula in Eq. (5.7) with λ_{K} according to Eq. (5.5). Dashed lines: Prediction of the hybrid BM-PA scheme, with self-part d_{S} according to Eq. (5.1), distinct part $H^d(q)$ from Eq. (4.74), and VW-PY input for $S(q)$.

From Fig. 5.9, the good agreement of the semi-empirical formula for $K(\phi, \gamma)$ in Eq. (5.7) with the spherical annulus simulation data [51] is noticed for $\gamma \geq 0.8$. Moreover, results for $K(\phi, \gamma)$ are displayed as predicted by the hybrid BM-PA scheme (Subsec. 4.4.3) with VW-PY structure factor input where the self-part contribution to K was calculated according to Eq. (5.1). While in good overall agreement with the simulation data, the hybrid BM-PA method results for K deviate significantly at larger ϕ. Different from Eq. (5.7) which applies to spherical particles with hard-core interactions only, the BM method is applicable also to particles with soft interactions.
The analytic expressions in Eqs. (5.7) and (5.1) for K and d_S are profitably used in the following discussion of the hydrodynamic function of core-shell particle systems.

5.2.3. Hydrodynamic function scaling

Due to the fact that $H(q)$ is given, according to Eq. (4.53), by an equilibrium average over hydrodynamic mobilities, its principal peak location and the wavenumber locations of its secondary maxima are nearly coincident with those of $S(q)$. As a static equilibrium property, $S(q)$ is independent of the hydrodynamic particle structure in particular and the HIs in general. This observation has led Abade *et al.* [48] to the following remarkable

finding, which they analyzed in the context of uniformly permeable hard spheres: While the amplitudes of the oscillations in $H(q)$ are strongly sensitive to the permeability (i.e., the hydrodynamic particle structure), the relative q-dependence of $H(q)$ is practically permeability independent, and can be scaled thus to that of no-slip hard spheres. To see this quantitatively, consider the so-called reduced hydrodymanic function [48],

$$h_d\left(q\right) = \frac{H^d(q)}{|H^d(q=0)|}\,, \tag{5.8}$$

where $H^d(q)$ is the wavenumber-dependent distinct part of $H(q)$ introduced in Eq. (4.56).

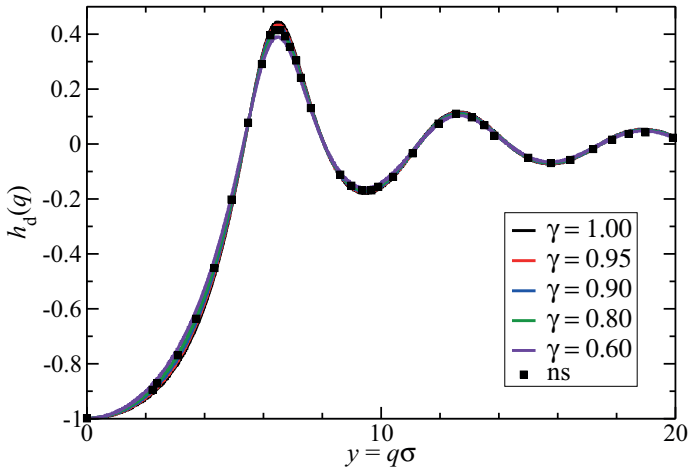

Fig. 5.10.: Reduced hydrodynamic function, $h_d(q)$, for spherical annulus particles at fixed volume fraction $\phi = 0.35$ and varying γ as indicated. The wavenumber is scaled in terms of the hard-sphere diameter $\sigma = 2a$. Solid lines: BM method results using VW-PY structure factors as input. Filled squares: Simulation result for no-slip (ns) hard spheres ($\gamma = 1$) taken from Ref. [48].

The reduced hydrodynamic function is defined such that $h_d(q = 0) = -1$ and $h_d(q \to \infty) = 0$. Abade *et al.* found that $h_d(q)$ is at all q nearly independent of the permeability parameter λ_x, practically in the complete liquid-phase concentration interval. In extrapolating their finding to the spherical annulus model as motivated by our general discussion in Subsec. 4.1.4, $H(q)$ can be expected to be well represented by

$$H\left(q\right) \approx \frac{d_{\mathrm{S}}\left(\phi,\gamma\right)}{d_0\left(\gamma\right)} - h_d^{ns}\left(q\right)\left[K(\phi,\gamma) - \frac{d_S\left(\phi,\gamma\right)}{d_0\left(\gamma\right)}\right]\,, \tag{5.9}$$

where $h_d^{ns}(q) = h_d(q, \gamma = 1)$ is the reduced hydrodynamic function of no-slip hard spheres. The hydrodynamic particle structure enters into this expression by the coefficients K and

d_S/d_0 only for which we have provided accurate analytic expressions. The relative q-dependence of $H(q)$ is described by the master function $h_d^{ns}(q)$ which can be conveniently calculated using the semi-analytic BM method for $H^d(q)$.

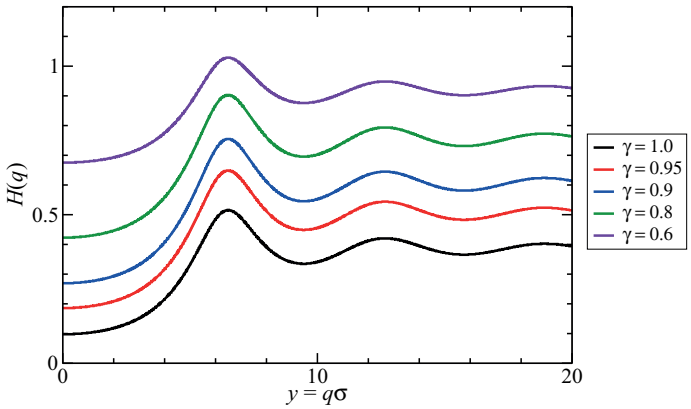

Fig. 5.11.: Hydrodynamic function, $H(q)$, of spherical annulus spheres for $\phi = 0.35$ and values of γ as indicated. The solid lines show results by the semi-analytic formula in Eq. (5.9), with d_S/d_0 and K according to Eqs. (5.1) and (5.7), respectively, and $h_d^{ns}(q)$ calculated using the BM method.

To validate hydrodynamic function scaling for the spherical annulus model, in Fig. 5.10 we present results for $h_d(q, \gamma)$ in a broad γ parameter range, obtained using the BM method in Subsec. 4.4.2. All curves collapse practically on a single master curve which in turn nicely agrees with the simulation data for no-slip (ns) hard spheres taken from Ref. [48]. The sensitivity of $H(q)$ on the reduced hydrodynamic radius γ is illustrated in Fig. 5.11, where $H(q)$ has been calculated according to Eq. (5.9). The strength of the HIs ceases with decreasing γ. Notice that $H(q) \to 1$ for $\gamma \to 0$.

To date, the validity of the hydrodynamic function scaling was scrutinized for particles with hard-sphere interactions only [47, 48]. As discussed in Sec. 2.1, the soft Hertz potential in Eq. (2.1) is a useful description of the coarse-grained interaction of certain types of mechanically soft microgel particles. For this reason, we investigate now the scaling of the hydrodynamic function for suspensions of Hertz particles of different interaction strengths ϵ. In Fig. 5.12, the functions $h_d(q)$ of Hertz particles are shown for various values of the reduced hydrodynamic radius, defined here by $\gamma = a_h/a_s$ with $a_s = \sigma_s/2$ denoting the effective soft radius of the Hertz potential. Two largely distinct interaction (softness) parameters $\epsilon = 10$ and 10^4 are considered, representing highly soft and weakly soft particle systems, respectively. The inset depicts the respective shapes of the Hertz potential. For $\epsilon = 10$, there is a significant likelihood of finding two particles at a distance smaller

than σ_s, as quantified by values of $g(r < \sigma_s)$ significantly larger than zero. Even then the HRM remains applicable, provided the hydrodynamic structure of the actual soft particles is not significantly distorted away (on average) from spherical symmetry during particle interpenetration.

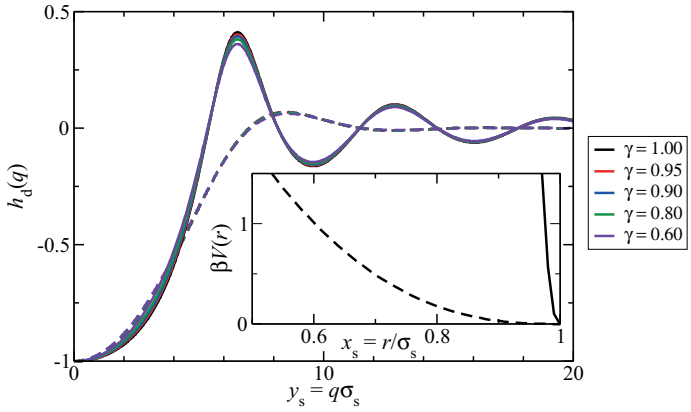

Fig. 5.12.: Reduced hydrodynamic function, $h_d(q)$, for a Hertzian spheres system of interaction strength $\epsilon = 10$ (dashed lines) and $\epsilon = 10^4$ (solid lines), respectively, for various reduced hydrodynamic radii, $\gamma = a_h/a_s$, as indicated. The effective volume fraction is $\phi_s = 0.35$. The depicted results have been calculated using the BM method with PY structure factor input. Inset: Excerpt of the Hertz potential curve for $\epsilon = 10$ (dashed) and $\epsilon = 10^4$ (solid), respectively. Wavenumber q and radial distance r are scaled by the effective soft diameter, $\sigma_s = 2a_s$, of the Hertz potential.

The curves for $h_d(q)$ in Fig. 5.12 have been obtained using the HRM-based BM method with the structure factor input for the Hertzian spheres calculated in PY approximation. The figure shows that hydrodynamic function scaling applies to Hertz model particles for a broad softness range, with the shape of the γ-independent master curve for $h_d(q)$ depending on the softness parameter. The scaling behavior of $H(q)$ can be expected to hold also for other soft pair potentials.

5.2.4. High-frequency viscosity

In Refs. [48, 50], a generalized Saitô formula for the high-frequency viscosity of permeable spheres with hard-core interactions has been introduced which, for $\phi \leq 0.5$, gives results in good agreement with simulation data. In the framework of the spherical annulus model,

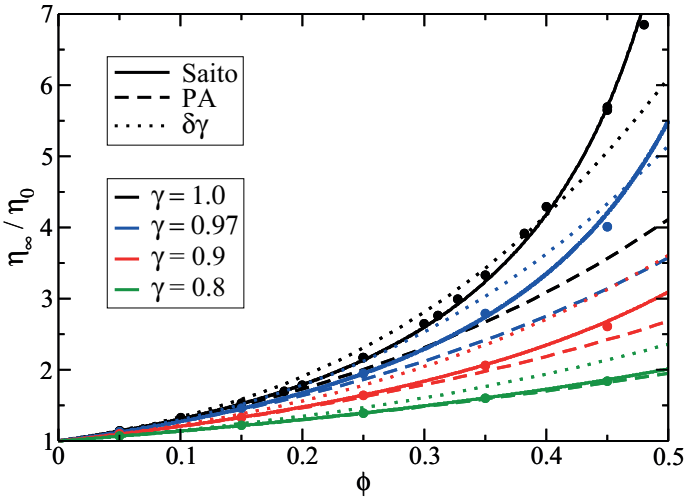

Fig. 5.13.: High-frequency viscosity, η_∞, of spherical annulus particles in dependence on ϕ, for values of γ as indicated. Filled symbols: Simulation data taken from Refs. [51, 136]. Solid lines: Generalized Saitô formula in Eqs. (5.10) - (5.12). Dashed lines: PA scheme results with VW-PY input for $g(r)$. Dotted lines: BM scheme results with VW-PY input for $S(q)$.

the formula reads

$$\frac{\eta_\infty(\phi,\gamma)}{\eta_0} = 1 + [\eta](\gamma)\,\phi \frac{1+\hat{S}(\phi,\gamma)}{1-\frac{2}{5}[\eta](\gamma)\,\phi\left(1+\hat{S}(\phi,\gamma)\right)}\,. \tag{5.10}$$

It expresses η_∞ in terms of the intrinsic viscosity, $[\eta](\gamma) = (5/2)\,\gamma^3$, depending on the hydrodynamic particle structure only, and the Saitô function $\hat{S}(\phi,\gamma)$. The latter is approximated linearly in ϕ as

$$\hat{S}(\phi,\gamma) = \left(\frac{\lambda_V(\gamma)}{[\eta](\gamma)} - \frac{2}{5}[\eta](\gamma)\right)\phi\,, \tag{5.11}$$

where $\lambda_V(\gamma)$ is the second-order virial coefficient in the expansion of η_∞/η_0 in powers of ϕ. Numerical values for the second virial coefficient of spherical annulus particles are given in Ref. [52]. For $\gamma \geq 2/3$, these values are well represented by the polynomial

$$\begin{aligned}\lambda_V(\gamma) = 5.0021 - 39.279\overline{\gamma} + 143.179\overline{\gamma}^2 \\ - 288.202\overline{\gamma}^3 + 254.581\overline{\gamma}^4\,.\end{aligned} \tag{5.12}$$

In Fig. 5.13, the predictions for η_∞ by the generalized Saitô formula in Eqs. (5.10) -

(5.12) are compared with existing simulation results [51] for the spherical annulus model. There is good agreement with the simulation in the displayed liquid-phase concentration range. For fixed concentration ρ and fixed hard-core radius a, the viscosity increases with increasing a_h, i.e. increasing γ, owing to the enlarged dissipation. Additionally shown in the figure are results for η_∞ by the PA and BM methods described in Subsecs. 4.4.1 and 4.4.2, respectively. Like in the PA scheme for short-time diffusion properties, two-body HIs contributions to η_∞ are fully accounted for but three-body and higher order contributions have been neglected. The PA scheme is in good agreement with the simulation data for $\phi < 0.2$ only. For small γ, the applicability of the PA method extends to somewhat larger ϕ. We attribute this, first, to the weaker hydrodynamic interactions for $\gamma < 1$, and second to the fast $\mathcal{O}(1/r^6)$ asymptotic decay of the shear mobility function associated with η_∞. While the BM scheme viscosity predictions for no-slip spheres are in better agreement with the simulation data than those by the PA scheme, for $\gamma < 1$ the BM scheme consistently overestimates the high-frequency viscosity. Quite interestingly, for all $\phi < 0.5$ the BM prediction for η_∞ scales to good accuracy with the hydrodynamic volume fraction $\phi_\mathrm{h} = \gamma^3\phi$.

5.2.5. Generalized Stokes-Einstein relation

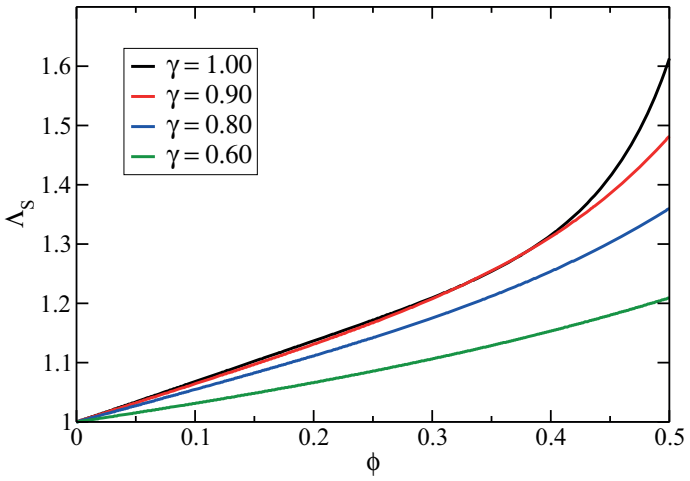

Fig. 5.14.: Test of the short-time GSE relation in Eq. (5.13) for spherical annulus particles with values of γ as indicated. Solid lines: Product function Λ_S of the generalized Saitô expression in Eq. (5.10) for η_∞/η_0 and Eq. (5.1) for d_S/d_0 in accord with Eq. (5.14).

As straightforward applications of the generalized Saitô formula (Eq. (5.10)), and Eq. (5.1) describing $\eta_\infty(\phi,\gamma)$ and $d_\mathrm{S}(\phi,\lambda)$ in the spherical annulus model, we analyze next the

validity of the short-time generalized Stokes-Einstein (GSE) relation,

$$\Lambda_{\mathrm{S}}(\phi,\gamma) \approx 1\,, \tag{5.13}$$

with the short-time GSE function

$$\Lambda_{\mathrm{S}}(\phi,\gamma) = \frac{d_{\mathrm{S}}(\phi,\gamma)}{d_0(\gamma)} \times \frac{\eta_\infty(\phi,\gamma)}{\eta_0}\,. \tag{5.14}$$

Eq. (5.13) expresses that $d_{\mathrm{S}}(\phi,\gamma)$ should be proportional for all concentrations to the inverse of $\eta_\infty(\phi,\gamma)$. This relation is trivially fulfilled at infinite dilution where it reduces to the single-sphere translational Stokes-Einstein relation for a hydrodynamically structured colloidal sphere. The approximate validity of this relation would be quite useful, since η_∞ can then be determined more easily, and using a smaller amount of particles, by a dynamic scattering experiment instead of a rheo-mechanical measurement. This is why GSE relations including the present one have been thoroughly subjected to theoretical explorations, for particulate systems including permeable hard spheres [50] and charge-stabilized particles [27, 136].

An exact GSE relation is reflected in Fig. (5.14) by a horizontal straight line of unit height. However, for all considered values of γ, significant deviations from $\Lambda_{\mathrm{S}} = 1$ are observed at larger volume fractions. The deviations are largest for no-slip hard-core particles where the HIs are strongest, amounting to about 40 % at $\phi = 0.45$. For concentrations $\phi \leq 0.4$, the displayed curves for $\Lambda_{\mathrm{S}}(\phi)$ are nearly straight lines, characterized by the linear coefficient, $\lambda_{\mathrm{S}}(\gamma)$, in the expansion of Λ_S to linear order in ϕ. The linear concentration coefficient derived from our analytic expressions for d_{S} and η_∞ is given by the polynomial

$$\lambda_{\mathrm{S}}(\gamma) = 0.6685 + 0.3201\overline{\gamma} + \mathcal{O}\left(\overline{\gamma}^2\right)\,. \tag{5.15}$$

For a given hydrodynamic particle model, the values of γ which should be used in calculating d_{S} and η_∞, respectively, are actually different if the $\mathcal{O}((L^*_{h,f})^2)$ corrections to $a_{h,f}$ in Eq. (4.41) cannot be neglected. However, this does not affect our general conclusion that the GSE relation is violated, as illustrated by the curves in Fig. (5.14) where for simplicity the same γ values were used in calculating d_{S} and η_∞.

According to Fig. (5.14), the ordering relation $\Lambda_{\mathrm{S}}(\phi) > 1$ is obeyed by particles with pure hard-core interactions. As shown in Ref. [136], the same ordering applies to charge-stabilized suspensions. In contrast, the long-time product function $\Lambda^{\mathrm{L}}_{\mathrm{S}}(\phi) = (d_{\mathrm{L}}/d_0) \times (\eta/\eta_0)$ relating long-time self-diffusion coefficient d_{L} to zero-frequency viscosity η has been shown for no-slip hard-sphere and charge-stabilized suspensions to fulfill the opposite

ordering $\Lambda_S^L(\phi) < 1$ for $\phi > 0$ [27]. Our results for the long-time GSE Λ_S^L are presented in Subsec. 5.4.3 where we show that $\Lambda_S^L(\phi) < 1$ for $\phi > 0$ is fulfilled for permeable hard-sphere suspensions independent of particle permeability.

5.3. Comparison with experiments on non-ionic microgels

We demonstrate now the accuracy of our easy-to-apply toolbox methods of calculating short-time diffusion properties by analyzing DLS measurements by Eckert and Richtering [66] on non-ionic PNIPAM microgels in DMF. As discussed in Subsec. 5.1, the microgel particles behave as hard spheres as far as their static properties are concerned. On modeling the microgels also hydrodynamically as no-slip hard spheres with $a_h = a$, and on basis of bare BM method results for $H(q)$, Eckert and Richtering came to the conclusion that short-time particle diffusion is underestimated by the no-slip hard-sphere model. This suggests that the non-uniform cross-linker density of the microgels should have a significant hydrodynamic effect.

To account for this effect, we model here the microgels as spherical annulus particles, and determine $H(q)$ using the scaling Eq. (5.9) in conjunction with the analytic expressions in Eqs. (5.7) and (5.1) for K and d_S, respectively. In the BM method calculation of $h_d^{ns}(q)$ which enters into the scaling expression of $H(q)$, we use the HS-VW structure factors depicted in Fig. 5.1, with the hard-core radius $a = 120$ nm. The only adjustable parameter in our model is thus the reduced hydrodynamic radius $\gamma = a_h/a$.

In Fig. 5.15, our theoretical results for $H(q)$ are presented and compared with the experimental findings in Ref. [66]. The latter have been obtained indirectly from multiplying the DLS first cumulant data for the diffusion function $D(q)$ by the VW-PY $S(q)$ (c.f. Eq. (4.52)). Using the constant ratio $\gamma = 0.97$, we obtain very good agreement between theory and experiment for all volume fractions. Our finding of a concentration-independent hydrodynamic radius $a_h = 0.97 \times a$ points to the consistency of our analytic method of calculating $H(q)$, since as an intrinsic particle property, a_h should not depend significantly on the volume fraction. While this holds for the strongly cross-linked non-ionic microgels considered here, for weakly cross-linked ionic microgels in the swollen-state temperature range, a significant size shrinkage with increasing concentration is observed [40].

The deduced hydrodynamic microgel radius is only 3% smaller than the excluded volume radius, corresponding to a likewise small value, $\lambda_x = 0.029$, of the reduced fluid penetration length. This exemplifies the common experimental situation of $a_h \approx a_{h,f}$, with a relative correction to the flat plane value $a_{h,f}$ being here of $\mathcal{O}\left((L_{h,f}^*)^2\right) \approx 10^{-3}$ small.

The small microgel permeability nonetheless significantly affects $H(q)$, in particular at

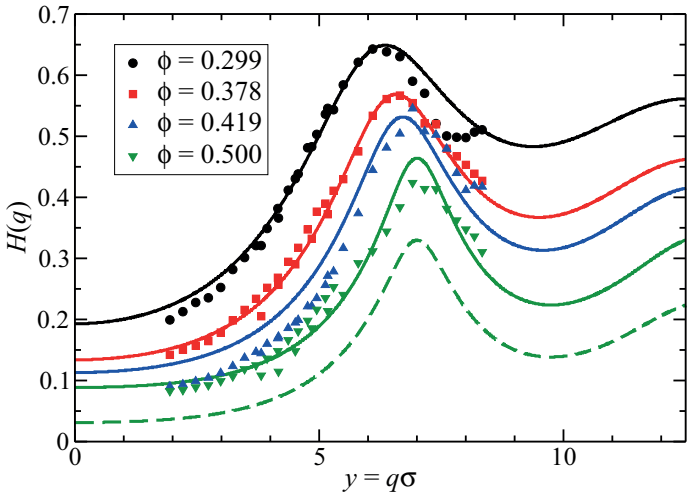

Fig. 5.15.: Experimentally deduced hydrodynamic function of PNIPAM microgels in DMF (filled symbols, taken from Ref. [66]) compared with the theoretical predictions (solid lines) for the spherical annulus model, using $\gamma = 0.97$ and Eq. (5.9) for $H(q)$, combined with Eq. (5.7) for K and Eq. (5.1) for d_S. Dashed line: Theoretical prediction for non-permeable particles ($\gamma = 1$) at $\phi = 0.5$. The wavenumbers are scaled by the hard-core diamter $\sigma = 240$ nm.

larger concentrations. This is shown in Fig. 5.15 for $\phi = 0.5$ by the comparison with the hydrodynamic function for zero permeability (dashed curve): The residual particle permeability enlarges the sedimentation velocity by more than 100 %, and the self-diffusion coefficient by more than 30 %.

In Fig. 5.16, our theoretical results for $D(q)/d_0$ are plotted together with the DLS data [66] for the same quantity. The theoretical curves have been obtained from dividing the spherical annulus $H(q)$'s depicted in Fig. 5.15 by the associated VW-PY structure factors, $S(q)$, of hard spheres in accordance with Eq. (4.52). At $q = 0$, the VW-PY $S(q)$ reduces to the CS expression for the reduced osmotic compressibility presented in Eq. (3.35), valid in the full fluid-phase volume fraction range of hard spheres. The agreement between theoretical and experimental diffusion functions is very good in the intermediate wavenumber range including the principal peak position, q_m, of $S(q)$ where $D(q)$ is minimal, and also for larger wavenumbers. At small q values and large volume fractions, the experimental data are overestimated. Even considering the remaining small-q deviations, the here presented theoretical results for $D(q)$ are in distinctly better agreement with the experimental data than the earlier ones presented in Ref. [66] where permeability effects were not included.

The deviations in $D(q)$ at small-q can be partially attributed to the high sensitivity of

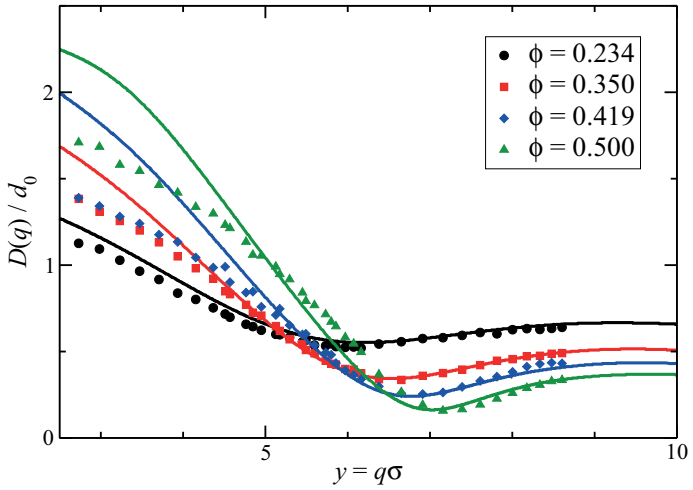

Fig. 5.16.: DLS data for the reduced diffusion function $D(q)/d_0$ (filled symbols) taken from Ref. [66], in comparison with our theoretical predictions for $\gamma = 0.97$, obtained by dividing the sperical annulus results for $H(q)$ depicted in Fig. 5.15 by the VW-PY values of $S(q)$ shown in Fig. 5.1.

the inverse compressibility factor, $1/S(0)$, multiplying $H(0)$ in Eq. (4.58), on the residual softness of the microgels. This is demonstrated in Fig. 5.17, where the concentration dependence of $1/S(0)$ for hard spheres is compared to that of the Hertz potential system for the strongly distinct softness parameters $\epsilon = 10^4$, 10^2 and 10. According to the figure, even a small residual softness characterized by $\epsilon = 10^4$ significantly enlarges the osmotic compressibility for large volume fractions, with $1/S(0)$ being lowered accordingly. Viewed on the scale of the structure factors in Fig. 5.2, the small-q differences are not resolved since $S(0)$ is very small for large concentrations. While the smaller factor $1/S(0)$ in the Hertz model would improve the agreement with the experimental $D(q)$ at small q, we recall in referring to Fig. 5.2 that a somewhat larger volume fraction ϕ_s, than that for hard spheres is required in the Hertz model for an equally good fit of the experimental $S(q)$. If the enlarged volume fraction is accounted for, there remains a small final reduction in $1/S(0)$ only. An additional cause for the small-q differences can be size polydispersity. It was shown in Ref. [189], that a small degree of polidispersity significantly enlarges, in concentrated suspensions, the measured diffusion function at small q.

In summarizing, we conclude that our HRM based toolbox methods reproduce the short-time diffusion properties of the non-ionic microgel suspensions very well, and with little numerical effort. The non-homogeneous cross-linker density is accounted for by a hydrodynamic radius which is only three percent smaller than the excluded volume radius.

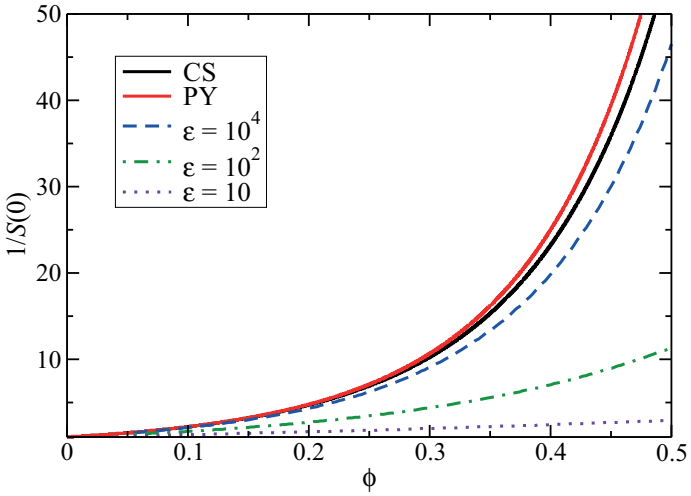

Fig. 5.17.: Influence of particle softness (elasticity) on the inverse compressibility factor $1/S(0)$, for hard-sphere and Hertz potential particles, plotted as a function of ϕ. The Carnahan-Starling (CS) (black solid line) and PY (red solid line) results for hard spheres are compared with the PY-based pedictions for Hertz model particles with softness parameters $\epsilon = 10^4$ (dashed line), 10^2 (dashed-dotted line), and 10 (dotted line).

5.4. Long-time dynamics

In the following, we present a theoretical scheme for the approximate calculation of d_{L} and η for suspensions of hydrodynamically structured particles, which as a bonus requires only little numerical effort. It is based on the HRM and a factorization approximation method proposed originally by Medina-Noyola for self-diffusion [24]. We point out that the HRM error estimation for short-time properties in Eq. (4.60) applies also to long-time properties including d_{L}/d_0 and η, and also to the dynamic structure factor, $S(q,t)$, for arbitrary correlation times. This follows from general expressions for long-time transport coefficients and $S(q,t)$ which have been obtained using the Mori-Zwanzig projection operator formalism in conjunction with the many-particle generalized Smoluchowski equation (Eq. (4.20)) for the configurational probability distribution function [61]. The crucial fact to notice here is that the hydrodynamic mobility tensors entering into the GSE have no explicit time dependence.

We exemplify the error estimate for d_{L} by starting from the configurational average expression presented in Eq. (4.62). The only information about the backward Smoluchowski operator $\hat{O}_B$ (Eq. (4.46)) needed here is its linear dependence on the mobility tensors $\boldsymbol{\mu}_{ij}$. From this and Eq. (4.59), it follows that the error introduced in approximating d_{L}/d_0 by

$d_{\mathrm{L;HRM}}/d_0$ is of $\mathcal{O}((L^*_{h,f})^2)$ small.

5.4.1. Self-diffusion coefficient

Using Eq. (4.62), d_{L} can be written as

$$d_{\mathrm{L}}(\phi) = d_S(\phi)\left[1 + \frac{\Delta D(\phi)}{d_{\mathrm{S}}(\phi)}\right], \tag{5.16}$$

where in the term in brackets, the explicit dependence on d_{S} has been scaled out. According to arguments first put forward by Medina-Noyola [24], and subsequently substantially elaborated by Brady also regarding the zero-frequency viscosity [25, 26], the factor function in brackets is not only scale invariant with respect to d_{S}, but for hard spheres it is to a decent approximation also independent of the HIs. This implies the no-HI factorization approximation,

$$\left[1 + \frac{\Delta D}{d_{\mathrm{S}}}\right] \approx \left[\frac{d_{\mathrm{L}}}{d_0}\right]_{\text{no-HI}}, \tag{5.17}$$

where the bracket term is approximated by a purely structural factor determined by excluded volume interactions only. For known d_{S}, the problem of calculating d_{L} is thus simplified to the calculation of the reduced long-time self-diffusion coefficient without HIs. The dependence of d_{L} on the HIs, and the hydrodynamic particle structure, is embodied here in d_{S} alone.

Brownian dynamics simulation results for $[d_{\mathrm{L}}(\phi)/d_0]_{\text{no-HI}}$ by Hinsen and Cichocki [162] and Moriguchi [190] are depicted in Fig. 5.18. In the fluid-phase concentration regime $\phi \leq \phi_f$, where $\phi_f = 0.494$ is the volume fraction at freezing, the simulation data are well described by the polynomial least-square fit,

$$\left[\frac{d_{\mathrm{L}}}{d_0}\right]_{\text{no-HI}} = 1 - 2\,\phi + 1.272\,\phi^2 - 1.951\,\phi^3, \tag{5.18}$$

where the exact first-order virial coefficient, $\lambda_L = 2$, for a hard-sphere suspension without HIs has been incorporated. The figure depicts furthermore the analytic approximation,

$$\left[\frac{d_{\mathrm{L}}}{d_0}\right]_{\text{no-HI}} \approx \frac{1}{1 + 2\phi\, g(\sigma^+;\phi)}, \tag{5.19}$$

given by Brady [25], where the structural factor is expressed in terms of the RDF contact value, $g(\sigma^+;\phi)$, of hard spheres. The contact value for the fluid-phase concentration range is to high accuracy described by the CS expression given in Eq. (3.34) [137], with $g(\sigma^+;\phi_f) = 5.81$. Eq. (5.19) incorporates the exact first-order virial coefficient, $\lambda_L = -2$.

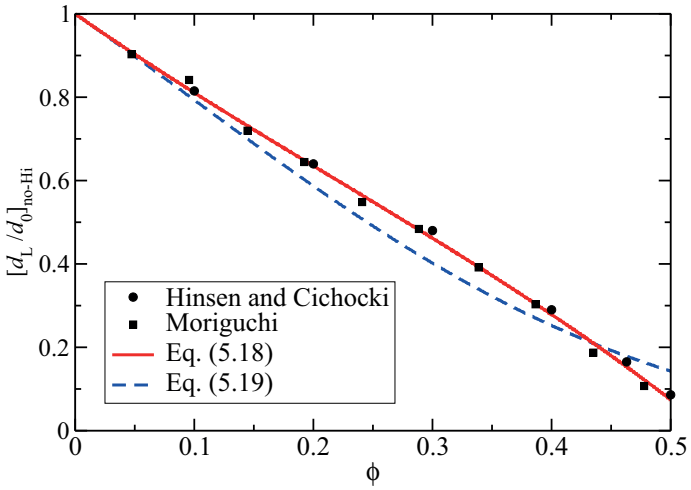

Fig. 5.18.: Reduced long-time self-diffusion coefficient, $[d_L/d_0]_{\text{no-HI}}$, of colloidal hard spheres without HIs. Filled circles and squares: Brownian dynamics simulation results by Hinsen and Cichocki [162] and Moriguchi [190], respectively. Solid line: Polynomial fit in Eq. (5.18). Dashed line: Eq. (5.19) with Carnahan-Starling contact value input.

Moreover, near random closed packing at $\phi_{\text{rcp}} \approx 0.64$ where a metastable hard-sphere fluid gets jammed, on basis of results for $g(\sigma^+;\phi)$ by Rintoul and Torquato [137] it predicts that $[d_{\text{L}}]_{\text{no-HI}}$ diminishes linearly like $0.59 \times (1 - \phi/\phi_{\text{rcp}})$. Since d_{S} vanishes likewise linearly in case of no-slip hard spheres, the quadratic scaling prediction $d_{\text{L}} \sim (1 - \phi/\phi_{\text{rcp}})^2$ near random closed packing is obtained in the factorization approximation.

The performance of the no-HI factorization approximation for the d_{L} of no-slip spheres on basis of Eq. (5.1) for d_{S} at $\gamma = 1$ and Eq. (5.18) for $[d_{\text{L}}/d_0]_{\text{no-HI}}$, is documented in Fig. 5.19 by the comparison with DLS data by van Megen *et al.* [191, 192], and simulation results by Phung [165] with HIs included. The Stokesian dynamics simulation data for Brownian hard spheres by Phung have been obtained for a small number ($N = 27$) of particles, and for a small albeit non-zero shear Péclet number $\text{Pe} = 0.01$. The Péclet number is defined as ratio of advective and diffusive transport rate, i.e.

$$Pe = \frac{\tau_{\text{D}}}{\tau_{\text{shear}}} = \frac{a^2\dot{\gamma}}{d_0}\,, \tag{5.20}$$

where $\tau_{\text{shear}} = 1/\dot{\gamma}$, so that for $\text{Pe} = 0.01$ diffusion dominates the system dynamics. The overall agreement of the no-HI factorization approximation with the experimental and simulation data is quite good. The factorization approximation gives $\lambda_L = -3.831$ for the first-order virial coefficient of hydrodynamically interacting no-slip spheres, while its

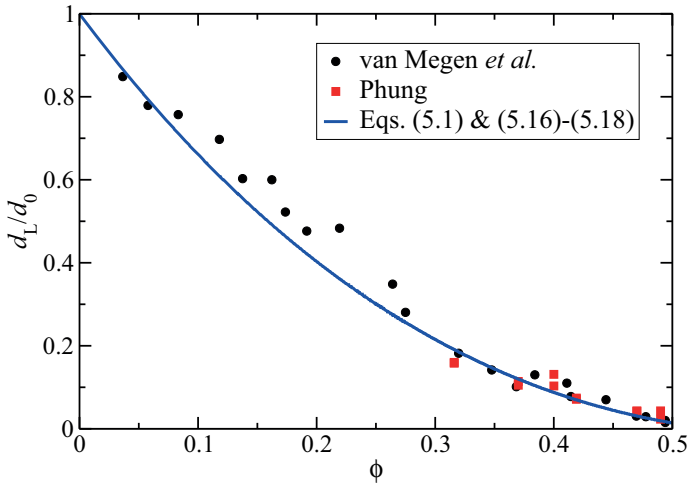

Fig. 5.19.: Reduced long-time self-diffusion coefficient, d_L/d_0, of no-slip colloidal hard spheres. Filled circles: Experimental data by van Megen *et al.* [191, 192]. Filled squares: Simulation data by Phung [165]. Solid line: No-HI factorization approximation in Eqs. (5.16)-(5.18), with the short-time factor d_S/d_0 according to Eq. (5.1) for $\gamma = 1$.

correct numerical value is given by $\lambda_L = -2.1$. The initial low-concentration decrease of d_L is thus overestimated.

The good performance of the no-HI factorization approximation for no-slip hard spheres gives support to its straightforward extension to hydrodynamically structured particles, by using for d_S/d_0 now the analytic expression in Eq. (5.1) for spherical annulus spheres. Our results for d_L/d_0 based on this extended factorization scheme are shown in Fig. 5.20. With decreasing γ, the slowing down effect of the HIs on d_L diminishes. In the limit $\gamma \to 0$ of hard spheres acting hydrodynamically as point particles, the long-time self-diffusion coefficient in the absence of HIs is recovered. According to Cichocki and Felderhof [185], the linear concentration coefficient of d_L/d_0 for small γ is $\lambda_L(\gamma) = -2\left[1 - 1.031\gamma + 0.111\gamma^2 + \mathcal{O}(\gamma^3)\right]$, where the linear and quadratic terms in γ are due to the so-called Oseen long-distance HIs contribution to the relaxation part ΔD. The contributions of the short-time part, d_S, to d_L appear first in quadratic order in γ. While this describes quantitatively how d_L approaches $[d_L]_{\text{no-HI}}$ for small γ, we reemphasize that $\gamma > 0.8$ is valid for most hydrodynamically structured colloidal particles.

The no-HI factorization approximation predicts the ratio, d_L/d_S, of long-time and short-time coefficients to be independent of HIs and hydrodynamic particle structure, with value

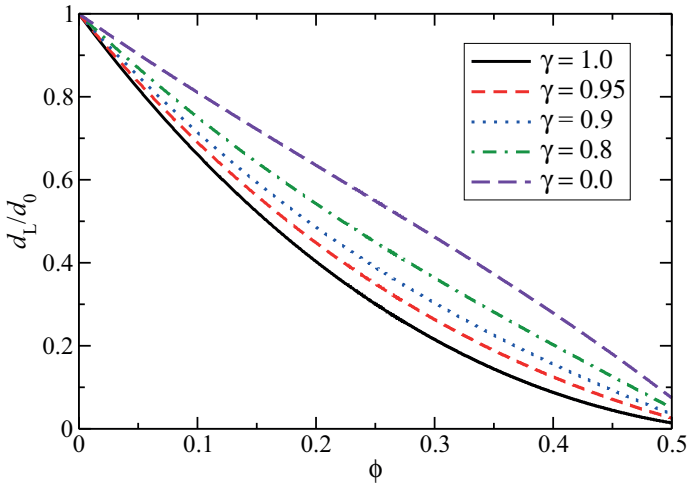

Fig. 5.20.: Generic influence of the intra-particle hydrodynamic structure on d_{L}/d_0, quantified in the no-HI factorization approximation, Eqs. (5.16)-(5.18), using for d_{S}/d_0 the spherical annulus model formula in Eqs. (5.1) and (5.2). Several values of γ are considered as indicated.

equal to $[d_{\mathrm{L}}/d_0]_{\text{no-HI}}$. This implies with Eqs. (5.16) and (5.17) that

$$\left(\frac{d_{\mathrm{L}}}{d_{\mathrm{S}}}\right)(\phi_f) \approx 0.1\,, \tag{5.21}$$

in good accord with the Löwen-Palberg freezing criterion value of about 0.1. Thus, a universal freezing value of 0.1 is predicted not only for colloidal suspensions with different repulsive pair potentials, but also with different hydrodynamic intra-particle structures. For pair interactions characterized by a single length scale, the dynamic Löwen-Palberg criterion has been shown to be equivalent to the static Hansen-Verlet freezing criterion for the value $S(q_m)$ of the structure factor peak height [159].

5.4.2. Zero-frequency viscosity

Analogous to Eq. (5.16) for d_L, in Eq. (4.61) for the low-shear zero-frequency viscosity η, we factor out the high-frequency (short-time) contribution η_∞ according to

$$\eta\,(\phi) = \eta_\infty\,(\phi)\left[1 + \frac{\Delta\eta\,(\phi)}{\eta_\infty\,(\phi)}\right]\,, \tag{5.22}$$

with the term in brackets expected to be approximately independent of the HIs. This suggests the no-HI factorization approximation,

$$\frac{\Delta\eta\,(\phi)}{\eta_\infty\,(\phi)} \approx \left[\frac{\Delta\eta\,(\phi)}{\eta_0}\right]_{\text{no-HI}}, \tag{5.23}$$

where $[\Delta\eta]_{\text{no-HI}}$ is the shear relaxation viscosity part without HIs. In this approximation, the HIs are assumed to affect η only by means of the factored out η_∞ in Eq. (5.22). The neglect of HIs simplifies the calculation of the shear relaxation viscosity part considerably. Following works by Brady [25, 26], an analytic estimate of $\Delta\eta$ for no-slip hard spheres without HIs is given by

$$\left[\frac{\Delta\eta}{\eta_0}\right]_{\text{no-HI}} \approx \frac{12}{5}\phi^2 g(\sigma^+;\phi)\,, \tag{5.24}$$

with $g\,(\sigma^+;\phi)$ given by Eq. (3.34) for $\phi \leq 0.49$. This estimate combines the exact low

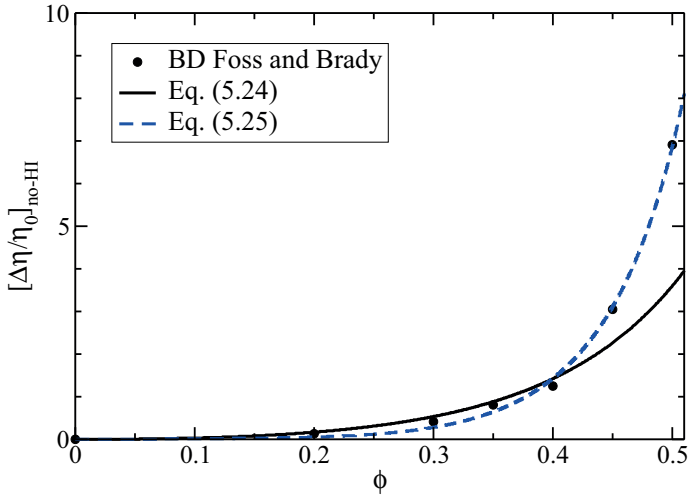

Fig. 5.21.: Reduced shear relaxation viscosity part without HIs, $[\Delta\eta/\eta_0]_{\text{no-HI}}$, of a suspension of Brownian hard spheres in dependence of ϕ. Filled circles: Brownian dynamics (BD) simulation data by Foss and Brady [164]. Solid line: Analytic estimate in Eq. (5.24). Dashed line: Semi-empirical expression in Eq. (5.25).

concentration limit, $2.4\,\phi^2 + \mathcal{O}(\phi^3)$, of $[\Delta\eta]_{\text{no-HI}}$ with its divergence at random closed packing according to $[\Delta\eta]_{\text{no-HI}} \sim (1-\phi/\phi_{\text{rcp}})^{-1}$, triggered by the divergence of the hard-sphere contact value. Together with the likewise linear divergence of η_∞ for no-slip hard spheres, a quadratic divergence $\eta \sim (1-\phi/\phi_{\text{rcp}})^{-2}$ is thus predicted for the zero-frequency viscosity. For hydrodynamically structured particles where $a_h < a$, there are no diverging lubrication forces for spheres in contact. The high-frequency viscosity remains then finite

at random closed packing, and the particles can still rotate individually. Moreover, η diverges only linearly as $\eta(\phi, \gamma < 1) \sim (1 - \phi/\phi_{\mathrm{rcp}})^{-1}$.
In Fig. 5.21, the outcome of Eq. (5.24) for $[\Delta\eta]_{\text{no-HI}}$ is compared to Brownian dynamics simulation results without HIs by Foss and Brady [164, 166]. Up to $\phi \approx 0.35$, the simulation data are decently well represented by the analytic expression, but the steep rise of $[\Delta\eta]_{\text{no-HI}}$ at large volume fractions is not reproduced. The simulation data are well captured for all ϕ by the semi-empirical expression

$$\left[\frac{\Delta\eta}{\eta_0}\right]_{\text{no-HI}} = \frac{\frac{12}{5}\phi^2\left(1 - 7.085\phi + 20.182\phi^2\right)}{\left(1 - \frac{\phi}{\phi_{\mathrm{rcp}}}\right)}\,, \tag{5.25}$$

combining the exact quadratic-order concentration dependence with the linear order divergence at random closed packing. Throughout this work, we restrict our analysis to the equilibrium fluid-phase concentration regime $\phi \leq 0.5$, while the viscosity simulations in Refs. [163, 164, 166] have been extended to the metastable fluid concentration regime $\phi_{\mathrm{f}} < \phi < \phi_{\mathrm{rcp}}$ where crystallization is kinetically suppressed. Regarding the shear relaxation viscosity part with HIs included, Brady has proposed the following approximate scaling expression [25, 26],

$$\frac{\Delta\eta}{\eta_\infty} \approx \frac{12}{5}\,\phi^2\,\frac{g(\sigma^+;\phi)}{\Lambda_{\mathrm{S}}(\phi)}\,, \tag{5.26}$$

where the influence of the HIs on the ratio $\Delta\eta/\eta_\infty$ is solely embodied in the short-time GSE function Λ_{S} defined in Eq. (5.14). For no-slip hard spheres, Λ_{S} is well represented for $\phi < 0.4$ by $\Lambda_{\mathrm{S}} \approx 1 + 0.67\phi$ according to Eq. (5.15), while without HIs Λ_{S} is equal to one. Consequently, Eq. (5.26) predicts $\Delta\eta/\eta_\infty$ to be only mildly affected by the HIs, giving some credit to the no-HI factorization approximation in Eq. (5.23). Eq. (5.26) was obtained from arguing that the adequate diffusion time scale in a concentrated suspension is a_h^2/d_{S} instead of a_h^2/d_0, and from using a low-concentration estimate of the weakly shear-distorted stationary pair distribution function with the prefactor $g(\sigma^+;\phi)$ preserved [25]. A detailed discussion of the approximations going into Eq. (5.26) is given by Lionberger and Russel [195, 196].
On using in place of Eq. (5.24) the semi-empirical fitting expression in Eq. (5.25) as the non-hydrodynamic factor in Eq. (5.26) , Brady's scaling relation is modified to

$$\frac{\Delta\eta}{\eta_\infty} \approx \frac{\frac{12}{5}\phi^2\left(1 - 7.085\phi + 20.182\phi^2\right)}{\left(1 - \frac{\phi}{\phi_{\mathrm{rcp}}}\right)\Lambda_{\mathrm{S}}(\phi)}\,. \tag{5.27}$$

The two here considered variants of the no-HI scaling approximation of η consist of using

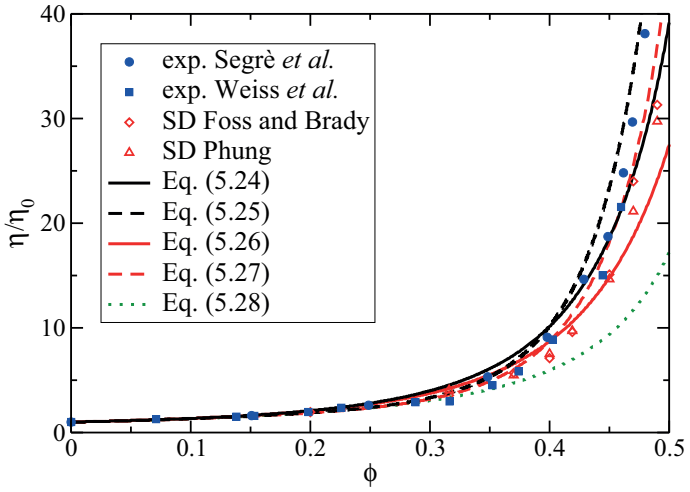

Fig. 5.22.: Zero-frequency viscosity, η/η_0, of no-slip Brownian hard spheres with HIs. Solid and dashed black lines: No-HI factorization predictions using $\eta_\infty(\phi, \gamma = 1)$ according to Eq. (5.10), and $[\eta/\eta_0]_{\text{no-HI}}$ according to Eqs. (5.24) and (5.25), respectively. Solid and dashed red lines: Brady's (modified) scaling approximations using Eqs. (5.26) and (5.27) for $\Delta\eta/\eta_\infty$, respectively, and Eq. (5.10) for the factored out η_∞. The factor $1/\Lambda_S$ in the (modified) scaling approximation is calculated using Eq. (5.10) for η_∞ and Eq. (5.1) for d_S. Dotted line: Eq. (5.28). Filled symbols: Experimental data by Segrè *et al.* [193] and Weiss *et al.* [194]. Open symbols: Stokesian dynamics (SD) simulation results for Brownian hard spheres by Foss and Brady [166] and Phung [165].

Eqs. (5.24) and (5.25), respectively, as input for the ratio $\Delta\eta/\eta_\infty$ in the bracket term in Eq. (5.22), in conjunction with the accurate generalized Saitô formula in Eq. (5.10) used for η_∞. In addition, Brady's scaling expression for η and its modification consist of approximating $\Delta\eta/\eta_\infty$ in the bracket term in Eq. (5.22) by Eqs. (5.26) and (5.27), respectively, with the generalized Saito formula used again for the factored out high-frequency viscosity. The hydrodynamic factor $1/\Lambda_S$ in the two scaling expressions is calculated analytically using Eq. (5.1) for d_S, and the generalized Saitô formula for η_∞. The results for $\eta(\phi, \gamma = 1)$ by the four inter-related analytic approximations are depicted in Fig. 5.22. They are compared with experimental data by Segrè *et al.* [193] and Weiss *et al.* [194], and Stokesian dynamics (SD) simulation data for Brownian hard spheres with HIs included by Foss and Brady [166] and Phung [165]. The latter have been obtained for a small number ($N = 27$) of particles in the basic simulation box. In Ref. [166], $\Delta\eta$ was deduced using a general Green-Kubo formula for the shear stress correlation function of hydrodynamically interacting particles [179]. The viscosity curves by all four approximations compare overall quite well with the simulation data. Depending on the used

approximation for $\Delta\eta/\eta_\infty$, deviations are visible at intermediate and large volume fractions. The neglect of HIs in $\Delta\eta/\eta_\infty$ results in an overestimation of the simulations data at large ϕ, but the low-ϕ experimental viscosity data are well described. On considering the simulation data to be more trustworthy than the experimental data, owing to experimental polydispersity effects and difficulties in determining the precise volume fraction, the modified scaling expression by Brady in Eq. (5.27) provides the overall best description of the SD data for η, slightly better than Brady's original scaling expression in Eq. (5.26). We use the modified scaling expression in the following discussion of hydrodynamically structured particles. Note that the second-order in concentration coefficient of η is predicted by all four factorization approximation variants as $5.01+2.4 = 7.41$, while the exact coefficient is equal to 5.931 [197]. This low-ϕ difference is not resolved on the scale of Fig. 5.22.

The figure includes additionally the viscosity prediction by the formula

$$\eta(\phi)/\eta_0 = \frac{1 - 0.4\overline{\phi} + 0.222\overline{\phi}^2}{\left(1-\overline{\phi}\right)^2}\,, \tag{5.28}$$

with $\overline{\phi} = \phi/\phi_{\mathrm{rcp}}$, which incorporates the first two known virial coefficients in $\eta/\eta_0 = 1 + 2.5\phi + 5.91\phi^2 + \mathcal{O}(\phi^3)$ and a quadratic divergence of η at ϕ_{rcp}. As seen in Fig. 5.22, the formula describes the simulation and experimental data well for $\phi \leq 0.35$, but it strongly underestimates them at larger ϕ.

Akin to long-time self-diffusion, we can straightforwardly extend our analysis to hydrodynamically structured particles, by using the generalized Saitô expression in Eq. (5.10) for $\eta_\infty(\phi,\gamma)$, in combination with the modified Brady scaling expression in Eq. (5.27) for $\Delta\eta/\eta_\infty$. The viscosity predictions for different reduced hydodynamic radii γ, and volume fractions extending up to ϕ_{f}, are depicted in Fig. 5.23. Note the pronounced reduction of $\eta(\phi,\gamma)$ with decreasing γ, owing to the reduced dissipation, inherited from the similar behavior of $\eta_\infty(\phi,\gamma)$. In the limit $\gamma \to 0$, the zero-frequency viscosity reduces to $\eta(\phi,0) = \eta_0 + [\Delta\eta]_{\text{no-HI}}$. In spite of being approximate, the analytic modified scaling expression for $\eta(\phi,\gamma)$ in Eqs. (5.22) and (5.27) can be expected to be useful for a quick analysis of experimental viscosity data of hydrodynamically structured colloidal suspensions. For the PNIPAM microgels in DMF, e.g., where $\gamma = 0.97$ has been deduced, a significant reduction both in η and η_∞ is predicted relative to the corresponding viscosities of non-permeable particles. It will be interesting to compare our zero-frequency and high-frequency viscosity predictions with future viscosity measurements on non-ionic PNIPAM in DMF systems.

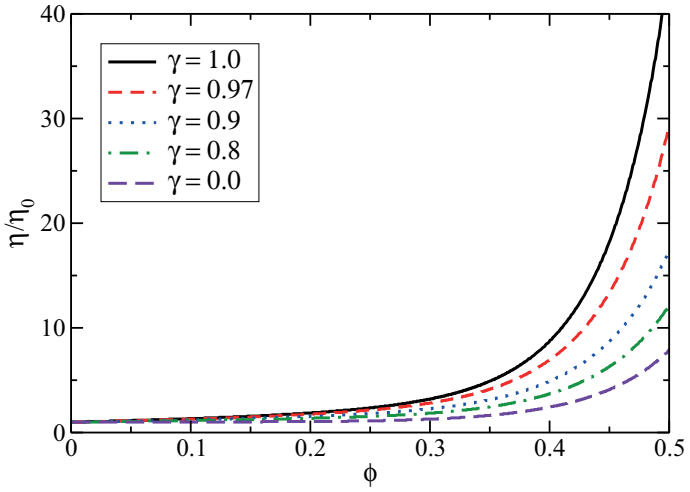

Fig. 5.23.: Predictions for the reduced zero-frequency viscosity, $\eta(\phi,\gamma)/\eta_0$, of hydrodynamically structured particles, based on the modified Brady scaling expression for $\Delta\eta/\eta_\infty$ in Eq. (5.27), and the generalized Saitô formula in Eq. (5.10) for $\eta_\infty(\phi,\gamma)$. The hydrodynamic factor $\Lambda_S(\phi,\gamma)$ is calculated using Eq. (5.10) for $\eta_\infty(\phi,\gamma)$, and Eq. (5.1) for $d_S(\phi,\gamma)/d_0(\gamma)$. Several values of γ are considered as indicated.

5.4.3. Long-time generalized Stokes-Einstein relations

The long-time analogue to the short-time GSE presented in Eq. (5.14) is given by $\Lambda_S^L \approx 1$ where

$$\Lambda_s^L(\phi,\gamma) = \frac{d_L(\phi,\gamma)}{d_0(\gamma)} \times \frac{\eta(\phi,\gamma)}{\eta_0} \,. \tag{5.29}$$

We use the the no-HI factorization approximation results for d_L (c.f. Fig. 5.20), and the modified scaling expression for η in Eq. (5.27) (c.f. Fig. 5.23), in order to asses the validity of $\Lambda_S^L = 1$ via Fig. 5.24. Our results show that the long-time GSE is strongly violated in the whole fluid-phase concentration regime, and that the deviations are enhanced with decreasing γ. The non-monotonic concentration dependence of Λ_S^L reflects a competition of the contributions coming from η and d_L, which both have a monotonic ϕ dependence. Further, we find for permeable hard-sphere systems that $\Lambda_S^L(\phi,\gamma) \leq 1$ for $\phi \leq \phi_f$, independent of the value of γ, in agreement with earlier results by Banchio *et al.* [27] for an impermeable hard-sphere suspension with stick BCs. The violation of the discussed long-time GSE is so pronounced that it is of no use for permeable hard sphere suspensions.

Note that in Fig. 5.24, we have assumed that the HRM parameter γ is the same for d_L and η. As discussed in Subsecs. 4.1.4 and 5.2.5, this is an approximation valid for small

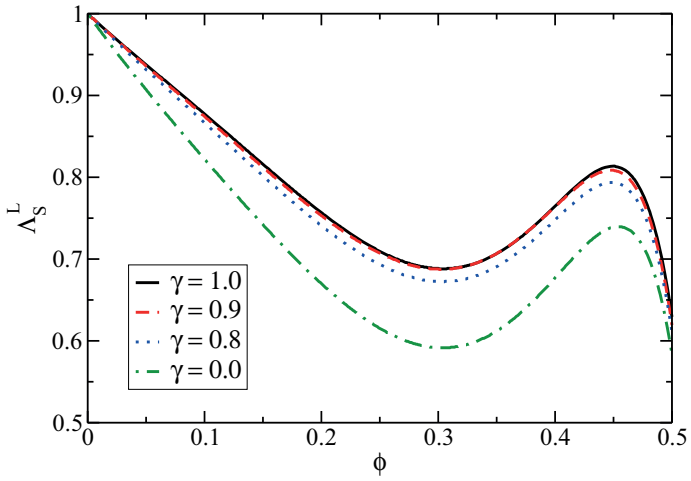

Fig. 5.24.: Test of the long-time GSE relation in Eq. (5.29), for spherical annulus particles with values of γ as indicated. For η, the modified scaling expression in Eq. (5.27) (c.f. Fig. 5.23) is used together with the no-HI factorization approximation for d_{L} in Eqs. (5.16)-(5.18) (c.f. Fig. 5.20).

values of the reduced slip length $L^*_{h,f}$.

6. Charged-particles dispersions: Results

In this chapter, we consider two different charged-particles systems. Firstly, we analyze how the softness and permeability influence the dynamics of ionic microgel suspensions. This is of interest for the analysis of dynamic scattering data. Secondly, aqueous colloidal suspensions of charged silica particles are investigated. The focus is here on the calculation of accurate transport properties expressions, used subsequently in a theoretical-experimental UF modeling study.

6.1. Ionic microgels: softness and permeability effects

We employ here the effective Denton pair potential for ionic microgels presented in Eqs. (2.4) and (2.6), with steric interactions given by the Hertz potential (Eq. (2.1)) to study the effect of particle softness and permeability on the structure and dynamics of ionic microgel suspensions. For this purpose, we use realistic experimentally determined parameters as described in [57]. These parameters include the inverse Debye screening length, κ, in units of the particle diameter determined as $\kappa\sigma_s = 7$, and the bare charge number of the microgels determined as $Z = 150$. The only varied potential parameter is the interaction strength $\epsilon \in [1 - 10^5]$ of the Hertz potential part. In Fig. 6.1, we show the corresponding interaction potentials.

To reveal the effect of softness and permeability on the dynamics of ionic microgels, it is sufficient to make a case study for a single concentration, which we select as $\phi = 0.15$. The Darcy permeability of the microgels is described using the HRM, with γ defined as the ratio of a_h and the soft interaction radius $a_\mathrm{s} = \sigma_\mathrm{s}/2$ (c.f. Eq. (2.1)).

It is not a priori obvious that the HRM can be applied to highly soft particles. While for particles with hard-sphere excluded volume interactions, e.g. for particles with a rigid mesh-like backbone, $g(r < \gamma\sigma)$ is ensured to be zero, this is not the case for particles interacting softly. The overlap of soft particles leads to their deformation which in turn affects the solvent-particle interaction. However, as long as a particle remains spherical on average, the model of impermeable spheres with effective stick BC diameter $\gamma\sigma_\mathrm{s}$ can be used. The accuracy of the HRM for transport property calculations of soft ionic microgels should be better for systems where only a shallow non-zero tail of $g(r)$ for $r < \sigma$ is present. This holds for moderate ϕ and/or in systems with strong electrostatic repulsion, where overlap configurations are unlikely. Keeping this in mind, we nonetheless vary γ without paying heed to the explicit softness of the pair potential and hence the actual form of $g(r)$,

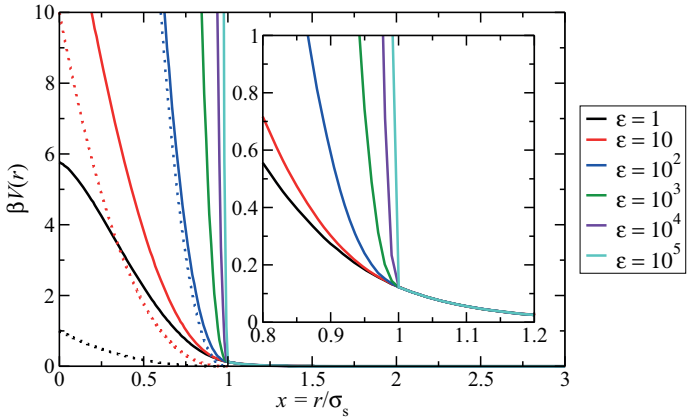

Fig. 6.1.: Pair potential of ionic microgels according to Eqs. (2.4), (2.6) and (2.1), for various values of ϵ as indicated. The reduced Debye screening length $\kappa\sigma_s$ is 7, and the bare charge number of the microgels $Z = 150$. The inter-particle distance r is scaled by the effective microgel diameter σ_s used in the Hertz potential part. The dotted lines are the contributions by the Hertz potential (Eq. (2.1)) to the total potential for selected values of ϵ. The inset focuses on the crossover from the overlap ($r \leq \sigma_s$) to the non-overlap region ($r > \sigma_s$).

for we are interested here in the qualitative behavior rather than quantitative results.

6.1.1. Structure functions

In Fig. 6.2, we illustrate the effect of particle softness on $g(r)$ and $S(q)$, for a suspension of ionic microgels with $\phi = 0.15$. For the calculation of $g(r)$ and $S(q)$, we use the PY closure discussed in Subsec. 3.4.2.

With increasing ϵ and consequential increase of the energy penalty for particle deformation, the probability of overlapping particles configurations decreases significantly. As a result, the distance up to which the RDF is practically zero shifts to larger values, reaching for $\epsilon = 10^4$ σ_s. We note that the Hertz potential (for $r < \sigma_s$) is bounded which is likewise the case for the Denton potential part. For the lowest considered value $\epsilon = 1$, the energy contribution from the electrostatic part on overlap (c.f. Eq. (2.4) and Fig. 6.1) is 5 times larger than the Hertz potential contribution. For the considered concentration $\phi = 0.15$, we have $g(0) = 0$ for $\epsilon = 1$, despite the energy penalty at full particle overlap of about $6\, k_B T$.

With increasing ϵ the $g(\sigma_s^+)$ grows, and for $\epsilon = 10^5$ a tiny depletion zone at $x \approx 1.8$ is appearing. A non-zero $g(\sigma_s^+)$ is due to the weak electrostatic repulsion for the discussed systems. To visualize the effect of the electrostatic repulsion, we show $g_{HS}(r)$ of neutral

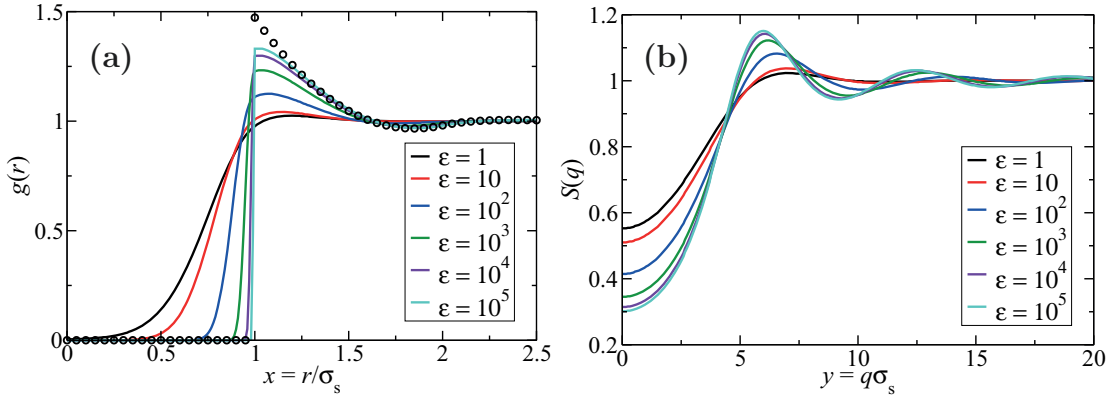

Fig. 6.2.: (a) RDF $g(r)$ and (b) $S(q)$ in PY approximation for the Denton plus Hertz pair potential presented in Eqs. (2.4), (2.6), and (2.1) for various values of ϵ as indicated, and using $\phi = 0.15$. The bare microgel charge number is $Z = 150$, and the reduced Debye screening length is $\kappa\sigma_s = 7$. These are realistic values for the ionic microgel systems studied in [57]. The symbols in (a) are the $g(r)$ of a hard-sphere suspension with diameter $\sigma = \sigma_s$ and $\phi = 0.15$.

hard spheres as the black symbols in Fig. 6.2a. Note that $g_{\rm HS}(r)$ is in good agreement with the RDF of a system of particles interacting by the Hertz potential with $\epsilon = 10^5$. The increase of $g(\sigma_s^+)$, and the decreasing likelihood of overlap configurations with increasing ϵ, is mirrored in $S(q)$ by a shift of the next-neighbor peak position, $q_{\rm m}$, to smaller q-values, and the increase of the respective peak height $S(q_{\rm m})$. In addition, $S(q)$ develops more pronounced oscillations, and the osmotic compressibility becomes strongly reduced.

6.1.2. Short-time dynamics

In Fig. 6.3, we study how changes in the Hertz interaction strength ϵ are affecting the short-time diffusion of ionic microgel systems as characterized by $H(q)$. We first study theoretically impermeable particles with stick surface BCs for which $\gamma = 1$. For the calculation of $H(q)$, we use the hybrid BM-PA scheme discussed in Subsec. 4.4.3, with self-part input $d_{\rm S}$ calculated in PA approximation. In the BM and PA methods, the PY $S(q)$ and $g(r)$ are used as input.

The hydrodynamic function has the same trends as $S(q)$ regarding the next-neighbor peak $S(q_{\rm m})$. In addition, the sedimentation coefficient, $K = H(0)$, reflects the trends in $S(0)$. A possible explanation for this similarity is that the particle softness leads to an increased likelihood for overlap which in turn results in an effective reduction of the friction exerted on the particles by the solvent back flow. As a consequence, K is larger for softer particles. Interestingly, K turns out to be particularly sensitive to ϵ. As an example, the functions

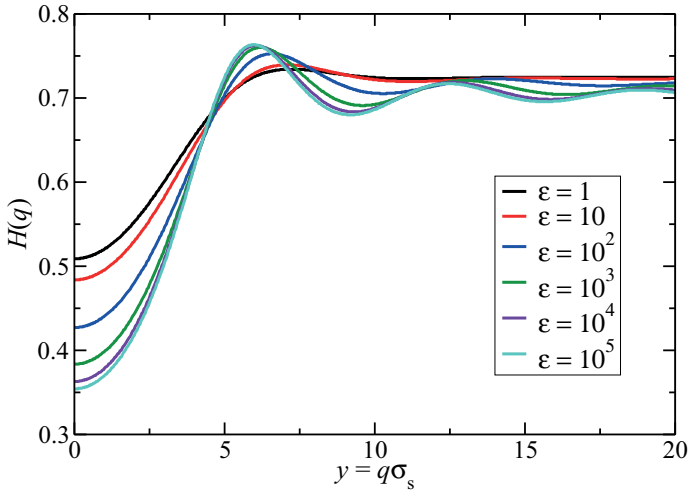

Fig. 6.3.: Hydrodynamic function of impermeable ionic microgel suspensions with $\kappa\sigma_s = 7$ and $Z = 150$, and values of ϵ as indicated for $\phi = 0.15$. The function $H(q)$ is calculated using the BM-PA hybrid method.

$H(q)$ for $\epsilon = 10^3$ and 10^5 are basically coincident in the whole q-range except for the low-q region.

Interestingly, the same ϵ dependence is observed for the self-diffusion coefficient, d_S, with its increase with decreasing ϵ, however, being small compared to the increase of K.

In Fig. 6.4a, we demonstrate the influence of solvent permeability on $H(q)$ for an ionic microgel suspension. The considered values $\gamma = \{0.9, 0.95, 1.0\}$ cover actually a broad range of experimentally realistic permeabilities (c.f. Subsec. 4.1.4). With increasing permeability (decreasing γ), the influence of HIs becomes weaker and $H(q)$ is shifted for all q to higher values, while the shape of the function remains practically unchanged. Moreover, with decreasing γ, the difference in the self-diffusion coefficients for $\epsilon = 1$ and 10^4 decreases. This reflects that the hydrodynamic mobilities associated with self-diffusion are faster decaying than those for $H(q)$.

Results for the diffusion function, $D(q)$, directly accessible in DLS experiments are shown in Fig. 6.4b. The particle softness leads to a lowering of the diffusion function for low-q while increasing permeability results in an up-shift of $D(q)$. The first feature can be attributed to the distinctly higher osmotic compressibility at smaller ϵ and the latter mirrors the behavior of $H(q)$. For a fixed value of ϵ, the increase in permeability leads to a down-shift of $D(q)$.

To conclude, we have shown theoretically that particle permeability and softness strongly affect the short-time diffusion of ionic microgel systems described using the Denton-Hertz

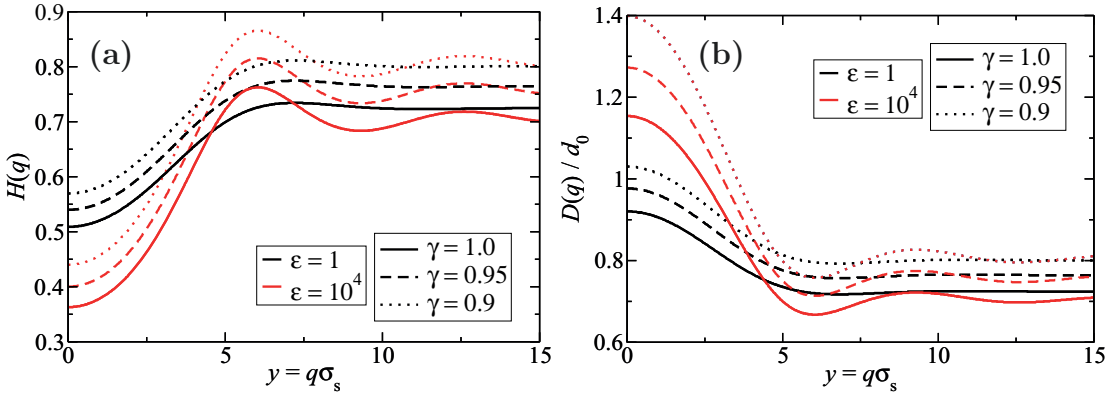

Fig. 6.4.: (a) $H(q)$ and (b) $D(q)$ of permeable ionic microgel suspensions, for $\phi = 0.15$ and $\epsilon = 1$ and 10^4. The permeability is characterized by the reduced HRM parameter γ. The hybrid BM-PA scheme is employed for the calculation of $H(q)$, and the PY $S(q)$ is used in the calculation of $D(q)/d_0 = H(q)/S(q)$.

pair potential. The effect of softness is stronger on sedimentation than on self-diffusion. In contrast, permeability distinctly affects $H(q)$ and $D(q)$ in the full q-range. Particle permeability results in an upturn in $D(q)$ for low-q values that is further enhanced in systems with large ϵ values due to the associated small χ_{T}. In fact, an upturn in $D(q)$ at low q has been seen in DLS studies on ionic microgel suspensions [198]. Finally, note that a small q upturn can be also caused by particle polydispersity [189] and additional attractive forces. The here presented discussion of $D(q)$ can be useful for the analysis of dynamic scattering measurements on permeable and / or soft charged-particles suspensions.

6.2. Application to ultrafiltration of charged particles

In this section, we discuss the importance of accurate transport properties expressions as input for the theoretical modeling of technological processes. We present here a model for cross-flow inside-out UF used by Roa *et al.* [39] to describe the filtration of permeable hard-sphere suspensions. In this thesis, this model is applied to the UF of aqueous charged-silica particles suspensions, described using the state-dependent inter-particle potential in Eq. (2.8). The charge renormalization of the silica surface charges due to surface-released counterions is accounted for by the determination of effective charges and screening lengths within a PB cell model approach. This allows for the accurate calculation of properties needed in the cross-flow UF modeling, namely the osmotic pressure, Π, the isothermal compressibility, χ_{OSM}, the collective diffusion coefficient, d_{C}, and the zero-frequency viscosity, η, as function of the particle concentration.

6.2.1. Cross-flow ultrafiltration (UF) model

In UF, the transport of a Brownian particles suspension is considered under laminar flow conditions where the system is only slightly perturbed from thermal equilibrium. Under continuous cross-flow operation, a steady-state is quickly reached, with fully developed suspension flow in the lumen side of the membrane fiber, and a stationary particles-enriched CP layer is formed at the inner membrane wall (c.f. Fig. 2.3). Owing to the very large Schmidt number of colloidal suspensions, given by the ratio of the characteristic single-particle diffusion and hydrodynamic vorticity diffusion times associated with the particle radius distance, the steady suspension flow is much faster developed than the CP layer. The CP layer becomes more pronounced and more extended with increasing distance from the fiber inlet. On a coarse-grained length scale where the size of the particles is not resolved, the stationary transport is governed by continuum mechanics equations. There is first the mass balance (particle conservation) described by the continuity equation,

$$\nabla \cdot \mathbf{J}(\mathbf{r}) = 0\,, \tag{6.1}$$

where

$$\mathbf{J}(\mathbf{r}) = -d_C^{\mathrm{L}}(\phi(\mathbf{r}))\,\nabla\phi(\mathbf{r}) + \phi(\mathbf{r})\mathbf{u}(\mathbf{r}) \tag{6.2}$$

is the particle flux, and $\phi(\mathbf{r})$ is the local particle volume fraction at position $\mathbf{r}$ inside the suspension. The flux $\mathbf{J}(\mathbf{r})$ has a diffusion contribution related to Brownian motion whose strength at given concentration gradient is quantified by the long-time collective or gradient diffusion coefficient $d_C^{\mathrm{L}}(\phi)$ (the short-time counterpart is given in Eq. (4.58)), and an advection contribution proportional to the suspension-averaged fluid velocity $\mathbf{u}$. The latter fulfills the incompressibility constraint of $\nabla \cdot \mathbf{u} = 0$.

Since in UF the local low-Reynolds number conditions are met, the momentum balance for the suspension-averaged fluid flow is governed by the effective Stokes equation introduced in Eq. (4.11). It contains the suspensions-averaged local pressure, $p(\mathbf{r})$, and the ϕ-dependent effective suspension viscosity, $\eta(\phi)$, of steady low-shear flow. In inhomogeneous suspension regions such as in the CP layer, there is an additional hydrodynamic force density proportional to $\nabla\eta$.

The governing Eqs. (4.11), (6.1) and (6.2), are subjected to boundary conditions imposing the inlet flow, and specifying flow conditions at the lumen side of the membrane. We assume a fully developed Poiseuille inlet flow, i.e.

$$\mathbf{u}(r, x = 0) = u_m \left(1 - \frac{r^2}{R^2}\right) \mathbf{e}_x, \tag{6.3}$$

of a homogeneous feed solution of volume fraction ϕ_0. The axis of the cylindrical fiber extends from $x = 0$ to L, in the direction of the unit vector $\mathbf{e}_x$, with r denoting the radial distance from this axis. The inflow velocity u_m at the fiber axis is related to the characteristic shear rate, $\dot{\gamma}$, by [199]

$$\dot{\gamma} = \frac{2u_m}{R} = \frac{4Q_{\text{feed}}}{\rho_{\text{m}}\pi R^2}\,, \tag{6.4}$$

where Q_{feed} is the integral suspension mass flow (in g/l) through the inlet cross section, and ρ_{m} the constant suspension mass density. The mass density difference between particles and fluid is neglected here.
Furthermore, we impose Darcy's law [199]

$$v_w(x) \equiv \mathbf{u}(R,x)\cdot\mathbf{e}_r = L_p^0\Big[\Delta p_{\text{TMP}}(x) - \Pi\left(\phi_w(x)\right)\Big]\,, \tag{6.5}$$

for the (reverse osmosis) inside-out permeate velocity, $v_w(x)$, along the membrane position x. Here, $\phi_w(x) = \phi(r = R, x)$ is the particle concentration, $\Delta p_{\text{TMP}}(x)$ the transmembrane pressure, $\Pi(\phi_w)$ the osmotic pressure at the inner membrane wall, and $\mathbf{e}_r$ the radial unit vector of the cylindrical coordinate system. Moreover, $L_p^0 = 1/(\eta_0 R_{\text{mem}})$ is the solvent permeability of the clean membrane and R_{mem} the clean membrane hydraulic resistance. It is important to note that the pressure leading to solvent permeation is equal to $\Delta p_{\text{TMP}}(x)$ reduced by $\Pi(\phi_w)$. We use furthermore the zero-tangential fluid velocity condition at the membrane-suspension interface,

$$\mathbf{e}_r \times \mathbf{u}(R,x) \times \mathbf{e}_r = \mathbf{0}\,, \tag{6.6}$$

and the reflecting boundary condition,

$$\mathbf{J}(R,x)\cdot\mathbf{e}_r = 0\,, \tag{6.7}$$

describing the particle-impermeability of the membrane.
Strictly speaking, the boundary conditions in Eqs. (6.3) - (6.7) should be taken not right at the membrane-suspension interface but at the external boundary of a transition layer adjacent to the inner membrane surface of thickness δ^*, which is required to be large compared to the particle size and mean pore size of the membrane, but small compared to the membrane thickness and fiber radius R. Furthermore, for charged particles and / or a charged membrane, the transition layer thickness δ^* should be large compared to the Debye screening length, but small compared to the extension of the CP layer. Provided such a

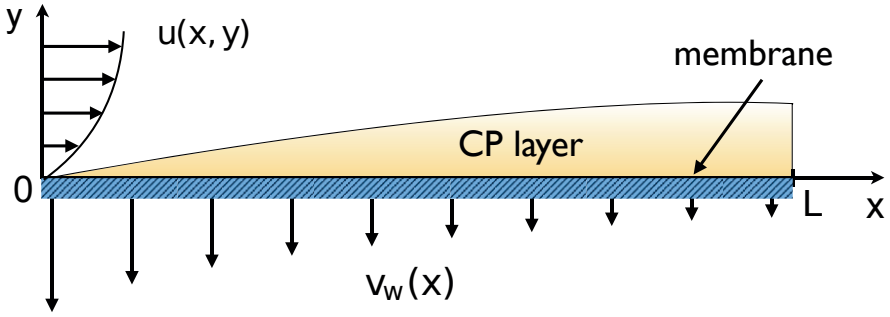

Fig. 6.5.: Sketch of the locally flat CP layer on top of the membrane surface at $y = 0$. The permeate velocity, v_w, is given by $v_w(x) = v(x, y = 0)$, and the zero-tangential fluid velocity condition in Eq. (6.6) results in $u(x, y = 0) = 0$. Sketch kindly provided by R. Roa [39]

thin transition layer can be identified, and the imposed flow driven by the transmembrane pressure does not significantly perturb thermodynamic equilibrium within the layer, Eqs. (6.3) - (6.7) can be used which implicitly imply an infinitely thin transition layer. In particular, the filtration behavior is then not affected by the membrane surface charge.
A more detailed discussion of the transition layer picture will be given in a forthcoming article, describing a systematic theoretical analysis of the UF of charge-stabilized suspensions for varying salt conditions [200]. In the present UF study, the requirements for an unperturbed transition layer are met. Moreover, since $u_m \gg v_w^0$ where $v_w^0 = L_p^0 \, \Delta \, p_{\mathrm{TMP}}$ is the maximal permeate velocity reached for a clean membrane and pure solvent as feed, also the CP layer is thin compared to R. Thus a boundary layer analysis of Eqs. (6.1), (6.2) and the Stokes equation (4.11) can be made, resulting in a similarity solution for the CP layer concentration profile $\phi(x, y)$. Here $y = R - r \ll R$ is the transversal distance from the membrane wall. From this profile, and for known concentration dependence of the osmotic pressure, the permeate velocity $v_w(x)$ is obtained using Darcy's law. Note that the fluid velocity $\mathbf{u}(\mathbf{r})$ inside the CP layer is split into an axial $u(x, y)$ and radial $v(x, y)$ velocity contribution according to $\mathbf{u}(\mathbf{r}) = u(x, y)\hat{\boldsymbol{e}}_x + v(x, y)\hat{\boldsymbol{e}}_y$. Thus, v_w is given by $v_w = v(x, y = 0)$ as sketched in Fig. 6.5.
The coupled set of non-linear ordinary differential equations from which the similarity solution $\phi(x, y)$ is obtained using the boundary conditions noted before, is described in detail in [39]. For given inlet feed flow and $\Delta p_L = p_{\mathrm{in}} - p_{\mathrm{out}}$ (c.f. Subsec. 2.2.2), the only input quantities required in this numerical solution are the osmotic pressure, $\Pi(\phi)$, the zero-frequency viscosity, $\eta(\phi)$, the collective diffusion coefficient, $d_{\mathrm{c}}(\phi)$, characterizing

the charge-stabilized suspension, and $\Delta_{\mathrm{TMP}}(x)$. All of these properties can be calculated using the methods presented in this thesis.

6.2.2. Experimental sample properties

In the cross-flow UF measurements, an aqueous suspension of charge-stabilized silica particle is used. The suspension consists of Ludox silica particles dispersed in purified water without added electrolyte. The mean hydrodynamic particle radius is $a_{\mathrm{h}} = 15\,\mathrm{nm}$. The concentration of the feed suspension is 0.1 wt% on assuming monodisperse particles, and on neglecting the mass density difference with respect to the solvent. Additionally to the monovalent counterions dissociated from the silica particles surfaces that neutralize the negative particle charges, the suspension includes ions from the self-dissociation of water molecules, and from atmospheric CO_2 contamination. All this amounts to pH = 5. The zeta potential was measured with a Mastersizer 3000 from Malvern Instruments giving the value $\zeta = -35\,\mathrm{mV}$.
The number of bare elementary charges on a silica particle surface is estimated as $Z_{\mathrm{bare}} \approx 106$, i.e. as $(l_B/a)Z_{\mathrm{bare}} = 5$ in reduced units. We have obtained this value using Fig. 4.10 in [201] from which for $pH = 5$ the surface charge density $0.0375\,e/\mathrm{nm}^2$ of SiO^- ions is deduced.
The Debye screening parameter, κ_{res}, of the permeate reservoir is estimated by assuming the pH of the permeate to be the same as that of the dilute feed suspension. The screening parameter follows then from using

$$\kappa_{\mathrm{res}}^2 = 8\pi l_B N_A [\mathrm{H}^+]\,, \tag{6.8}$$

where $[\mathrm{H}^+] = 10^{-pH}$ is the molar hydronium concentration, and N_A denotes Avogadro's number. This leads to $\kappa_{\mathrm{res}} a = 0.15$. The values for Z_{bare} and κ_{res} noted here are used in the cell model calculations of Z_{eff} and κ_{eff} going into the OCM potential.

6.2.3. Renormalized charge and screening length

As discussed in Subsec. 2.2.2, we employ the OCM (c.f. Eq. (2.8)) for the description of a charge-stabilized suspension of rigid colloidal spheres. Here, we discuss how the concentration dependent potential parameters Z_{eff} and κ_{eff} are calculated.
For monovalent microions that can be treated as pointlike in comparison with the colloidal macroions, and for small microion correlation effects disregarded, Z_{eff} and κ_{eff} can be obtained using the mean-field Poisson-Boltzmann (PB) spherical cell model description of

Alexander *et al.* [202] (see also Trizac *et al.* [82, 203]). In the PB cell model, the bulk suspension is represented by a single spherical macroion with uniformly distributed bare surface charge $Z_{\rm bare}e$, placed at the centre of a spherical cell, whose radius $R = a/\phi^{1/3}$ is set by the colloid volume fraction. The fluid and the microions, with the latter described by radially smeared out concentration profiles, are confined to the outer shell of thickness $R-a$. For a system with monovalent counterions dissociated from the colloid surfaces such as for the considered silica suspension, which is in osmotic equilibrium with a 1-1 strong electrolyte reservoir with concentration $c_{\rm res}$ of salt ion pairs, the mean-field electrostatic potential $\Phi(r)$, expressed in units of k_BT/e, is the solution of the non-linear PB equation [203]

$$\Phi''(r) + 2\,\frac{\Phi'(r)}{r} = \kappa_{\rm res}^2 \sinh\{\Phi(r)\}\,. \tag{6.9}$$

Here, the prime denotes differentiation with respect to the radial distance r. For the considered osmotic Donnan equilibrium, the appropriate inner and outer boundary conditions rendering the solution $\Phi(r)$ unique are $\Phi'(a) = -l_B Z_{\rm bare}/a^2$ and $\Phi'(R) = 0$, respectively, in accord with the global electroneutrality of the cell and zero potential inside the reservoir. Following Alexander *et al.* [202], the effective colloid charge number, $Z_{\rm eff}$, is then obtained from the solution, $\Phi_l(r)$, of the PB equation linearized at the cell boundary using $\Phi_l'(a) = -l_B Z_{\rm eff}/a^2$. This leads to [203]

$$\frac{l_B}{a}\,Z_{\rm eff} = \gamma_R\, F(\kappa_{\rm eff}a, \phi^{-1/3})\,, \tag{6.10}$$

where

$$\kappa_{\rm eff}^2 = 4\pi l_B\big[n_+(R) + n_-(R)\big] = \kappa_{\rm res}^2 \cosh\{\Phi(R)\}\gamma_R F(\kappa_{\rm eff}a, \phi^{-1/3})\,, \tag{6.11}$$

and

$$F(x,y) = \frac{1}{x}\big[\,\big(x^2y - 1\big)\sinh\{xy-1\} \tag{6.12}$$

$$+\,x\,(y-1)\cosh\{xy-x\}\big]\,, \tag{6.13}$$

with $\gamma_R = \tanh\{\phi(R)\}$. Here, $n_\pm(R)$ are the co- and counterion concentration at the cell boundary. The Donnan potential $\phi(R)$ is associated with the lowering of the salt concentration $n_s = N_s/V_R$, with $V_R = (4\pi/3)R^3$, in the suspension relative to the reservoir concentration $c_{\rm res}$. It is obtained from numerically solving the non-linear PB boundary

value problem for $\Phi(r)$. For this purpose, the MATLAB routine bvp4c [204] has been employed. The overall electroneutrallity of the cell commands, with $x = r/\sigma$ ($\sigma = 2a$), that

$$\frac{n_s}{c_{\rm res}} = 24\,\phi(1-\phi)\int_{1/2}^{R/\sigma} dx\, x^2 \exp\{\Phi(x)\}\,, \tag{6.14}$$

where $Z_{\rm bare} < 0$ and thus $\Phi < 0$ has been used. In using the here described PB cell model to obtain $Z_{\rm eff}$ and $\kappa_{\rm eff}$ as functions of $l_B/aZ_{\rm bare}$, $\kappa_{\rm res}a$ and ϕ, we ignore chemical charge regulation effects arising from an incomplete dissociation of colloidal surface groups.
In our silica filtration experiments, the role of the microion reservoir is played by the permeate. On assuming that the membrane is fully retentive to the silica spheres, the ion concentration in the aqueous reservoir is practically set by the water-adsorbed atmospheric CO_2 resulting in $\kappa_{\rm res}a = 0.15$. The Donnan equilibrium corresponds to a semi-grand canonical ensemble description where microions can be exchanged between suspension and reservoir. A closed suspension of given salt concentration n_s is treated most easily by mapping it on a corresponding semi-open system. The reservoir concentration $c_{\rm res}$, for which $c_{\rm res} > n_s$, is then uniquely determined from solving Eq. (6.14) for the searched-for $c_{\rm res}$ at given n_s using a root-finding procedure.
The PB cell model predictions for the concentration dependence of the effective charge number and screening parameter of the low-salinity aqueous silica suspension in Donnan equilibrium are depicted in Fig. 6.6 and its inset, respectively, for a concentration independent bare charge number $Z_{\rm bare} \approx 106$ in units of the elementary charge. Owing to the quasi-condensation of counterions at the colloid sphere surface, the effective charge $Z_{\rm eff}$ is in general smaller than the bare one. At very small ϕ, the salt ions contribute dominantly to the electrostatic screening (salt-dominated regime) and $Z_{\rm eff}$ and $\kappa_{\rm eff}$ are nearly concentration independent. This is the regime where the OCM effective potential $V_{\rm eff}(r)$ is practically state-independent, with values of $\kappa_{\rm eff}$ close to the reservoir value $\kappa_{\rm res}$ constituting its lower bound. At sufficiently large ϕ, screening is mainly due to the non-condensed part of the surface-released counterions (counterion-dominated regime). In this higher concentration regime, both $Z_{\rm eff}$ and $\kappa_{\rm eff}$ change significantly with increasing ϕ, giving rise to a distinctly state-dependent OCM potential, and values of $\kappa_{\rm eff}$ significantly larger than $\kappa_{\rm res}$. According to Dobnikar *et al.* [82], the crossover region connecting the two regimes in the PB cell model is roughly characterized by the threshold concentration value,

$$\phi^* = 0.2 \times \frac{(\kappa_{\rm res}a)^2}{(l_{\rm B}/a)Z_{\rm bare}}\,, \tag{6.15}$$

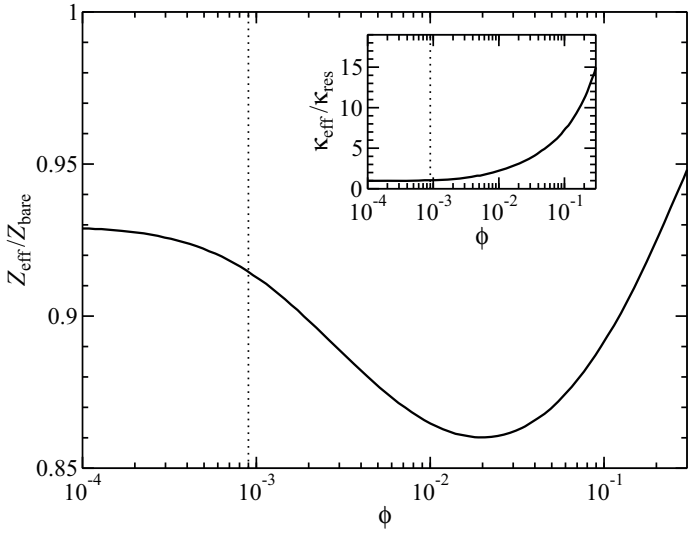

Fig. 6.6.: Charge number ratio, $Z_{\text{eff}}/Z_{\text{bare}}$, (main figure part) and screening parameter ratio, $\kappa_{\text{eff}}/\kappa_{\text{res}}$, (inset) as functions of colloid volume fraction ϕ, calculated using the Alexander PB cell model. The employed systems parameters $(l_{\text{B}}/a)Z_{\text{bare}} = 5, \kappa_{\text{res}}a = 0.15$, $a = 15$ nm, and $l_B = 0.71$ nm are those of the low-salinity aqueous silica particles suspension in osmotic equilibrium with an aqueous 1-1 electrolyte reservoir. The vertical dotted line marks the threshold concentration value ϕ^*. See Eq. (6.15) and the text for details.

which for our low-salinity silica system amounts to $\phi^* = 0.9 \times 10^{-3}$, as indicated by the dotted vertical lines in Fig. 6.6. This concentration value is one order in magnitude smaller than the concentration $\phi \approx 0.02$ where the minimal (i.e., maximally charge-renormalized) value of $Z_{\text{eff}}(\phi)$ occurs which is 14% smaller in magnitude than Z_{bare}. In our filtration experiments using silica suspensions, the constant feed concentration is $\phi_0 = 0.001$, implying silica concentration values, $\phi_w(x)$, along the membrane wall larger than ϕ^*. It is noticed from Fig. 6.6 that the concentrations in the UF experiments belong to the counterion-dominated region where Z_{eff}, and hence $V_{\text{eff}}(r)$, change significantly if ϕ is varied.

6.2.4. Osmotic pressure and compressibility

The OCM potential, V_{eff}, with Z_{eff} and κ_{eff} determined using the PB cell model, is employed for the calculation of static system properties, namely $g(r)$, $S(q)$, the isothermal osmotic compressibility, χ_{osm}, and the total suspension pressure P. While the first two serve as input in the BM-PA hybrid scheme for the calculation of accurate transport properties, the latter are used for the filtration modeling. As mentioned in the discussion of

thermodynamic properties in Sec. 3.3, the calculation of the suspension pressure for systems with state dependent interaction potentials is more intricate and will be discussed in the following.
The total suspension pressure, P, caused by microions and macroions can be formally split as [82, 205]

$$P = P_{\text{micro}} + P_{\text{corr}} \,, \tag{6.16}$$

into a microionic pressure part, P_{micro}, deriving from the so-called free volume contribution to the total PM free energy originating from the non-condensed microions, and the correlation pressure part, P_{corr}, due to correlations among the microion-dressed colloids. In the considered Donnan equilibrium situation with a lower-concentrated monovalent ion reservoir, the osmotic pressure, Π, i.e. the difference between suspension pressure and the reservoir pressure, P_{res}, is given by

$$\Pi = P - 2\,c_{\text{res}}\,k_B T \,, \tag{6.17}$$

where in accord with the PB level of description, P_{res} has been approximated by its ideal gas form. This simplification is justified, since the leading non-ideal (limiting-law) contribution, $-k_B T \kappa_{\text{res}}^3/(24\pi)$, to the reservoir pressure is, for $\kappa_{\text{res}} a = 0.15$, three orders of magnitude smaller than the ideal gas part .
For lower-salinity systems of colloids having many surface charges, the microionic (counterion) pressure contribution is dominant so that $P \approx P_{\text{micro}}$ [82]. This holds true in particular for our filtration experiments where $\phi > \phi^*$ is valid, as we are going to discuss below. In the cell model, P_{micro} is determined by the microion densities at the cell boundary,

$$\beta P_{\text{micro}} = n_+(R) + n_-(R) = 2\,c_{\text{res}} \left(\frac{\kappa_{\text{eff}}}{\kappa_{\text{res}}} \right)^2 \,, \tag{6.18}$$

where the second equality holds in PB approximation.
The correlation pressure part, P_{corr}, is in general quite different from the pressure, P_{OCM}, obtained from treating the suspension as an effective one-component fluid of dressed macroions with the concentration-dependence of the OCM potential disregarded. Under isothermal conditions, and without significant effective three-body correlation contributions arising at very low salinity only, the total suspension pressure can be determined from the generalized virial equation, presented in Eq. (3.28) for a one-component fluid system with concentration-dependent effective pair potential.
Additionally to the colloidal ideal gas contribution, and the contributions associated with

the macroion $g(r)$ appearing on the right-hand-side of Eq. (3.28), there is a pressure contribution deriving from the free volume energy, $f_0(\rho)$, whose colloid concentration dependence is basically inherited from the non-condensed counterions owing to the total electroneutrallity constraint. While f_0 has no influence on $g(r)$ which is determined solely by $V_{\rm eff}(r)$, it must be considered for smaller salinity to obtain thermodynamic properties from an effective one-component treatment.

The general applicability of Eq. (3.28) has been questioned in the literature [81, 206]. However, at least in the linear screening case of weakly charged colloids where $Z_{\rm eff} = Z_{\rm bare}$, it exactly reproduces the PM pressure, provided a consistent expression for the free volume pressure contribution on the right-hand-side of Eq. (3.28) is used which accounts for the ideal gas pressure contribution, $n|Z_{\rm bare}|k_{\rm B}T$, of surface-released counterions (see [207–211]). The bare OCM pressure, $P_{\rm OCM}$, is given in units of k_BT by the following part of Eq. (3.28)

$$\beta P_{\rm OCM} = \rho + \frac{2\pi}{3}\rho^2\Big\{\sigma^3 g(\sigma^+) - \int_{\sigma^+}^{\infty} dr\, r^3\, g(r)\, \frac{\partial\left(\beta V_{\rm eff}(r)\right)}{\partial r}\Big\}, \tag{6.19}$$

with the negative-valued pressure contribution by the concentration derivative of $V_{\rm eff}(r)$ omitted, and the discontinuity of $V_{\rm eff}(r)$ already considered by the integrated-out contact value term. Eq. (6.19) is a good approximation of the total suspension pressure P for very high salinity only, when the effect of the surface-released counterions becomes negligible, and f_0 and $V_{\rm eff}(r)$ are ρ-independent.

Different pressure contributions are shown in Fig. 6.7, for concentration values extending up to $\phi = 0.3$, and using the same low-salinity silica system parameters as in Fig. 6.6. Since according to the inset in Fig. 6.8, $g(\sigma^+) \approx 0$ even at $\phi = 0.3$, it follows that the contact-value pressure contribution in Eq. 6.19 is negligibly small. Moreover, since the HNC generated principal structure factor peak height, $S(q_m;\phi)$, at wavenumber q_m is smaller than 3 for all $\phi \leq 0.3$, we conclude that the suspension is liquid-like structured. We have used here the semi-empirical Hansen-Verlet rule, stating that $S(q_m) \approx 3$ is the peak value for which charge-stabilized systems (characterized in particular by $g(\sigma^+) \approx 0$) start to crystallize [212].

According to Fig. 6.7, the main contribution to the suspension pressure is due to the microions. That $P \approx P_{\rm micro}$ holds true for our silica suspension is expected for systems in the counter-ion dominated concentration regime, as scrutinized in numerous Monte-Carlo simulations of strongly charge- and size asymmetric PM systems (see, e.g., [82, 83]). Note further from the figure that $P_{\rm micro} \gg P_{\rm id}$. For reference, also the pressure curve of a hard-sphere suspension is shown, obtained by the Carnahan-Starling equation of state (c.f. Eq.

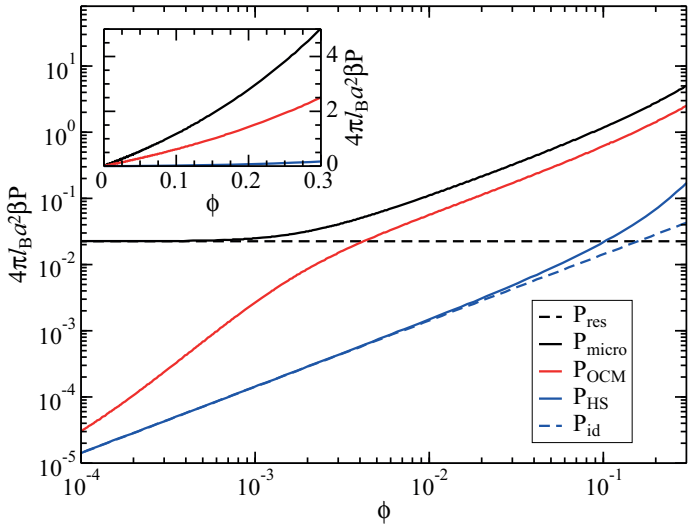

Fig. 6.7.: Colloid volume fraction dependence of different reduced pressure contributions listed in the legend, for system parameters as in Fig. 6.6. P_{res}: ideal gas reservoir pressure; P_{micro}: PB cell model microionic pressure part according to Eq. (6.18); P_{OCM}: OCM pressure part in Eq. (6.19), calculated using the HNC $g(r)$ of colloidal macroions. P_{HS}: hard-sphere pressure according to Carnahan-Starling equation of state. $P_{\mathrm{id}} = nk_BT$: colloidal ideal gas pressure. The inset depicts P_{micro}, P_{OCM} and P_{HS} on a double-linear scale.

(3.35)). The pressure P_{OCM} in Fig. 6.7 is about one half of P_{micro}, illustrating that it strongly overestimates P_{corr} in the low-salinity regime [82, 205].
The crux of the present discussion is that we can use

$$\beta\Pi \approx \frac{1}{4\pi l_B}\left(\kappa_{\mathrm{eff}}^2 - \kappa_{\mathrm{res}}^2\right) \tag{6.20}$$

as a good approximation for the osmotic pressure of the silica suspension.
The long-wavelength limit, $S(0) = S(q \to 0)$, of the macroion static structure factor is required as another thermodynamic input to the UF calculation in addition to Π, since it goes into the calculation of d_{c}. According to an exact relation by Kirkwood and Buff, the osmotic isothermal compressibility factor, χ_{osm}, in Donnan equilibrium can be expressed solely in terms of $S(0)$, i.e., [213]

$$\chi_{\mathrm{osm}}^{-1} \equiv \left(\frac{\partial\beta\Pi}{\partial\rho}\right)_{T,\mathrm{res}} = \frac{1}{S(0)}\,, \tag{6.21}$$

without the explicit colloid-microion and microion-microion static correlation functions be-

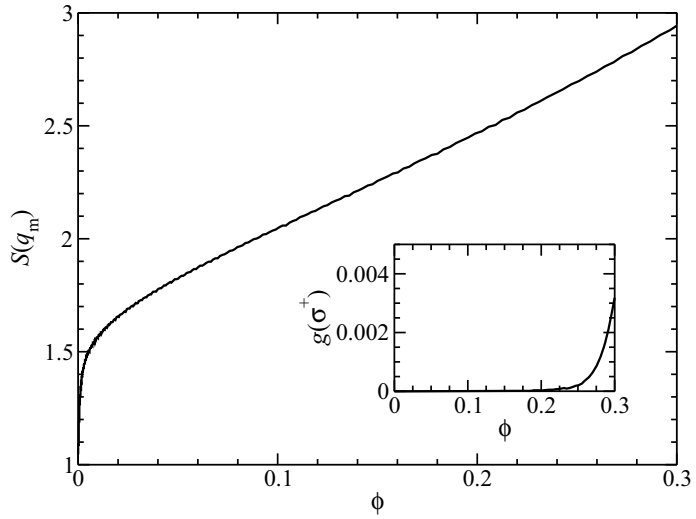

Fig. 6.8.: Colloidal structure factor principal peak height, $S(q_m)$, as a function of ϕ, calculated in HNC approximation using the OCM potential with PB cell model values for Z_{eff} and κ_{eff}. System parameters as in Fig. 6.6. Inset: Contact value, $g(\sigma^+)$, of the HNC colloidal radial distribution function.

ing involved. The concentration derivative of Π is taken here for fixed reservoir properties, namely fixed electrolyte ion chemical potential and concentration c_{res}. Since $P \approx P_{\text{micro}}$ is valid for our low-salinity system, we obtain the compressibility factor straightforwardly from

$$\chi_{\text{osm}}^{-1} \approx \frac{\kappa_{\text{eff}}}{2\pi l_B} \left(\frac{\partial \kappa_{\text{eff}}}{\partial \rho} \right)_{T,\text{res}} , \tag{6.22}$$

using the PM cell model result for κ_{eff}. At low salinity, $\chi_{\text{T}} \sim 1/Z_{\text{eff}}$ is approximately valid, making explicit the low osmotic compressibility of the strongly repelling macroions. The Kirkwood-Buff relation is useful also for testing the degree of self-consistency of the approximations, namely the PB cell model and HNC approximations, employed in calculating χ_{osm} and $S(0)$, respectively. In the concentration range of the present UF study, the difference between the two quantities is less than 20 %.

While the cell model P_{micro} is a good approximation for the suspension pressure of our silica system, with the compressibility factor determined from Eq. (6.22), for completeness we shortly address how Π can be calculated for conditions where P is not well approximated any more by P_{micro}. First, a so-called extrapolated-point-charge method of calculating P has been developed recently by Boon *et al.* [214] which uses likewise the Alexander cell model input, but now for a modified OCM potential. Second, in two closely related

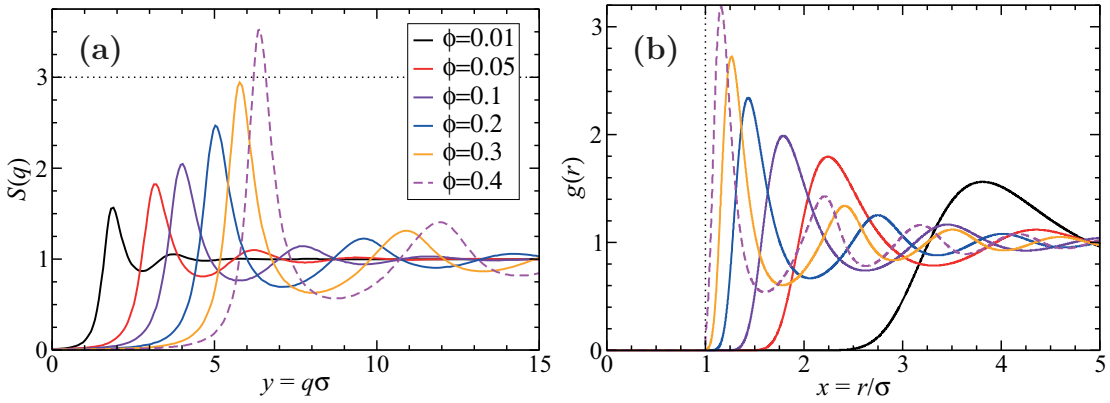

Fig. 6.9.: (a) $S(q)$ and (b) $g(r)$ calculated in HNC approximation for the OCM potential with PB-cell model values for Z_{eff} and κ_{eff} as presented in Fig 6.6, and for values of ϕ as indicated. In (a), the dotted black line indicates the Hansen-Verlet freezing criterion value $S(q_m) \approx 3$ (see text for more details) and in (b), the same color code as in (a) is used.

set of approaches put forward by Castañeda-Priego *et al.* [215, 216], and Colla *et al.* [217] (see also [218]), the exact validity of the Kirkwood-Buff relation is enforced by a self-consistent combination of the PB-based renormalized jellium model for calculating Z_{eff} and κ_{eff}, and the Rogers-Young integral equation scheme for calculating $S(q)$ with its mixing parameter being adjusted. Which of these methods of calculating Π is more accurate in comparison with benchmark PM simulations is still a matter of future assessment. For suspensions whose colloidal electric double layers are thin compared with the particle radius, a perturbation method (free energy minimalization) can be used based on an effective hard-sphere reference system (see, e.g., [209]).

6.2.5. Pair-structure functions

The effective charge and screening length obtained from the PB cell model calculations are used in the OCM potential for the calculation of the macroion-macroion $g(r)$ and $S(q)$. For numerical simplicity, we have employed the HNC approximation presented in Eq. (3.36). While the HNC lacks thermodynamic self-consistency, different from the more elaborate Rogers-Young scheme [128], it can be expected to be decently accurate for the here considered lower salinity systems (cf. Heinen *et al.* in [65]).

In Fig. 6.9a, we present $S(q)$ results for the OCM potential with PB-cell model values for Z_{eff} and κ_{eff} as presented in Fig 6.6, and for various values of ϕ. With increasing ϕ, the next-neighbor peak in $S(q)$ increases distinctly and shifts to higher wavenumbers, characteristic of a reduction of the mean particle distance. At the same time, the oscillations in $S(q)$

become more pronounced. For the highest volume fraction considered, $\phi = 0.4$, the Hansen-Verlet freezing criterion value $S(q_\mathrm{m}) \approx 3$ is exceeded suggesting the crystallization of the system. As we will show in the comparison with UF measurements, the ϕ values observed in the model calculations are so small that the fluidity of the sample is guaranteed. The corresponding HNC $g(r)$ results are presented in Fig. 6.9b. For all considered ϕ, $g(\sigma^+)$ is practically zero due to the strong electrostatic repulsion between the macroions. With increasing ϕ, the next-neighbor peak in $g(r)$ is shifting from about 4σ to 1.2σ for $\phi = 0.3$, accompanied by a distinct increase of its height. In addition, more pronounced higher order peaks of $g(r)$ are formed pointing to an increased structural ordering of the system.

6.2.6. Transport properties

The concentration-dependent long-time collective diffusion coefficient, $d_\mathrm{C}^\mathrm{L}(\phi)$, in the constitutive equation invoking the coarse-grained silica particles flux $\mathbf{J}(\mathbf{r}, t)$, can be expressed in Donnan equilibrium as [136]

$$d_\mathrm{C}^\mathrm{L}(\phi) = d_0 \frac{K^\mathrm{L}(\phi)}{\chi_\mathrm{osm}}\,, \tag{6.23}$$

where $\chi_\mathrm{osm} = S(0)$ is the osmotic compressibility coefficient calculated using Eq. (6.22). Here, $K^\mathrm{L}(\phi)$ is the long-time sedimentation coefficient. As discussed in Subsec. 4.2.1 and, e.g., [136], K^L is in principle smaller than the corresponding short-time sedimentation coefficient $K = H(q \to 0)$. However, for low-salinity systems where two-body HIs prevail, the difference between the two coefficients is minuscule and can be ignored. Consequently, we will use the short-time collective diffusion coefficient d_C as an excellent approximation for d_C^L.

For the calculation of $H(q)$, K, and d_S we use the hybrid BM-PA scheme introduced in Subsec. 4.4.3. The accuracy of BM-PA scheme calculations of $H(q)$ has been exemplified for charge-stabilized suspensions whose colloidal interactions are described by an OCM-type potential, by comparison with experiment and simulation [65, 85, 136, 178].

In Fig. 6.10, we display the BM-PA results for $H(q)$ for the same system parameters as used in Fig. 6.9. With increasing ϕ, $H(q)$ shifts to lower values mirroring a growing slowing-down effect of HIs on the system dynamics. As a consequence, both, d_S, and K attain distinctly smaller values. For $\phi = 0.4$, non-physical negative $H(q)$ values are caused by the inaccuracy of the employed BM-PA hybrid scheme at large ϕ. As discussed in Subsec. 4.4.3, the PA method used for the calculation of d_S, disregards any hydrodynamic shield-

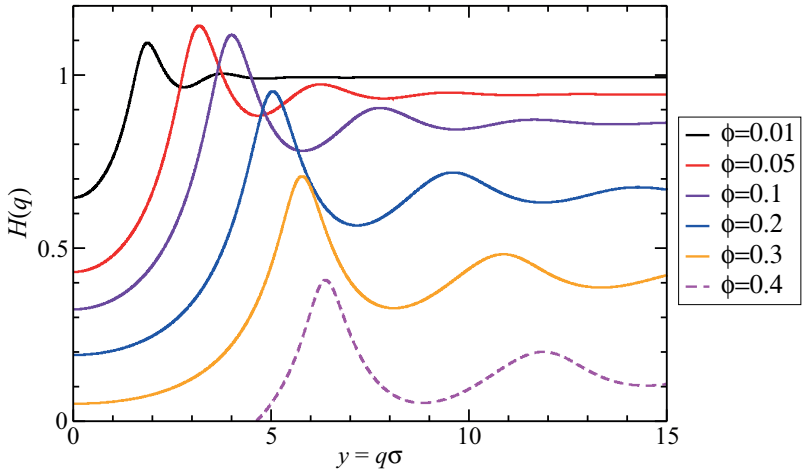

Fig. 6.10.: Hydrodynamic function of charged-silica sphere suspensions for the same parameters as for $S(q)$ and $g(r)$ presented in Figs. 6.9a and 6.9b.

ing effects which are of importance in more dense colloidal suspensions. Consequently, the PA scheme strongly underestimates d_S at large ϕ. For hard-sphere suspensions, the PA approximation is known to give accurate predictions for d_S up to $\phi \lesssim 0.15$ [178]. However, since in the UF model presented in the remainder of this section considerably lower ϕ values are considered the usage of the hybrid BM-PA scheme is appropriate.

Fig. 6.11 depicts the concentration dependence of $d_C = d_0 K/\chi_{OSM}$ for the silica particles system, calculated by the theoretical BM-PA method calculations. This result is compared with the corresponding result where the long-ranged colloidal HIs are disregarded, and with the d_C for neutral hard spheres. Both the sedimentation coefficient, K, and the osmotic compressibility factor, χ_{osm}, are monotonically decreasing with increasing ϕ. At small ϕ, the decrease of χ_{osm} outbalances that of K, owing to the strong electrostatic inter-particle repulsion, with the consequence that d_C rises steeply initially (see inset). At larger ϕ, the slowing influence of the HIs becomes stronger, with the effect that d_C passes through a maximum at $\phi \approx 0.003$, followed up by its moderate decline at larger ϕ values. When HIs are neglected so that $K = 1$, a monotonically increasing d_C is predicted instead in the considered concentration range. The key point to notice from Fig. 6.11 is that owing to the strong electrostatic repulsion between the silica particles, d_C is largely enhanced by one order in magnitude relative to the collective diffusion coefficient of neutral hard spheres. The hard-sphere results for d_C with HIs included shown in the figure as the dashed-dotted

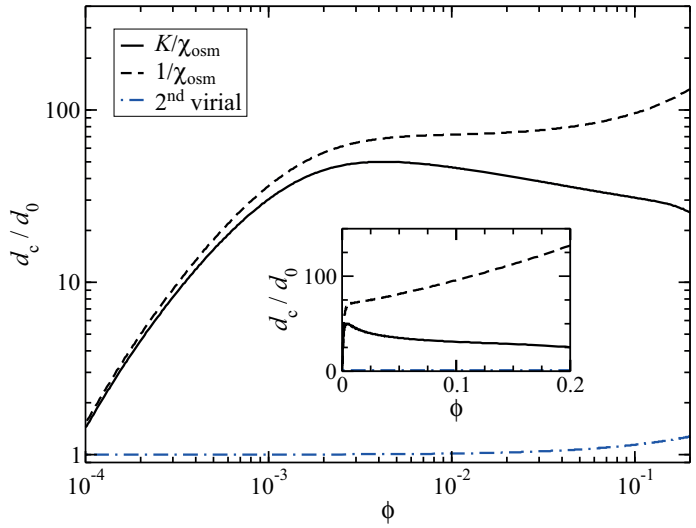

Fig. 6.11.: Reduced collective diffusion coefficient, $d_C(\phi)/d_0$, as a function of ϕ, for same system parameters as in Fig. 6.6. Solid line: Charged-silica suspension, with $K = H(0)$ calculated using the BM-PA method with HNC input for $S(q)$ and $g(r)$, and χ_T calculated using Eq. (6.22). Dashed line: Hypothetical silica suspension without HIs for which $K = 1$. Dashed-dotted line: Second-order virial expansion result for neutral hard spheres.

line has been generated using the second-order virial expansion expression [46, 136, 219],

$$d_c(\phi)/d_0 = 1 + 1.454\phi - 0.45\phi^2\,, \tag{6.24}$$

which is in good agreement with simulation data even up to $\phi = 0.494$ where a non-sheared hard-sphere suspension starts to solidify (see, eg., [39]).
Note that the electrokinetic reduction of d_C, arising from the non-instantaneous relaxation of the microion clouds surrounding each colloidal macroion, is not accounted for in the BM-PA method based on the OCM. This reduction can be estimated using the PM-based coupled-mode theory [220], showing that it is negligibly small owing to the large silica-microion size asymmetry.

6.2.7. PA-MCT results for the zero-frequency viscosity

The second important transport property input to the filtration model is the concentration-dependent effective suspension viscosity, $\eta(\phi)$, discussed in Subsec. 4.3.2 and presented in Eq. (4.61). Just like $d_C(\phi)$, it depends additionally on salinity and colloidal sur-

face charges. In suspensions of strongly correlated particles such as the present silica system, the long-time zero-shear viscosity η is significantly larger than the short-time high-frequency viscosity η_∞. This distinguishes the viscosity from the collective diffusion coefficient since for the latter the difference between short- and long-time forms stays very small.

Shear-thinning effects can be neglected under UF conditions where the shear Péclet-number is small. Moreover, since for moderate salinity near-contact configurations of three or more silica spheres are unlikely, we can use the PA method for calculating the low-shear η_∞.

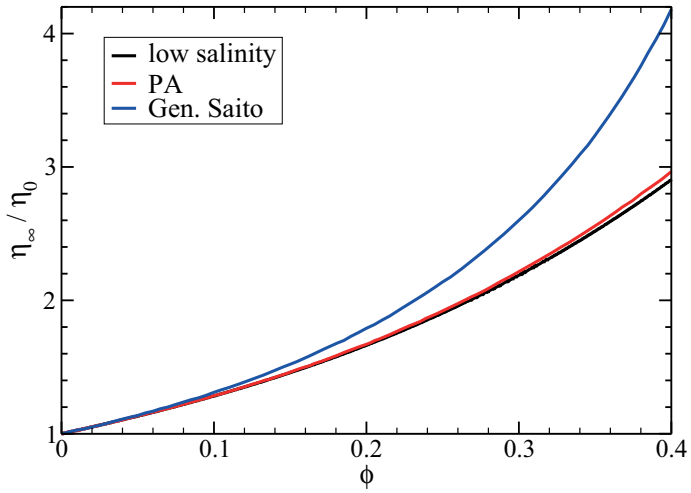

Fig. 6.12.: Comparison of the reduced high-frequency viscosity, η_∞/η_0, in PA approximation of charged-silica spheres with parameters presented in Fig. 6.6 (red solid line) with the low-salinity polynomial prediction presented in Eq. (6.25) (black) [136], and the Saito formula expression for impermeable HS in Eq. (5.10) (blue).

In Fig. 6.12, we show that up to $\phi \leq 0.3$, the PA result for η_∞ of the silica system is quantitatively described by the polynomial

$$\frac{\eta_\infty}{\eta_0} = 1 + \frac{5}{2}\phi\,(1+\phi) + 7.9\phi^3\,. \tag{6.25}$$

We emphasize that this polynomial is not a truncated virial expansion expression. It has been derived in [136] on basis of the PA method and additional simplifications justifiable for low-salinity systems, and it is shown therein to be in good agreement with elaborate hydrodynamic simulation viscosity results. Note that η_∞ of charged-silica particles is somewhat smaller than that of uncharged hard spheres at the same concentration, owing

to the smaller likelihood of near-contact configurations in the former case (c.f. Fig. 5.13). For the calculation of the zero-frequency viscosity, η, we use the first iteration solution in Eq. (4.79) of the one-component MCT expression for $\Delta\eta_{\mathrm{MCT}}$ (Eq. (4.78)) discussed in Subsec. 4.4.4. The first iteration expression can be used since we restrict ourselves to concentration values $\phi < 0.2$ where $S(q_m)$ is distinctly smaller than the Hansen-Verlet freezing criterion value of 3. The effect of HIs is incorporated in Eq. (4.79) only through the hydrodynamic function $H(q)$. As shown in [179], HIs modify also the static vertex functions in the MCT expression for $\Delta\eta$. This modification is disregarded here since its effect can be expected to be small for the range of smaller concentration values encountered inside the CP layer of the studied UF experiments (see below).

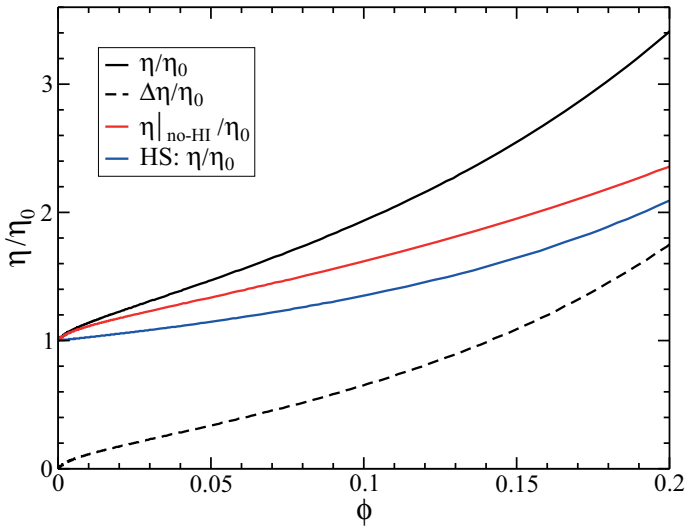

Fig. 6.13.: Theoretical predictions of the concentration-dependent reduced steady-shear viscosity, $\eta(\phi)/\eta_0$, of charged-silica spheres (solid black line), in comparison with the corresponding viscosity of neutral hard spheres (HS, solid blue line). Additionally shown are the shear-relaxation viscosity contribution, $\Delta\eta$, of silica spheres (dashed black line), and the steady-shear viscosity obtained for the HIs disregarded (solid red line). System parameters of the silica system are as in Fig. 6.6.

The result for the steady-shear viscosity of our silica system as a function of ϕ is included in Fig. 6.13. The high-frequency part, η_∞, of the viscosity has been calculated using Eq. (6.25), and the shear-relaxation part is obtained using Eq. (4.79). Regarding the $\Delta\eta$ part, we employ as input the BM-PA $H(y)$ presented in Fig. (6.10), and the HNC $S(y)$ (Fig. 6.9a) based on the OCM potential with the PB cell model result for Z_{eff} and κ_{eff}.

For $\phi = 0.2$, η is enlarged relative to the solvent viscosity η_0 by a factor of 3.4, while the high-frequency viscosity is raised by a factor of 1.7 only. Notice here that $\Delta\eta(\phi = 0) = 0$. To see the influence of the HIs, in Fig. 6.13 we additionally show the steady-shear viscosity result without HIs, where η_∞ is equal to the Einstein expression $\eta_\infty/\eta_0 = 1 + 2.5\phi$ for no-slip spheres, and $H(y)$ is identical to one in Eq. (4.79). For $\phi \gtrsim 0.1$, HIs significantly enhance the steady-shear viscosity of the silica suspension. Additionally shown is the viscosity of hard spheres, which we have calculated using the accurate scaling expression discussed in detail in Subsec. 5.4.2 (see Eqs. (5.22)-(5.24)). Different from charged-silica particles, the $\Delta\eta$ for neutral hard spheres is for $\phi < 0.2$ small compared to η_∞.

Note that we are dealing here with the demanding case of low-salinity systems with extended electric double layers and long-ranged electric repulsion. Electrokinetic viscosity effects are not considered here, for these are secondary effects expected to become smaller with increasing concentration. For higher-salinity systems with thin electric double layers, a simple thermodynamic perturbation theory approach becomes useful where the viscosity calculation can be mapped to that for an effective hard-sphere system (see, e.g., [221]).

In closing the discussion on transport coefficient calculations, we note that the PB cell model is used here only for deriving the effective charge and screening length but not for a direct calculation of transport coefficients. Thus, different from a pure cell model approach such as the one by Jönsson and Jönsson [222], particle correlations are accounted for. In the work by Jönsson and Jönsson [222], the collective friction coefficient defined by $f_c = k_B T/d_C$ and hence d_C have been estimated on assuming the approximate validity of the GSE relation, $d_C/d_0 \approx \eta/\eta_0$, between d_C and η, by using a spherical cell model viscosity expression. This approach is flawed for various reasons. First, it has been shown both in theory and simulations, and in experiments on BSA protein solutions [86] that the aforementioned GSE between d_C and η is invalid unless the concentration is very small. And indeed, according to Fig. 6.11, the d_C of a lower-salinity system has a non-monotonic concentration dependence, whereas η and η_∞ are monotonically increasing with increasing concentration. The so-called Kholodenko-Douglas GSE relation between d_C and η involving in addition the osmotic compressibility factor $S(0)$ (short-time counterpart in Eq. (8.5)), is likewise invalid for low-salinity systems, albeit it holds decently well for hard spheres (see [86] for details).

Second, a comparison with simulation results revealed that cell model predictions for η and K are in general not reliable, giving poor predictions in particular for smaller concentrations [39]. Moreover, owing to the neglected inter-particle correlations, the viscosity obtained from the standard PB cell model scheme should be more adequately identified with η_∞ rather than η. As seen in Fig. 6.13, the latter is distinctly larger for a low-salinity

system than the first one.

6.2.8. UF experimental details

The inside-out cross-flow ultrafiltration measurements have been performed using an OSMO Inspector device from Con-vergence. In this device, the silica suspension is steadily pumped, at constant temperature $T = 303\,\mathrm{K}$, through a membrane module containing 10 hollow cylindrical fiber membranes in parallel mode. The fiber membranes are HFs PES (polyethersulfon, negatively charged) with a nominal mean pore size of 10 nm. The fibers have a mean length $L = 40\,\mathrm{cm}$ and an inner diameter $2R = 0.8\,\mathrm{mm}$, with a total area $A_{\mathrm{membr}} = 2\pi RL = 0.01\,\mathrm{m}^2$ of the membrane module.
The OSMO Inspector allows to set the feed and retentate (outlet) mass fluxes Q_{feed} and Q_{ret}, respectively. The permeate flux follows from mass conservation as $Q_{\mathrm{perm}} = Q_{\mathrm{feed}} - Q_{\mathrm{ret}}$. Moreover, the mechanical (i.e. non-osmotic) pressure values at the feed, retentate and permeate positions are measured. From these values, the fiber-length-averaged transmembrane pressure, Δp_{TMP}, is calculated using

$$\Delta p_{\mathrm{TMP}} = \frac{P_{\mathrm{feed}} + P_{\mathrm{ret}}}{2} - P_{\mathrm{perm}}\,, \tag{6.26}$$

wherein a linear axial pressure drop from inlet to outlet is assumed for constant permeate pressure. Using a linear pressure profile is an approximation sufficient for the present analysis. The form of the lumen-side axial pressure decline is actually more complicated, as discussed by Mondor and Moresoli on basis of the momentum and continuity equation combined with Darcy's law [223, 224].
In the UF experiments, the feed flux was kept constant at $Q_{\mathrm{feed}} = 600\,\mathrm{g/h}$, while the retentate flux was stepwise decreased. Accordingly, the permeate flux increased stepwise from $Q_{\mathrm{perm}} = 100 - 500\,\mathrm{g/h}$. The fiber-length-averaged permeate velocity is obtained using

$$\langle v_w \rangle = Q_{\mathrm{perm}} / \rho_{\mathrm{m}}\, A_{\mathrm{mem}}\,, \tag{6.27}$$

with the suspension mass density $\rho_{\mathrm{m}} = 1000\,\mathrm{g/liters}$ taken to be constant. The selected process parameters lead to permeate velocities in the range $\langle v_w \rangle = 10 - 50\,\mathrm{LMH}$ (liters/m^2/h), i.e. $2.8 - 13.9\,\mu\mathrm{m/s}$.
The pure water permeability, L_p^0, of the membrane was measured before and after the silica UF experiment. This measurement was done in constant flux mode, with $v_w^0 = 50\,\mathrm{LMH} = 13.9\,\mu\mathrm{m/s}$, and Δp_{TMP} obtained from inserting the associated measured pressure values

into Eq. (6.26). The permeability follows then from Darcy's law,

$$L_p^0 = \frac{u_w^0}{\Delta p_{\mathrm{TMP}}}\,, \tag{6.28}$$

without osmotic pressure contribution since pure water is used as feed. In this way, the value $L_p^0 \approx 155\,\mathrm{LMH/bar} = 4.3 \times 10^{-10}\,\mathrm{m/Pa \cdot s}$ is obtained which is used in our UF model calculations of the permeate flux and CP layer profiles discussed in the following subsection.

6.2.9. Theoretical results

We present here our theoretical results for cross-flow UF of low-salinity charge-stabilized suspensions based on the boundary layer filtration model, with input for Π, χ_{T}, $d_{\mathrm{c}}(\phi)$, and $\eta(\phi)$ as described in Subsecs. 6.2.3 - 6.2.7. The selected system parameters are those characterizing the OSMO Inspector cross-flow UF setup, and the employed low-salinity aqueous silica suspensions for $T = 303$ K. For explicit values of the operating parameters we refer to [225]. The feed volume fraction $\phi_0 = 1.0 \times 10^{-3}$ is large enough for Eqs. (6.20) and (6.22) describing the osmotic pressure and compressibility in the counterion-dominated regime to apply. Moreover, $Pe \ll 1$ so that shear-induced hydrodynamic diffusion is negligible in comparison to thermal diffusion [226]. Since $R \ll L$, the boundary-layer description condition $u_m \gg v_w^0$, and with $Re_{\mathrm{R}} \sim 10$ also the Rayleigh number condition of laminar pipe flow, are fulfilled. We have checked that the (effective) Debye length is much smaller than the (typical) thickness of the CP layer. Furthermore, the UF condition of local thermodynamic equilibrium is fulfilled.

The CP layer profile and the permeate velocity are calculated using the boundary layer method described in Subsec. 6.2.1, with d_{C}, η, and Π as input. We will see in the following that for our operating conditions, membrane fouling due to a cake layer of jammed particles is avoided.

Fig. 6.14(a) and (b) depict the calculated CP concentration profile, $\phi_w(x)$, and permeate velocity profile, $v_w(x)$, at the membrane surface in their dependence on the reduced axial distance, x/L, from the fiber inlet. The solid curves are the results for the low-salinity silica suspension, while the dashed curves in the inset describe neutral hard spheres. Note that for the electrically repelling silica particles, $\phi_w(x)$ increases only slightly above the feed concentration ϕ_0 with increasing distance x. This can be attributed to the large values of the collective diffusion coefficient $d_{\mathrm{C}}(\phi)$ of charge-stabilized particles even for small ϕ (see Fig. 6.11), causing particles flow-advected towards the membrane surface to be strongly

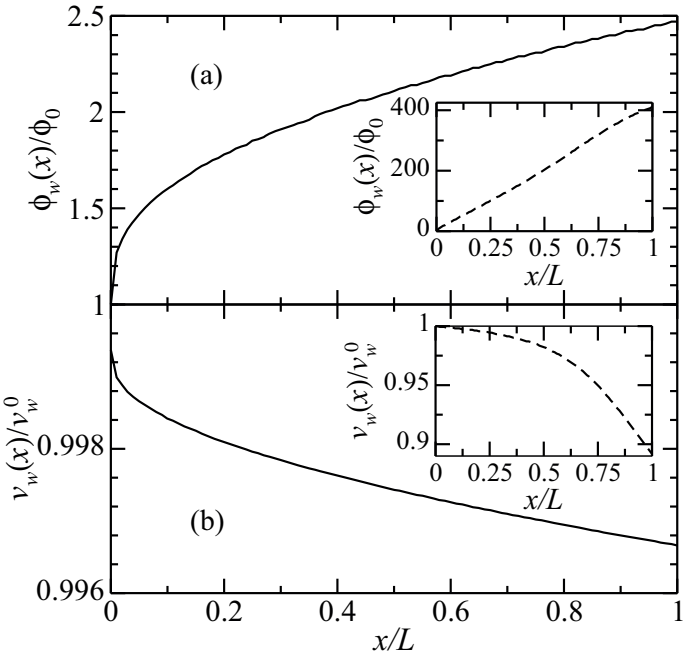

Fig. 6.14.: (a) Calculated membrane surface volume fraction profile, $\phi_w(x)$, scaled by the feed volume fraction ϕ_0, and (b) permeate velocity profile, $v_w(x)$, scaled by the pure solvent velocity, v_w^0, for the charge-stabilized low-salinity silica suspension (solid lines). Insets: same as in main figure, but for hard spheres (dashed lines). System parameters: $\Delta p_{\mathrm{TMP}} = 0.08\,\mathrm{bar}$, $\dot{\gamma} = 332\,\mathrm{s}^{-1}$, $a = 15\,\mathrm{nm}$, $\phi_0 = 10^{-3}$, $L_p^0 = 4.3 \times 10^{-10}$ m/Pa · s.

driven away by diffusion. In Fig. 6.14(b), the permeate velocity, $v_w(x)$, of the silica system decreases only slightly with increasing x: With increasing axial distance from the inlet, ϕ_w and hence $\Pi(\phi_w) \approx P_{\mathrm{micro}} - P_{\mathrm{res}}$ (see Fig. 6.7) are only mildly enhanced so that according to Eq. (6.5), $v_w(x)$ is only slightly lowered below its clear solvent value $v_w^0 = L_p^0\,\Delta p_{\mathrm{TMP}}$ at given TMP. This should be contrasted with the theoretical UF predictions for hard spheres at unchanged operating conditions (see insets of Figs. 6.14(a) and (b)) where ϕ_w is enhanced, and v_w lowered, by two orders of magnitude. This marked difference can be attributed to the, for hard spheres, significantly smaller collective diffusion coefficient giving rise to a significant enrichment of particles at the membrane wall with osmotic pressure and viscosity values much larger than those of the silica system.

It is instructing to quantify the effects on the CP layer and permeate flux induced by individually replacing $\Pi(\phi)$, $d_{\mathrm{C}}(\phi)$, and η of the charged-silica particles (CS) by those of neutral HS. This quantification is made in Figs. 6.15(a) and (b). The black curves marked

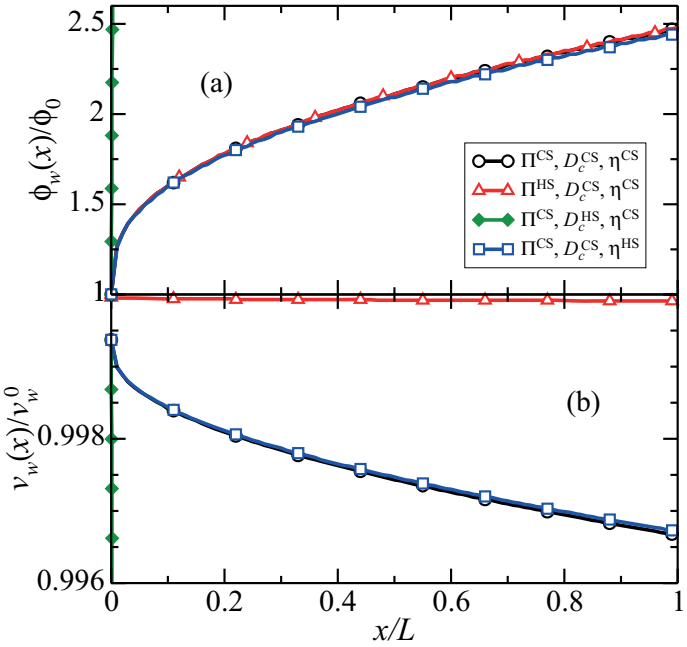

Fig. 6.15.: (a) Surface particles volume fraction profile, $\phi_w(x)$ scaled by the feed volume fraction, ϕ_0, and (b) permeate velocity profile, $v_w(x)$, scaled by the pure solvent velocity, v_w^0. The solid black lines marked with ∘ are results for low-salinity silica suspensions. Red lines marked with △ are results using osmotic pressure, Π^{HS}, for hard spheres, and collective diffusion coefficient d_C^{CS}, and viscosity, η^{CS}, for charged spheres. Green lines marked with ◊ are obtained using collective diffusion coefficient for hard spheres, and osmotic pressure and viscosity for charged spheres. Blue lines marked with □ are obtained using viscosity for hard spheres, and osmotic pressure and collective diffusion coefficient for charged spheres. System parameters as in Fig. 6.13.

by ∘ are the results for $\phi_w(x)$ and $v_w(x)$ of the silica system shown before in Fig. 6.14. If in the UF calculations the Carnahan-Starling osmotic pressure for hard spheres is used (Eq. (3.35)) in place of the charged-particles pressure, the red curves marked with △ are obtained. While the CP profile at the membrane remains practically the same, the permeate velocity is now larger and practically equal to v_w^0, owing to $\Pi^{HS}(\phi) < \Pi^{CS}(\phi)$ (see Fig. 6.7 and Eq. 6.5). If the osmotic pressure and effective viscosity remain those of the silica system but the collective diffusion coefficient of hard spheres is used instead, the green curves marked with ◊ are obtained for $\phi_w(x)$ and $v_w(x)$. The CP profile (permeate velocity) is now much larger (smaller) than the ones of the silica system, with values comparatively close to those for the hard-sphere system. This behavior is explained by

noting $d_C^{HS}(\phi) \ll d_C^{CS}(\phi)$ (see Fig. 6.11) leading to a strongly reduced transverse diffusion flux of particles away from the membrane surface, and hence to an enhanced CP layer. Finally, if the osmotic pressure and collective diffusion coefficient of the silica spheres is used in combination with the viscosity of hard spheres (blue curve marked with □), $\phi_w(x)$ and $v_w(x)$ remain practically equal to the profiles of the original silica system. Thus, the UF performance for the investigated low-salinity suspensions is rather insensitive to changes in the CP layer viscosity.

6.2.10. Comparison with experiment

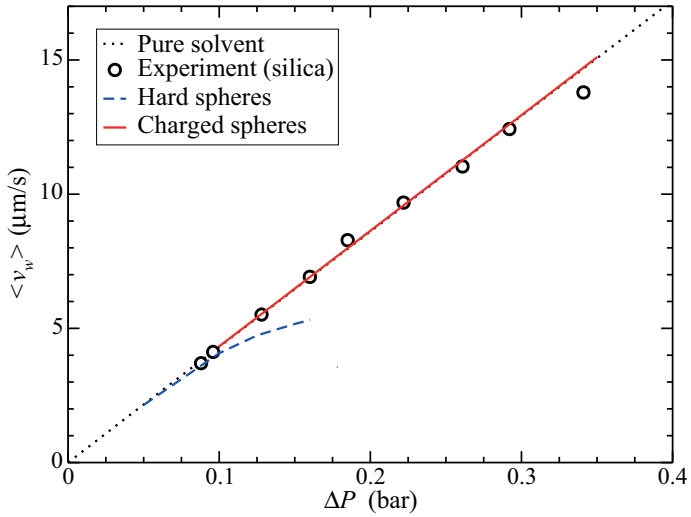

Fig. 6.16.: Fiber-length-averaged permeate velocity, $\langle v_w \rangle$, as function of transmembrane pressure Δp_{TMP}. Comparison of our theoretical model predictions for aqueous charged-silica particles suspensions (red solid line) with the experimental UF results (open circles). Dashed blue line: theoretical prediction for (non-permeable) hard spheres. The black dotted curve is the result for pure water where $\langle v_w \rangle = L_p^0 \Delta p_{TMP}$. System parameters as in Fig. 6.6.

The UF model results are compared here with the outcome of our silica suspension UF measurements described in Subsec. 6.2.8.

In Fig. 6.16, the fiber-length-averaged permeate velocity, $\langle v_w \rangle$, is plotted as function of Δp_{TMP}, with the TMP determined using Eq. (6.26) from the measured pressure values at the feed, retentate and permeate points. The dotted black curve is the pure water filtration result, $\langle v_w \rangle = L_p^0 \, \Delta p_{TMP}$, where $L_p^0 = 155$ LMH/bar (cf. Subsec. 6.2.8). The open circles are the experimental findings obtained using Eq. (6.27). From the theoretical

predictions for $v_w(x)$, $\langle v_w \rangle$ is calculated using its definition,

$$\langle v_w \rangle = \frac{1}{L} \int_0^L v_w(x) dx \,. \tag{6.29}$$

The dashed blue curve is the theoretical result for no-slip hard spheres. The influence of the for hard spheres well developed CP layer becomes visible at $\Delta p_{\mathrm{TMP}} > 0.1$ bar where $\langle v_w \rangle$ is reduced below the pure water feed straight line. The hard-sphere curve of $\langle v_w \rangle$ is truncated above $\Delta p_{\mathrm{TMP}} \approx 0.17$ where the random closed packing membrane surface concentration $\phi_w = 0.64$ is reached, and an amorphous cake layer of jammed particles is formed. In this thesis, cake layer formation and other membrane fouling mechanisms are not discussed theoretically. For charge-stabilized particles and charged membranes, this requires an elaborate modeling outside the scope of the present work. The solid red curve is the theoretical prediction for the charged-silica particles, obtained by the theoretical methods described in Subsec. 6.2.1.

In Fig. 6.16, full agreement is observed between the experimental $\langle v_w \rangle$ and the theoretical prediction for the silica system, except for the data point at the largest experimentally considered TMP. The experimental and theoretical data points are close to the pure solvent curve, showing that the osmotic pressure influence is insignificant for the UF of low-salinity suspensions. While this finding is surprising on first sight, it has been shown in Subsec. 6.2.9 that the strong transversal diffusion flux pointing away from the membrane surface causes the CP layer to be only weakly developed. The reason why the experimental data point at the largest TMP is below the theoretical straight line is definitely not a cake formation by crystallization or vitrification. This fouling mechanism is ruled out since the concentration values along the membrane surface (cf. Fig. 6.14) are way too small for the structure factor peak height, $S(q_m; \phi_w)$, to reach the Hansen-Verlet freezing value 3 of low-salinity charge-stabilized systems (see again Fig. 6.8 and [212]). The straight line deviation of the last data point may be due instead to some preferential adsorption of silica particles at the membrane. The fouling is mechanically reversible, since the same value of L_p^0 is measured after the silica filtration experiment followed by a backwashing cycle. The high-TMP data point can be accounted for in Eq. (6.5) by adding the fouling resistance, R_{foul}, to the membrane resistance according to

$$L_p = \frac{1}{\eta_0 (R_{\mathrm{mem}} + R_{\mathrm{foul}})} \,. \tag{6.30}$$

Different from the silica system, the osmotic membrane wall pressure, $\Pi(\phi_w)$, of the reference hard-sphere system is an important contribution to Darcy's law in Eq. (6.5), lowering

the permeate velocity well below the pure solvent values.

7. Zwitterionic microgels

In this chapter, we present work in collaboration with A. J. Schmid, T. Eckert and W. Richtering from RWTH Aachen University regarding the characterization of the direct interactions in amphoteric microgel suspensions. As discussed already in Sec. 2.4, amphoteric microgels containing both acidic and basic co-monomers swell in acidic and basic environments, and collapse in the so-called zwitterionic regime of intermediate pH values. We systematically vary here the amount of zwitterions inside the microgel particles, and compare the resulting concentration series of measured static structure factors to polydisperse hard-sphere calculations, identifying hereby the influence of the zwitterion on the particle interactions.

7.1. Sample preparation

A series of zwitterionic microgels with increasing amount of the zwitterionic co-monomer sulfobetaine is synthesized. A pure PNIPAM system is serving as a reference (sample N0). In the other systems (N1-N3), the amount of sulfobetaine was increased up to about $\sim 3\,\mathrm{mol\%}$ in the monomer feed (N1: $0.9\,\mathrm{mol\%}$, N2: $1.9\,\mathrm{mol\%}$, and N3: $2.8\,\mathrm{mol\%}$). In addition, the cross-linking ratio of $1:20$, which is the molar ratio of cross-linker to monomer, is kept constant to achieve a similar volume swelling ratio, S, for all samples. The surfactant SDS is used to stabilize the particle surface during the synthesis, and to produce small particles, which can be analysed by small angle neutron scattering techniques. For more details about the monomer feeds of the microgels, see [227]. Detailed information about the physicochemical properties of the invesitaged zwitterionic microgels in dilute solution, and the role of sulfobetaine during their synthesis in the presence of SDS, are published by our experimental coworkers in [29].

7.2. Measured structure functions including polydispersity

In a first set of experiments, the angular dependent scattering intensity, $I(q)$, is measured in the dilute regime for all samples in D_2O, well below the volume phase transition temperature (VPTT) (Fig. 7.1). The zwitterionic microgels samples are measured at $20°C$, and the pure PNIPAM samples (N0) at $24°C \pm 2°C$. The scattering curves are fitted according to the form factor model of Stieger *et al.* [120] (c.f. Eq. (2.19)). These fits describe the data very well over the entire q-range. The slight deviations in the large-q

region can be due to small errors in the treatment of incoherent scattering. The important fit parameters are summarized in Table 7.1. The mean excluded-volume radius. $\overline{R}_{\mathrm{HC}}$, is calculated from these fitting parameters using Eq. (2.20).

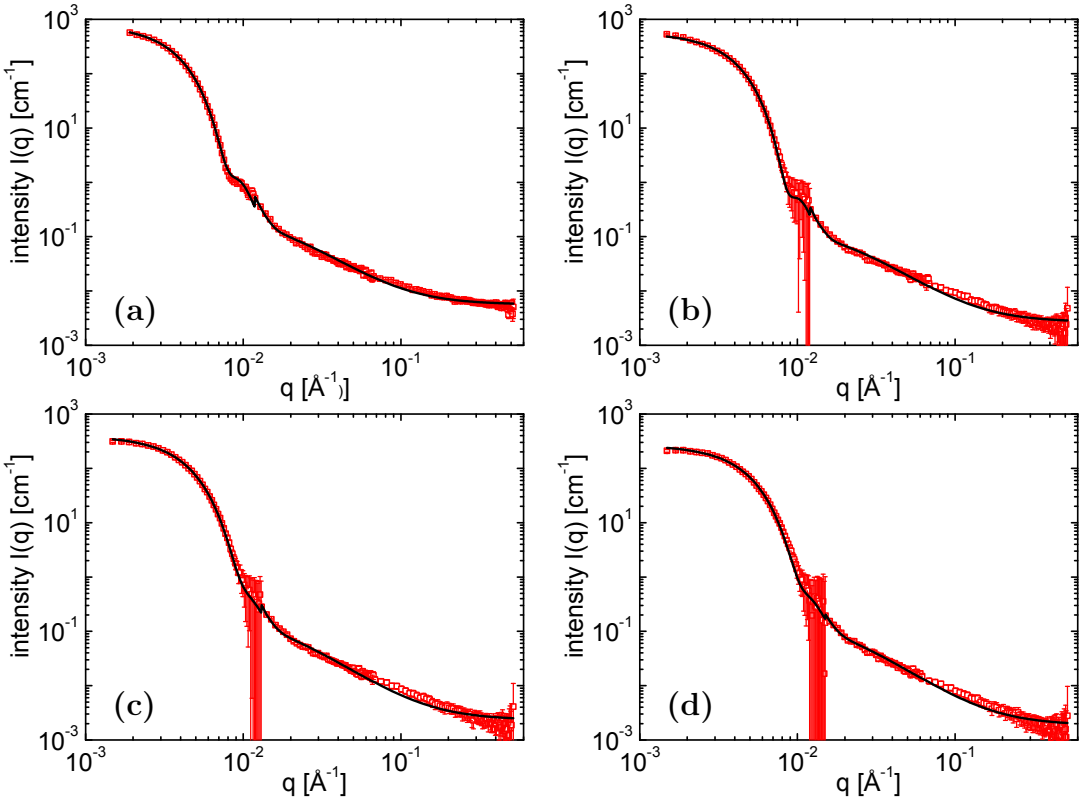

Fig. 7.1.: SANS scattering curves of samples (a) N0, (b) N1, (c) N2, and (d) N3 in D_2O at $20°C$ (sample N0 was measured at $24°C \pm 2°C$). The concentration is about 0.2 wt%. Solid lines represent fits according to the form factor model of Stieger *et al.* [120] given in Eq. (2.19). Large error bars in the intermediate q-range are due to the low signal statistics at the border of the detector.

In the second set of SANS experiments, for all samples a series of $I(q)$ measurements with increasing particle mass fraction in the range of 1 wt% to 6 wt% in heavy water are performed. In Fig. 7.2, we present the comparison of the experimental $S_{\mathrm{M}}(q)$ inferred from the corresponding normalized scattering curves using Eq. (3.46), and our theoretical predictions calculated using the polydisperse hard-sphere model with parameters presented in Table 7.1. In the theoretical calculations, the total volume fraction, ϕ_{T}, in Eq. (3.52) is the only fit parameter. As discussed in detail in Sec. 3.5, instead of a fully polydisperse description we use the decoupling approximation approach in conjunction with the Verlet-Weis approximation for the structure factor of monodisperse hard spheres.

sample	$\overline{R}$ [nm]	σ_{surf} [nm]	s_{R} [%]	$\overline{R}_{\text{HC}}$ [nm]	$\overline{R}_{\text{h}}$ [nm]	$\overline{R}_{\text{HC}}/\overline{R}_{\text{h}}$
N0	54.2	13.1	13.5	80.4	92	0.874
N1	50.7	14.1	10.5	78.9	90	0.877
N2	42.6	12.7	17.5	68.0	81	0.840
N3	39.9	10.3	17.0	60.5	78	0.776

Table 7.1.: Parameters obtained from the theoretical form factor fit of the SANS scattering curves for samples N0 - N4 in D_2O in the dilute regime using the form factor model of Stieger *et al.* [120] given in Eq. (2.19). Samples N1 - N3 were measured at $20°C$ while sample N0 was measured at $24°C \pm 2°C$. Note that $\overline{R}_{\text{HC}} = \overline{R} + 2\sigma_{\text{surf}}$. For completeness, also values for the effective hydrodynamic radius R_{h} determined by low-q DLS are presented [227]. (The hydrodynamic radius of sample N0 was measured in D_2O at $24°C$.)

The peak position q_{m}, of $S_{\text{M}}(q)$ is shifted to larger q-values with increasing concentration, for all considered samples. This is indicative of a lowering inter-particle distance with increasing ϕ_{T}.

For values $\phi_{\text{T}} \lesssim 0.4$, the theoretical fits based on the (poly-disperse) hard-sphere model describe the experimental structure factor data quite well for all samples. At larger volume fractions $\phi_{\text{T}} > 0.4$, theoretical and experimental data deviate significantly from each other for all considered samples. The experimental principal peak position, q_{m}, of $S_{\text{M}}(q)$ attains larger q-values than that of the theoretical prediction indicating a smaller center-to-center distance in the experimental system. The pure PNIPAM based microgels can achieve this either by deswelling with associated lowering of the particle size, or by particle overlapping. The latter mechanism appears reasonable at high volume fractions owing to the inhomogeneous structure and lower polymer density on the particle surfaces. The former mechanism leads to a visible change in the scattering curve, in particular regarding the locations of the local minima. It should be noticed here that the form of $I(q)$ at high concentrations is changed not only through the changing form factor, but also through the changing $S_{\text{M}}(q)$.

The temperature responsiveness, and by this the particle sizes of PNIPAM microgels in aqueous solution, are altered by the solvent quality. The solvent quality is determined by the strength of the hydrogen bonds between water molecules and NIPAM. These should not depend on the particle concentration, which renders a shrinking of the particles as rather unlikely. Contrast variation experiments of a mixture of deuterated and protonated PNIPAM microgels can provide information on the particle form factor in concentrated solutions, and on the particle shrinking or overlapping. This will be the topic of future investigation.

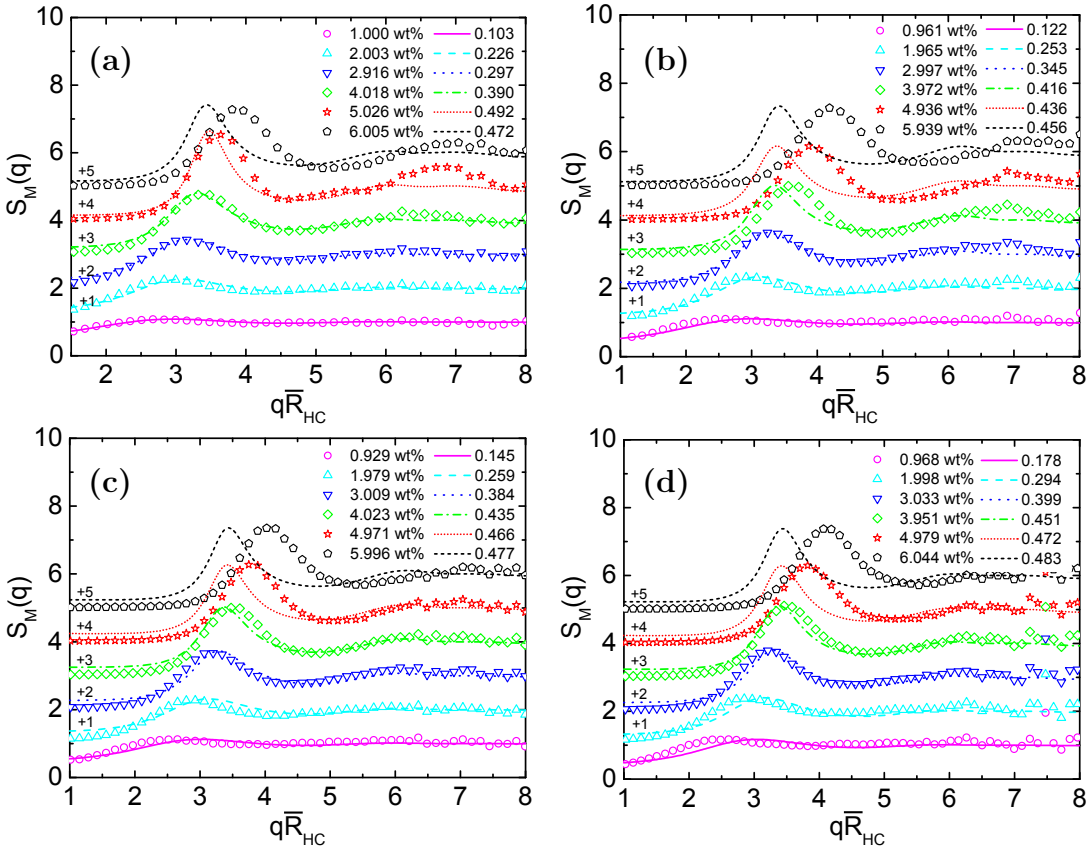

Fig. 7.2.: Open symbols: SANS measurable static structure factor, $S_{\mathrm{M}}(q)$, of microgel samples (a) N0, (b) N1, (c) N2, and (d) N3 in D_2O at $20°C$ (sample N0 was measured at $24°C \pm 2°C$) at various concentrations as indicated. The lines are theoretical structure factors based on the decoupling approximation combined with the PY-VW hard-sphere solution for $S_{\mathrm{id}}(q)$. In the legend, the total volume fraction ϕ_{T} resulting from the theoretical fit is given.

There is no visible influence of the zwitterionic comonomer, since the hard-sphere model structure factors describe all scattering data equally well for the four considered systems. We conclude thus that at low ϕ_{T}, the hard-sphere potential suitably describes the (effective) pair interactions between pure PNIPAM (N0) microgels, and between the zwitterionic microgels (N1-N3). It is also noticeable for all samples that $S_{\mathrm{M}}(q \to 0)$ decreases monotonically with increasing ϕ_{T}. A significant increase of $S_{\mathrm{M}}(q)$ in the low-q regime with increasing ϕ_{T} is an indicator for the existence of (effective) attractive forces between the particles. For an example relevant in this context, Baxter [228] uses an attractive surface adhesion potential in addition to the hard-sphere potential, leading to a $S_{\mathrm{M}}(q)$ which increases with concentration in the low-q regime.

On first sight, one might expect an attractive contribution to the pair potential due to the incorporation of the zwitterionic comonomer. However, the purely repulsive hard-sphere potential is sufficient to describe the $S_{\mathrm{M}}(q \to 0)$ of the zwitterionic microgels even up to $\phi_{\mathrm{T}} \approx 0.4$. At very high volume fractions, however, when the microgels can overlap, the experimental data show no evidence for attractive forces between the zwitterionic microgels. This absence of attraction can be due to two possible mechanisms: Firstly, the rather low amount of incorporated charges is not sufficient to cause attraction. Secondly, the formation of internal salt between the sulfonate headgroup and the quaternary ammonium group of sulfobetaine is more favourable than intermolecular salt formation.

8. Systems with short-range attraction and long-range repulsion

8.1. Two-Yukawa SALR systems

We investigate here in detail the influence of the strength and range of competing short-range attractive and long-range repulsive interactions between globular particles such as proteins, on the dispersion structure and dynamics. Our focus is on the two-Yukawa potential model in the fluid phase state where only transient particle clusters occur.

8.1.1. Parameter models

We employ the two-Yukawa SALR potential (see Eq. (2.9)) introduced in Subsec. 2.3.2. The investigation of the effects of the individual potential contributions necessitates a systematic variation of the associated potential parameters. Due to the presence both of SA and LR potential contributions a variation of one parameter affects the total potential. For example, increasing the attraction strength K_1 alters not only the SA part, but results in the change of the effective attraction range, x_0, and the repulsive barrier height.
As discussed in Subsec. 2.3.2, K_1, and K_2 can be expressed as functions of the attraction and repulsion ranges z_1 and z_2, respectively, and of x_0. In the following, our way of selecting these three free parameters is discussed.
The second virial coefficient, B_2, is a global measure of the interaction strength. It is given by [107]

$$B_2 = 2\pi\sigma^3 \int_0^\infty \mathrm{d}x\, x^2 \left[1 - e^{-\beta V(x)}\right] , \tag{8.1}$$

with $x = r/\sigma$. For the two-Yukawa SALR potential, $V(x)$, the parameters are the interaction strength α, x_0, z_1, and z_2. In place of B_2, it is useful to consider instead the reduced second virial coefficient $B_2^* = B_2/B_2^{\mathrm{HS}}$, where $B_2^{\mathrm{HS}} = (2\pi/3)\sigma^3$ is the hard-sphere reference value. It has been found empirically that if the B_2^*'s of two pair potentials are close to each other at a given $T^* = 1/\alpha$, the $B_2^*(T^*)$ curves are close in the full fluid-phase temperature range (c.f. 8.1b) [91, 107].
Costa *et al.* [91] suggest a B_2^*-based procedure to select the potential parameters for a systematic variation of the potential features. On fixing the effective attraction range to $x_0 = 1.1$, they select three different z_1 values: In model M_1: $z_1 = 19$, in M_2: $z_1 = 13$, and in M_3: $z_2 = 10$. In addition, for model M_3 the repulsion range $z_2 = 0.5$ is selected. The

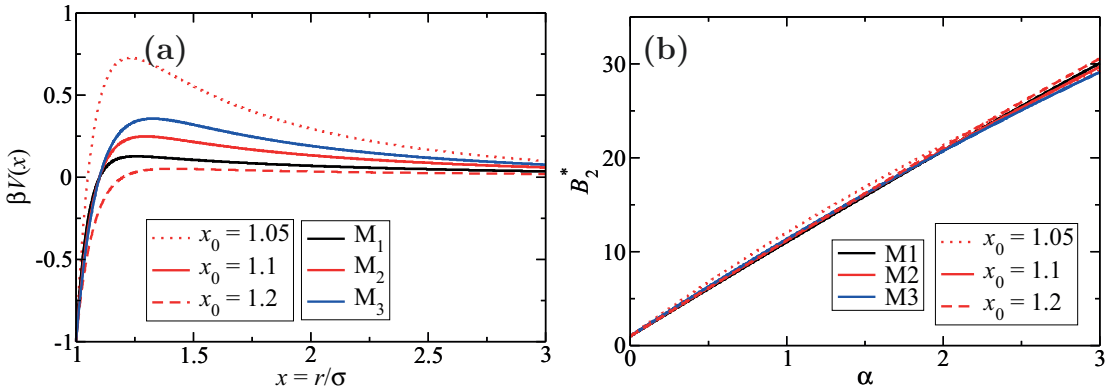

Fig. 8.1.: (a) The potential curves for models M_1 (black), M_2 (red), and M_3 (blue) with effective attraction range $x_0 = 1.1$ are shown as solid lines. The dotted line represents model M_2 for $x_0 = 1.05$, and the dashed line for $x_0 = 1.2$. (b) α dependence of the reduced second virial coefficient $B_2^*(\alpha)$ for the three models with x_0 values as indicated.

z_2 values of models M_1 and M_2 are then determined such that the equality of $B_2^*(\alpha)$ in the three models is enforced in the full fluid-phase temperature range, as shown in Fig. 8.1b. Note that $B_2^*(\alpha)$ increases from 1 at $\alpha = 0$ to 28 at $\alpha = 3$. Note further that with increasing α, the depth of the attractive well, and the height of the potential barrier, are both enlarged for fixed ratio, K_1/K_2, of the attractive and repulsive soft potential strengths. After the determination of z_1 and z_2 using Eqs. (2.11) and (2.12), all potential parameters are fixed. For $x_0 = 1.1$, the potential parameters of M_1, M_2, and M_3 are shown in Table 8.1.

Model	z_1	z_2	K_1	K_2	$x_{\max}$	$\beta V(x_{\max})/\alpha$
M_1	19	0.257	1.1813	0.1813	1.256	0.128
M_2	13	0.390	1.3954	0.3954	1.297	0.249
M_3	10	0.500	1.6306	0.6306	1.326	0.357

Table 8.1.: Two-Yukawa SALR potential parameters z_1, z_2, K_1 and K_2 for fixed interaction range $x_0 = 1.1$, as used by Costa *et al.* [91]. In addition, the reduced height of the first potential maximum, $\beta V(x_{\max})/\alpha$, and its position, $x_{\max}$, are presented.

The procedure of Costa *et al.* [91] has the advantage that for fixed x_0, the attractive parts, $\beta V(x < x_0)$, of the models M_1-M_3 are almost indistinguishable. However, since the equality of B_2^* is enforced, model M_1 having the smallest z_2 has the lowest repulsive barrier value, $V(x_{\max})$ (c.f Table 8.1).
Costa *et al.* [91] studied an effective interaction range of $x_0 = 1.1$ only, while here we

Model	z_1	z_2	K_1	K_2
$M_2(x_0 = 1.05)$	13	0.685	2.17503	1.17503
$M_2(x_0 = 1.1)$	13	0.390	1.3954	0.3954
$M_2(x_0 = 1.2)$	13	0.166	1.08317	0.08317

Table 8.2.: Potential parameters of model $M_2(x_0)$ for $x_0 = 1.05$, 1.1, and 1.2.

additionally consider $x_0 = 1.05$ and $x_0 = 1.2$. To this end, we use the z_1 value of potential model M_2, and determine z_2 such that the B_2^*'s of the new potentials for $x_0 = 1.05$ and $x_0 = 1.2$, respectively, agree with the B_2^*'s of M_1, M_2, M_3 for $x_0 = 1.1$ (c.f. Fig. 8.1b). We denote the potential parameter sets with $x_0 = 1.1$ by $M_1(x_0 = 1.1)$, $M_2(x_0 = 1.1)$ and $M_3(x_0 = 1.1)$. The potential parameter sets with $x_0 = 1.05$ and 1.2 will be denoted as $M_2(x_0 = 1.05)$ and $M_2(x_0 = 1.2)$, since they share the same z_1 value with $M_2(x_0 = 1.1)$. The parameters of the model M_2 are presented in Table 8.2. For decreasing x_0, $\beta V(x_{\max})$ increases and the repulsion range decreases as shown in Fig. 8.1a.

8.1.2. Gas-liquid critical temperature

As discussed in [31, 33, 98], the gas-liquid critical temperature, T_c^*, of an appropriately chosen short-range attractive reference system of the SALR system allows for accurate predictions of the phase behavior of the SALR system. To ensure that the investigated systems are all part of the dispersed-fluid phase (see Sec. 2.3), we calculate here T_c^* of reference attractive systems by employing the ELCS proposed by Noro and Frenkel [107]. This extended law states that the equation of state for systems with sufficiently short-ranged attractive interaction is solely dependent on three parameters: effective diameter, σ_{eff}, energy scale, ϵ, given typically by the depth of the attractive well, and reduced second virial coefficient, $B_2^* = B_2/((2/3)\pi\sigma_{\text{eff}}^3)$, where σ_{eff} is used in the calculation of B_2^{HS}. In particular, the mapping on a square-well potential system sharing the same σ_{eff}, ϵ, and B_2^* allows for the calculation of T_c^*. For the attractive reference potential, we use in our calculations the full SALR potential in Eq. (2.9), with the additional cutoff requirement that $\beta V(x \geq x_0) = 0$. We find that T_c^* for all considered models lies outside the temperature range discussed in this thesis, i.e. $T_c^* < 1/3$ and $\alpha_c > 3$. Thus, according to the T_c^* values, only fluid-like systems in the monomer-dominated regime are considered as intended. The values for T_c^* and the corresponding interaction parameter α_c are presented in Table 8.3. Note that the long-range repulsive potential part in the SALR system shifts the liquid-liquid phase transition line to lower temperatures [229].
In addition, we restrict our calculations to small concentrations $\phi \leq 0.15$ such that all

Model	$x_0 = 1.05$		$x_0 = 1.1$		$x_0 = 1.2$	
	T_c^*	α_c	T_c^*	α_c	T_c^*	α_c
M_1			0.291	3.431		
M_2	0.282	3.551	0.297	3.363	0.316	3.167
M_3			0.301	3.325		

Table 8.3.: Critical temperatures, T_c^*, of the attractive reference system for the SALR models $M_i(x_0)$ with $i \in \{1, 2, 3\}$, and potential cutoff at $x = x_0$.

considered systems are in the dispersed-fluid state where most particles diffuse individually. There still remains the tendency of clustering as noticed, e.g., by the presence of an IRO low-q peak in $S(q)$ that grows with increasing α and ϕ as the transition line to the equilibrium-cluster phase is approached.

Thus, when referring in the remainder of this work to clustering (clusters) we actually consider highly transient clusters in a fluid-phase system where the mean cluster size is 1-3 particles.

The transition line between the dispersed-fluid and equilibrium-cluster phases marks a microphase separation into clusters, owing to the suppression of macroscopic phase separation by the long-range repulsive part [33, 34, 230]. Combinations of density functional theory and perturbation theory approaches where the clusters are modeled for simplicity as spherical, suggest a first-order-like phase transition between the two thermodynamically stable phases, as characterized by the discontinuous jump of the cluster size above a critical colloidal particle density [88, 229].

8.1.3. Variation of attraction strength

Here, we discuss our theoretical results for a two-Yukawa SALR system of specific potential parameters $\{K_1, K_2, z_1, z_2\}$, and study structural and dynamical properties for different interaction strength α, and ϕ. As in Ref. [91], we employ model $M_3(x_0 = 1.1)$ with parameters $K_1 = 1.6306$, $K_2 = 1 - K_1 = 0.6306$, $z_1 = 10$ and $z_2 = 0.5$, characterized by SALR potential curves of constant effective attraction range $x_0 = 1.1$, but varying $\alpha > 0$, where $\beta V(x_{\max}) \approx 0.36\alpha$ at $x_{\max} \approx 1.33$, and $K_1/K_2 = 2.59$.

Static pair structure

Before presenting results for the short-time properties, we discuss first the behavior of the SALR static structure functions, $S(q)$ and $g(r)$, constituting the salient input to the dynamic calculations. We employ the thermodynamically self-consistent ZH integral

equation scheme [129] (c.f Subsec. 3.4.3) for calculating the static input which is well suited for pair potentials with an attractive soft pair potential part. For simplicity, the potential parameters $\{K_1, K_2, z_1, z_2, \alpha\}$ are held fixed in taking the concentration derivative of the virial pressure needed for the enforcement of thermodynamic self-consistency between the virial pressure and osmotic compressibility thermodynamic routes.

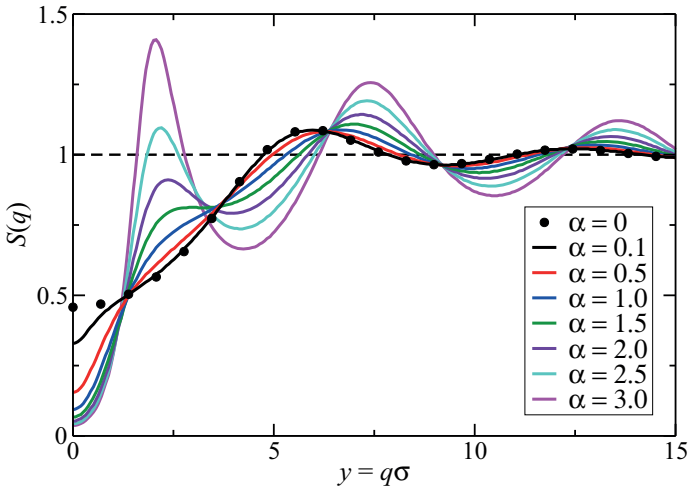

Fig. 8.2.: Zerah-Hansen (ZH) scheme results for the static structure factor, $S(q)$, of the two-Yukawa SALR system as a function of reduced wavenumber $y = q\sigma$, for $\phi = 0.1$ and various interaction parameter values α as indicated. The $S(q)$ of the hard-sphere reference system ($\alpha = 0$) is included for comparison (filled black circles).

Results for $S(q)$ obtained by the ZH scheme are shown in Fig. 8.2, for $\phi = 0.1$ and several values of α as indicated. With increasing α, the osmotic compressibility factor, $S(0)$, decreases monotonically. In contrast, the next-neighbor peak of individual particles of height, $S(q_m)$, decreases initially slightly for increasing α, taking its minimal value at $\alpha \approx 0.5$ with a subsequent monotonic increase with further increasing α. The next-neighbor peak location, q_m, however, is monotonically increasing. The IRO peak in $S(q)$ at a $q_c < q_m$ becomes first visible for $\alpha \approx 1.5$ and at $q_c\sigma \approx 2.5$. It increases with increasing α, while its position is shifted slightly to smaller values. Note that if the attraction strength $\overline{K}_1 = \alpha K_1$ were increased for constant repulsion strength $\overline{K}_2 = \alpha K_2$, the osmotic compressibility is raised instead of being depressed. In completing the discussion of $S(q)$, notice the succession of isosbestic wavenumber points, $q_i^{\rm iso}$, where the structure factor curves intersect. The α-independent isosbestic points in Fig. 8.2 can be easily and alternatively identified, to good accuracy, in the framework of the simple random phase approximation for $S(q)$, by the roots of the spatial Fourier transform of the soft potential part of $V(r)$, extended

into the non-overlap region as $V(x < 1) = 0$, as discussed in detail in Subsec. 8.1.3.

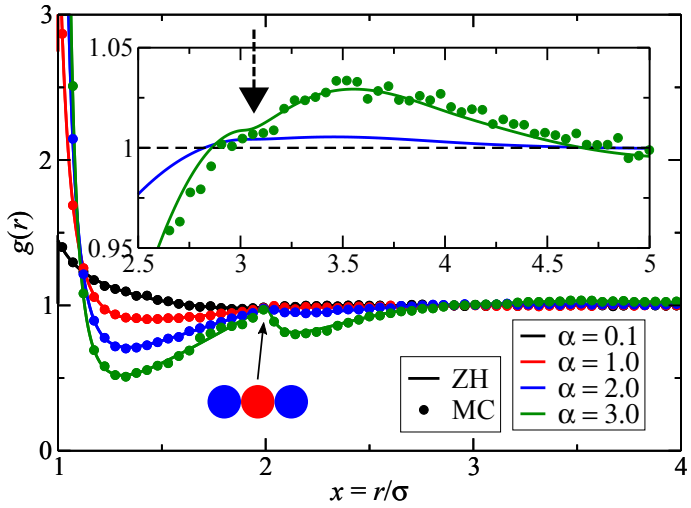

Fig. 8.3.: Radial distribution function, $g(r)$, for $\phi = 0.1$ plotted versus reduced distance $x = r/\sigma$. Solid lines: ZH scheme results. Filled circles: MC simulation data. The peak at $x = 2$ is due to particle pairs with a third (red) particle in between as sketched. The inset magnifies the larger-distance region of $g(r)$ for $\alpha = 2$ and 3. The vertical dashed arrow in the inset marks the inflection point visible for $\alpha = 3$, and located roughly at $2\pi/(q_c\sigma)$.

The here discussed features of $S(q)$ are reflected in the ZH-calculated RDFs, shown in Fig. 8.3, in comparison with our MC simulation data (filled circles). The RDFs quantify the growing influence of both the SA and LR potential parts with increasing α, giving rise to a more pronounced microstructure than the one of the hard-core reference system at the same concentration. As it is seen in the main figure part, with increasing α the RDF contact value, $g(x = 1^+)$, grows strongly from 1.3 at $\alpha = 0$ to 28 at $\alpha = 3$ (see Fig. 8.4), accompanied by the buildup of a pronounced depletion zone inside $1 < x < 2$, and a peak at $x = 2$ of height smaller than one for $\phi = 0.1$ which sharpens and renders larger than one with increasing concentration. The pronounced contact value of $g(r)$, and its adjacent depletion zone, reflect primarily the strong influence of the SA, while the peak at $x = 2$ quantifies the enhanced probability, due to the concerted effect of SA and LR, of finding a linear alignment of two particles with a third one fitting snugly in between (see also [89]). For α values where the IRO peak has developed, and for pair separations $x \geq 2\pi/y_c = x_c$ where $y_c = q_c\sigma \approx 2.1$, a broad region of $g(x)$ with values weakly enhanced above one is observed (see the inset of Fig. 8.3) that extends roughly across two particle diameters indicative of the mean transient cluster size [88]. In this larger-distance region, $g(x)$ has for $\alpha = 3$ a shallow inflection point at $x_c \approx 3$, marked in the inset by the vertical dashed

arrow.

In addition to the indicators discussed in Subsec. 2.3.3 and the gas-liquid critical temperature of the attractive reference system (c.f. Subsec. 8.1.2) ensuring that the investigated SALR systems are in the dispersed-fluid phase region, the present findings reassure this point. Firstly, according to Figs. 8.3 and 8.4, the MC data for $g(r)$ are in excellent agreement with the ZH scheme results applying to a homogeneous fluid-like system. Secondly, the IRO peak heights are all well below the critical value $S_{\text{crit}}(q_c) \sim 2.7$, obtained by Godfrin *et al.* [33] as an empirical criterion for the two-Yukawa SALR model for signaling in the here considered concentration range a first-order transition from the dispersed-fluid to the equilibrium-cluster phase. The IRO peak position, q_c, shifts to larger values as ϕ is increased (cf. [30]).

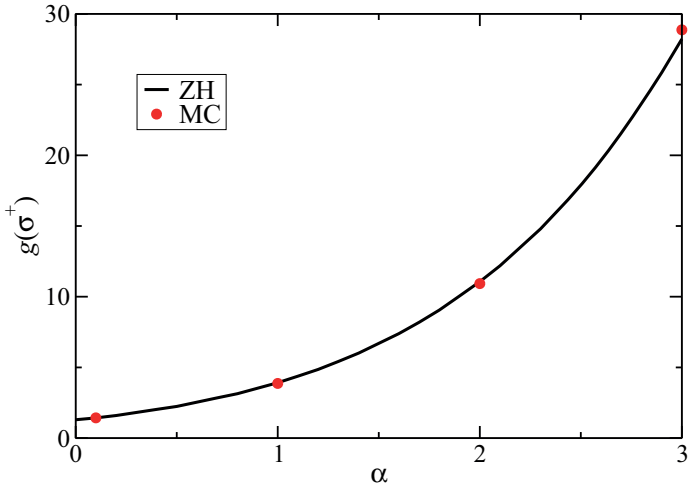

Fig. 8.4.: Contact value, $g(\sigma^+)$, of the RDF for $\phi = 0.1$, as a function of interaction strength α. Solid line: ZH scheme result. Filled red circles: MC simulation data.

In Fig. 8.5, we present a comparison of the ZH-results of $g(r)$ with MC simulations for the most concentrated system for which $\phi = 0.15$ (see page 157 for details about the MC simulations). For $\alpha = 3$ only, an additional shallow peak in the MC-generated $g(r)$ becomes visible at $x \approx \sqrt{3}$, corresponding to the distance between a pair of spheres where an orthogonally aligned dimer of two touching spheres fits snugly in between [89]. Yet, also this system of largest concentration and interaction strength belongs to the dispersed-fluid phase region.

So far, only the dependence of $g(r)$ and $S(q)$ on the interaction strength, α, has been discussed. In Fig. 8.6, we present $S(q)$ for model system $M_3(x_0 = 1.1)$ with $\alpha = 3$ and

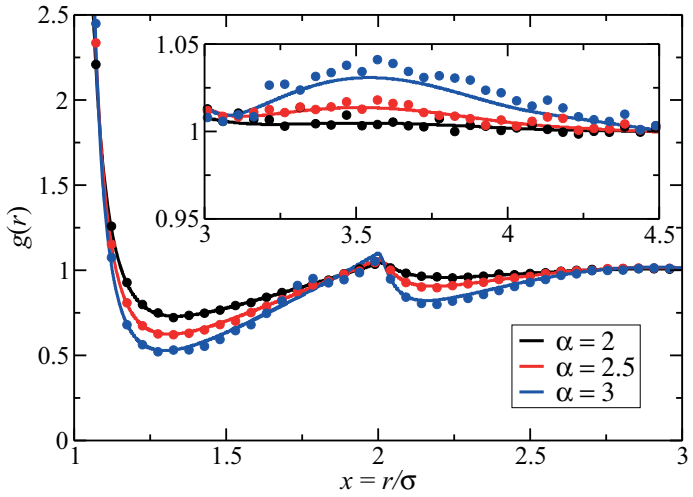

Fig. 8.5.: Radial distribution function, $g(r)$, for $\phi = 0.15$ plotted versus reduced distance $x = r/\sigma$. Solid lines: ZH scheme results. Filled circles: MC simulation data. The inset magnifies the larger-distance region of $g(r)$.

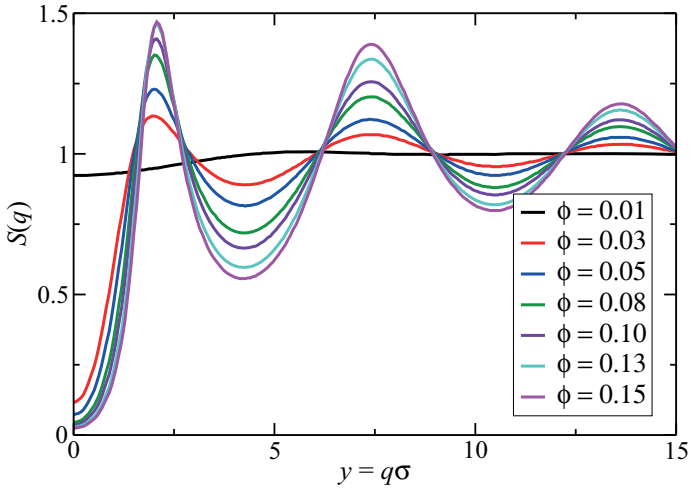

Fig. 8.6.: ZH-calculated static structure factor of model system $M_3(x_0 = 1.1)$, for $\alpha = 3$ and various values of ϕ as indicated.

various ϕ values. With increasing ϕ, the inverse isothermal compressibility, χ_T, proportional to $1/S(0)$ is strongly reduced revealing the dominant role of the long-range repulsion for the system ordering. For a purely attractive system, χ_T increases with increasing ϕ. For $\phi > 0.01$, a distinct IRO peak is observable exceeding the next-neighbor peak in its height. The more pronounced structure of the system at higher ϕ is mirrored by the increased amplitude of oscillations in $S(q)$. While the position q_m of the next-neighbor peak remains practically unchanged, a small shift of the IRO peak position q_c to higher wavenumbers is observable. This indicates that while the structure of the cluster regions of locally higher density is not changing, due to the increased number of particles the inter-cluster distance decreases. The dependence of q_m on ϕ is clearly different from its dependence on the interaction strength α, where an increase in α dramatically changes the next-neighbor distance. This suggests that in the case of high α and moderate ϕ, the system structure and here especially the typical next-neighbor distance is set by the interaction potential.

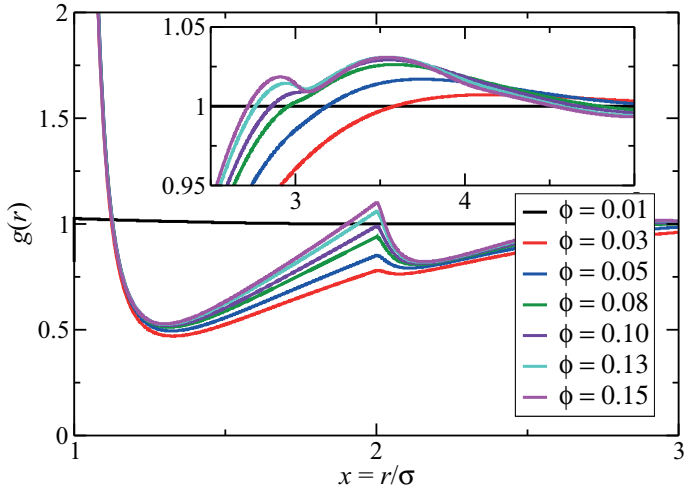

Fig. 8.7.: RDF $g(r)$ corresponding to the $S(q)$ of model system $M_3(x_0 = 1.1)$ in Fig. 8.6, for $\alpha = 3$ and various values of ϕ. The inset highlights that with increasing ϕ, a broad peak region of roughly two-particle diameters extension arises which is indicative of the mean cluster size (see text for details).

The behavior of $S(q)$ for changing ϕ in Fig. 8.6 is reflected by the behavior of $g(r)$ shown in Fig. 8.7. With increasing ϕ, the peak in $g(r)$ mirroring the inline configuration of three particles sharpens without changing its position. For $\phi > 0.03$, the broad peak in $g(r)$ for $x \gtrsim 2.75$ is shifted to smaller distances while maintaining its approximate width of 2σ. If one relates the width of this peak at about x_c to the mean cluster size, its constancy suggests that the transient clusters do not change their mean size but approach

each other with increasing ϕ. However, we note that this interpretation requires future confirmation by simulations since it is hard to draw definite conclusions about the system microstructure based alone on the radially averaged distribution functions $S(q)$ and $g(r)$. Note that additionally to the ZH-scheme employed in this thesis, alternative OZ closure relations have been used for SALR systems that are of comparable accuracy. For example, Costa *et al.* [91] use the modified HNC by Rosenfeld and Ashcroft [126], and the self-consistent Bomont-Bretonnet [231, 232] closures, respectively. In the context of two-Yukawa SALR systems, the importance of thermodynamic self-consistency of the employed integral equation scheme is discussed by Kim *et al.* [233].

Cluster-size distribution function (CSD)

We have discussed various indicators to confirm that the investigated systems are fluid-like. As an additional check, we have performed MC simulations and analyzed the data by calculating the cluster-size distribution function. The CSD,

$$N(s) = \left\langle \frac{s}{N_\mathrm{p}} n(s) \right\rangle , \tag{8.2}$$

characterizes the average fraction of particles, $N(s)$, which are members of a cluster of size s [31]. Here, $\langle \ldots \rangle$ is an average over representative configurations of a simulation and / or multiple simulation runs, and $n(s)$ is the number of clusters of size s within a specific configuration. Moreover, N_p is the total number of particles in the system such that $\sum_{s=1}^{N_\mathrm{p}} N(s) = 1$.
A cluster is defined using a cutoff-distance, r_cluster, by demanding that a particle i and at least another particle j of a cluster have the center-to-center distance $|\mathbf{r}_{ij}| < r_\mathrm{cluster}$. For the two-Yukawa and the LJY SALR systems, we use $r_\mathrm{cluster}\sigma = x_0$, where x_0 is the effective attraction range (i.e. $V(x_0) = 0$, for $x_0 > 1$), in agreement with the cluster identification procedures in [31, 33, 34].
Based on the characteristics of $N(s)$, four different phases depicted in the generalized phase diagram for SALR systems in Fig. 2.6 are identified [33]:

1. **Dispersed-fluid phase:**
   Here, the CSD is monotonically decaying with increasing s, indicative of a monomer-dominated system where only transient small clusters are formed.

2. **Equilibrium-cluster phase:**
   In addition to the dominating monomer peak ($s = 1$), the CSD has another distinct

peak at $s^* > 2$, indicative of equilibrium clusters of a preferred size around s^* in thermodynamic equilibrium with monomers (c.f Fig. 8.36b).

3. **Cluster-percolated phase:**
   The CSD has multiple peaks at different cluster sizes plus an additional peak at $s = N_\mathrm{p}$, signaling a percolating system of clusters. In addition, the fraction of monomers is severely reduced.

4. **Random-percolated phase:**
   Characterized by a monotonically decaying CSD with a distinct peak at system size $s = N_\mathrm{p}$, representing a random percolated system.

We have conducted Metropolis algorithm MC simulations in the NVT ensemble. The simulations were performed with $N = 4096$ particles in a cubic simulation box with periodic boundary conditions and potential cutoff $r_\mathrm{cutoff} = 10\sigma$. As random number generator, the *ranlxs1* routine of the GSL-package [234] has been used. We have analyzed the generated configurations, and have calculated the CSDs using an evaluation program kindly provided by S. Das (ICS-2 / IAS-2, FZ Jülich).

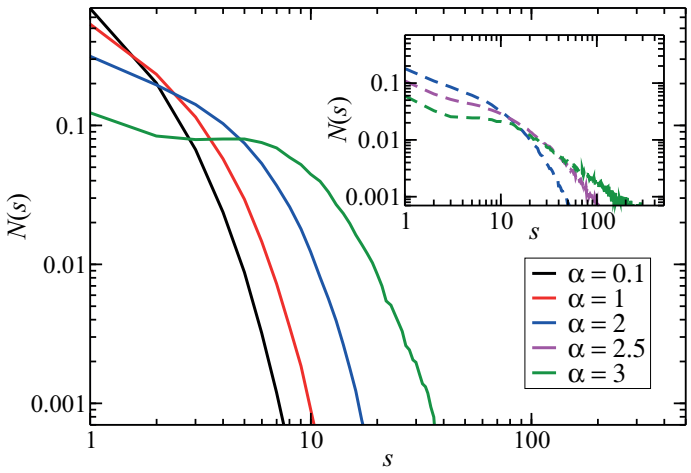

Fig. 8.8.: Cluster-size distribution function, $N(s)$, as function of cluster size s for system $M_3(x_0 = 1.1)$, and α values as indicated. The volume fraction is $\phi = 0.1$ in the main figure, and $\phi = 0.15$ in the inset. The evaluation code for the calculation of $N(s)$ from our MC data has been kindly provided by Shibananda Das (ICS-2 / IAS-2, FZ Jülich).

In Fig. 8.8, we show the CSD for system $M_3(x_0 = 1.1)$ and a set of different α values. For $\phi = 0.1$ (main part of Fig. 8.8) and $\alpha \leq 2$, strictly monotonically decaying CSDs are observed, confirming the fluid-phase behavior of the systems. For $\alpha = 3$, the onset of a

plateau in the CSD is visible but there is no distinct peak. This suggests that the fluid system is close to the transition to the equilibrium-cluster phase. The inset of Fig. 8.8 displays CSDs for $\phi = 0.15$ and $\alpha \geq 2$. With increasing α, a slightly pronounced plateau is formed. In addition, the decay of the CSD for $\phi = 0.15$ is slower than for $\phi = 0.1$, resulting in a larger mean cluster size $\langle s \rangle$. However, a distinct peak in $N(s)$ for $s > 2$ is for $\phi = 0.15$ not yet visible.

The CSDs shown here confirm the finding of the previous subsections that for $\alpha \lesssim 3$ the systems are in the dispersed-fluid phase state. For $\alpha \approx 3$, however, the equilibrium-cluster phase transition line is approached, with slight inaccuracies in the employed ZH-IET for $g(r)$ being visible in comparison with the MC results in Fig. 8.5.

Short-time diffusion properties

For the calculation of the equilibrium short-time diffusion properties, $H(q)$, $D(q)$, d_S, and K of SALR systems presented in this chapter, we use the hybrid BM-PA scheme presented in Subsec. 4.4.3. For dispersions with a hard-core plus purely repulsive Yukawa potential such as that of charge-stabilized colloids, the BM-PA hybrid method gives results in good overall agreement with simulation and experimental data [65, 85, 136, 178]. It can be expected to provide semi-quantitative results also for the considered homogeneous SALR systems. Its analytic simplicity makes the BM-PA scheme a convenient tool for assessing general dynamic trends. For the calculation of η_∞, the PA method is employed.

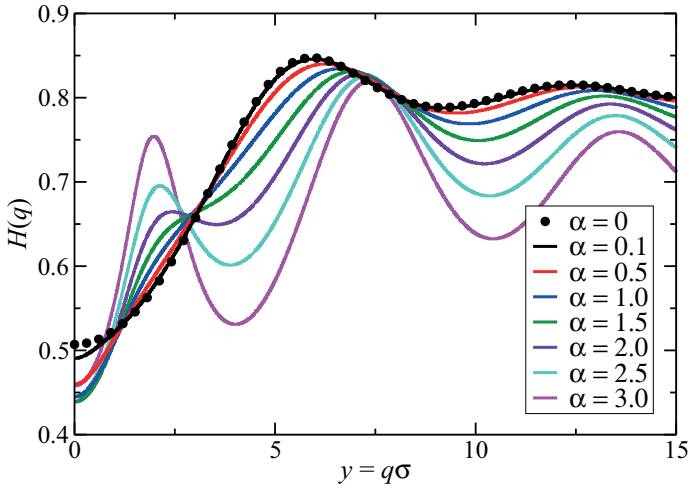

Fig. 8.9.: Hydrodynamic function, $H(q)$, calculated using the BM-PA hybrid method with structural input presented in Fig. 8.2, for $\phi = 0.1$.

We merely note here that while the bare PA method with its exact account of two-body

lubrication works well for the self-diffusion coefficient and the high-frequency viscosity up to the largest considered concentration $\phi = 0.15$, for $\phi \gtrsim 0.08$ it has the tendency to overestimate the q-dependent oscillations in $H^{\mathrm{d}}(q)$. This has been demonstrated for purely repulsive Yukawa systems by the comparison with Stokesian dynamics simulations [186], and a similar trend is observed likewise for the SALR systems in a comparison between BM-PA and pure PA results for $H(q)$ not shown in this thesis. The overestimation of oscillations has been attributed to the neglect of (non-pairwise additive) hydrodynamic shielding effects by the PA method. This shielding is approximately accounted for in the BM method by the inclusion of ring diagrams as discussed in Subsec. 4.4.2.

Hydrodynamic function

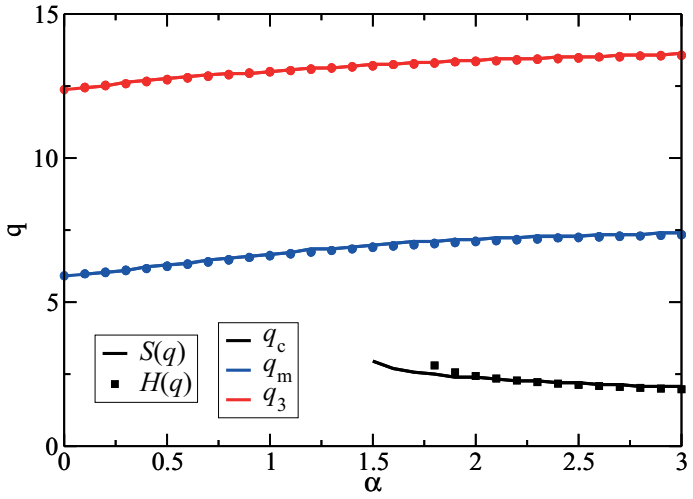

Fig. 8.10.: Comparison of the position of the IRO peak, q_{c}, the next-neighbor peak position, q_{m}, and the following peak position denoted by q_3 in $H(q)$ and $S(q)$ as functions of the interaction strength α. Here, results for $M_3(x_0 = 1.1)$ at $\phi = 0.1$ are shown.

Results for $H(q)$ obtained by the BM-PA scheme with ZH $g(r)$ and $S(q)$ input are shown in Fig. 8.9, for the same system parameters as in Fig. 8.2. To our knowledge, this is the first theoretical prediction of a low-q IRO peak in $H(q)$. This peak of $H(q)$ emerges first at larger interaction strengths $\alpha > 1.5$ as for the IRO peak of $S(q)$. In the considered parameter range, the IRO peak of $H(q)$ does not supersede the next-neighbor peak $H(q_{\mathrm{m}})$. Note that the oscillations in $H(q)$ are triggered by the ones in $S(q)$ which explains why the positions of the IRO and next-neighbor peaks in $H(q)$ are practically coincident with the respective positions, q_c and q_m, of $S(q)$. This is shown explicitly in Fig. 8.10, where

the position of the IRO peak, q_c, the next-neighbor peak, q_m, and the following peak, q_3, in $H(q)$ and $S(q)$ are compared.
It is further noticed that the hard-sphere $H(q)$ obtained for $\alpha = 0$ is essentially an upper bound for the curves of $H(q)$ for non-zero α, for wavenumbers located to the right of the IRO peak region. The next-neighbor peak values, $H(q_m)$, are smaller than one which is indicative of a significant influence of the near-distance part of the HIs. In contrast, $H(q_m)$ is larger than one for lower-concentrated systems having purely LR [85].

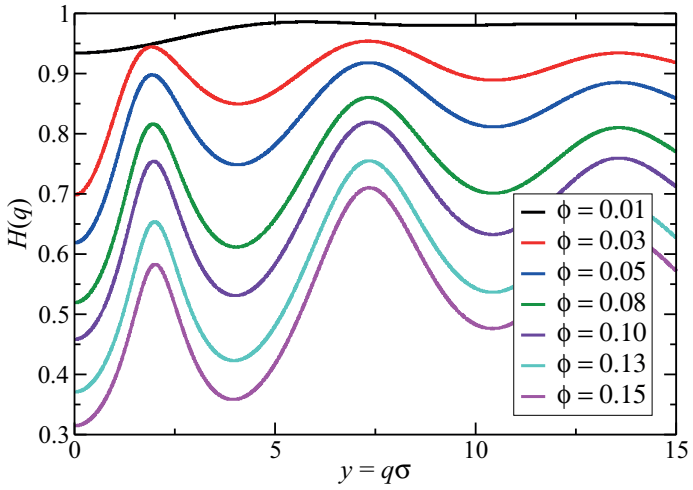

Fig. 8.11.: Hydrodynamic function, $H(q)$, of model system $M_3(x_0 = 1.1)$ and $\alpha = 3$, for various ϕ values as indicated. The corresponding $S(q)$ and $g(r)$ are shown in Figs. 8.6 and 8.7, respectively.

The ϕ dependence of $H(q)$ for system $M_3(x_0 = 1.1)$ and $\alpha = 3$ is presented in Fig. 8.11. The oscillations in $H(q)$ get more pronounced with increasing ϕ, in accordance with the $S(q)$ results in Fig. 8.6. In addition, with increasing ϕ the slowing down effect of HIs becomes stronger resulting in a shift of $H(q)$ to smaller values. For the considered system parameters, the IRO peak is observable for considerably low ϕ. For $\phi = 0.03$, the IRO peak in $H(q)$ and the next-neighbor peak $H(q_m)$ are of comparable height, while for larger ϕ the peak at q_c decreases stronger than that at q_m. Clearly visible is the strong decrease of d_S, associated with $H(q \to \infty)$, and of $K = H(q \to 0)$ for increasing ϕ. This is discussed in more detail in the following.

Self-diffusion coefficient

In Fig. 8.12a, we depict the ϕ dependence of d_S for Model $M_3(x_0 = 1.1)$ and several α values. Triggered by the rising $g(\sigma^+)$ with increasing α accompanied by an enhanced

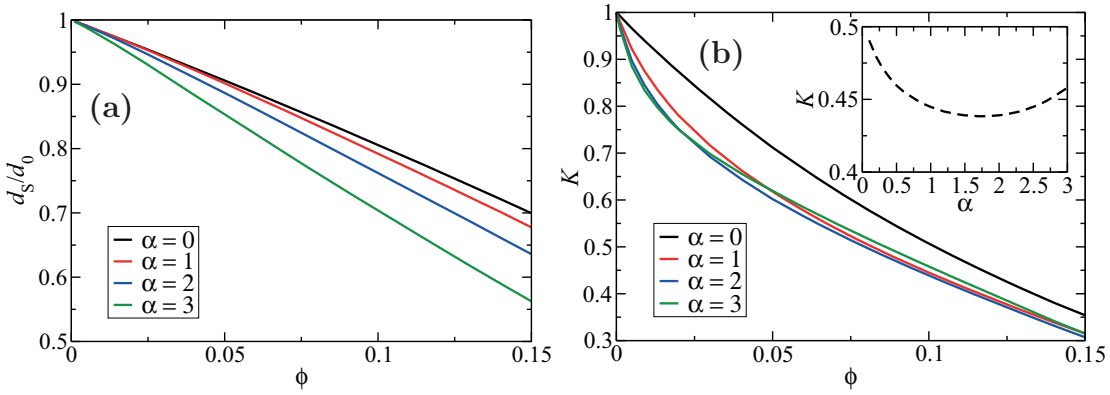

Fig. 8.12.: Concentration dependence of (a) the short-time self-diffusion coefficient, d_S, and (b) the sedimentation coefficient, $K = V_{sed}/V_0$, for $M_3(x_0 = 1.1)$ and values of α as indicated. The inset in (b) depicts the non-monotonic α dependence of K, for $\phi = 0.1$.

transient clustering tendency, d_S decreases monotonically with increasing α and ϕ, with values below those for hard spheres (namely $d_S(\alpha = 0, \phi)$) at the same concentration. In fact, transient clustering slows self-diffusion both at short and long times, as it has been shown theoretically for sticky hard spheres, and hard spheres with additional square-well attraction [197, 235, 236]. While d_S is lowered in systems with enhanced SA having no LR, in systems with pure LR such as in a low-salinity suspension of charge-stabilized particles, the decline of d_S with increasing ϕ is less pronounced than that for the hard-sphere reference system, showing typically a $\phi^{4/3}$ fractional concentration dependence [136]. Incidentally, an enhancement of self-diffusion for systems having LR only, and its slowing for systems with pure SA, can be expected both regarding d_S and d_L [159]. That d_S decreases with increasing α when the strength both of the SA and LR potential parts are enlarged in proportion to each other, is due to the rapid $\mathcal{O}(r^{-4})$ long-distance decay of the hydrodynamic self-mobility tensor associated with d_S [61], putting thus more weight to the near-contact region of $g(r)$. The monotonic decrease of d_S with increasing α explains why the α-independent isosbestic points seen in $S(q)$, and discussed in more detail in Subsec. 8.1.3, are absent in $H(q)$.

Sedimentation velocity

We proceed in discussing the sedimentation coefficient, K, whose monotonic decrease with increasing ϕ is shown in Fig. 8.12b. The predicted sedimentation velocity for the considered non-zero α values is smaller than the sedimentation velocity of the corresponding hard-sphere system, i.e. $K(\alpha > 0, \phi) < K(0, \phi)$. This reflects the overall dominant in-

fluence of the LR part regarding sedimentation which is known in systems with pure LR to reduce the sedimentation velocity [65, 136]. The additional influence of the SA part is seen in the, on first sight, surprising non-monotonic α-dependence of K exemplified in the inset of Fig. 8.12b for $\phi = 0.1$: K decreases for small α at constant ϕ, with a subsequent moderate increase for increasingly large α values once it has passed through a minimum at $\alpha \approx 1.8$. The non-monotonic behavior of K as a function of α is a consequence of the delicate interplay of the SA potential part, which by itself enhances sedimentation, with the LR part that has the opposite effect. Different from self-diffusion which is most strongly influenced by the near-distance part of the HIs, as a collective property K is also strongly affected by the $\mathcal{O}(r^{-1})$ long-distance part of the HIs. In this context, we refer to a recent multiparticle collisions dynamics (MPC) simulation study by Moncha-Jorda *et al.* [237] for the sedimentation coefficient of a dispersion of Brownian particles with short-range interactions only where the SA dominates (i.e., $B_2^* < 0$). In their systems, the slope of the low-ϕ linear form of K changes from negative to positive values when B^* is lowered roughly below -0.87. Due to transient clustering, a non-monotonic ϕ dependence of K is observed for $B_2^* \approx -1.42$. Moncho-Jordá *et al.* note further that their systems belong to the dispersed-fluid-phase region such as ours. At this point, we remark again that different from self-diffusion where the long-time coefficient d_L in concentrated systems is substantially smaller than d_S owing to pronounced dynamic caging effects [178], the short-time coefficient K can be expected to be only slightly larger than its long-time counterpart.

Collective diffusion coefficient

In Fig. 8.13, we present the collective diffusion coefficient, d_C, introduced in Eq. (4.58), as function of ϕ. For non-zero α, d_C is dominated by the strong decrease of the osmotic compressibility, χ_T, with increasing ϕ and α, respectively, resulting in larger d_C values. Since the changes in χ_T become smaller with increasing ϕ (c.f. Fig. 8.6), the monotonic decrease of K with increasing ϕ leads to a peak in d_C at $\phi \approx 0.125$ for $\alpha = 3$. Different from K, d_C has a monotonic α dependence due to the strong decay of χ_T with increasing α.

Wavenumber-dependent diffusion function

Fig. 8.14 displays the inverse of the diffusion function, $D(q)$, in units of d_0. The figure highlights the importance of HIs by the comparison with the prediction, $d_0/D(q)|_{\text{no HI}} = S(q)$, for hydrodynamically non-interacting particles (dashed lines in Fig. 8.14) which differs

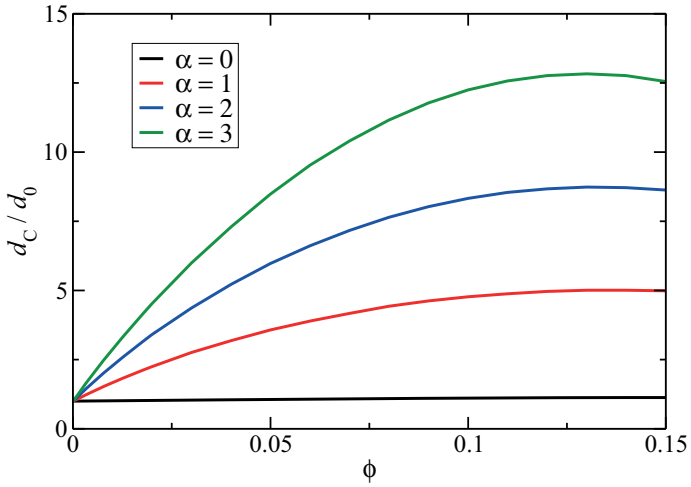

Fig. 8.13.: Concentration dependence of the collective diffusion coefficient, d_C, for model $M_3(x_0 = 1.1)$ and α values as indicated.

significantly from the result with HIs included. Like for $S(q)$, the IRO peak, $d_0/D(q_c)$, at $\alpha = 3.0$ is larger than the next-neighbor peak, $d_0/D(q_m)$.

Fig. 8.14 serves further to explain how d_S can be inferred approximately from DLS and NSE experiments where only a finite wavenumber band is accessed. As first suggested by Pusey [238] and theoretically corroborated later by Abade *et al.* [47], a decent estimate of d_S within a few percent error is given by $D(q)$ evaluated at a wavenumber q^* equal to the first wavenumber situated to the right of q_m where $S(q^*) = 1$. Our results for d_S and $D(q)$ show that this practical way of determining d_S is applicable likewise to SALR systems as shown in Fig. 8.15. However, if $D(q)$ is evaluated instead at a wavenumber q^*, with $S(q^*) = 1$, situated in between the IRO and next-neighbor peaks, d_S is significantly underestimated by about 15%. For a decent estimate of d_S, it is thus essential to cover a sufficiently broad q-range extending beyond the next-neighbor peak region.

Discussion of isosbestic points

In Fig. 8.2, there are α-independent isosbestic points in the $S(q)$ of model $M_3(x_0 = 1.1)$. These are likewise found for varying temperature in experiments and theoretical work on, e.g., SALR Lysozyme solutions [93], SA-type potential systems [122], and suspensions of sterically stabilized silica particles interacting effectively as sticky hard spheres [239]. In addition, concentration-independent isosbestic points exist in the $S(q)$'s and $H(q)(d_0/d_S)$'s of hard-sphere suspensions where only a single interaction length scale exist [240]. To understand the origin of α-independent isosbestic points, we study the two-Yukawa potential

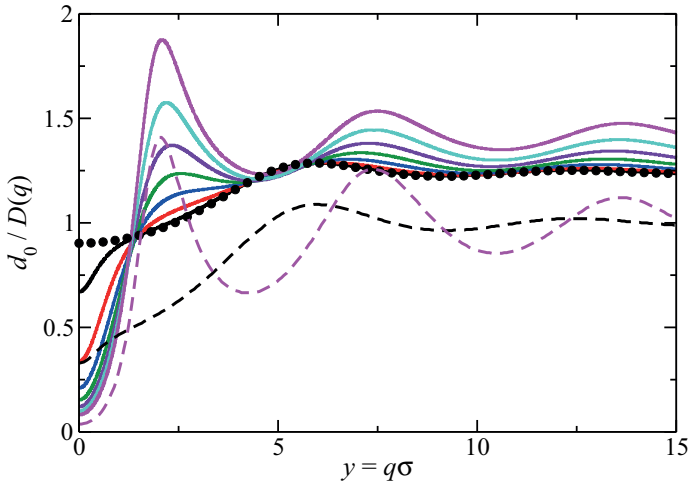

Fig. 8.14.: Inverse, $d_0/D(q)$, of the short-time diffusion function, $D(q)$, in units of the single-particle diffusion coefficient, d_0, obtained using the results for $S(q)$ and $H(q)$ in Figs. 8.2 and 8.9, respectively. The color code is the same as in Fig. 8.2. To highlight the strong influence of the HIs, the dashed lines depict $d_0/D(q)|_{\text{no HI}} = S(q)$ for $\alpha = 0.1$ (black) and $\alpha = 3$ (magenta), respectively, describing hydrodynamically non-interacting particles characterized by $H(q) = 1$.

using for analytic simplicity the RPA described in Subsec. 3.4.4.

For this purpose, we use the hard-sphere system as the reference system such that the perturbation potential $w(r)$ is given by the soft two-Yukawa potential part, i.e.

$$\beta w(r) = \begin{cases} 0\,, & r < \sigma \\ \alpha \left(K_1 \frac{e^{-z_1(x-1)}}{x} + K_2 \frac{e^{-z_2(x-1)}}{x} \right), & r \geq \sigma\,. \end{cases} \tag{8.3}$$

We have set here $w(r < \sigma) = 0$. The resulting expression for $S(q)$ in RPA approximation reads (c.f. Eq. (3.44))

$$\frac{1}{S_{\text{RP}}(y)} = \frac{1}{S_0(y)} + 3\phi\alpha \left[\left(-\frac{K_1}{z_1^2 + y^2} + \frac{K_2}{z_2^2 + y^2} \right) \cos(y) \right. \\ \left. \left(-\frac{K_1 z_1}{z_1^2 + y^2} + \frac{K_2 z_2}{z_2^2 + y^2} \right) \frac{\sin(y)}{y} \right], \tag{8.4}$$

with $y = q\sigma$, and $S(q)$ of the hard-sphere reference system denoted by $S_0(q)$.

In Fig. 8.16, we present the RPA $S(q)$ results for system $M_3(x_0 = 1.1)$, for various α values and $\phi = 0.1$. The RPA $S(q)$'s visibly deviate from $S_0(q)$ for low q-values only. With

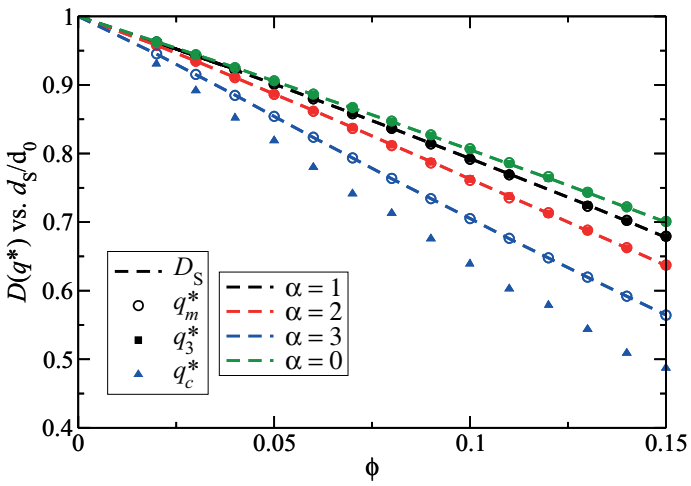

Fig. 8.15.: d_S in PA-approximation (dashed line) for system M3($x_0 = 1.1$) and selected α values in comparison with $D(q_i^*)$. The different q_i^* values refer to the first $q_m^* > q_m$ (open circles), $q_3^* > q_3$, and $q_c^* > q_c$ (filled triangles) for which $S(q_i^*) = 1$. The different colors distinguish between the different α-values considered: $\alpha = 1$ black, $\alpha = 2$ red, and $\alpha = 3$ blue. For comparison, the results for hard spheres ($\alpha = 0$) are presented in green.

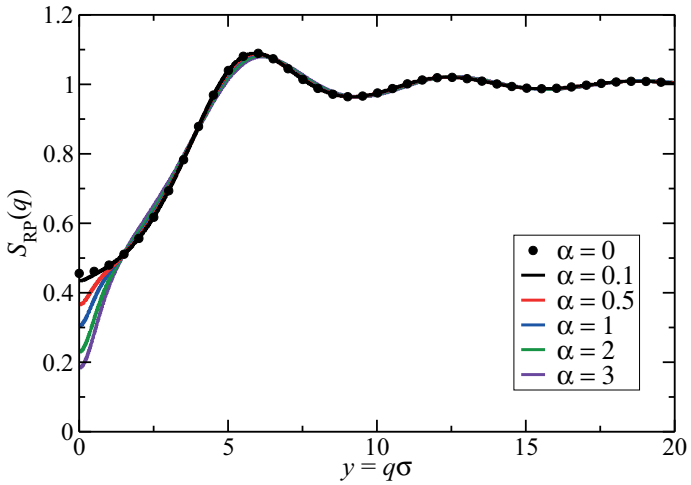

Fig. 8.16.: RPA-$S(q)$ for system $M_3(x_0 = 1.1)$ and $\phi = 0.1$, with α values as indicated. As hard-sphere reference structure factor, the analytic PY solution is used (black filled circles).

$y_{\rm iso}$	1.48433	3.86007	6.48705	9.26627	12.1498
$S_{\rm RP}\,(y_{\rm iso})$	0.509566	0.850394	1.07481	0.964358	1.01983

Table 8.4.: RPA predicted α-isosbestic points of $S(q)$, for $M_3(x_0 = 1.1)$ and $y \leq 15$.

increasing α, χ_T significantly decreases as it is typically found for purely repulsive particles. On basis of the analytic RPA solution for $S(q)$, we have calculated the wavenumber positions of the α-independent isosbestic points, $\{y_{\rm iso}\}$, equal to the roots of the Fourier Transform of $w(r)$ (c.f. Eq. (8.4)). The results are presented in Table 8.4 for $y \leq 15$.
A comparison of the RPA α isosbestic points with the more elaborate ZH results for $S(q)$ is presented in Fig. 8.2 illustrating the very good agreement. Only in the low-q region the ZH and RPA calculated $\{y_{\rm iso}^{(i)}\}$'s deviate, with an RPA-predicted isosbestic point not observed in the ZH results. Since in RPA the SA and LR potential parts are treated as perturbations, the IRO peak originating from the competition of SA and LR is not reproduced. For $q \gtrsim q_m$, however, the RPA describes the α-isosbestic points of the ZH-$S(q)$ quite well. This finding suggests that the locations and values of the α-isosbestic points of the ZH $S(q)$ are basically due to the hard-core part of the two-Yukawa SALR potential.

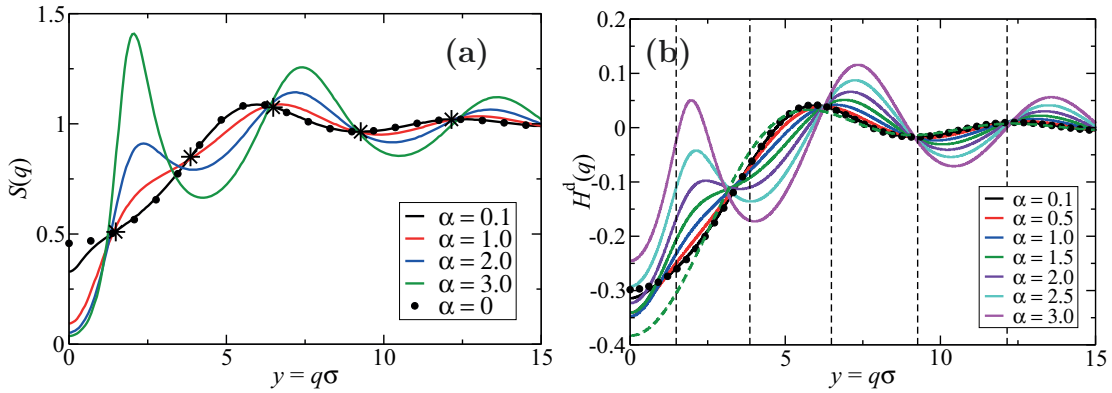

Fig. 8.17.: Comparison of α-independent isosbestic points of the RPA $S(q)$ for $M_3(x_0 = 1.1)$ and $\phi = 0.1$ with (a) $S(q)$ and (b) $H^{\rm d}(q)$ in PY and BM approximation, respectively. In (a), the positions of the RPA isosbestic points, $\{y_{\rm iso}^{(i)}\}$, are shown by stars, while in (b) the $\{y_{\rm iso}^{(i)}\}$'s are marked by dashed vertical lines.

Louis [122] suggested an extended corresponding states principle for SA potentials where ϕ, B_2^*, and different from Noro and Frenkel [107] an effective attraction range related to the position of the first (lowest-q) isosbestic point are used. In addition, he finds the first isosbestic point $y_{\rm iso}^{(1)}$ to approach the value π for infinitely short-ranged attraction,

with attaining smaller values for increasing attraction range. Our result for $y_{\rm iso}^{(1)}$ distinctly differs from π due to the encountered finite attraction range, and the presence of the LR. Owing to the significant decrease of $d_{\rm S}$ with increasing α, there are no α-isosbestic points in $H(q)$ as noticed from Fig. 8.9. According to Fig. 8.17b, the distinct part $H^{\rm d}(q)$, however, shares the wavenumber locations, $\{y_{\rm iso}^{(i)}\}$, of isosbestic points with $S(q)$ for $y_{\rm iso}^{(i)} \gtrsim q_{\rm m}\sigma$.

High-frequency viscosity and GSE relations

For a comprehensive assessment of short-time transport properties of SALR systems in the fluid-phase region, we discuss next our predictions for the high-frequency viscosity η_∞. Its concentration dependence is shown in Fig. 8.18.

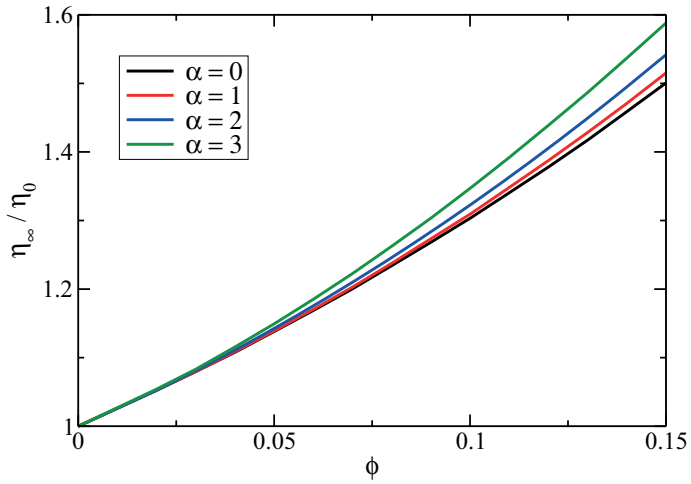

Fig. 8.18.: High-frequency viscosity, $\eta_\infty\,(\phi)$, in units of the solvent viscosity η_0, as function of ϕ, and for values of α as indicated.

Increasing ϕ implies more pronounced stress relaxations, and an enhanced viscous dissipation, resulting in an enlarged viscosity. Furthermore, a monotonic increase of η_∞ above the corresponding hard-sphere values is observed with increasing α. This should be contrasted with a dispersion having LR interactions only, where η_∞ is smaller than in a hard-sphere system of equal concentration [136]. To comprehend this notice that the hydrodynamic shear mobility tensor coupling the hydrodynamic stress dipole acting on a particle surface to the fluid rate-of-strain tensor at the position of another particle is rather short-ranged [170], with an $\mathcal{O}(1/r^6)$ asymptotic decay. The near-contact region of the RDF has thus the strongest influence on the high-frequency viscosity so that with increasing RDF contact value, η_∞ is accordingly increased.

As a useful application, for our SALR systems we discuss finally the applicability of two

short-time GSE relations relating η_∞ to d_S and d_C, respectively. Additionally, to the GSE function Λ_S introduced in Eq. (5.14), consider the GSE function Λ_C defined by

$$\Lambda_C = \frac{\eta_\infty(\phi)}{\eta_0}\frac{d_C(\phi)}{d_0}\sqrt{S(q\to 0,\phi)}\,. \tag{8.5}$$

Kholodenko and Douglas [241] suggested the validity of the GSE relation $\Lambda_C(\phi) \approx 1$ which was applied in particular to protein solutions [86, 242].

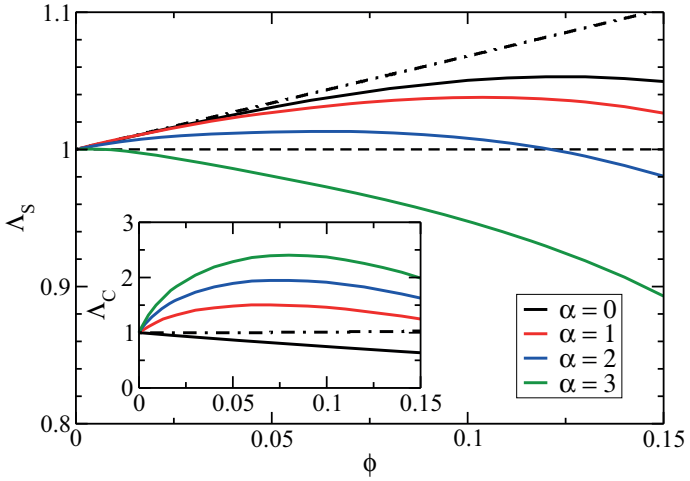

Fig. 8.19.: Concentration dependence of the self-diffusion GSE function, $\Lambda_S(\phi)$, defined in Eq. (5.14), for values of α as indicated. Inset: Corresponding curves for the Kholodenko-Douglas collective diffusion GSE function $\Lambda_C(\phi)$. The dashed-doted black lines are accurate hard-sphere results ($\alpha = 0$) obtained from the analytic expressions for $d_S(\phi)$, $d_C(\phi)$, and $\eta_\infty(\phi)$ given in [178].

The validity of GSE relations $\Lambda_S(\phi) \approx 1$ and $\Lambda_C(\phi) \approx 1$, would be especially useful for protein solutions, allowing for determining the solution viscosity from a scattering experiment.

Our results for the $\Lambda_S(\phi)$ and $\Lambda_C(\phi)$ of SALR systems are shown in the main part and inset of Fig. 8.19, respectively. Notice here the different ordinate scales in main figure part and the inset. In the considered ϕ range, the maximal deviation of Λ_S from one is about 10%, showing that the GSE relation for d_S is a useful tool for a semi-quantitative assessment of η_∞ in a dynamic scattering experiment. While the Kholodenko-Douglas GSE relation for d_C applies quite well to hard spheres, with $\Lambda_C(\phi)$ being rather close to one even at $\phi = 0.15$, its applicability worsens significantly with increasing α. Note again the approximate character of the BM-PA scheme, as illustrated in Fig. 8.19 by the showing of the dashed-dotted curves for $\Lambda_S(\alpha = 0, \phi)$ and $\Lambda_C(\alpha = 0, \phi)$, obtained from

accurate analytic expressions for the hard-sphere d_S, d_C, and η_∞ [178]. The deviations of the PA curves for $\alpha = 0$ from these numerically precise GSE functions is due to the underestimation of d_S and η_∞ at larger ϕ by the PA scheme which does not account for hydrodynamic shielding effects associated with non-pairwise additive man-body HIs contributions. The individually smaller errors in d_S, d_C, and η_∞ introduced by the PA method are amplified by the GSE functions Λ_S and Λ_C described in Eqs. (5.14) and (8.5).

8.1.4. Effect of short-range attraction

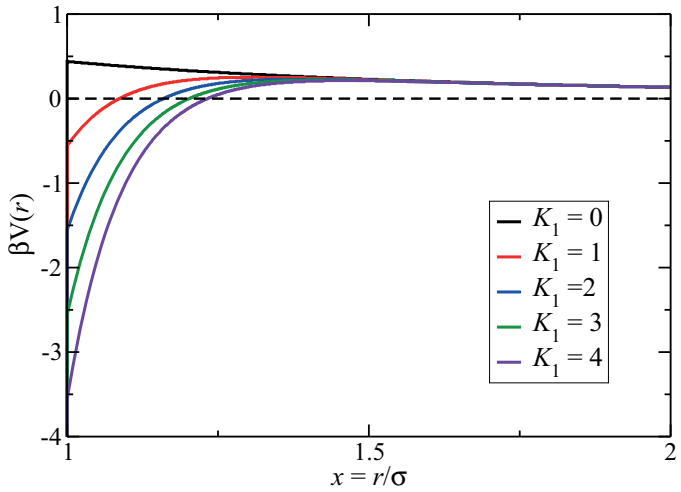

Fig. 8.20.: Reduced interaction potentials, $\beta V(r)$, for $z_1 = 10$, $z_2 = 0.5$, $K_2 = 0.44$ and $\alpha = 1$. The reduced attraction strength K_1 is varied from 0-4.

In the previous section, we discussed the effect of changing α on the structure and dynamics in SALR systems. The strength of the SA and LR was varied by keeping the ratio constant. To learn more about IRO peak formation caused by the interplay of SA and LR, we focus now on the effect of adding attraction to an originally purely repulsive pair potential. For this study, we select $z_1 = 10$, $z_2 = 0.5$, $K_2 = 0.44$, and $\alpha = 1$. Only the reduced attraction strength K_1 is varied from 0-4 for constant $\phi = 0.05$, with $V(r)$ shown in Fig. 8.20.
This procedure helps to elucidate the individual role of SA and LR shown in the last section to lead to interesting phenomena like the non-monotonic α dependence of the sedimentation velocity.

Pair structure using the Zerah-Hansen scheme

How attraction affects the pair structure of a hard-core plus two-Yukawa system is shown in Figs. 8.21a and 8.21b displaying $S(q)$ and $g(r)$ for varying attraction strength K_1.

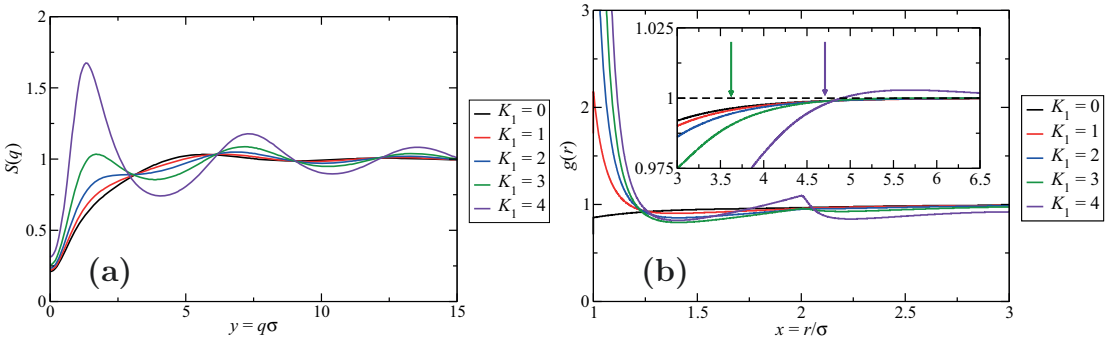

Fig. 8.21.: ZH-approximation (a) of $S(q)$, and (b) of $g(r)$ for a hard-core plus two-Yukawa system at $\phi = 0.05$, with $z_1 = 10$, $z_2 = 0.5$, $K_2 = 0.44$, and $\alpha = 1$. The reduced attraction strength K_1 is varied from 0-4. In (b) the arrows mark the positions $x_c \approx 2\pi/q_c$ for $K_1 = 3$ (green), and 4 (purple).

Due to the moderate repulsion strength $K_2 = 0.44$, for $\alpha = 1$ and $\phi = 0.05$, the purely repulsive system where $K_1 = 0$ has only small undulations in $g(r)$. For $K_1 = 1$, a negative contact value, $V(\sigma^+)$, has developed as seen in Fig. 8.20. This causes a distinct increase in $g(\sigma^+)$ (not shown explicitly). Due to the simultaneous buildup of a potential barrier in $V(r)$ with increasing K_1, a slight depletion zone starts to develop in $g(r)$ at $x \approx 1.25$. For $K_1 = 4$, the behavior of $g(r)$ becomes different from that for lower K_1, with now a peak occurring at $x = 2$ characteristic of the in-line configuration of three touching particles. Additionally, a broad peak in $g(r)$ becomes visible whose onset at x_c can be linked to the IRO peak position, $q_c \approx 2\pi/x_c$, in $S(q)$ as observed before in Subsec. 8.1.3. The x_c-q_c positions linkage does not hold for $K_1 = 3$, for which there is a shallow IRO peak in $S(q)$ (see the inset of Fig. 8.21b with $x_c \approx 2\pi/q_c$ marked by the green arrow). The IRO peak is observed for $K_1 \gtrsim 2$, only, indicating the importance of a competition between SA and LR for its formation.

In addition, q_c shifts to lower q-values indicating an increased mean transient cluster distance. This interpretation is underlined by the position of the one-crossings in $g(r)$ for $x \gtrsim 4$ shifting to larger x values with increasing K_1 as seen in the inset of Fig. 8.21b. The next-neighbor peak position q_m has the opposite trend, shifting to larger q-values associated with a reduction of the typical next-neighbor distances when K_1 becomes larger. Different from the α-variation studies in the previous subsection, here, χ_T is enhanced with increasing K_1 as expected for pure SA systems. The changes in χ_T are small, however.

Diffusion properties

According to Fig. 8.22, $H(q)$ shares the same trends with $S(q)$ regarding its IRO and next-neighbor peak positions when K_1 is varied. Due to the strong decrease of d_S with increasing K_1, however, the cage diffusion coefficient, $D(q_m)$, associated with $H(q_m)$ decreases with increasing attraction strength. This can be at least partially attributed to the strong increase of $g(\sigma^+)$, causing an increased HIs-induced slowing.

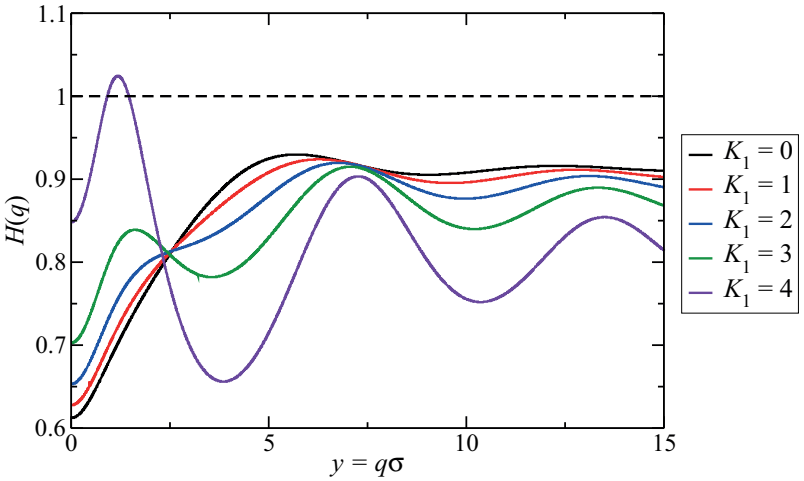

Fig. 8.22.: Hydrodynamic function, $H(q)$, calculated using the hybrid BM-PA scheme for K_1 values as indicated. The corresponding $S(q)$ and $g(r)$ are shown in Fig. 8.21.

In agreement with results for SA systems, a monotonic increase of K with increasing K_1 is observed unlike the non-monotonic behavior discovered for a variation of α. Further, the peak $H(q_c)$ associated with diffusion processes related to the IRO length scale distinctly exceeds one and the value of the cage diffusion coefficient $H(q_m)$ for $K_1 = 4$. Hence, HIs enhance the decay of density correlations on the IRO length scale as found, e.g., for purely repulsive systems for the next-neighbor length scale [186].

High-frequency viscosity

In Fig. 8.23, the effect of SA on η_∞ is shown. The increase of η_∞ with increasing K_1 can be explained by the high sensitivity of η_∞ to $g(\sigma^+)$ in particular, and the next-neighbor region in general, owing to the fast decay of the two-sphere shear-mobility function according to $J(x) \propto x^{-6}$. With increasing K_1, the hydrodynamic coupling between particles becomes stronger resulting in a higher viscous dissipation.
To conclude, the introduction of SA to an originally purely repulsive particles system leads

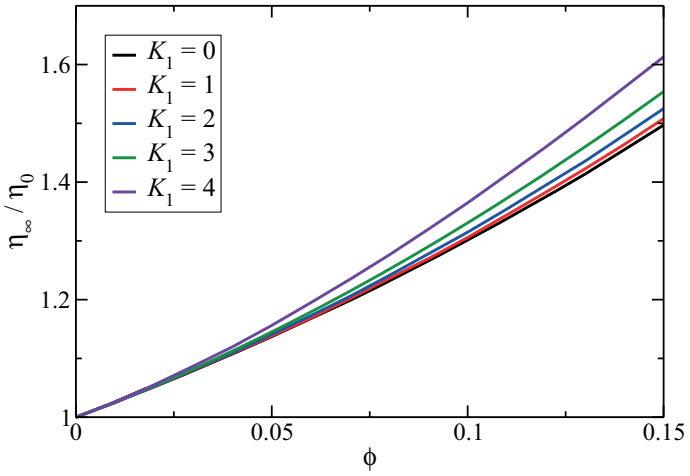

Fig. 8.23.: Effect of attraction on the high-frequency limiting viscosity, η_∞, of a hard-core plus two-Yukawa system, calculated using the PA approximation in Eq. (4.72). The same potential parameters as in Figs. 8.21 and 8.22 are used.

to the formation of an IRO peak both in $S(q)$ and $H(q)$. Moreover, the sedimentation coefficient K increases with increasing SA due to reduced hydrodynamic friction, whereupon d_S decreases due to the larger likelihood of near-contact configurations. For the same reason, the increased viscous dissipation causes η_∞ to grow with increasing K_1.

8.1.5. Variation of the repulsion range

In this subsection, we discuss shortly the effect of the variation of the range of the LR, z_2, on the statics and dynamics of SALR systems for constant B_2^*. To this end, we employ the potential models $M_i(x_0 = 1.1)$ for $i \in \{1, 2, 3\}$, with parameters shown in Table 8.1 and introduced in Subsec. 8.1.1, denoted here for short by M_i. As visible in Fig. 8.24, an increase of z_2 is accompanied by the increase of the potential maximum, $V(r_\mathrm{max})$, as a consequence of the equality of $B_2^*(\alpha)$ for the three models and a particular $\alpha \in [0, 3]$ (c.f. Fig. 8.1b). Note that the attractive potential part, $V(x < x_0)$, is practically unaffected when varying z_2, implying that T_c^* based on the attractive reference potential varies only weakly (c.f. Table 8.3).

Pair structure using the ZH scheme

The pair strutcure of the three potential models for $x_0 = 1.1$ has been previously investigated by Costa *et al.* [91]. Using two different self-consistent integral equation schemes, they found that the reduced temperature, T^*, for which an IRO peak arises, decreases in

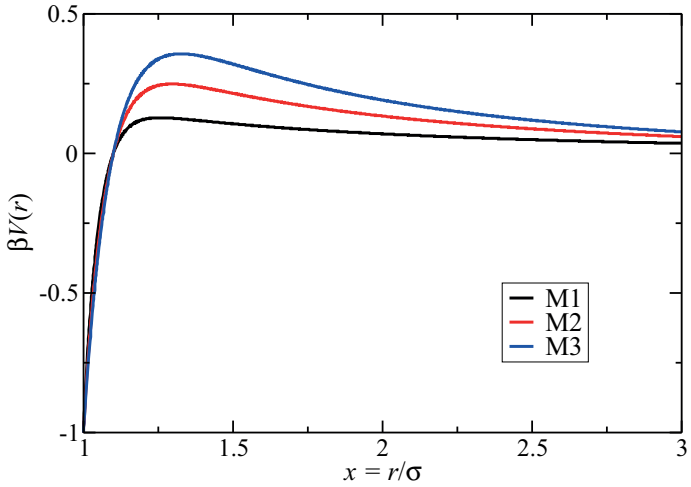

Fig. 8.24.: Reduced pair potentials of models $M_i(x_0 = 1.1)$ for $i \in \{1, 2, 3\}$ and $\alpha = 1$. The associated potential parameters are given in Table 8.1.

going from $M_3 \to M_2 \to M_1$, i.e. in decreasing $V(r_{\max})$. The same trend is observed in our ZH results for $S(q)$ in Fig. 8.25a. The model system M_3 has the smallest z_2 and largest $V(r_{\max})$, giving rise to an enlarged stability of near-contact configurations in comparison to the other models, reflected in larger values of $g(\sigma^+)$ not depicted here.

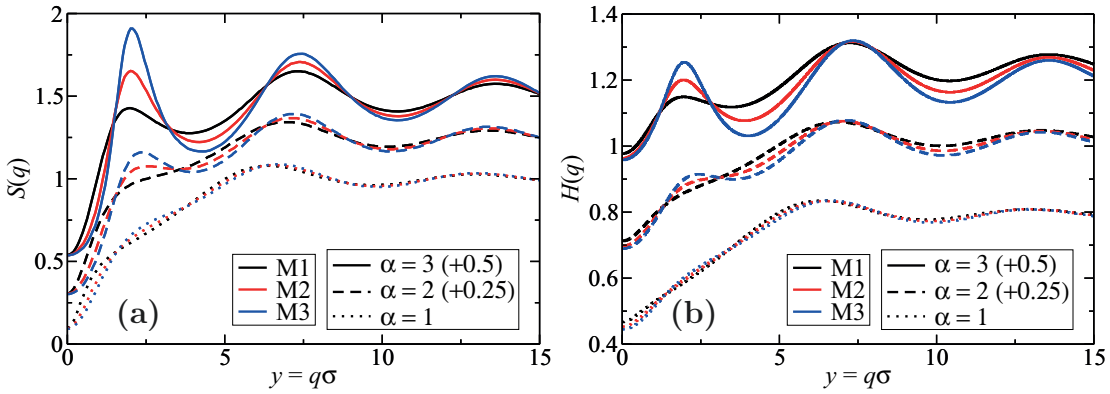

Fig. 8.25.: Model dependence of (a) ZH $S(q)$, and (b) BM-PA $H(q)$ for $x_0 = 1.1$, and $\phi = 0.1$. Black: model M_1, red: M_2, and blue: M_3. The curves for different values of α are distinguished by different line types, and vertical offsets as indicated.

The peak positions $q_{\rm m}$ and $q_{\rm c}$ of $S(q)$ both shift to larger q-values for increasing z_2, indicative of decreasing next-neighbor, and IRO structure distances. The peak in $g(r)$ at roughly $x_{\rm c}$ is shifted to smaller distances as expected, while its width remains practically unchanged (not shown).

Transport properties

Different from $S(q_{\rm m})$, the hydrodynamic function peak height $H(q_{\rm m})$ stays practically constant in going from $M_3 \to M_2 \to M_1$. This can be attributed to the different values of $d_{\rm S}$ of the three models in Fig. 8.26a. Model M_3 with the most pronounced IRO peak and largest $g(\sigma^+)$ has the smallest $d_{\rm S}$. This result points to the sensitivity of $d_{\rm S}$ to the near distance pair structure owing to $\boldsymbol{\mu}_{ii} \sim 1/r^4$ and the dominant influence of the SA implying $d_{\rm S} < d_{\rm S}^{\rm HS}$. By the same token, η_∞ increases in going from $M_3 \to M_2 \to M_1$.

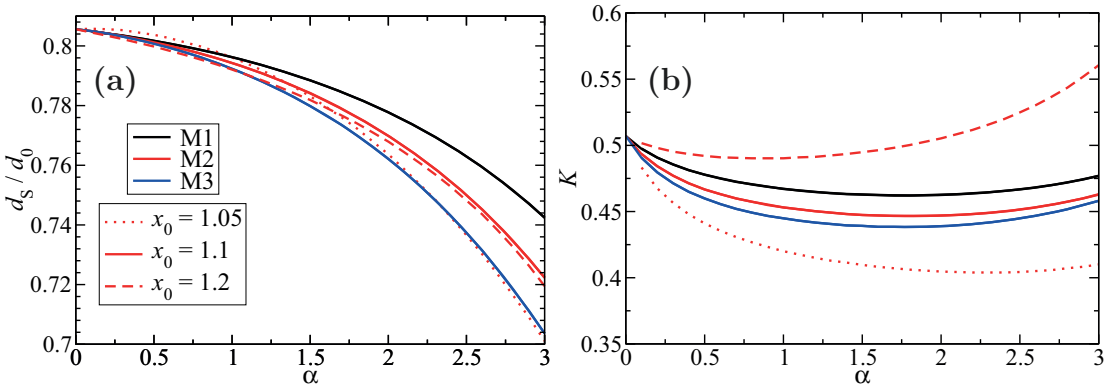

Fig. 8.26.: Model dependence of (a) $d_{\rm S}$ and (b) K (same color code) on the effective attraction range, x_0, and interaction strength, α, for $\phi = 0.1$. Black: model M_1, red: M_2, and blue: M_3. Different x_0 values are distinguished by different line types as indicated. For the discussion of the x_0-dependence, see Subsec. 8.1.6.

The IRO peak $H(q_{\rm c})$ is less pronounced than $S(q_{\rm c})$ for the same α value. In Fig. 8.26b, we present that the non-monotonic α dependence of K, resulting from the competition of SA and LR, is found for all three potential models. Model M_3 with the largest $V(r_{\rm max})$ and smallest range of the LR has the smallest K values. This observation suggests that for the considered potential models sharing the same $B_2(\alpha)$, an increase of the repulsive potential barrier results in a stronger slowing of sedimentation than the increase of z_2.

8.1.6. Variation of the effective attraction range

We briefly discuss here the effect of changing the effective range of attraction, x_0, for fixed interaction strength α implying constant B_2^*. Consider model $M_2(x_0)$ for $x_0 = \{1.05, 1.1, 1.2\}$ and $\alpha = 3$ in Fig. 8.27. A decreasing x_0 is accompanied by an increasing potential barrier, and a faster decay of the LR potential part. We use here $\phi = 0.1$ and $\alpha = 3$, which guarantees that all systems are in the dispersed-fluid state with a distinct IRO peak in $S(q)$. See Table 8.3 for the gas-liquid critical temperature $T_{\rm c}^*$ of the attractive

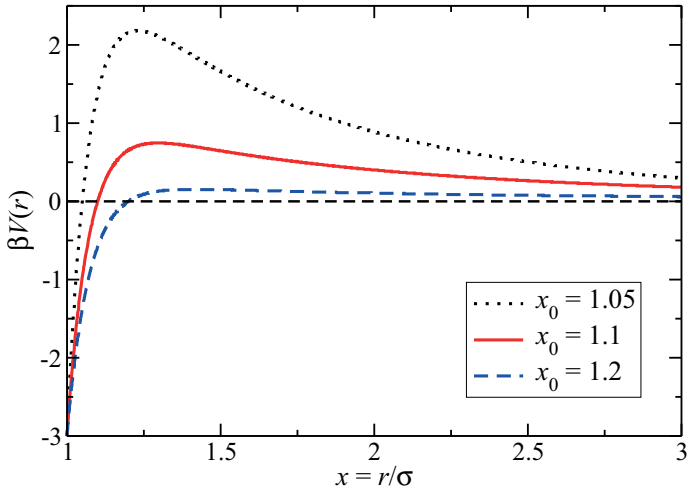

Fig. 8.27.: Pair potential of model M_2, for $\alpha = 3$ and three effective attraction ranges, x_0, as indicated.

reference system.

Pair structure using the ZH scheme

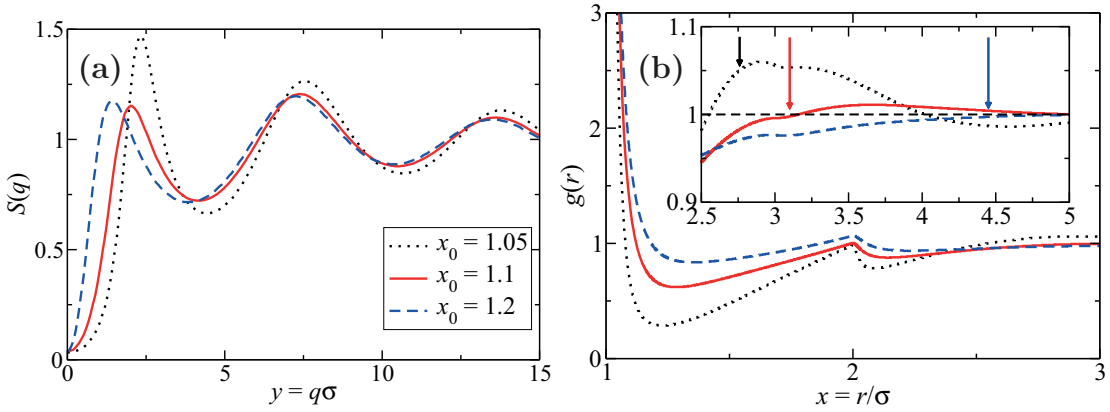

Fig. 8.28.: ZH-calculated (a) $S(q)$, and (b) $g(r)$ (same color code) for model $M_2(x_0 = 1.05)$ (dotted), $M_2(x_0 = 1.1)$ (solid), and $M_2(x_0 = 1.2)$ (dashed), for $\phi = 0.1$ and $\alpha = 3$. The inset in (b) is a magnification of the peak region in $g(r)$ at $x_c \approx 2\pi/y_c$. The respective peak positions for $M_2(x_0)$ are $x_c(x_0 = 1.05) \approx 2.76$, $x_c(x_0 = 1.1) \approx 3.10$, and $x_c(x_0 = 1.2) \approx 4.45$, marked by arrows of respective color.

Fig. 8.28 shows $S(q)$ and $g(r)$ for models $M_2(x_0)$, with $x_0 = \{1.05, 1.1, 1.2\}$ and $\alpha = 3$. With increasing x_0, $g(\sigma^+)$ increases and q_m shifts to larger wavenumber values. While

$S(q_m)$ is only mildly affected by changing x_0, $S(q_c)$ has a surprising non-monotonic dependence on x_0. The most strongly developed IRO peak is at $x_0 = 1.05$ which can be associated with a clearly visible peak in $g(r)$ at $x_c = 2\pi/q_c \approx 2.76$ as marked in the inset of Fig. 8.28b. The larger IRO peak for $x_0 = 1.2$ in comparison to that for $x_0 = 1.1$ can not be attributed to the peak in $g(r)$ at x_c, since for $x_0 = 1.2$ only a very shallow peak can be observed. Our results suggest that regarding model $M_2(x_0 = 1.2)$, the broad attractive potential part taken together with the long-ranged but weak repulsion, favor intermediate-range order. In addition, it can be expected that the IRO structure in systems with $x_0 = 1.05$, and 1.1 will differ from the one for $x_0 = 1.2$, since a larger effective attraction range results in more diffuse near-contact configurations. To what extent changes in the IRO structure affect $g(x_c)$ is a topic for future simulations. We conclude that a peak in $g(r)$ at $x_c \approx 3 \sim 5$ can be an indication of IRO but not necessarily so.

Transport properties

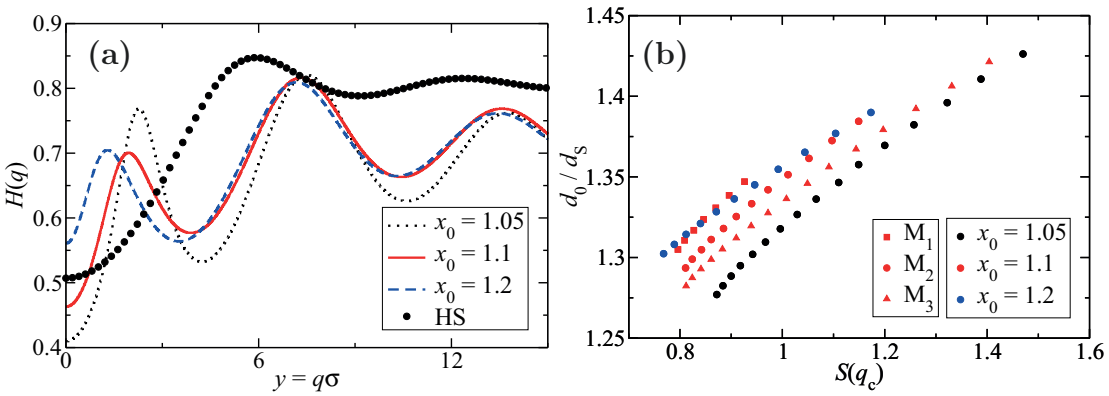

Fig. 8.29.: (a) BM-PA calculated $H(q)$ of the systems in Fig. 8.28. For comparison, the $H(q)$ of a hard-sphere system of same $\phi = 0.1$ is represented by the filled black circles. (b) d_0/d_S versus height, $S(q_c)$, of the IRO peak. Shown are results of all potential models M_1 (squares), M_2 (circle), and M_3 (upper triangles) for $x_0 = 1.05$ (black), $x_0 = 1.1$ (red), and $x_0 = 1.2$ (blue).

Using Fig. 8.29a, we show that also $H(q_c)$ has a non-monotonic x_0 dependence. Very interestingly, d_S, $S(q_c)$ and $H(q_c)$ share a non-monotonic x_0 dependence. This is exemplified in Fig. 8.29b where d_0/d_S is plotted versus $S(q_c)$. For systems with more pronounced IRO, d_S becomes smaller. As one expects, an increasing clustering tendency signaled by a larger $S(q_c)$ is reflected by a smaller d_S. The onset of a non-monotonic x_0 dependence of d_S for $\alpha \approx 1.5$ is accompanied by the first occurrence of an IRO peak for $x_0 = 1.05$ (c.f. Fig 8.26a).

Results for the sedimentation velocity, K, are presented in Fig. 8.26b. It is shown that K increases significantly with increasing x_0, and a concurrent increase of $g(\sigma^+)$ as observed for purely attractive systems. Note that for all considered SALR systems and fixed α, K follows the same trends as $1/q_c$.

8.2. Comparison with experiment

To investigate the applicability and accuracy of our structural and transport coefficients calculations for SALR systems, we have compared our results to NSE measurements of $H(q)$ and $D(q)$ of Lysozyme proteins in deuterium oxide (D_2O). The NSE experiments have been performed at the National Institute of Standards and Technology (NIST) by P. D. Godfrin and Y. Liu. Lysozyme is a frequently used protein of nearly spherical tertiary structure with mean radius $a \approx 1.5\,\mathrm{nm}$ [98]. More specifically, its shape is that of a prolate ellipsoid [243]. For details of the sample preparation, we refer to Chapter 5 of [98].
The volume fraction of the Lysozyme samples has been calculated on basis of the mass fraction, X_L, of purified lyophilized Lysozyme in D_2O [98]. With the known specific volume of Lysozyme, $V_0 = 0.717\mathrm{ml/g}$, [98, 244] and the known mass density, ρ_S, of D_2O, the volume fraction ϕ of a sample can be calculated using [98]:

$$\phi = \frac{X_L V_0}{X_L V_0 + \frac{(1-X_L)}{\rho_S}}\,. \tag{8.6}$$

For each sample, $S(q)$ and $D(q)$ have been measured, with $H(q) = S(q)\,D(q)/d_0$. In addition, a fitting procedure has been employed using the hard-core plus two-Yukawa SALR potential to infer the potential parameters αK_i, and z_i ($i \in \{1, 2\}$) from the IET-fit to the experimental $S(q)$. The effective protein $\beta V(r)$ has been fitted individually for each sample to account for effects such as the variation of the pH value with changing ϕ. For simplicity, the proteins have been modeled as spherical with a diameter of $\sigma \approx 30.74$Å.
An overview over the different samples and the corresponding potential parameters obtained by this fitting is presented in Table 8.5.

Pair structure

In Figs. 8.30 (a)-(c), for selected systems we compare the SANS measured $S(q)$ with our ZH calculations using the fit parameters in Table 8.5. The agreement of the theoretical curves with the experimental ones is overall good, with deviations most visible for larger q in the region around q_m, where, however, the scatter in the SANS data is quite large.

Sample	T [°C]	wt [%]	ϕ	αK_1	αK_2	z_1	z_2
1	25	5	0.0398	6.0291	4.2743	10	1.2473
2	5	20	0.1432	6.4666	3.2868	10	2.7839
3	25	20	0.1472	5.8511	3.5588	10	2.9338
4	50	20	0.1551	6.1753	4.3252	10	3.3055
5	5	25	0.2017	6.3	3.0811	10	3.6117
6	25	25	0.2099	5.743	3.3574	10	3.8785
7	50	25	0.2091	5.2251	3.7215	10	4.0331

Table 8.5.: Temperature, T, and concentration, in wt [%], of the Lysozyme samples in D_2O. In addition, the parameters of the hard-sphere plus two-Yukawa potential $V(r)$ obtained from the IET-fit of the experimental $S(q)$ are presented.

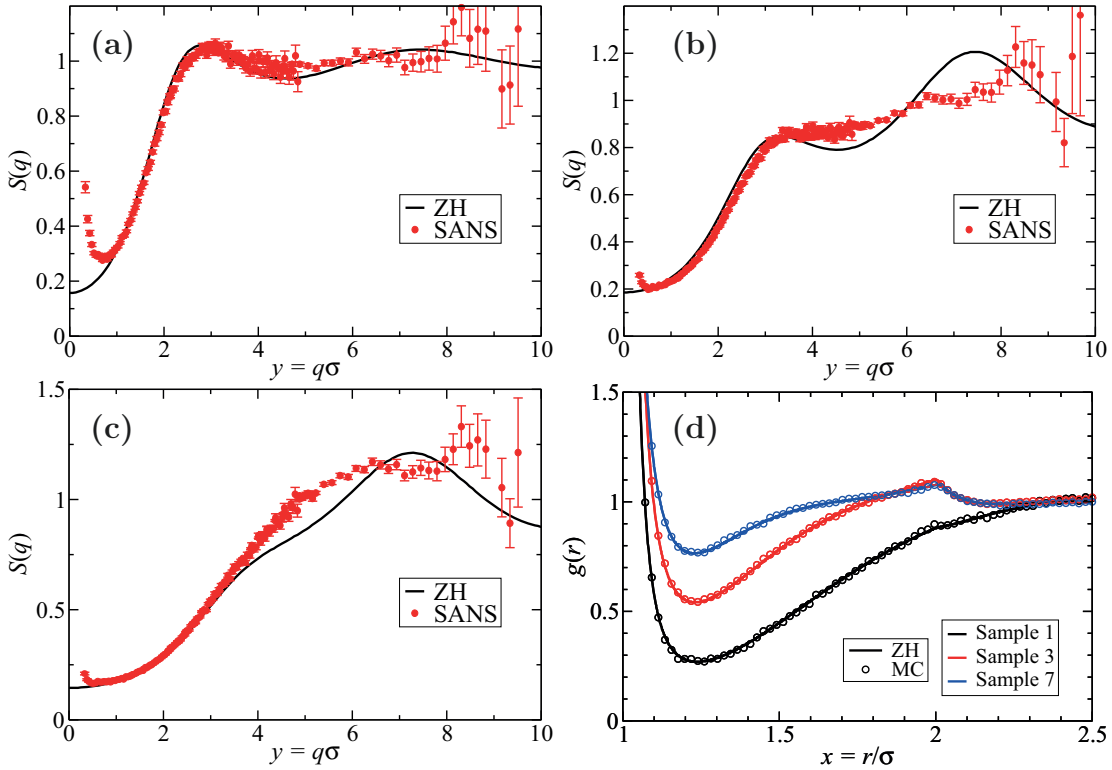

Fig. 8.30.: (a), (b), and (c): Comparison of the experimental measured $S(q)$ of Lysozyme solution samples (a) 1, (b) 3, and (c) 7 in D_2O with the ZH-calculated $S(q)$ using the potential parameters in Table. 8.5. (d): ZH $g(r)$ of samples 1, 3, and 7 in comparison with corresponding MC simulation data using potential parameters in Table 8.5.

The scanned q range in the SANS measurements is focused on the IRO peak region, extending roughly up to q_m. The experimental $S(q)$ of samples 1 and 3 have an IRO peak, while for sample 7 no low-q peak is visible.
In Fig. 8.30d, we exemplify the high accuracy of our ZH calculations of $g(r)$ by the comparison with MC data for the systems in Figs. 8.30 (a)-(c). The perfect agreement of the MC simulations with the ZH-$S(q)$ calculations indicates that all samples are in the dispersed-fluid state.

Short-time dynamics

As discussed in Subsec. 4.1.6, one great advantage of NSE in comparison to light scattering is that $S(q,t)$ is determined from atomic or molecular positions such that the scattering signal is not dominated by particle clusters or aggregates as it is in DLS. The comparison of the NSE determined $H(q)$ for various Lyszoyme solutions with the BM-PA calculations using ZH input for $g(r)$ and $S(q)$ is presented in Fig. 8.31. Triggered by the high cost of NSE measurements, the experimental q-range is limited to the IRO peak region.

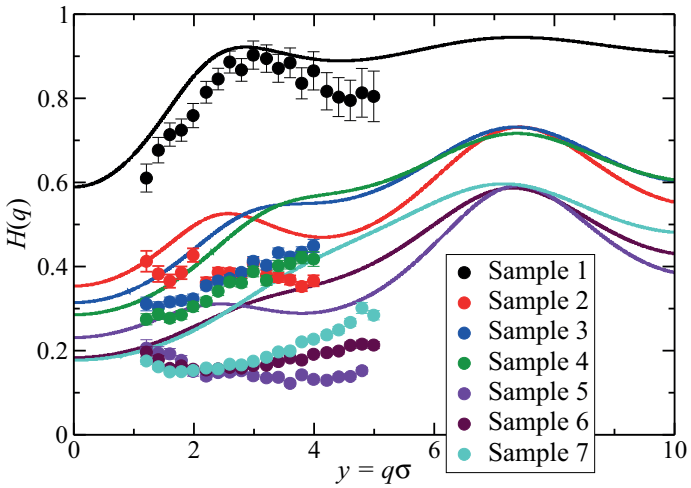

Fig. 8.31.: NSE results (symbols) for the $H(q)$ of the Lysozyme samples in D_2O listed in Table 8.5. Here, $H(q)$ is deduced from the experimental $D(q)$, and $S(q)$ by $H(q) = S(q) \cdot D(q)/d_0$. For comparison, our BM-PA $H(q)$ results are shown using the ZH $g(r)$ and $S(q)$ as input (solid lines). The parameters of the hard-sphere plus two-Yukawa potential are given in Table 8.5.

Our calculations of $H(q)$ are in overall good agreement with the experimental data. For the lowest concentrated Sample 1 with $\phi = 0.0398$, the agreement is nearly quantitative. With increasing ϕ, the quantitative agreement worsens but it remains qualitatively good. The

BM-PA $H(q)$ reproduce all the trends observed for the experimental data, i.e., the crossing points of the different sample curves. The offset between experimental and theoretical results for $H(q)$ for larger ϕ can be partially attributed to the inaccuracy of the PA scheme regarding the d_s part. The disregarded non-spherical shape of Lysozyme proteins may be also of importance. While the validity of the theoretical description of Lysozyme as globular has been verified by the comparison of the theoretical and experimental $S(q)$ [98], the actually ellipsoidal shape may have a significant impact on the dynamics especially for large ϕ. In addition, the presence of protein hydration layers could also lead to the overestimation of the experimental $H(q)$ by our theoretical predictions.

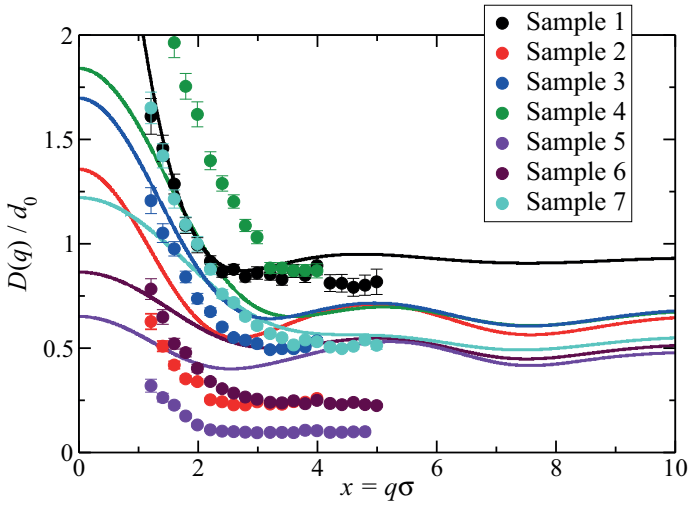

Fig. 8.32.: NSE results for the experimentally directly accessible diffusion function, $D(q)$ (symbols), with the theoretical predictions. $D(q)$ is obtained by division of the BM-PA $H(q)$ in Fig. 8.31 by the respective ZH $S(q)$ (solid lines).

The agreement between theory and experiment becomes less good when $D(q)$ is considered. As it is observable in Fig. 8.32, owing to the smallness of $S(q)$ at low q experimental-theoretical deviations in $H(q)$ are enhanced after division by $S(q)$ leading to quantitative differences. However, and quite importantly, one infers from the experimental-theoretical comparison that for the NSE measurement of d_S a sufficiently broad q-range is required extending well beyond q_m, as discussed earlier in Subsec. 8.1.3. Note that the oscillations in the experimental $D(q)$ are weak for $q \gtrsim q_c$.

To conclude, the comparison of our calculations of $S(q)$, $H(q)$, and $D(q)$ with NSE measurements on Lysozyme solutions shows the applicability of our theoretical methods originally designed for larger colloidal particles also to solutions of nanometer-sized proteins.

8.3. Modified Lennard-Jones-Yukawa system

In this section, we present our study of a second SALR system with a Lennard-Jones plus Yukawa pair potential given in Eq. (2.13). For this SALR system, we have similar structural and diffusion results as for the already considered two-Yukawa SALR system, with the IRO peak as an universal feature of SALR systems. While the hard- core potential part in the two-Yukawa SALR system renders dynamical simulations more difficult, the LJY potential has a steep but soft short-range repulsion allowing for the usage, e.g., of MD techniques. MD based mesoscale simulation methods (c.f. Subsec 8.3.3) allow for a detailed investigation of the structure and dynamics of (transient) clusters. Especially in the equilibrium-cluster and percolated phases, knowledge of the cluster shape (e.g., elongated vs. spherical) is indispensable for the understanding of dynamic properties such as the zero-shear viscosity [4].
Firstly, we investigate the influence of the variation of the parameter ϵ characterizing the strength of attraction in the LJY potential (c.f. Eq. (2.13)), and of varying ϕ on pair distribution functions and transport properties. For this purpose, we employ the ZH and BM-PA scheme, for $S(q)$, $g(r)$, and transport properties, respectively. To quantify the accuracy of the ZH results for $g(r)$, we compare them with MD simulations using the HOOMD-blue software package [245–247] run on GPU. Our MD simulations are performed for the NVT ensemble with $N = 2000$ particles in a cubic simulation box, using a Nosé-Hoover thermostat. Based on the phase diagram of Mani *et al* [34], we select ϵ and ϕ such that the investigated systems are mostly in the dispersed-fluid phase.
Secondly, we shortly describe an ongoing theory-simulation collaboration with S. Das, G. Gompper, and R. G. Winkler from the IAS-2/ICS-2 of the Forschungszentrum Jülich. The collaboration aims at the assessment of the accuracy of our dynamic calculation schemes in the dispersed-fluid phase state, and the exploration of possible extensions of the analytic methods to the equilibrium-cluster phase. We are in the process of comparing our theoretical $S(q)$ and $H(q)$ results with multi-particle collision dynamics (MPC) simulation results by the IAS-group, in which the effect of HIs is included.

8.3.1. Pair structure

The ZH-calculated $S(q)$ and $g(r)$ for LJY systems of constant $\rho^* = \rho\sigma^3 = 0.2$ and different values of ϵ are shown in Fig. 8.33. The corresponding pair potentials are depicted in Fig. 2.5. Similar to the case of increasing K_1 in the two-Yukawa SALR system, q_m is shifted to larger q-values with increasing ϵ, while $S(q_\mathrm{m})$ has a non-monotonic ϵ dependence. Furthermore, a significant IRO peak develops with increasing ϵ. For the largest considered

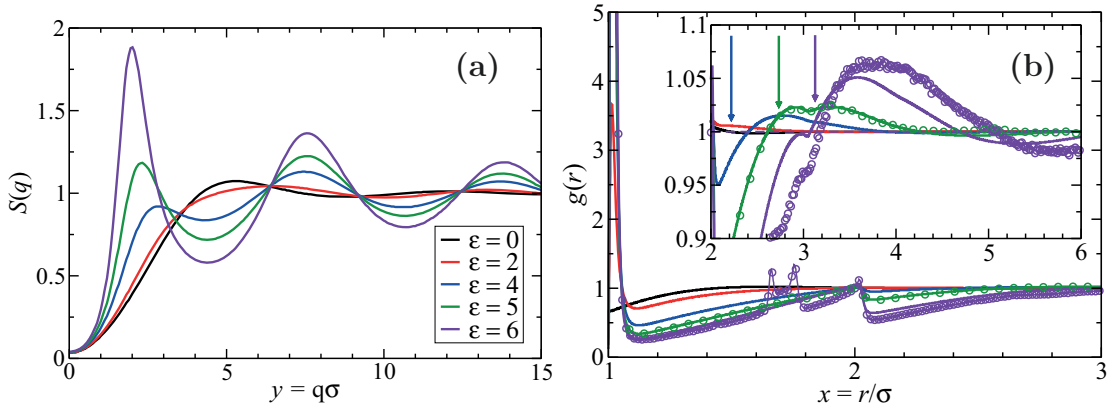

Fig. 8.33.: Solid lines: ZH (a) $S(q)$, and (b) $g(r)$ (same color code) of LJY systems with $\rho^* = 0.2$ and various ϵ values as indicated. Accoridng to Mani *et al.* [34], the system is in the equlibrium cluster phase for $\epsilon = 6$. In (b), MD simulation results for $\epsilon = 5$ (green), and $\epsilon = 6$ (violet) are shown by the symbols and the thin lines. The onset of peak formation in $g(r)$ at $x \approx 1.59$ and $x \approx 1.85$ indicates the formation of non-highly transient structures. The inset focuses on the peak region of $g(r)$ associated with the IRO peak in $S(q)$. Here, the arrows mark the positions $x_c = 2\pi/q_c$.

value, $\epsilon = 6$, the system is in the equilibrium cluster phase state according to the phase diagram of Mani *et al.* [34]. While for smaller ϵ the simulation and ZH $g(r)$ are in perfect agreement as seen in Fig. 8.33b, for $\epsilon = 6$ our MD simulations show additional peaks at $x \approx 1.59$ and $x \approx 1.85$. The positions of these peaks are similar to the values observed in hard-core SALR systems representing the presence of an octahedron structure ($x = \sqrt{8/3}$), and two eqilateral triangles with a common side ($x = \sqrt{3}$) as discussed by Valadez-Pérez *et al.* [89]. For the LJY systems, we have again that $x_c = 2\pi/q_c$ does not strictly coincide with the onset of a peak in $g(r)$ at $x \sim 2.5$, associated with IRO (c.f. inset of Fig. 8.33b). Note that $S(q_c)$ does not exceed the critical value $S_{crit}(q_c) \sim 2.7$, given by Godfrin *et al.* [33] as an empirical criterion for the onset of a first-order equilibrium-cluster phase transition for the two-Yukawa SALR system.

8.3.2. Short-time dynamics

BM-PA results for the $H(q)$ of the LJY-SALR systems are shown in Fig. 8.34. Like in two-Yukawa systems, $H(q)$ shares the positions q_c and q_m with those of $S(q)$. The monotonic decrease of $H(q_m)$ with increasing ϵ results from the associated strong decrease of d_S depicted in Fig. 8.35a. An enlarged attraction strength leads to an increased likelihood of near-contact configurations, and thus to a decrease of d_S. Moreover, K is distinctly

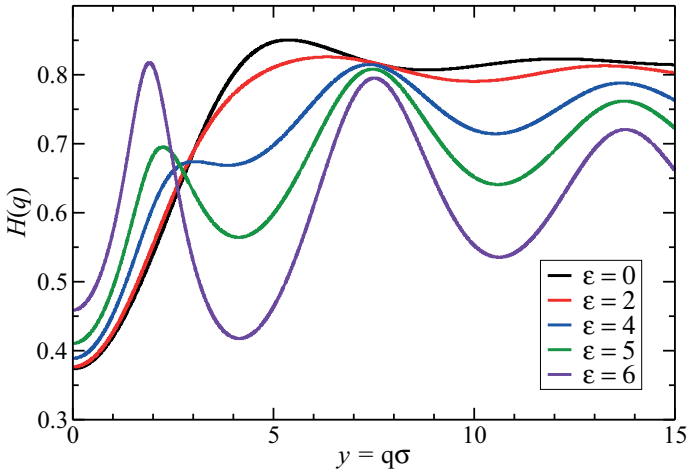

Fig. 8.34.: BM-PA calculated $H(q)$ for LJY systems of various attraction strengths ϵ, and $\rho^* = 0.2$. As input to the hybrid BM-PA scheme, the ZH $S(q)$ and $g(r)$ in Figs. 8.33 are used.

increased for increasing ϵ (c.f. inset of Fig. 8.35a), and the IRO peak of $H(q)$ starts to develop for larger ϵ values than that of $S(q)$. Note that the system for $\epsilon = 6$ is in the equilibrium cluster phase where the simulated and ZH-calculated $g(r)$ differ. Hence, a comparison of the BM-PA $H(q)$ with simulations of $H(q)$ regarding the influence of HIs is important to investigate to what extent clusters affect the short-time dynamics.

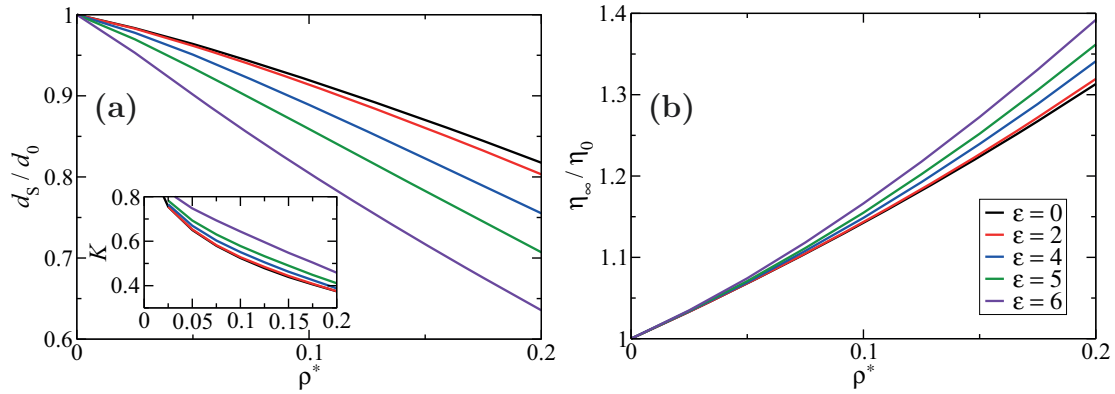

Fig. 8.35.: Reduced density dependence of (a) d_S, and inset K, and (b) η_∞ for values of ϵ as indicated. For d_S and η_∞ the PA approximation, and for K the hybrid BM-PA scheme have been used, with ZH input $S(q)$ and $g(r)$ from Fig. 8.33. The color code in (a), and its inset is the same as in (b).

In Fig. 8.35b, we show the ϵ and ρ^* dependence of η_∞ for LJY systems. Since η_∞ is highly sensitive to near-contact configurations, it increases with increasing ϵ. While not shown

here, $g(r)$, $S(q)$, and $H(q)$ of LJY systems in the dispersed-fluid phase behave similarly to those of the two-Yukawa SALR systems in their ρ^* dependence.
In conclusion, our theoretical and MD simulation results for the LJY system have the same characteristic behavior as the two-Yukawa SALR system underpinning the IRO peak formation as an universal feature of SALR systems. Owing to the soft nature of the Lennard-Jones repulsion part, the LJY system is more amenable to dynamic simulations considered in the following subsection.

8.3.3. Comparison with MPC simulations

To test the accuracy of our analytic methods, and to study the dynamics also in the equilibrium cluster phase, we use the mesoscale multi-particle collision dynamics (MPC) method. The MPC method is a hybrid simulation technique combining MD simulations for the colloidal particles with the multi-particle collision dynamics method for the fluid, with HIs being accounted for [248, 249]. The MPC method is useful for a broad variety of systems, from colloidal suspensions [250–252] to active swimmers [253, 254]. In this section, we present preliminary results of our collaboration with S. Das, G. Gompper, and R. G. Winkler [255], who have performed the MPC simulations.
The simulations include 1560 particles in the NVT ensemble. For the achievement of a better statistics, the calculated properties are averaged over 15 individual runs with 2 million iterations each. The same LJY potential (Eq. (2.13)) as in our theoretical calculations is employed.
As noted before, the MPC simulations can be readily used for the study of the equilibrium-cluster phase where the accuracy and also the convergence of the ZH method is usually poor. Using MPC, we explore here the effect of increasing the attraction strength ϵ while keeping ρ^* fixed. The two investigated systems are in the dispersed-fluid phase ($\epsilon = 4$) and the equilibrium-cluster phase ($\epsilon = 7$), respectively, and we study the difference in the $g(r)$ and $S(q)$ in the two phases. Fig. 8.36a shows a simulation snapshot for the cluster phase system, with $\epsilon = 7$ and $\rho^* = 0.1$. The CSD of this system, $N(s)$, obtained from the simulations is shown in Fig. 8.36b, giving a preferred cluster size including 7 particles. In contrast, the $N(s)$ of the dispersed-fluid phase system is monotonically decaying.
In Fig. 8.37, the $S(q)$ and $g(r)$ of the two systems are shown to highlight characteristic differences in their behavior for the dispersed-fluid and equilibrium-cluster phase, respectively. While for $\epsilon = 4$, the ZH $S(q)$ and $g(r)$ are in very good agreement with the MPC data including the $g(x \approx \sigma)$ region, the ZH calculations do not converge for $\epsilon = 7$. In the simulation data for $\epsilon = 7$, a large IRO peak, $S(q_c)$, is visible exceeding clearly the critical

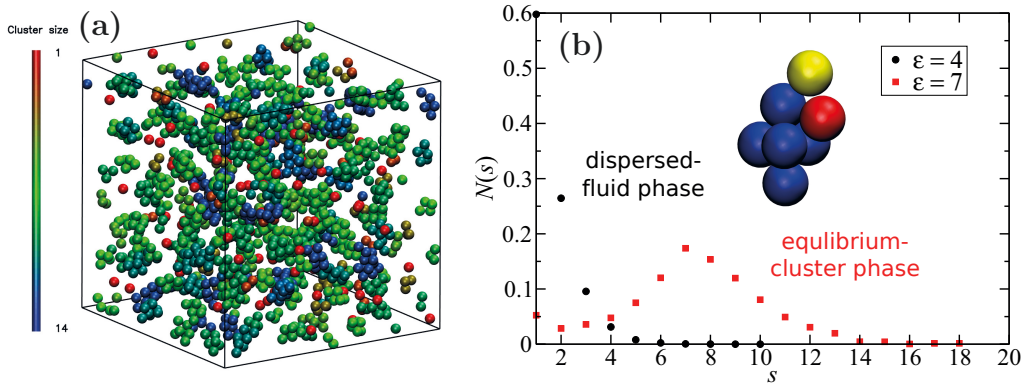

Fig. 8.36.: (a) MPC simulation snapshot of a LJY system with $\epsilon = 7$, and $\rho^* = 0.1$ in the equilibrium-cluster state. The color signals the membership of particles to a cluster of size s (see left vertical color bar). (b) Cluster-size distribution function, $N(s)$, for $\epsilon = 4$ and $\epsilon = 7$, and $\rho^* = 0.1$, gained from the MPC simulations. The inset shows a typical equilibrium cluster observed in the simulations. Snapshot kindly provided by S. Das (ICS-2 / IAS-2).

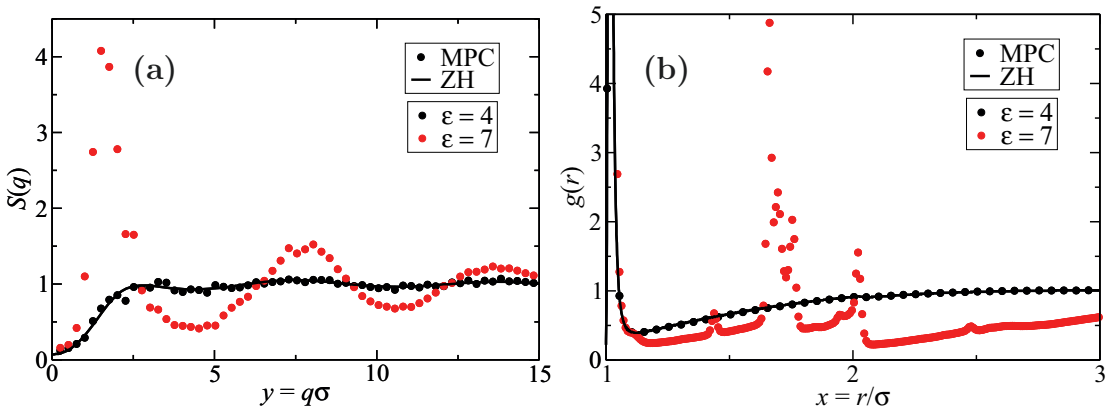

Fig. 8.37.: MPC simulation results for (a) $S(q)$, and (b) $g(r)$ of LJY systems with $\epsilon \in \{4, 7\}$ and $\rho^* = 0.1$, in comparison with the ZH result for $\epsilon = 4$. Our ZH approximation calculations are not converging for $\epsilon = 7$.

value 2.7 by Godfrin *et al.* [33]. The corresponding $g(r)$ is strongly peaked at soft particle contact distance $x = 1$ ($g(r \approx \sigma) \sim 150$), with additional peaks at $x \approx 1.43$, 1.66, and about 2. As discussed earlier, the pronounced peak at $x \approx 1.66$ corresponds to particles forming two equilateral triangles with a common side [89]. Using the reduced position, $x_{\min}$, of the pair potential minimum as characteristic distance, we obtain $\sqrt{8/3}\, x_{\min} \approx 1.68$ in good agreement with the peak position 1.66 observed in simulation. Moreover, the small peak at $x \approx 1.43 \approx \sqrt{2}$ reflects the presence of cubically located particles. Note that the structure of clusters is strongly influenced by the balance of SA and LR potential parts. For the $\epsilon = 7$, the clusters observed in the MPC simulations are spherical rather than elongated as seen, e.g., in the present simulation snapshot (Fig. 8.36a) and likewise in [34].

We are not in the position yet to present a comparison of our predictions of $H(q)$ and $D(q)$ with the MPC simulation data for LJY systems. We expect the short-time properties presented in this thesis, and based on the PA and BM methods to be in qualitative agreement with the future MPC simulation results for systems also in the equilibrium-cluster phase state as long as the particles forming clusters can move individually, i.e. as long as the clusters do not form rigid objects. Otherwise, there will be hydrodynamic screening inside a cluster, and a polydisperse modeling of the system is more appropriate.

9. Conclusions and outlook

In this thesis, we have developed and assessed the performance of a variety of versatile and easy-to-apply calculation methods for static and dynamic properties of dispersions of globular colloidal particles. The calculated properties encompass dynamic short- and long-time diffusion functions and coefficients, and static pair distribution and scattering functions as well as osmotic pressures and compressibilities. The explored dispersions include hard-sphere-like particles with internal hydrodynamic structure, charged-particles suspensions of submicron colloidal spheres, and solutions of nanometer-sized globular (Lysozyme) proteins with competing short-range attraction and long-range repulsion. We have validated the good accuracy of the theoretical calculation schemes by a comprehensive comparison with experimental and simulation results. Furthermore, we have presented a bottom-up approach to the modeling of the cross-flow UF process. For this purpose, we have explored first how the internal hydrodynamic particle structure and surface charge affect the transport properties of concentrated systems. Secondly, we have used the accurate transport coefficient expressions as input in our ultrafiltration (UF) model for calculating the near-membrane concentration profile and trans-membrane permeate flow. In this way, we have bridged the gap from individual particle properties via the transport and structure in concentrated bulk systems to an important technological process.

In particular, we have presented a toolbox of easy-to-implement analytic methods for calculating short-time and long-time transport properties of suspensions of spherical particles with intrinsic hydrodynamic structure. The analytic transport coefficient expressions for hard-sphere-like systems given in the thesis combine high accuracy with a practical implementation, and they apply to the full liquid-phase concentration regime. The expressions are particularly useful to experimenters for a fast yet precise data analysis of scattering and rheo-mechanical measurements. We have highlighted this by our analysis of SLS and DLS experiments on non-ionic PNIPAM microgels in DMF. By a detailed comparison of hard-sphere with soft Hertz potential calculations, we have shown that non-ionic and strongly cross-linked microgels behave statically to good accuracy as hard spheres, but hydrodynamically as permeable spheres with a reduced penetration length $\lambda_x \approx 0.03$ corresponding to a reduced hydrodynamic radius of $\gamma = 0.97$.

The intra-particle hydrodynamic structure has been accounted for using the hydrodynamic radius model (HRM) where the particles are described hydrodynamically as no-slip spheres, characterized by a hydrodynamic radius derived from a single-particle transport property for unchanged direct interactions. In spite of its simplicity, the HRM is univer-

sally applicable since correction terms are usually quite small, i.e. of quadratic order in the reduced slip length. In many particulate systems, these corrections are negligible, and a unique hydrodynamic radius, a_h, can be used independent of the considered transport property. As we have shown in comparison with existing computer simulation results, the HRM-based scaling expressions are decent approximations also for strongly structured hard-sphere-like particles, characterized by values of γ significantly smaller than one, provided a_h is deduced from an associated single-particle transport coefficient, namely from the intrinsic viscosity $[\eta]$ in viscosity calculations, and d_0 in self-diffusion and sedimentation calculations for concentrated suspensions. The toolbox results for the collective diffusion coefficient, d_C, and the steady-shear viscosity, η, in this thesis have been already profitably used by Roa *et al.* [39] in their generic cross-flow UF study of uncharged solvent-permeable particles suspensions.

We have presented a vast number of results for hydrodynamically structured, rigid particles with hard-core interactions. The HRM, and a part of our toolbox methods, are likewise applicable, with appropriate modifications, to spherical particles with short-ranged soft interactions. We have shown this in detail for the reduced hydrodynamic function, $h_d(q)$, of soft Hertz-potential particles of reduced interaction strength $\epsilon = 10$. According to our calculations based on the BM method, the useful hydrodynamic function scaling is valid also for soft-particles dispersions.

However, the presented scaling relations for d_S, K, and the long-time self-diffusion coefficient, d_L, are not valid any more for particles with long-range soft repulsion that can not be adequately described statically by an effective excluded volume diameter. Examples in case are low-salinity suspensions of charge-stabilized particles [186], and quasi-two dimensional systems of magnetically repelling particles at a liquid-gas interface [256]. While the presented scaling expressions are invalid for these systems, their hydrodynamic structures are still well described by the HRM, so that our HRM expressions based on the hybrid BM-PA scheme can be used for the calculation of their transport properties.

The applicability of the HRM to charge-stabilized dispersions was explicitly demonstrated in our study of permeability and softness effects on static and dynamic system properties of ionic microgel suspensions. For this purpose, an effective pair potential describing ionic microgels due to Denton [63, 78] was used and complemented by the Hertz potential for description of the soft steric interactions [57]. We employed realistic values for the effective particle charge and screening length determined in a previous study from experimentally measured values [57], and we have investigated theoretically the effect of different particle softness and permeability, as characterized by the Hertz potential interaction strength ϵ, and the HRM parameter γ, respectively. We find that both the particle softness and

the permeability severely influence short-time diffusion properties of ionic microgel suspensions. Quite interestingly, the sedimentation coefficient K is particularly sensitive to particle softness, being strongly enhanced for decreasing ϵ. The short-time self-diffusion coefficient, d_S, follows the same trend, however with a weak ϵ dependence only. A non-zero microgel permeability attenuates the slowing effect of the HIs, as signaled by the shift of the $H(q)$ curve to larger values with decreasing γ. Regarding the diffusion function, $D(q)$, a low-q upturn is predicted theoretically with decreasing γ especially for larger ϵ values, in accord with experimental observation [198]. Our theoretical predictions for $H(q)$ and $D(q)$ are useful for the analysis of dynamic scattering measurements on permeable and / or soft charged-particles suspensions.

In a joint experimental-theoretical work [227], we studied additionally amphoteric microgels in the zwitterionic regime. We have investigated the influence of opposite charges of same amounts inside the backbone of the PNIPAM microgel particles on the equilibrium suspension microstructure. For this purpose, zwitterionic microgels with increasing amounts of zwitterionic comonomer have been used, with the pure PNIPAM system serving as a reference. Based on SANS measurements and our polydisperse hard-sphere model calculations combined with the decoupling approximation, we could show that the measurable static structure factor, $S_M(q)$, is well described by the hard-sphere model up to a total volume fraction $\phi_T \approx 0.4$. At larger volume fractions, the experimental scattering data deviate significantly from those predicted by the hard-sphere model. At very large concentrations, the microgels are likely to overlap or de-swell. In summary, the sophisticated intra-particle structure of the microgels containing acidic and basic comonomers affects the particle interactions for volume fractions $\phi_T \geq 0.4$ only. At small ϕ, the zwitterionic microgels behave similarly to pure PNIPAM microgels.

In addition to dispersions with purely repulsive interactions, we have comprehensively explored systems with competing SA and LR such as low-salinity Lysozyme protein solutions. Our theoretical analysis of these systems has shown that the competition of SA and LR leads to unusual features in the concentration and interaction strength dependence of transport properties in the dispersed-fluid phase that are not encountered in systems with purely repulsive or attractive soft interactions. Two different SALR systems have been investigated, namely the hard-core plus two-Yukawa potential model system, and the Lennard-Jones plus repulsive Yukawa potential system. We have shown that the observed structural and dynamical features of these two systems are general effects of the subtle interplay of SA and LR. For the two-Yukawa SALR system, we studied the effects of variations in the interaction strength, α, attraction strength, K_1, range of repulsion, z_2, effective attraction range, x_0, and particle volume fraction ϕ. For the LJY-SALR system,

we analyzed the effect of varying the attraction strength, and discussed the ϕ dependence of d_S, sedimentation coefficient, K, and high-frequency viscosity η_∞.

For the first time to our knowledge, we showed that an IRO peak signaling a (transient) clustering tendency, is present also in the hydrodynamic function, $H(q)$, and the diffusion function $D(q)$. The IRO peak of both functions grows with increasing α. While the self-diffusion coefficient, d_S, and the high-frequency viscosity, η_∞, change monotonically with increasing α, the sedimentation coefficient, K, varies non-monotonically, owing to a subtle interplay of the SA and LR soft potential parts with the short-range and long-range HIs contributions. While d_S and η_∞ are most strongly influenced by the SA through the resulting changes in the near-contact part of the RDF $g(r)$, K has a subtle dependence on several potential features. Interestingly, d_0/d_S scales monotonically with the height, $S(q_c)$, of the IRO peak in $S(q)$. Furthermore, the collective diffusion coefficient, d_C, is strongly enhanced with increasing ϕ or increasing α. Our transport properties results allow to assess the validity of two GSEs relating η_∞ to d_S and d_C, respectively. While the GSE related to d_S is valid to good approximation in the whole considered concentration regime $\phi \leq 0.15$ where the SALR system is in the dispersed-fluid phase state, the GSE relation for d_C is violated for all α, and all non-zero ϕ.

Moreover, we have analyzed how a decent estimate of d_S in SALR systems is obtained from NSE or DLS experiments performed at a specific wavenumber, $q^* > q_m$, for which $S(q^*) = 1$ is valid. Our general results for SALR systems in the dispersed-fluid phase are helpful as a prerequisite and reference in future studies aimed to identify so far unknown dynamic features, e.g., in the equilibrium-cluster phase.

Furthermore, our toolbox of analytic methods for the calculation of short-time dynamic properties of globular particles suspensions has been successfully applied to analyze NSE measurements on low-salinity solutions of nanometer-sized Lysozyme proteins. Albeit overestimating the NSE results for $H(q)$ at larger ϕ, our calculations are in good qualitative agreement with the measurements, reproducing in particular all experimental trends. Our BM-PA scheme calculations use the ZH-calculated structure factors and RDFs as the only input. Pair potential parameters have been obtained from the IET structure factor fitting of the experimental $S(q)$, using the two-Yukawa SALR potential. Differences between the experimental and theoretical $H(q)$ can be attributed to the disregarded non-sphericity of the (Lysozyme) protein shape, and the presence of a protein hydration layer potentially giving rise to a larger effective hydrodynamic particle radius.

Regarding SALR systems described by the Lennard-Jones plus repulsive long-ranged Yukawa potential, we have presented first results of the comparison of our analytic toolbox calculations for $S(q)$ and $g(r)$ with corresponding MPC simulations by our Jülich collab-

orators from the ICS-2 / IAS-2. The simulations reveal characteristic differences in the pair distribution functions of systems in the dispersed-fluid and equilibrium-cluster phase, respectively.

Finally, we demonstrated the importance of accurate analytic expressions for static and dynamic dispersion properties forming the input to our cross-flow UF modeling of charged-particles dispersions under low-salinity conditions. To account for the strong effect of surface-released counterions on the renormalized colloid charge and screening parameter, we have employed a PB cell model approach to determine the state-dependent parameters of the OCM effective pair potential. Subsequently, we have combined these results with the HNC approximation to calculate the osmotic suspension pressure and compressibility, and to predict accurate pair distribution functions. The latter served also as input to our hybrid BM-PA calculations of the collective diffusion coefficient, d_C, and high-frequency viscosity, η_∞, and to the simplified mode-coupling theory calculation of the shear relaxation part, $\Delta\eta$, of the steady low-shear viscosity η. Using the calculated static and dynamic suspension properties as input to our UF model has allowed us to quantitatively reproduce the cross-flow UF measurements of the permeate flux for aqueous feed suspensions of charge-stabilized silica particles. Our theoretical findings show that the osmotic pressure has no significant effect on the UF of low-salinity suspensions, with the permeate flux versus TMP curve being close to that for pure solvent as the feed. Only for the largest considered transmembrane pressure is a deviation of the experimental from the theoretical curves visible, which is likely due to preferential adsorption of the silica particles on the membrane surface. Our findings substantiate an assertion by Cohen and Probstein [257], in the related context of reverse osmosis that there is a threshold permeate flux below which no flux decline caused by concentration-polarization or cake layer formation occurs. Note that an account of chemical charge regulation does not qualitatively change our findings about the permeate flux of low-salinity systems, since charge regulation only moderately enhances the effective particle charge [258].

We close this section by discussing possible future extensions of the thesis work:

Our toolbox of analytic methods is useful not only for experimental data analysis of scattering and rheological measurements. It can be also used for the optimization of technological processes such as filtration, where transport properties are essential ingredients [39]. The presented (short-time) transport coefficient expressions can further serve as input in the calculation of frequency- and time-dependent transport properties on basis of mode-coupling and dynamic density functional theory methods with HIs included [259, 260].

Regarding the HRM, it is feasible to generalize it to size polydisperse particles using an appropriate particle size distribution function. This allows to search for extensions of the discussed analytic scaling relations for d_S, K, and η_∞ to polydisperse colloidal systems and mixtures. These generalized scaling relations would be an important ingredient for the study of filtration processes using polydisperse or multi-component systems. The partial static structure factors determined in this thesis for the polydisperse amphoteric microgels, e.g, can serve as an ingredient for the calculation of multi-component microgel transport coefficients.

In the framework of a current SFB 985 on Functional Microgels and Microgel Systems, we will continue our work on microgel systems. It will be interesting to scrutinize our viscosity predictions for the viscosities η_∞ and η of hydrodynamically structured particles against future rheo-mechanic measurements on non-ionic PNIPAM microgel systems. A set of measurements of short- and long-time diffusion and rheological properties for a single experimental system will allow to find out experimentally whether a single hydrodynamic radius parameter γ suffices for characterizing different dynamic properties. The UF study of low-salinity silica suspensions presented here is part of the SFB 985 project B6 encompassing the joint theoretical-experimental study of microgel separation and concentration. The here studied silica suspension has served as a simplifying model of ionic microgels, with strongly reduced complexity. While silica particles are rigid, ionic microgels can change their shape under applied strong pressure. Moreover, their size is concentration and salinity dependent in addition to the pH and temperature dependence. This complicates the modeling of microgel filtration considerably. In future work, we will extend our filtration modeling to ionic microgels where, in addition to charge-renormalization effects, the particle elasticity and deformability, and environmental-dependent size changes need to be considered (see, e.g, [40]).

The presented results about the statics and dynamics of SALR systems in the dispersed-fluid phase is a necessary ingredient for future explorations of the dynamics in equilibrium-cluster and percolated phases. A deeper understanding of the physical mechanisms leading to the formation of clusters, and of their effect on transport properties is of importance for industrial applications of proteins. A recent example in case by Godfrin *et al.* [4] is the cluster-induced viscosity increase in monoclonal antibody dispersions affecting the possibility to deliver them as a therapeutic product. Moreover, the establishment of useful novel GSE relations would allow for an easy rheological characterization of protein systems in research and industry. Furthermore, we plan to use MCT schemes for calculating the zero-frequency viscosity of Lysozyme suspensions, and to compare our results to existing experimental data [98].

In future work, we will provide a detailed assessment of the accuracy of the BM-PA method for SALR systems by comparison with MPC simulations both for the dispersed-fluid and the equilibrium-cluster phase.

Due to the widespread usage of protein filtration methods in research laboratories and chemical and pharmaceutical industry [261], our intention is to combine the gained knowledge about transport properties of protein solutions with our UF model of charged-particles dispersions in order to study the UF of protein solutions. In this context, the observed large collective diffusion coefficient values for SALR systems can be of particular importance, although other effects such as the surface adhesion of the proteins to the filter membrane will also play an important role.

Finally, it will be interesting to study the influence of patchy interaction contributions in proteins on the dispersion dynamics. Here, the work on SALR systems in this thesis can be a good starting point.

Abbreviations

BCs	boundary conditions, page 52
BDB	Brinkman-Debye-Bueche equation, page 10
BM	renormalized concentration fluctuation method by Beenakker and Mazur, page 70
CS	Carnahan-Starling, page 43
CSD	cluster-size distribution function, page 27
DLS	dynamic light scattering, page 16
DMF	dimethylformamide, page 16
ELCS	extended law of corresponding states by Noro and Frenkel [107], page 27
GSE	generalized Smoluchowski equation, page 53
HIs	hydrodynamic interactions, page 1
HNC	hypernetted-chain approximation (c.f Subsec 3.4.2), page 21
HRM	hydrodynamic radius model, page 11
IET	integral equation theory, page 23
IRO	intermediate-range microstructural ordering, page 22
LJY	Lennard-Jones plus Yukawa potential, page 25
LR	long-range repulsion, page 21
MC	Monte Carlo, page 27
MD	Molecular Dynamics, page 26
MPC	multi-particle collision dynamics, page 26
NSE	neutron spin echo, page 22
OZ	Ornstein-Zernike, page 41

PA	pairwise-additivity approximation, page 70
PA-BM	hybrid scheme combining the BM method for $H^{\mathrm{d}}(q)$ with the PA method for d_{S}, page 70
PB	Poisson-Boltzmann, page 19
PDF	probability density function, page 35
PNIPAM	poly(N-isopropylacrylamide), page 14
PY	Percus-Yevick, page 14
RDF	radial distribution function $g(r)$, page 14
RP	Rotne-Prager approximation, page 56
RPA	random phase approximation, page 46
SA	short-range attraction, page 21
SALR	short-range attraction plus long-range repulsion, page 21
SANS	small angle neutron scattering, page 34
SMSA	soft-core mean spherical approximation, page 44
TMP	trans-membrane pressure, page 19
UF	ultrafiltration, page 16
VW	Verlet-Weis correction to the PY solution for hard spheres, page 15
ZH	Zerah-Hansen scheme, page 28

A. OZ-based integral equation theory

A.1. Percus-Yevick closure for hard spheres

The analytic PY solution for the static structure factor of hard-spheres is [75]

$$S_{\mathrm{PY}}(y) = \frac{1}{X^2(y) + Y^2(y)}\,, \tag{A.1}$$

with

$$X(y) = 1 - 12\phi\left[Af_1(y) + Bf_2(y)\right]\,, \tag{A.2}$$

$$Y(y) = -12\phi\left[Af_3(y) + Bf_4(y)\right]\,, \tag{A.3}$$

and $y = q\sigma$. Furthermore,

$$f_1(y) = \frac{y - \sin(y)}{y^3}\,, \qquad f_2(y) = \frac{\cos(y) - 1}{y^2}\,, \tag{A.4}$$

$$f_3(y) = \frac{f_2(y)}{y} + \frac{1}{2y}\,, \qquad f_4(y) = -yf_1(y)\,. \tag{A.5}$$

The reduced isothermal compressibility, $\chi_{\mathrm{T}}/\chi_{\mathrm{T}}^{\mathrm{id}}$, follows in PY approximation as

$$\left.\frac{\chi_{\mathrm{T}}}{\chi_{\mathrm{T}}^{\mathrm{id}}}\right|_{\mathrm{PY}} = \frac{(1-\phi)^4}{(1+2\phi)^2}\,, \tag{A.6}$$

which for large ϕ differs form the accurate Carnahan-Starling compressibility. The RDF can be calculated by Fourier inversion of $S_{\mathrm{PY}}(q)$, using Eq. (3.20) expressed in terms of the continuous function $\gamma(r) = h(r) - c(r)$.

A.2. Verlet-Weis correction

The VW correction of the PY $g(r)$ reads [75]

$$g_{\mathrm{VW}}(x;\phi) = g_{\mathrm{PY}}(x\frac{\sigma}{\sigma'};\phi') + A\frac{e^{-\mu(x-1)}}{x}\cos\left[\mu\,(x-1)\right]\,, \tag{A.7}$$

with $x = r/\sigma$, and

$$\phi' = \phi\left(1 - \frac{1}{16}\phi\right) , \tag{A.8}$$

$$\sigma' = \left(\frac{\phi'}{\phi}\right)^{\frac{1}{3}} < \sigma\,. \tag{A.9}$$

The parameters A and μ are determined such that the CS-expressions (3.34) and (3.35) are fullfilled [75]:

$$A\left(\phi'\right) = \frac{3\phi'^2(1 - 0.7117\phi' - 0.114\phi'^2)}{4(1-\phi')^4}\,, \tag{A.10}$$

$$\mu(\phi') = \frac{24\,A(\phi')}{\phi' g_{\mathrm{PY}}(1^+;\phi')}\,, \tag{A.11}$$

resulting in very good agreement of the VW $g(r)$ with MC simulation data.
The $S(q)$ in the Verlet-Weis corrected PY approximation follows form Fourier inversion of Eq. (A.7).

B. Dynamic calculation methods

B.1. PA mobilities in far-distance expansion

The far-distance expansion expressions for the hydrodynamic mobility functions in PA approximation are [168]

$$x_{11}(x) = 1 - \frac{15}{64}\frac{1}{x^4} + \frac{11}{128}\frac{1}{x^6} + \frac{21}{512}\frac{1}{x^8} - \frac{167}{2048}\frac{1}{x^{10}} + \mathcal{O}\left(\frac{1}{x^{12}}\right) \tag{B.1}$$

$$y_{11}(x) = 1 - \frac{17}{1024}\frac{1}{x^6} + \frac{5}{1024}\frac{1}{x^8} - \frac{69}{16384}\frac{1}{x^{10}} + \mathcal{O}\left(\frac{1}{x^{12}}\right) \tag{B.2}$$

$$x_{12}(x) = \frac{3}{4x} - \frac{1}{8}\frac{1}{x^3} + \frac{75}{512}\frac{1}{x^7} - \frac{15}{1024}\frac{1}{x^9} - \frac{393}{8192}\frac{1}{x^{11}} + \mathcal{O}\left(\frac{1}{x^{13}}\right) \tag{B.3}$$

$$y_{12}(x) = \frac{3}{8x} + \frac{1}{16}\frac{1}{x^3} + \frac{567}{262144}\frac{1}{x^{11}} + \mathcal{O}\left(\frac{1}{x^{13}}\right), \tag{B.4}$$

with $x = r\sigma_\mathrm{h}$ and pair distance r.

B.2. Implementation of the BM method

The explicit expressions for the functions $S_{\gamma_0}(x)$ and $\gamma_0^{(n)}$ appearing in the BM method expressions for $H(q)$ (Eqs. (4.73) and (4.74)) and η_∞ (Eq. (4.75)) are given by [160, 175]

$$S_{\gamma_0}(x) = \sum_{p=2}^{\infty} \frac{9\pi}{4}\epsilon_p \frac{\gamma_0^{(p)}}{\rho}(2p-1)^2 \frac{J^2_{p-\frac{1}{2}}(x)}{x^3}, \tag{B.5}$$

with

$$\epsilon_p = \begin{cases} \frac{5}{9}, & ; p = 2 \\ 1, & ; p \geq 3 \end{cases} \tag{B.6}$$

and

$$\rho = \gamma_0^{(m)} - \gamma_0^{(m)}\phi_\mathrm{h}(2m-1)\int_0^\infty \mathrm{d}k\, \frac{J^2_{m-\frac{1}{2}}(k)}{k}\frac{S_{\gamma_0}(k)}{1+\phi_\mathrm{h}S_{\gamma_0}(k)}. \tag{B.7}$$

Here, $\phi_{\mathrm{h}} = \gamma^3\phi$ denotes the hydrodynamic volume fraction and J_n is the Bessel function of the first kind and order n.
We have calculated the $\gamma_0^{(n)}$ coefficients in an iterative procedure up to order $n = 10$, using a fine grid of volume fractions within $\left[10^{-8} - 0.5\right]$ with varying grid size. The tabulated values have been used as input in a spline interpolation procedure. This has resulted in an improved accuracy as compared to the original work by Beenakker and Mazur. However, the differences in $H^d(q)$ and η_∞ are quite small, i.e. there is no more than a 3% difference [173]. A selection of the coefficients $\gamma_0^{(n)}$ is presented in Table B.1.

ϕ	$n=2$	$n=3$	$n=4$	$n=5$	$n=6$	$n=7$	$n=8$	$n=9$	$n=10$
0.01	1.020	1.016	1.013	1.010	1.008	1.007	1.006	1.005	1.005
0.05	1.107	1.085	1.066	1.052	1.042	1.035	1.031	1.027	1.024
0.1	1.229	1.179	1.137	1.107	1.087	1.073	1.062	1.055	1.048
0.15	1.368	1.283	1.214	1.166	1.133	1.111	1.095	1.083	1.073
0.2	1.526	1.396	1.296	1.228	1.183	1.152	1.129	1.112	1.099
0.25	1.702	1.520	1.385	1.294	1.234	1.194	1.164	1.142	1.125
0.3	1.897	1.654	1.479	1.363	1.288	1.237	1.201	1.173	1.151
0.35	2.110	1.797	1.578	1.436	1.344	1.283	1.238	1.205	1.178
0.4	2.340	1.947	1.682	1.512	1.403	1.329	1.277	1.237	1.205
0.45	2.585	2.105	1.790	1.590	1.463	1.377	1.316	1.270	1.233
0.5	2.843	2.269	1.901	1.671	1.525	1.427	1.356	1.303	1.261

Table B.1.: Coefficents $\gamma_0^{(n)}$ for various volume fractions ϕ up to order $n = 10$.

Bibliography

[1]C. N. Likos, "Colloidal Interactions: From Effective Potentials to Structure", in *Proceedings of the international school of physics "enrico fermi", course clxxxiv on "physics of complex colloids"*, edited by C. Bechinger, F. Sciortino, and P. Ziherl (IOS Press, SIF, Amsterdam, Bologna, 2013), pp. 1–60.

[2]A. Stradner, H. Sedgwick, F. Cardinaux, W. C. K. Poon, S. U. Egelhaaf, and P. Schurtenberger, "Equilibrium cluster formation in concentrated protein solutions and colloids", Nature **432**, 492–495 (2004).

[3]Y. Liu, E. Fratini, P. Baglioni, W.-R. Chen, and S.-H. Chen, "Effective Long-Range Attraction between Protein Molecules in Solutions Studied by Small Angle Neutron Scattering", Physical Review Letters **95**, 118102 (2005).

[4]P. D. Godfrin, I. E. Zarraga, J. Zarzar, L. Porcar, P. Falus, N. J. Wagner, and Y. Liu, "Effect of Hierarchical Cluster Formation on the Viscosity of Concentrated Monoclonal Antibody Formulations Studied by Neutron Scattering", The Journal of Physical Chemistry B **120**, 278–291 (2016).

[5]N. Kovalchuk, V. Starov, P. Langston, and N. Hilal, "Formation of stable clusters in colloidal suspensions", Advances in Colloid and Interface Science **147-148**, 144–154 (2009).

[6]A. Saxena, B. P. Tripathi, M. Kumar, and V. K. Shahi, "Membrane-based techniques for the separation and purification of proteins: An overview", Advances in Colloid and Interface Science **145**, 1–22 (2009).

[7]M. M. Rohani and A. L. Zydney, "Role of electrostatic interactions during protein ultrafiltration", Advances in Colloid and Interface Science **160**, 40–48 (2010).

[8]G. M. Eichenbaum, P. F. Kiser, A. V. Dobrynin, S. a. Simon, and D. Needham, "Investigation of the Swelling Response and Loading of Ionic Microgels with Drugs and Proteins: The Dependence on Cross-Link Density", Macromolecules **32**, 4867–4878 (1999).

[9]V. C. Lopez, S. Raghavan, and M. Snowden, "Colloidal microgels as transdermal delivery systems", Reactive and Functional Polymers **58**, 175–185 (2004).

[10]N. Sahiner, C. Silan, S. Sagbas, P. Ilgin, S. Butun, H. Erdugan, and R. S. Ayyala, "Porous and modified HA particles as potential drug delivery systems", Microporous and Mesoporous Materials **155**, 124–130 (2012).

[11]L. Bromberg, M. Temchenko, and T. A. Hatton, "Dually responsive microgels from polyether-modified poly(acrylic acid): Swelling and drug loading", Langmuir **18**, 4944–4952 (2002).

[12]S. Lally, P. Mackenzie, C. L. LeMaitre, T. J. Freemont, and B. R. Saunders, "Microgel particles containing methacrylic acid: pH-triggered swelling behaviour and potential for biomaterial application", Journal of Colloid and Interface Science **316**, 367–375 (2007).

[13]P. Panda, S. Ali, E. Lo, B. G. Chung, T. A. Hatton, A. Khademhosseini, and P. S. Doyle, "Stop-flow lithography to generate cell-laden microgel particles.", Lab on a chip **8**, 1056–61 (2008).

[14]J. Shen, T. Ye, A. Chang, W. Wu, and S. Zhou, "A colloidal supra-structure of responsive microgels as a potential cell scaffold", Soft Matter **8**, 12034–12042 (2012).

[15]S. Saxena, M. W. Spears, H. Yoshida, J. C. Gaulding, A. J. García, and L. A. Lyon, "Microgel film dynamics modulate cell adhesion behavior.", Soft matter **10**, 1356–1364 (2014).

[16]"Microgel-based thermo-responsive membranes for water filtration", Membrane Technology **2014**, 10 (2014).

[17]D. Menne, F. Pitsch, J. E. Wong, A. Pich, and M. Wessling, "Temperature-Modulated Water Filtration Using Microgel-Functionalized Hollow-Fiber Membranes", Angewandte Chemie International Edition **53**, 5706–5710 (2014).

[18]K. Chari, R. Hsu, P. Bhargava, B. Figura, W. Yang, J. H. Park, T. Clifford, and M. Kadir, "Surfactant-Activated Microgels: A New Pathway to Rheology Modification", Langmuir **29**, 15521–15528 (2013).

[19]L. A. Hough, A. M. Alsayed, C. Badre, and R. Dreyfus, "Applications of Colloids in Industry", in *Proceedings of the international school of physics "enrico fermi", course clxxxiv on "physics of complex colloids"*, edited by C. Bechinger, F. Sciortino, and P. Ziherl (IOS Press, SIF, Amsterdam, Bologna, 2013), pp. 425–446.

[20]S. Xu, J. Zhang, C. Paquet, Y. Lin, and E. Kumacheva, "From hybrid microgels to photonic crystals", Advanced Functional Materials **13**, 468–472 (2003).

[21]M. Zhou, F. Xing, M. Ren, Y. Feng, Y. Zhao, H. Qiu, X. Wang, C. Gao, F. Sun, Y. He, Z. Ma, P. Wen, and J. Gao, "A Facile Method to Assemble PNIPAM-Containing Microgel Photonic Crystals", ChemPhysChem **10**, 523–526 (2009).

[22]M. Chen, L. Zhou, Y. Guan, and Y. Zhang, "Polymerized microgel colloidal crystals: Photonic hydrogels with tunable band gaps and fast response rates", Angewandte Chemie - International Edition **52**, 9961–9965 (2013).

[23]M. Chen, Y. Zhang, S. Jia, L. Zhou, Y. Guan, and Y. Zhang, "Photonic Crystals with a Reversibly Inducible and Erasable Defect State Using External Stimuli", Angewandte Chemie International Edition **54**, 9257–9261 (2015).

[24]M Medina-Noyola, "Long-Time Self-Diffusion in Concentrated Colloidal Dispersions", Physical Review Letters **60**, 2705–2708 (1988).

[25]J. F. Brady, "The rheological behavior of concentrated colloidal dispersions", The Journal of Chemical Physics **99**, 567–581 (1993).

[26]J. F. Brady, "The long-time self-diffusivity in concentrated colloidal dispersions", Journal of Fluid Mechanics **272**, 109–133 (1994).

[27]A. J. Banchio, G. Nägele, and J. Bergenholtz, "Viscoelasticity and generalized Stokes-Einstein relations of colloidal dispersions", The Journal of Chemical Physics **111**, 8721–8740 (1999).

[28]M. Das and E. Kumacheva, "From polyelectrolyte to polyampholyte microgels: comparison of swelling properties", Colloid and Polymer Science **284**, 1073–1084 (2006).

[29]A. J. Schmid, R. Schroeder, T. Eckert, A. Radulescu, A. Pich, and W. Richtering, "Synthesis and solution behaviour of stimuli-sensitive zwitterionic microgels", Colloid and Polymer Science **293**, 3305–3318 (2015).

[30]F. Cardinaux, E. Zaccarelli, A. Stradner, S. Bucciarelli, B. Farago, S. U. Egelhaaf, F. Sciortino, and P. Schurtenberger, "Cluster-Driven Dynamical Arrest in Concentrated Lysozyme Solutions", The Journal of Physical Chemistry B **115**, 7227–7237 (2011).

[31]P. D. Godfrin, R. Castañeda-Priego, Y. Liu, and N. J. Wagner, "Intermediate range order and structure in colloidal dispersions with competing interactions", The Journal of Chemical Physics **139**, 154904 (2013).

[32]Y. Liu, L. Porcar, J. Chen, W. R. Chen, P. Falus, A. Faraone, E. Fratini, K. Hong, and P. Baglioni, "Lysozyme protein solution with an intermediate range order structure", Journal of Physical Chemistry B **115**, 7238–7247 (2011).

[33]P. D. Godfrin, N. E. Valadez-Pérez, R. Castañeda-Priego, N. J. Wagner, and Y. Liu, "Generalized phase behavior of cluster formation in colloidal dispersions with competing interactions", Soft Matter **10**, 5061 (2014).

[34]E. Mani, W. Lechner, W. K. Kegel, and P. G. Bolhuis, "Equilibrium and non-equilibrium cluster phases in colloids with competing interactions", Soft Matter **10**, 4479–4486 (2014).

[35]F Cardinaux, A Stradner, P Schurtenberger, F Sciortino, and E Zaccarelli, "Modeling equilibrium clusters in lysozyme solutions", Europhysics Letters (EPL) **77**, 48004 (2007).

[36]A. J. Chinchalikar, V. K. Aswal, J. Kohlbrecher, and A. G. Wagh, "Small-angle neutron scattering study of structure and interaction during salt-induced liquid-liquid phase transition in protein solutions", Physical Review E **87**, 062708 (2013).

[37]R. Piazza, M. Pierno, S. Iacopini, P. Mangione, G. Esposito, and V. Bellotti, "Microheterogeneity and aggregation in β2-microglobulin solutions: Effects of temperature, pH, and conformational variant addition", European Biophysics Journal **35**, 439–445 (2006).

[38]S. Yannopoulos and V. Petta, "Understanding the dynamics of biological colloids to elucidate cataract formation and develop a methodology for its early diagnosis", Philosophical Magazine **88**, 4161–4168 (2008).

[39]R. Roa, E. K. Zholkovskiy, and G. Nägele, "Ultrafiltration modeling of non-ionic microgels", Soft Matter **11**, 4106–4122 (2015).

[40]P. Holmqvist, P. S. Mohanty, G. Nägele, P. Schurtenberger, and M. Heinen, "Structure and Dynamics of Loosely Cross-Linked Ionic Microgel Dispersions in the Fluid Regime", Physical Review Letters **109**, 048302 (2012).

[41]D. M. Heyes and A. C. Brańka, "Interactions between microgel particles", Soft Matter **5**, 2681 (2009).

[42]W. Richard Bowen and P. M. Williams, "Prediction of the rate of cross-flow ultrafiltration of colloids with concentration-dependent diffusion coefficient and viscosity — theory and experiment", Chemical Engineering Science **56**, 3083–3099 (2001).

[43]P. Debye and a. M. Bueche, "Intrinsic Viscosity, Diffusion, and Sedimentation Rate of Polymers in Solution", The Journal of Chemical Physics **16**, 573–579 (1948).

[44]H. C. Brinkman, "A calculation of the viscous force exerted by a flowing fluid on a dense swarm of particles", Applied Scientific Research **1**, 27–34 (1949).

[45]J. M. Deutch and B. U. Felderhof, "Frictional properties of dilute polymer solutions. II. The effect of preaveraging", The Journal of Chemical Physics **62**, 2398–2405 (1975).

[46]B. Cichocki, M. L. Ekiel-Jezewska, and E. Wajnryb, "Lubrication corrections for three-particle contribution to short-time self-diffusion coefficients in colloidal dispersions", The Journal of Chemical Physics **111**, 3265–3273 (1999).

[47]G. C. Abade, B. Cichocki, M. L. Ekiel-Jezewska, G. Nağele, and E. Wajnryb, "Short-time dynamics of permeable particles in concentrated suspensions", The Journal of Chemical Physics **132**, 014503 (2010).

[48]G. C. Abade, B. Cichocki, M. L. Ekiel-Jezewska, G. Nägele, and E. Wajnryb, "Dynamics of permeable particles in concentrated suspensions", Physical Review E **81**, 020404 (2010).

[49]G. C. Abade, B. Cichocki, M. L. Ekiel-Jezewska, G. Nägele, and E. Wajnryb, "High-frequency viscosity of concentrated porous particles suspensions.", The Journal of chemical physics **133**, 084906 (2010).

[50]G. C. Abade, B. Cichocki, M. L. Ekiel-Jezewska, G. Nägele, and E. Wajnryb, "High-frequency viscosity and generalized Stokes–Einstein relations in dense suspensions of porous particles", Journal of Physics: Condensed Matter **22**, 322101 (2010).

[51]G. C. Abade, B. Cichocki, M. L. Ekiel-Jezewska, G. Nägele, and E. Wajnryb, "Diffusion, sedimentation, and rheology of concentrated suspensions of core-shell particles", The Journal of Chemical Physics **136**, 104902 (2012).

[52]B. Cichocki, M. L. Ekiel-Jezewska, and E. Wajnryb, "Short-time dynamics and high-frequency rheology of suspensions of spherical core–shell particles with thin-shells", Colloids and Surfaces A: Physicochemical and Engineering Aspects **418**, 22–28 (2013).

[53]B. Cichocki, M. L. Ekiel-Jezewska, and E. Wajnryb, "Hydrodynamic radius approximation for spherical particles suspended in a viscous fluid: influence of particle internal structure and boundary", The Journal of Chemical Physics **140**, 164902 (2014).

[54]G. C. Abade, B. Cichocki, M. L. Ekiel-Jezewska, G. Nägele, and E. Wajnryb, "Dynamics and effective slip of permeable and coated particle suspensions", in preparation.

[55]J. L. Anderson, P. F. McKenzie, and R. M. Webber, "Model for hydrodynamic thickness of thin polymer layers at solid/liquid interfaces", Langmuir **7**, 162–166 (1991).

[56]J. L. Anderson and Y. Solomentsev, "Hydrodynamic Effects of Surface Layers on Colloidal Particles", Chemical Engineering Communications **148-150**, 291–314 (1996).

[57]J. Riest, P. Mohanty, P. Schurtenberger, and C. N. Likos, "Coarse-Graining of Ionic Microgels: Theory and Experiment", Zeitschrift für Physikalische Chemie **226**, 711–735 (2012).

[58]D. Gottwald, C. N. Likos, G. Kahl, and H. Löwen, "Phase Behavior of Ionic Microgels", Physical Review Letters **92**, 068301 (2004).

[59]B. Cichocki, M. L. Ekiel-Jezewska, G. Nägele, and E. Wajnryb, "First-order virial expansion of short-time diffusion and sedimentation coefficients of permeable particles suspensions", Physics of Fluids **23**, 083303 (2011).

[60]M. G. McPhie and G. Nägele, "Long-time self-diffusion of charged colloidal particles: Electrokinetic and hydrodynamic interaction effects", The Journal of Chemical Physics **127**, 034906 (2007).

[61]G. Nägele, "On the dynamics and structure of charge-stabilized suspensions", Physics Reports **272**, 215–372 (1996).

[62]A. R. Denton, "Effective interactions and volume energies in charged colloids: Linear response theory", Physical Review E **62**, 3855–3864 (2000).

[63]A. R. Denton, "Counterion penetration and effective electrostatic interactions in solutions of polyelectrolyte stars and microgels", Physical Review E **67**, 011804 (2003).

[64]J. K. Chung and A. R. Denton, "Effective electrostatic interactions in mixtures of charged colloids", Physical Review E **88**, 022306 (2013).

[65]M. Heinen, A. J. Banchio, and G. Nägele, "Short-time rheology and diffusion in suspensions of Yukawa-type colloidal particles", The Journal of Chemical Physics **135**, 154504 (2011).

[66]T. Eckert and W. Richtering, "Thermodynamic and hydrodynamic interaction in concentrated microgel suspensions: Hard or soft sphere behavior?", The Journal of Chemical Physics **129**, 124902 (2008).

[67]D. Paloli, P. S. Mohanty, J. J. Crassous, E. Zaccarelli, and P. Schurtenberger, "Fluid–solid transitions in soft-repulsive colloids", Soft Matter **9**, 3000–3004 (2013).

[68]C. N. Likos, "Structure and Thermodynamics of Ionic Microgels", in *Microgel suspensions: fundamentals and applications*, edited by A. Fernandez-Nieves, H. M. Wyss, J. Mattsson, and D. A. Weitz (Wiley-VCH Verlag GmbH Co. KGaA, Weinheim, 2011) Chap. 7, pp. 165–193.

[69]H. M. Wyss, T. Franke, E. Mele, and D. A. Weitz, "Capillary micromechanics: Measuring the elasticity of microscopic soft objects", Soft Matter **6**, 4550–4555 (2010).

[70]J. Riest, L. Athanasopoulou, S. A. Egorov, C. N. Likos, and P. Ziherl, "Elasticity of polymeric nanocolloidal particles", Scientific Reports **5**, 15854 (2015).

[71]J. C. Pàmies, A. Cacciuto, and D. Frenkel, "Phase diagram of Hertzian spheres", The Journal of Chemical Physics **131**, 044514 (2009).

[72]J. K. Percus and G. J. Yevick, "Analysis of classical statistical mechanics by means of collective coordinates", Physical Review **110**, 1–13 (1958).

[73]J.-P. Hansen and I. R. McDonald, *Theory of Simple Liquids, Third Edition* (Academic Press, 2006).

[74]L. Verlet and J.-J. Weis, "Equilibrium Theory of Simple Liquids", Physical Review A **5**, 939–952 (1972).

[75]G. Nägele, *The Physics of Colloidal Soft Matter* (Polish Academy of Sciences, Warsaw, 2004), p. 182.

[76]G. C. Abade, B. Cichocki, M. L. Ekiel-Jezewska, G. Nägele, and E. Wajnryb, "Rotational and translational self-diffusion in concentrated suspensions of permeable particles", The Journal of Chemical Physics **134**, 244903 (2011).

[77]P. S. Mohanty, D. Paloli, J. J. Crassous, E. Zaccarelli, and P. Schurtenberger, "Effective interactions between soft-repulsive colloids: experiments, theory, and simulations.", The Journal of Chemical Physics **140**, 094901 (2014).

[78]A. R. Denton, "Erratum: Counterion penetration and effective electrostatic interactions in solutions of polyelectrolyte stars and microgels [Phys. Rev. E 67, 011804 (2003)]", Physical Review E **68**, 049904 (2003).

[79]A. Deboeuf, G. Gauthier, J. Martin, Y. Yurkovetsky, and J. F. Morris, "Particle Pressure in a Sheared Suspension: A Bridge from Osmosis to Granular Dilatancy", Physical Review Letters **102**, 108301 (2009).

[80]A. M. Leshansky, J. F. Morris, and J. F. Brady, "Collective diffusion in sheared colloidal suspensions", Journal of Fluid Mechanics **597**, 305–341 (2008).

[81]L. Belloni, "Colloidal interactions", Journal of Physics: Condensed Matter **12**, R549–R587 (2000).

[82]J. Dobnikar, R Castañeda-Priego, H. H. von Grünberg, and E Trizac, "Testing the relevance of effective interaction potentials between highly-charged colloids in suspension", New Journal of Physics **8**, 277 (2006).

[83]J. Dobnikar, "Many-Body Interactions in Colloidal Suspensions", in *Electrostatics of soft and disordered matter*, edited by D. Dean, J. Dobnikar, A. Naji, and R. Podgornik (Pan Stanford Publishing, 2014), pp. 221–237.

[84]K. van Gruijthuijsen, M. Obiols-Rabasa, M. Heinen, G. Nägele, and A. Stradner, "Sterically Stabilized Colloids with Tunable Repulsions", Langmuir **29**, 11199–11207 (2013).

[85]F. Westermeier, B. Fischer, W. Roseker, G. Grübel, G. Nägele, and M. Heinen, "Structure and short-time dynamics in concentrated suspensions of charged colloids.", The Journal of chemical physics **137**, 114504 (2012).

[86]M. Heinen, F. Zanini, F. Roosen-Runge, D. Fedunová, F. Zhang, M. Hennig, T. Seydel, R. Schweins, M. Sztucki, M. Antalík, F. Schreiber, and G. Nägele, "Viscosity and diffusion: crowding and salt effects in protein solutions", Soft Matter **8**, 1404–1419 (2012).

[87]J Gapinski, A Wilk, A Patkowski, W Häussler, a. J. Banchio, R Pecora, and G Nägele, "Diffusion and microstructural properties of solutions of charged nanosized proteins: experiment versus theory.", The Journal of chemical physics **123**, 054708 (2005).

[88]A. Archer and N. Wilding, "Phase behavior of a fluid with competing attractive and repulsive interactions", Physical Review E **76**, 031501 (2007).

[89]N. E. Valadez-Pérez, R. Castañeda-Priego, and Y. Liu, "Percolation in colloidal systems with competing interactions: the role of long-range repulsion", RSC Advances **3**, 25110–25119 (2013).

[90]J.-M. Bomont, J.-L. Bretonnet, and D. Costa, "Temperature study of cluster formation in two-Yukawa fluids", The Journal of Chemical Physics **132**, 184508 (2010).

[91]D. Costa, C. Caccamo, J.-M. Bomont, and J.-L. Bretonnet, "Theoretical description of cluster formation in two-Yukawa competing fluids", Molecular Physics **109**, 2845–2853 (2011).

[92]F. Platten, J. Hansen, J. Milius, D. Wagner, and S. U. Egelhaaf, "Additivity of the Specific Effects of Additives on Protein Phase Behavior", The Journal of Physical Chemistry B **119**, 14986–14993 (2015).

[93]A Tardieu, A. Le Verge, M Malfois, F. Bonneté, S. Finet, M. Riès-Kautt, and L. Belloni, "Proteins in solution:from X-ray scattering intensities to interaction potentials", Journal of Crystal Growth **196**, 193–203 (1999).

[94]M. Farnum and C. Zukoski, "Effect of Glycerol on the Interactions and Solubility of Bovine Pancreatic Trypsin Inhibitor", Biophysical Journal **76**, 2716–2726 (1999).

[95]D. E. Leckband, F.-J. Schmitt, J. N. Israelachvili, and W Knoll, "Direct Force Measurements of Specific and Nonspecific Protein Interactions", Biochemistry **33**, 4611–4624 (1994).

[96]S. Nir, "Van der Waals interactions between surfaces of biological interest", Progress in Surface Science **8**, 1–58 (1977).

[97]G. Pellicane, D. Costa, and C. Caccamo, "Microscopic Determination of the Phase Diagrams of Lysozyme and γ-Crystallin Solutions", The Journal of Physical Chemistry B **108**, 7538–7541 (2004).

[98]P. D. Godfrin, "Thermodynamic and material properties of reversible cluster formation - Application to concentrated protein solutions", PhD thesis (University of Delaware, 2015), p. 327.

[99]M. C. Abramo, C. Caccamo, M. Cavero, D. Costa, G. Pellicane, R. Ruberto, and U. Wanderlingh, "Effective protein-protein interaction from structure factor data of a lysozyme solution", The Journal of Chemical Physics **139**, 054904 (2013).

[100]S. Kundu, K. Das, and V. Aswal, "Modification of attractive and repulsive interactions among proteins in solution due to the presence of mono-, di- and tri-valent ions", Chemical Physics Letters **578**, 115–119 (2013).

[101]S Grobelny, M Erlkamp, J Möller, M Tolan, and R Winter, "Intermolecular interactions in highly concentrated protein solutions upon compression and the role of the solvent", The Journal of Chemical Physics **141**, 22D506 (2014).

[102]W. E. J. Verwey and J. T. G. Overbeek, *Theory of the stability of lyophobic colloids*, English (Dover Publications, Mineola, N.Y., 1999).

[103]N. E. Valadez-Peŕez, A. L. Benavides, E. Schöll-Paschinger, and R. Castañeda-Priego, "Phase behavior of colloids and proteins in aqueous suspensions: Theory and computer simulations", The Journal of Chemical Physics **137**, 084905 (2012).

[104]J Torres-Arenas, L. a. Cervantes, a. L. Benavides, G. a. Chapela, and F del Río, "Discrete perturbation theory for the hard-core attractive and repulsive Yukawa potentials", The Journal of Chemical Physics **132**, 034501 (2010).

[105]D. Pini, A. Parola, and L. Reatto, "Freezing and correlations in fluids with competing interactions", Journal of Physics: Condensed Matter **18**, S2305–S2320 (2006).

[106]D. Gazzillo and D. Pini, "Self-Consistent Ornstein-Zernike Approximation (SCOZA) and exact second virial coefficients and their relationship with critical temperature for colloidal or protein suspensions with short-ranged attractive interactions", The Journal of Chemical Physics **139**, 164501 (2013).

[107]M. G. Noro and D. Frenkel, "Extended corresponding-states behavior for particles with variable range attractions", The Journal of Chemical Physics **113**, 2941–2944 (2000).

[108]F. Platten, N. E. Valadez-Pérez, R. Castañeda-Priego, and S. U. Egelhaaf, "Extended law of corresponding states for protein solutions", The Journal of Chemical Physics **142**, 174905 (2015).

[109]L. V. Woodcock, "Percolation transitions in the hard-sphere fluid", AIChE Journal **58**, 1610–1618 (2012).

[110]A. Campbell, V. Anderson, J. van Duijneveldt, and P. Bartlett, "Dynamical Arrest in Attractive Colloids: The Effect of Long-Range Repulsion", Physical Review Letters **94**, 208301 (2005).

[111]M. J. Snowden, B. Z. Chowdhry, B. Vincent, and G. E. Morris, "Colloidal copolymer microgels of N-isopropylacrylamide and acrylic acid: pH, ionic strength and temperature effects", Journal of the Chemical Society, Faraday Transactions **92**, 5013–5016 (1996).

[112]C. Johansson, P. Hansson, and M. Malmsten, "Interaction between lysozyme and poly-(acrylic acid) microgels", Journal of Colloid and Interface Science **316**, 350–359 (2007).

[113]C. D. Jones and L. A. Lyon, "Shell-restricted swelling and core compression in poly(N-isopropylacrylamide) core-shell microgels", Macromolecules **36**, 1988–1993 (2003).

[114]J. Kleinen and W. Richtering, "Defined complexes of negatively charged multisensitive poly(N- isopropylacrylamide-co-methacrylic acid) microgels and poly(diallydimethyl-ammonium chloride)", Macromolecules **41**, 1785–1790 (2008).

[115]G. Huang and Z. Hu, "Phase behavior and stabilization of microgel arrays", Macromolecules **40**, 3749–3756 (2007).

[116]V. J. Cornelius, M. J. Snowden, J Silver, and G. R. Fern, "A study of the binding of the biologically important hematin molecule to a novel imidazole containing poly(N-isopropylacrylamide) microgel", Reactive & Functional Polymers **58**, 165–173 (2004).

[117]V. T. Pinkrah, M. J. Snowden, J. C. Mitchell, J. Seidel, B. Z. Chowdhry, and G. R. Fern, "Physicochemical Properties of Poly(N -isopropylacrylamide- c o -4-vinylpyridine) Cationic Polyelectrolyte Colloidal Microgels", Langmuir **19**, 585–590 (2003).

[118]H. Ni, H. Kawaguchi, and T. Endo, "Preparation of pH-sensitive hydrogel microspheres of poly(acrylamide-co-methacrylic acid) with sharp pH–volume transition", Colloid and Polymer Science **285**, 819–826 (2007).

[119]M. Das, N. Sanson, and E. Kumacheva, "Zwitterionic Poly(betaine-N-isopropylacrylamide) Microgels: Properties and Applications", Chemistry of Materials **20**, 7157–7163 (2008).

[120]M. Stieger, W. Richtering, J. S. Pedersen, and P. Lindner, "Small-angle neutron scattering study of structural changes in temperature sensitive microgel colloids.", The Journal of Chemical Physics **120**, 6197–6206 (2004).

[121]G. Nägele, "Theories of Fluid Microstructure", in *Soft matter: from synthetic to biological materials*, edited by J. K. G. Dhont, G. Gompper, G. Nägele, D. Richter, and R. G. Winkler (Forschungszentrum Jülich GmbH Institut für Festkörpertorschung, Jülich, 2008), B2.1–B2.47.

[122]A. A. Louis, "Extracting short-ranged interactions from structure factors", Molecular Physics **109**, 2945–2951 (2011).

[123]Y. Rosenfeld and G. Kahl, "The inverse problem for simple classical liquids: a density functional approach", Journal of Physics: Condensed Matter **9**, L89–L98 (1997).

[124]M. D'Alessandro and F. Cilloco, "Information-theory-based solution of the inverse problem in classical statistical mechanics", Physical Review E **82**, 021128 (2010).

[125]J. Riest, *Dichtefunktionaltheorie deformierbarer Kugeln*, 2010.

[126]Y. Rosenfeld and N. Ashcroft, "Theory of simple classical fluids: Universality in the short-range structure", Physical Review A **20**, 1208–1235 (1979).

[127]M Frigo and S. Johnson, "The Design and Implementation of FFTW3", Proceedings of the IEEE **93**, 216–231 (2005).

[128]F. J. Rogers and D. A. Young, "New, thermodynamically consistent, integral equation for simple fluids", Physical Review A **30**, 999–1007 (1984).

[129]G. Zerah and J.-P. Hansen, "Self-consistent integral equations for fluid pair distribution functions: Another attempt", The Journal of Chemical Physics **84**, 2336 (1986).

[130]J. Chihara, "Integral Euqations for Fluids with Long-Range and Short-Range Potentials", Progress of Theoretical Physics **50**, 409–423 (1973).

[131]W. G. Madden and S. A. Rice, "The mean spherical approximation and effective pair potentials in liquids", The Journal of Chemical Physics **72**, 4208 (1980).

[132]J. D. Weeks, D. Chandler, and H. C. Andersen, "Role of Repulsive Forces in Determining the Equilibrium Structure of Simple Liquids", The Journal of Chemical Physics **54**, 5237–5247 (1971).

[133]P.-G. de Gennes, *Scaling Concepts in Polymer Physics* (Cornell University Press, 1979), p. 324.

[134]L. Blum and J. S. Hoeye, "Mean spherical model for asymmetric electrolytes. 2. Thermodynamic properties and the pair correlation function", The Journal of Physical Chemistry **81**, 1311–1316 (1977).

[135]J. S. Pedersen, "Analysis of small-angle scattering data from colloids and polymer solutions: modeling and least-squares fitting", Advances in Colloid and Interface Science **70**, 171–210 (1997).

[136]A. J. Banchio and G. Nägele, "Short-time transport properties in dense suspensions: from neutral to charge-stabilized colloidal spheres", The Journal of chemical physics **128**, 104903 (2008).

[137]M. D. Rintoul and S. Torquato, "Metastability and Crystallization in Hard-Sphere Systems.", Physical review letters **77**, 4198–4201 (1996).

[138]M. D. Rintoul and S. Torquato, "Computer simulations of dense hard-sphere systems", The Journal of Chemical Physics **105**, 9258–9265 (1996).

[139]S. B. Yuste, A. Santos, and M. López de Haro, "Structure of multi-component hard-sphere mixtures", The Journal of Chemical Physics **108**, 3683–3693 (1998).

[140]G. Nägele, "Colloidal Hydrodynamics", in *Proceedings of the international school of physics "enrico fermi", course clxxxiv on "physics of complex colloids"*, edited by C. Bechinger, F. Sciortino, and P. Ziherl (IOS Press, SIF, Amsterdam, Bologna, 2013), pp. 507–601.

[141]M. Lisicki and G. Nägele, "Colloidal Hydrodynamics and Interfacial Effects", English, in *Soft matter at aqueous interfaces*, Vol. 917, edited by P. R. Lang and Y. Liu, Lecture Notes in Physics (Springer International Publishing, 2016), pp. 313–386.

[142]J. K. G. Dhont, *An Introduction to Dynamics of Colloids* (Elsevier, Amsterdam, 1996).

[143]K. Makuch, "Scattering series in the mobility problem for suspensions", Journal of Statistical Mechanics: Theory and Experiment **2012**, P11016 (2012).

[144]B. Felderhof, "Frictional properties of dilute polymer solutions", Physica A: Statistical Mechanics and its Applications **80**, 63–75 (1975).

[145]B. U. Felderhof and J. M. Deutch, "Frictional properties of dilute polymer solutions. I. Rotational friction coefficient", The Journal of Chemical Physics **62**, 2391–2397 (1975).

[146]C.-L.-M.-H. Navier, *Sur les lois du mouvement des fluides*, 6th ed. (Mémoires de l'Académie Royale des Sciences de l'Institut de France, 1827).

[147]S. Kim and S. Karrila, *Microhydrodynamics: Principles and Selected Applications* (Butterworth-Henemann, Boston, 1991).

[148]J. H. Masliyah, G. Neale, K. Malysa, and T. G. M. Van De Ven, "Creeping flow over a composite sphere: Solid core with porous shell", Chemical Engineering Science **42**, 245–253 (1987).

[149]M. Zackrisson, A. Stradner, P. Schurtenberger, and J. Bergenholtz, "Structure, dynamics, and rheology of concentrated dispersions of poly(ethylene glycol)-grafted colloids", Physical Review E **73**, 011408 (2006).

[150]B. Cichocki and B. U. Felderhof, "Hydrodynamic friction coefficients of coated spherical particles", The Journal of Chemical Physics **130**, 164712 (2009).

[151]N. Lecoq, R. Anthore, B. Cichocki, P. Szymczak, and F. Feuillebois, "Drag force on a sphere moving towards a corrugated wall", Journal of Fluid Mechanics **513**, 247–264 (2004).

[152]D. Lopez and E. Lauga, "Dynamics of swimming bacteria at complex interfaces", Physics of Fluids **26**, 071902 (2014).

[153]G. Nägele, *Introduction to Colloid Physics* (Fakultät für Physik, Dekanat, Universität Konstanz, Konstanz, 1998), p. 110.

[154]R. Zorn, "Scattering", in *46th iff spring school 2015: functional soft matter*, edited by J. K. G. Dhont, G. Gompper, G. Meier, D. Richter, G. Vliegenthart, and R. Zorn (Schriften des Forschungszentrums Jülich, Jülich, 2015), pp. C1.1–C1.39.

[155]Z. Bu, R. Biehl, M. Monkenbusch, D. Richter, and D. J. E. Callaway, "Coupled protein domain motion in Taq polymerase revealed by neutron spin-echo spectroscopy", Proceedings of the National Academy of Sciences **102**, 17646–17651 (2005).

[156]G. Nägele, "Colloidal hydrodynamics", in *Physics of complex colloids*, edited by C. Bechinger, F. Sciortino, and P. Ziherl, Proceeding (IOS Press, 2013), pp. 507–601.

[157]E. Wajnryb, P. Szymczak, and B. Cichocki, "Brownian dynamics: divergence of mobility tensor", Physica A: Statistical Mechanics and its Applications **335**, 339–358 (2004).

[158]H. Löwen, T. Palberg, and R. Simon, "Dynamical criterion for freezing of colloidal liquids", Physical Review Letters **70**, 1557–1560 (1993).

[159]G. Nägele, M. Kollmann, R. Pesché, and A. J. Banchio, "Dynamic properties, scaling and related freezing criteria of two- and three-dimensional colloidal dispersions", Molecular Physics **100**, 2921–2933 (2002).

[160]U. Genz and R. Klein, "Collective diffusion of charged spheres in the presence of hydrodynamic interaction", Physica A: Statistical Mechanics and its Applications **171**, 26–42 (1991).

[161]W. B. Russel, "The Huggins coefficient as a means for characterizing suspended particles", Journal of the Chemical Society, Faraday Transactions 2 **80**, 31 (1984).

[162]B. Cichocki and K. Hinsen, "Dynamic computer simulation of concentrated hard sphere suspensions", Physica A: Statistical Mechanics and its Applications **187**, 133–144 (1992).

[163]P Strating, "Brownian dynamics simulation of a hard-sphere suspension", Physical Review E **59**, 2175–2187 (1999).

[164]D. R. Foss and J. F. Brady, "Brownian Dynamics simulation of hard-sphere colloidal dispersions", Journal of Rheology **44**, 629–651 (2000).

[165]T. N. Phung, "Behavior of concentrated colloidal suspensions by Stokesian Dynamics simulations", PhD thesis (California Institute of Technology, Pasadena, California, 1993), p. 498.

[166]D. R. Foss and J. F. Brady, "Structure, diffusion and rheology of Brownian suspensions by Stokesian Dynamics simulation", Journal of Fluid Mechanics **407**, 167–200 (2000).

[167]A. J. Banchio and J. F. Brady, "Accelerated Stokesian dynamics: Brownian motion", The Journal of Chemical Physics **118**, 10323–10332 (2003).

[168]D. J. Jeffrey and Y Onishi, "Calculation of the resistance and mobility functions for two unequal rigid spheres in low-Reynolds-number flow", Journal of Fluid Mechanics **139**, 261–290 (1984).

[169]R. Jones and R. Schmitz, "Mobility matrix for arbitrary spherical particles in solution", Physica A: Statistical Mechanics and its Applications **149**, 373–394 (1988).

[170]D. J. Jeffrey, "The calculation of the low Reynolds number resistance functions for two unequal spheres", Physics of Fluids A: Fluid Dynamics **4**, 16 (1992).

[171]S. Kim and R. T. Mifflin, "The resistance and mobility functions of two equal spheres in low-Reynolds-number flow", Physics of Fluids **28**, 2033–2045 (1985).

[172]N. J. Wagner and A. T. J. M. Woutersen, "The viscosity of bimodal and polydisperse suspensions of hard spheres in the dilute limit", Journal of Fluid Mechanics **278**, 267–287 (1994).

[173]M. Heinen, "Charged colloids and proteins : Structure, diffusion, and rheology.", PhD thesis (Heinrich-Heine-Universität Düsseldorf, 2011), p. 186.

[174]C. Beenakker and P. Mazur, "Self-diffusion of spheres in a concentrated suspension", Physica A: Statistical Mechanics and its Applications **120**, 388–410 (1983).

[175]C. Beenakker and P. Mazur, "Diffusion of spheres in a concentrated suspension II", Physica A: Statistical Mechanics and its Applications **126**, 349–370 (1984).

[176]K. Makuch and B. Cichocki, "Transport properties of suspensions-critical assessment of Beenakker-Mazur method", The Journal of chemical physics **137**, 184902 (2012).

[177]C. Beenakker, "The effective viscosity of a concentrated suspension of spheres (and its relation to diffusion)", Physica A: Statistical Mechanics and its Applications **128**, 48–81 (1984).

[178]J. Riest, T. Eckert, W. Richtering, and G. Nägele, "Dynamics of suspensions of hydrodynamically structured particles: analytic theory and applications to experiments", Soft Matter **11**, 2821–2843 (2015).

[179]G. Nägele and J. Bergenholtz, "Linear viscoelasticity of colloidal mixtures", The Journal of Chemical Physics **108**, 9893–9904 (1998).

[180]A. J. Banchio, J. Bergenholtz, and G. Nägele, "Rheology and Dynamics of Colloidal Suspensions", Physical Review Letters **82**, 1792–1795 (1999).

[181]H. Senff and W. Richtering, "Temperature sensitive microgel suspensions: Colloidal phase behavior and rheology of soft spheres", The Journal of Chemical Physics **111**, 1705–1711 (1999).

[182]M. Stieger and W. Richtering, "Shear-Induced Phase Separation in Aqueous Polymer Solutions: Temperature-Sensitive Microgels and Linear Polymer Chains", Macromolecules **36**, 8811–8818 (2003).

[183]C. N. Likos, M Schmidt, H. Löwen, M. Ballauff, D. Pötschke, and P. Lindner, "Soft Interaction between Dissolved Flexible Dendrimers: Theory and Experiment", Macromolecules **34**, 2914–2920 (2001).

[184]C. N. Likos, S. Rosenfeldt, N. Dingenouts, M. Ballauff, P. Lindner, N. Werner, and F. Vögtle, "Gaussian effective interaction between flexible dendrimers of fourth generation: A theoretical and experimental study", The Journal of Chemical Physics **117**, 1869 (2002).

[185]B. Cichocki and B. U. Felderhof, "Diffusion of Brownian particles with hydrodynamic interaction and hard core repulsion", The Journal of Chemical Physics **94**, 556–562 (1991).

[186]M. Heinen, P. Holmqvist, A. J. Banchio, and G. Nägele, "Short-time diffusion of charge-stabilized colloidal particles: generic features", Journal of Applied Crystallography **43**, 970–980 (2010).

[187]C. C. Aburto and G. Nägele, "A unifying mode-coupling theory for transport properties of electrolyte solutions. II. Results for equal-sized ions electrolytes", The Journal of chemical physics **139**, 134110 (2013).

[188]W. T. Gilleland, S. Torquato, and W. B. Russel, "New bounds on the sedimentation velocity for hard, charged and adhesive hard-sphere colloids", Journal of Fluid Mechanics **667**, 403–425 (2011).

[189]J. Phalakornkul, A. Gast, R Pecora, G. Nägele, A Ferrante, B. Mandl-Steininger, and R Klein, "Structure and short-time dynamics of polydisperse charge-stabilized suspensions", Physical Review E **54**, 661–675 (1996).

[190]I. Moriguchi, "Self-diffusion coefficient in dense hard sphere colloids", The Journal of Chemical Physics **106**, 8624–8625 (1997).

[191]W. van Megen, S. M. Underwood, and I. Snook, "Tracer diffusion in concentrated colloidal dispersions", The Journal of Chemical Physics **85**, 4065–4072 (1986).

[192]W. van Megen and S. M. Underwood, "Tracer diffusion in concentrated colloidal dispersions. III. Mean squared displacements and self-diffusion coefficients", The Journal of Chemical Physics **91**, 552–559 (1989).

[193]P. Segrè, S. Meeker, P. Pusey, and W. Poon, "Viscosity and Structural Relaxation in Suspensions of Hard-Sphere Colloids", Physical Review Letters **75**, 958–961 (1995).

[194]A Weiss, N Dingenouts, M Ballauff, H. Senff, and W. Richtering, "Comparison of the Effective Radius of Sterically Stabilized Latex Particles Determined by Small-Angle X-ray Scattering and by Zero Shear Viscosity", Langmuir **14**, 5083–5087 (1998).

[195]R. A. Lionberger, "A Smoluchowski theory with simple approximations for hydrodynamic interactions in concentrated dispersions", Journal of Rheology **41**, 399–425 (1997).

[196]R. A. Lionberger and W. B. Russel, "Microscopic Theories of the Rheology of Stable Colloidal Dispersions", in *Advances in chemical physics*, Vol. 111, edited by I. Prigogine and S. A. Rice, Advances in Chemical Physics (John Wiley & Sons, Inc., Hoboken, NJ, USA, 1999), pp. 399–474.

[197]B. Cichocki and B. U. Felderhof, "Diffusion coefficients and effective viscosity of suspensions of sticky hard spheres with hydrodynamic interactions", The Journal of Chemical Physics **93**, 4427–4432 (1990).

[198]P. Holmqvist, *Private communication*, 2015.

[199]R. F. Probstein, *Physicochemical Hydrodynamics* (Butterworths, London, 1989).

[200]R. Roa, J. Riest, and G. Nägele, "Ultrafiltration modeling of charge-stabilized colloidal dispersions", in preparation (2016).

[201]R. K. Iler, *The Chemistry of Silica*, Solubility, Polymerization, Colloid and Surface Properties and Biochemistry of Silica (Wiley-Interscience, 1979).

[202]S. Alexander, P. M. Chaikin, P. Grant, G. J. Morales, P. Pincus, and D. Hone, "Charge renormalization, osmotic pressure, and bulk modulus of colloidal crystals: Theory", The Journal of Chemical Physics **80**, 5776–5781 (1984).

[203]E. Trizac, L. Bocquet, M. Aubouy, and H. H. von Grünberg, "Alexander's Prescription for Colloidal Charge Renormalization", Langmuir **19**, 4027–4033 (2003).

[204]J. Kierzenka and L. F. Shampine, "A BVP Solver Based on Residual Control and the Matlab PSE", ACM Transactions on Mathematical Software **27**, 299–316 (2001).

[205]E. Trizac, L. Belloni, J. Dobnikar, H. H. von Grünberg, and R. Castañeda-Priego, "Macroion virial contribution to the osmotic pressure in charge-stabilized colloidal suspensions", Physical Review E **75**, 011401 (2007).

[206]A. A. Louis, "Beware of density dependent pair potentials", Journal of Physics: Condensed Matter **14**, 9187–9206 (2002).

[207]A. R. Denton, "Electroneutrality and phase behavior of colloidal suspensions", Physical Review E **76**, 051401 (2007).

[208]A. R. Denton, "Coarse-Grained Modeling of Charged Colloidal Suspensions: From Poisson-Boltzmann Theory to Effective Interactions", in *Electrostatics of soft and disordered matter*, edited by D. Dean, J. Dobnikar, and A. Naji (Pan Stanford Publishing, 2012), p. 14.

[209]A. R. Denton, "Poisson–Boltzmann theory of charged colloids: limits of the cell model for salty suspensions", Journal of Physics: Condensed Matter **22**, 364108 (2010).

[210]D. Y. C. Chan, P. Linse, and S. N. Petris, "Phase Separation in Deionized Colloidal Systems: Extended Debye-Hückel Theory", Langmuir **17**, 4202–4210 (2001).

[211]D. Y. C. Chan, "Density functional theory of charged colloidal systems", Physical Review E **63**, 061806 (2001).

[212]J. Gapinski, G. Nägele, and A. Patkowski, "Freezing lines of colloidal Yukawa spheres. II. Local structure and characteristic lengths", The Journal of Chemical Physics **141**, 124505 (2014).

[213]J. G. Kirkwood and F. P. Buff, "The Statistical Mechanical Theory of Solutions. I", The Journal of Chemical Physics **19**, 774–777 (1951).

[214]N. Boon, G. I. Guerrero-García, R. van Roij, and M. Olvera de la Cruz, "Effective charges and virial pressure of concentrated macroion solutions", Proceedings of the National Academy of Sciences **112**, 9242–9246 (2015).

[215]R Castañeda-Priego, V Lobaskin, J. C. Mixteco-Sánchez, L. F. Rojas-Ochoa, and P Linse, "On the calculation of the structure of charge-stabilized colloidal dispersions using density-dependent potentials", Journal of Physics: Condensed Matter **24**, 065102 (2012).

[216]R. Castañeda-Priego, L. F. Rojas-Ochoa, V Lobaskin, and J. C. Mixteco-Sánchez, "Macroion correlation effects in electrostatic screening and thermodynamics of highly charged colloids", Physical Review E **74**, 051408 (2006).

[217]T. E. Colla, Y. Levin, and E. Trizac, "A self-consistent renormalized jellium approach for calculating structural and thermodynamic properties of charge stabilized colloidal suspensions", The Journal of Chemical Physics **131**, 074115 (2009).

[218]T. E. Colla, A. P. Dos Santos, and Y. Levin, "Equation of state of charged colloidal suspensions and its dependence on the thermodynamic route", Journal of Chemical Physics **136** (2012) 10.1063/1.4718367.

[219]B. Cichocki, M. L. Ekiel-Jezewska, P. Szymczak, and E. Wajnryb, "Three-particle contribution to sedimentation and collective diffusion in hard-sphere suspensions", The Journal of Chemical Physics **117**, 1231–1241 (2002).

[220]J. Gapinski, A. Wilk, A. Patkowski, W. Häußler, A. J. Banchio, R. Pecora, and G. Nägele, "Diffusion and microstructural properties of solutions of charged nanosized proteins: Experiment versus theory", The Journal of Chemical Physics **123**, 054708 (2005).

[221]Berli, C. L. A, J. A. Deiber, and D. Quemada, "On the viscosity of concentrated suspensions of charged colloids", Latin American Applied Research **35**, 15–22 (2005).

[222]A.-S. Jönsson and B. Jönsson, "Ultrafiltration of Colloidal Dispersions - A Theoretical Model of the Concentration Polarization Phenomena", Journal of Colloid and Interface Science **180**, 504–518 (1996).

[223]M. Mondor and C. Moresoli, "Theoretical analysis of the influence of the axial variation of the transmembrane pressure in cross-flow filtration of rigid spheres", Journal of Membrane Science **152**, 71–87 (1999).

[224]M. Mondor and C. Moresoli, "Effect of fiber lumen radius on the permeate flux of hollow fiber membrane modules", Desalination **191**, 365–370 (2006).

[225]R. Roa, D. Menne, P. Buzatu, J. Riest, J. K. G. Dhont, E. K. Zholkovskiy, M. Wessling, and G. Nägele, "Ultrafilltration of charge-stabilized colloidal dispersions at low salinity", to be submitted (2015).

[226]G. Belfort, R. H. Davis, and A. L. Zydney, "The behavior of suspensions and macromolecular solutions in crossflow microfiltration", Journal of Membrane Science **96**, 1–58 (1994).

[227]A. J. Schmid, J. Riest, T. Eckert, P. Lindner, G. Naegele, and W. Richtering, "Comparison of the Microstructure of Stimuli Responsive Zwitterionic PNIPAM-co-Sulfobetaine Microgels with PNIPAM Microgels and Classical Hard-Sphere Systems", Zeitschrift für Physikalische Chemie **228**, 1033–1052 (2014).

[228]R. J. Baxter, "Percus–Yevick Equation for Hard Spheres with Surface Adhesion", The Journal of Chemical Physics **49**, 2770–2774 (1968).

[229]T. Jiang and J. Wu, "Cluster formation and bulk phase behavior of colloidal dispersions", Physical Review E **80**, 021401 (2009).

[230]J. C. F. Toledano, F. Sciortino, and E. Zaccarelli, "Colloidal systems with competing interactions: from an arrested repulsive cluster phase to a gel", Soft Matter **5**, 2390–2398 (2009).

[231]J.-M. Bomont and J.-L. Bretonnet, "A consistent integral equation theory for hard spheres.", The Journal of chemical physics **121**, 1548–52 (2004).

[232]J.-M. Bomont, "Excess chemical potential and entropy for pure fluids", The Journal of Chemical Physics **119**, 11484 (2003).

[233]J. M. Kim, R. Castañeda-Priego, Y. Liu, and N. J. Wagner, "On the importance of thermodynamic self-consistency for calculating clusterlike pair correlations in hard-core double Yukawa fluids", The Journal of Chemical Physics **134**, 064904 (2011).

[234]*GSL - GNU Scientific Library*, 2013.

[235]B. Cichocki and B. U. Felderhof, "Self-diffusion of Brownian particles with hydrodynamic interaction and square step or well potential", The Journal of Chemical Physics **94**, 563–568 (1991).

[236]C. Van Den Broeck, "An exact result for the incoherent scattering function in dilute suspensions", The Journal of Chemical Physics **82**, 4248–4253 (1985).

[237]A. Moncho-Jordá, A. A. Louis, and J. T. Padding, "Effects of Interparticle Attractions on Colloidal Sedimentation", Physical Review Letters **104**, 068301 (2010).

[238]P. N. Pusey, "Intensity fluctuation spectroscopy of charged Brownian particles: the coherent scattering function", Journal of Physics A: Mathematical and General **11**, 119–135 (1978).

[239]M. H. G. Duits, R. P. May, A Vrij, and C. G. De Kruif, "Small-angle neutron scattering of concentrated adhesive-hard-sphere dispersions", Langmuir **7**, 62–68 (1991).

[240]A. J. Banchio, M. G. McPhie, and G. Nägele, "Hydrodynamic and electrokinetic effects on the dynamics of charged colloids and macromolecules", Journal of Physics: Condensed Matter **20**, 404213 (2008).

[241]A. L. Kholodenko and J. F. Douglas, "Generalized Stokes-Einstein equation for spherical particle suspensions", Physical Review E **51**, 1081–1090 (1995).

[242]A. Gaigalas, V. Reipa, J. Hubbard, J. Edwards, and J. Douglas, "A non-perturbative relation between the mutual diffusion coefficient, suspension viscosity, and osmotic compressibility: Application to concentrated protein solutions", Chemical Engineering Science **50**, 1107–1114 (1995).

[243]S. B. Dubin, "Measurement of the Rotational Diffusion Coefficient of Lysozyme by Depolarized Light Scattering: Configuration of Lysozyme in Solution", The Journal of Chemical Physics **54**, 5158 (1971).

[244]K. Gekko and H. Noguchi, "Compressibility of globular proteins in water at 25°C", The Journal of Physical Chemistry **83**, 2706–2714 (1979).

[245]*HOOMD-blue, available online at: http://codeblue.umich.edu/hoomd-blue*, 2015.

[246]J. Glaser, T. D. Nguyen, J. A. Anderson, P. Lui, F. Spiga, J. A. Millan, D. C. Morse, and S. C. Glotzer, "Strong scaling of general-purpose molecular dynamics simulations on GPUs", Computer Physics Communications **192**, 97–107 (2015).

[247]J. A. Anderson, C. D. Lorenz, and A. Travesset, "General purpose molecular dynamics simulations fully implemented on graphics processing units", Journal of Computational Physics **227**, 5342–5359 (2008).

[248]J. S. Myung, R. G. Winkler, and G. Gompper, "Self-organization in suspensions of end-functionalized semiflexible polymers under shear flow", The Journal of Chemical Physics **143**, 243117 (2015).

[249]G Gompper, T Ihle, D. M. Kroll, and R. G. Winkler, "Multi-Particle Collision Dynamics: A Particle-Based Mesoscale Simulation Approach to the Hydrodynamics of Complex Fluids", in *Advanced computer simulation approaches for soft matter sciences iii*, Vol. 221, edited by C. Holm and K. Kremer, Advances in Polymer Science (Springer Berlin Heidelberg, 2009), pp. 1–87.

[250]S. P. Singh, R. G. Winkler, and G. Gompper, "Nonequilibrium forces between dragged ultrasoft colloids", Physical Review Letters **107**, 1–5 (2011).

[251]M. Ripoll, P. Holmqvist, R. G. Winkler, G. Gompper, J. K. G. Dhont, and M. P. Lettinga, "Attractive colloidal rods in shear flow", Physical Review Letters **101**, 15–18 (2008).

[252]A. Wysocki, C. P. Royall, R. G. Winkler, G. Gompper, H. Tanaka, A. van Blaaderen, and H. Löwen, "Multi-particle collision dynamics simulations of sedimenting colloidal dispersions in confinement", Faraday Discuss. **144**, 245–252 (2010).

[253]J. Elgeti, R. G. Winkler, and G. Gompper, "Physics of microswimmers - single particle motion and collective behavior: a review", Reports on Progress in Physics **78**, 056601 (2015).

[254]J. Hu, M. Yang, G. Gompper, and R. G. Winkler, "Modelling the Mechanics and Hydrodynamics of Swimming E. coli", Soft Matter **11**, 7867–7876 (2015).

[255]J. Riest, S. Das, G. Gompper, G. Nägele, and R. G. Winkler, "Simulation and theory of generalized Lennard-Jones Yukawa systems with competing interactions", in preparation.

[256]K. Zahn, J. Méndez-Alcaraz, and G. Maret, "Hydrodynamic Interactions May Enhance the Self-Diffusion of Colloidal Particles", Physical Review Letters **79**, 175–178 (1997).

[257]R. Cohen and R. Probstein, "Colloidal fouling of reverse osmosis membranes", Journal of Colloid and Interface Science **114**, 194–207 (1986).

[258]R. Roa, F. Carrique, and E. Ruiz-Reina, "Ion size effects on the electric double layer of a spherical particle in a realistic salt-free concentrated suspension", Physical Chemistry Chemical Physics **13**, 9644–9654 (2011).

[259]G. Nägele and P. Baur, "Influence of hydrodynamic interactions on long-time diffusion in charge-stabilized colloids", Europhysics Letters (EPL) **38**, 557–562 (1997).

[260]M Rex and H Löwen, "Dynamical density functional theory for colloidal dispersions including hydrodynamic interactions", The European Physical Journal E **28**, 139–146 (2009).

[261] J. Rieger, *Private communication*, 2014.

Acknowledgments

First of all, I would like to thank Gerhard Nägele for his enthusiastic supervision and guidance in the past 3 years. He not only provided me with an interesting and versatile research project, but encouraged me to pursue my own ideas. Based on his broad knowledge and experience, he always provided valuable input by constructively questioning every result and offering plenty of time for discussions. Especially, his curiosity driven approach to science has been very inspiring to me and created a very good working atmosphere. To cite one of our referees: "It was joyful to" work with you.
In particular, I would like to thank Gerhard and Jan Dhont for the sympathy and the flexibility they offered me, e.g., during the pregnancy of my wife which has been a tremendous help. I am grateful to Jan as well for the great time I have in his group and for giving me the opportunity to attend several conferences.
In addition, I would like to express my gratitude to Hartmut Löwen for having accepted to review my thesis.
I want to thank Andreas J. Schmid, Thomas Eckert, and Walter Richtering for the good collaboration and for providing me with the DLS data of non-ionic microgels.
I am grateful to our American collaborators, Yun Liu, Doug Godfrin and Norman J. Wagner for sharing their knowledge about dynamic clustering in protein suspensions with us, and I am looking forward to intensify our collaboration in the future.
I would like to thank Shibanandan Das and Roland G. Winkler for their willingness to share their expertise in computer simulations with us to explore the dynamics in clustering systems. I am very confident that the combination of simulation and theory will be able to make an important contribution to this topic. In addition, I thank Shiba for allowing me to use his code for the analysis of the cluster-size distribution function.
I acknowledge the support of the International Helmholtz Research School of Biophysics and Soft Matter (BioSoft) and would like to thank, in particular, Thorsten Auth for his effort to organize the school.
Marco Heinen is thanked for the helpful discussions at the beginning of my Phd work and for providing me with his notes and benchmark results for the validation of my code.
I would like to thank the whole ICS-3 for the nice atmosphere which made it very easy to work in the group. In addition, I appreciated it very much that everyone was always willing to answer questions or to assist with his expertise where needed. In particular, I thank Marie for her help with all bureaucratic issues and her support in all questions regarding the life in and around Jülich. My special thanks go to Rafael Roa, with whom

I shared the office in the past three years. You have been a very pleasant officemate, a skilled collaborator and became a good friend.
I am also grateful to the supervisor of my Bachelor and Master theses, Christos N. Likos. At a very early stage, he gave me the opportunity to participate in conferences and summer schools which allowed me to get a broader perspective of the field of soft matter. In addition, he provided me with interesting projects stimulating my interest in research.
A special thanks to my parents who have always supported my personal development and provided me with the opportunity to study abroad.
I would like to thank my wife, Carina, for her absolute support and especially patience. Last but not least, I would like to thank my daughter, Mathilda, who teaches me every morning what really matters in life when she smiles at me.

Eidesstattliche Versicherung

Ich versichere an Eides Statt, dass die Dissertation von mir selbstständig und ohne unzulässige fremde Hilfe unter Beachtung der "Grundsätze zur Sicherung guter wissenschaftlicher Praxis an der Heinrich-Heine-Universität Düsseldorf" erstellt worden ist.
Des Weiteren wurde die Dissertation in der vorgelegten oder in ähnlicher Form noch bei keiner anderen Institution eingereicht und ich habe bisher keine erfolglosen Promotionsversuche unternommen.

Düsseldorf, den 22.02.2016

Jonas Riest